

THE UNIVERSITY OF ASTON IN BIRMINGHAM

MEASUREMENT OF FAST NEUTRON SPECTRA

FROM EXTENDED SAMPLES

Thesis submitted for the Degree

of

Doctor of Philosophy

by

Abdul Wahid R. Al-Saji, B.Sc., M.Sc.

January 1976

196316 - 6 AUG 1976
539.1251625AL
Department of Physics

ABSTRACT

The scattering of fast neutrons after passing through LiF and iron materials that are of possible use in the future fusion reactors has been studied at an incident neutron energy of 14.1 MeV using a neutron spectrometer employing the associated particles time-of-flight technique. The neutrons were produced by the $T(d,n)^4\text{He}$ reaction using a 150 KV SAMES accelerator. The time of origin of the neutron was determined by detecting the associated alpha particles, and the neutron energy was determined by measuring its flight time over a fixed flight path. The angular energy distribution of fast neutrons after passing through samples of LiF and Fe were measured at several scattering angles. Fast neutron detection and associated alpha particle detection was by means of scintillation counters employing plastic scintillator type NE-102A. The samples used were of extended slab geometry of thickness approximately two mean free paths for Fe and of approximately one mean free path for LiF.

Theoretical calculations based on primary and secondary scatter models have been carried out in the present work for computing the emerging flux from different thicknesses of LiF and Fe samples. The cross-section data and the angular energy distribution probabilities data for ^6Li , ^7Li , ^{19}F and Fe were obtained from U.K.N.D.L. file.

Experimental results show a reasonably good agreement with the theoretical results predicted by taking into account first and second scatters only, the predominant reaction being elastic scattering.

ACKNOWLEDGEMENTS

I am very much indebted to my supervisor, Dr. P.N. Cooper, for his continuous guidance and help throughout the period of this research. Thanks are also due to Professor S.E. Hunt for his interest in the work.

I would like to thank Mr. J. Phull and Mr. H. Biggs, the laboratory technical staff, for their help in the maintenance of the accelerator during the measurements.

I am grateful to the Iraqi Atomic Energy Commission for financial assistance.

TABLE OF CONTENTS

	page
CHAPTER 1 INTRODUCTION	
1.1 Introduction	1
1.2 The Research Project	2
1.3 Practical Applications	4
CHAPTER 2 NEUTRON INTERACTIONS WITH MATTER	
2.1 Introduction	6
2.2 Elastic Scattering (n,n)	7
2.3 Inelastic Scattering (n,n ¹)	9
2.4 Neutron absorption reaction (nf), (n,p), (n,α), (n,γ)	11
CHAPTER 3 NEUTRON DETECTION	
3.1 Introduction	13
3.2 Choosing the detector	14
3.3 Recoil proton energy spectrum	16
3.4 NE-102A Scintillator	17
3.5 Scintillator Efficiency	18
3.5.1 Non-linear responses of Scintillators	19
3.5.2 Detector efficiency with discrimination	22
3.6 The Scintillator-photomultiplier coupling	25
3.7 Magnetic field effect	26
3.8 Neutron detector shielding	27
3.8.1 Neutron shielding materials	28
3.8.2 The shadow bar position	30

TABLE OF CONTENTS (CONTD)

	page
CHAPTER 4 THE NEUTRON PRODUCTION	
4.1 Introduction	31
4.2 S.A.M.E.S. Accelerator and the target assembly	31
4.3 The $T(d,n)^4He$ reaction	32
4.3.1 Kinematics of $T(d,n)^4He$ reaction	33
4.3.2 Angular relationship of the associated particles	34
4.4 The neutron yield	35
4.5 The alpha-particle detector	37
4.6 Alpha-detector shielding	40
CHAPTER 5 THE TIME-OF-FLIGHT TECHNIQUE AND THE EXPERIMENTAL ARRANGEMENTS	
5.1 Introduction	42
5.2 Experimental considerations for the associated particle method	46
5.3 Time-of-flight spectrometer electronics	47
5.4 Discrimination adjustment	48
5.5 Time-to-pulse-height converter	49
5.6 The spectrometer resolution	50
5.7 Experimental efficiency of the neutron detector	51
5.8 Energy calibration of the spectrometer	57
CHAPTER 6 THEORETICAL CONSIDERATIONS	
6.1 Introduction	60
6.2 Consideration of possible reaction to be seen	61
6.3 Single and secondary scattering	70
6.4 Flux Computing Programmes	76

TABLE OF CONTENTS (CONTD)

	page
CHAPTER 7	EXPERIMENTAL AND THEORETICAL RESULTS
7.1	Introduction 78
7.2	Conversion of pulse-height analyser spectra to energy spectra 81
7.3	The measured spectra from LiF samples 83
7.4	The measured spectra from Fe samples 84
7.5	Results of Computer programme 85
7.6	Comparison of experimental and computer results 89
CHAPTER 8	CONCLUSIONS 93
<u>APPENDIX 1</u>	Mathematical derivation of neutron energy from the $T(d,n)^4\text{He}$ reaction 97
<u>APPENDIX 2</u>	Programme NREACTION: computing the neutron energy as a function of angle from the $T(d,n)^4\text{He}$ reaction 104
<u>APPENDIX 3</u>	Programme ONESCAT: Computing the elastic angular energy spectrum from the primary scatter model 105
<u>APPENDIX 4</u>	Programme TWOSCAT: Computing the elastic angular energy spectrum from the secondary scatter model 108
<u>APPENDIX 5</u>	Programme SPECTRUM: Computing the angular energy spectrum from the $(n,n\alpha)$, (n,n^1) , $(n,2n)$ reactions using the primary scatter model 111
<u>REFERENCES</u>	112

FIGURES

Figures in general, are placed after the page where they are first mentioned and discussed.

INTRODUCTION

1.1 Introduction

The study of fast neutron spectra after passing various thicknesses of different materials which are of interest in nuclear technology ^(1,2) is of great importance in the design of nuclear reactors. The most important characteristic of the neutron flux outside shielding is its angular energy distribution. The angular flux emerging from a shield does not directly tell about gamma ray production which must occur within the shield but by measuring the angular flux outside the shield, the internal flux could be deduced by setting up a calculation model for the external flux which will then be able to predict the internal flux and hence gamma ray production. Such a measurement is most suitable for thinner shields with large leakage.

Neutrons having energies of 14 MeV are not directly important for shields and blankets of fission reactors, since they are above the extreme top end of the fission spectrum, but they are extremely important for possible future fusion reactors.. The relevant fields of applications for these materials are the blanket and the structure vessel of the fusion reactor.

1.2 The Research Project

The principle objective of the present work was to study the angular energy distribution spectra of the 14 MeV neutrons after being scattered from various thicknesses of different materials which are of interest for future fusion reactors.

It is very important to collect more experimental data on the angular energy distribution spectra of the 14 MeV neutrons after being scattered by these materials of interest which then provide information by which the theoretical calculations adopted here could be tested. Theoretical predictions of the angular distribution for the fast neutrons when compared with the experiment may yield further information of the behaviour of fast neutrons in the materials of interest, but the extent of this must depend on the accuracy with which the experimental data can be obtained.

Neutron energy is often determined in scattering studies by measuring the neutron time of flight over a known flight path. The time of flight technique requires two timing signals, one related to the instant of neutron production (zero time) and the second related to the instant of detection. The accuracy of detecting the start-to-stop signals and the accuracy of the associated electronics determines the spectrometer energy resolution which in effect determines the accuracy of the data collected throughout the experiment.

14 MeV neutrons from $T(d,n)^4\text{He}$ reaction have been used to study neutron energy spectra after being scattered by

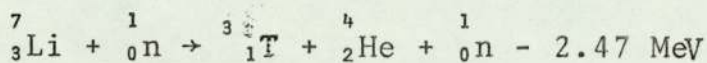
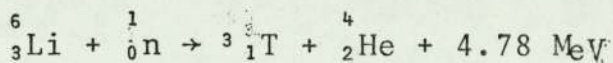
samples of LiF and Fe. These two samples were chosen because of their possible use in the future fusion reactors as coolant and structure.

The angular energy distribution was measured by moving the neutron detector through different angles with respect to the sample position. Different thicknesses of both LiF and Fe samples were used, experimental data also provides information about the cross-section, since the cross-section is the probability of interaction that is measured by the fraction of neutrons scattered from the sample in a given direction.

The angular energy distribution of the scattered neutrons from both LiF and Fe was obtained using an associated particle time-of-flight spectrometer to separate the neutrons of different energies. The thickness of the scattering samples used was about one mean free path for LiF sample and about two mean free paths for Fe. Multiple scattering for sample thickness less than even .1 mean free path was appreciable⁽³⁾, so neutrons scattered by such sample thicknesses are going to suffer secondary and multiple scattering. The study of the angular energy distribution of fast neutrons after they suffer single and secondary scattering is carried out in this project. A theory based on the single and secondary scattering of neutrons from an extended sample was used here for the calculation of the angular energy distribution of the scattered neutrons.

1.3 Practical Application

The lithium fluoride and steel samples were chosen in the present work due to their useful applications in the future fusion reactors. A fusion reactor using the deuterium-tritium fuel cycle may have a cross-sectional appearance like that shown in figure 1.1⁽⁴⁾. The plasma is confined in the centre of the reactor by the magnetic coils on the outside^(5,6,7). The neutrons produced from the D-T reaction that carries 80% of the reaction energy⁽⁸⁾ are absorbed in a liquid lithium blanket surrounding the plasma according to the reactions



lithium contains 7.56% ${}^6\text{Li}$ and 92.44% ${}^7\text{Li}$. ${}^6\text{Li}$ has a very high (n,α) cross-section at thermal neutron energies but at 14 Mev the (n,nα) cross-section for ${}^7\text{Li}$ is about 12 times the (n,α) cross-section for ${}^6\text{Li}$. The above reactions breed tritium some of which is re-used in the fuel cycle. The lithium used in the blanket will probably be in the form of molten lithium fluoride which will act as a moderator and neutron absorber that receives the high-energy neutron of the D.T. reaction and converts their kinetic energy to heat. The energy generated in the lithium fluoride acts as the heat source for the power plant. Another form of molten lithium

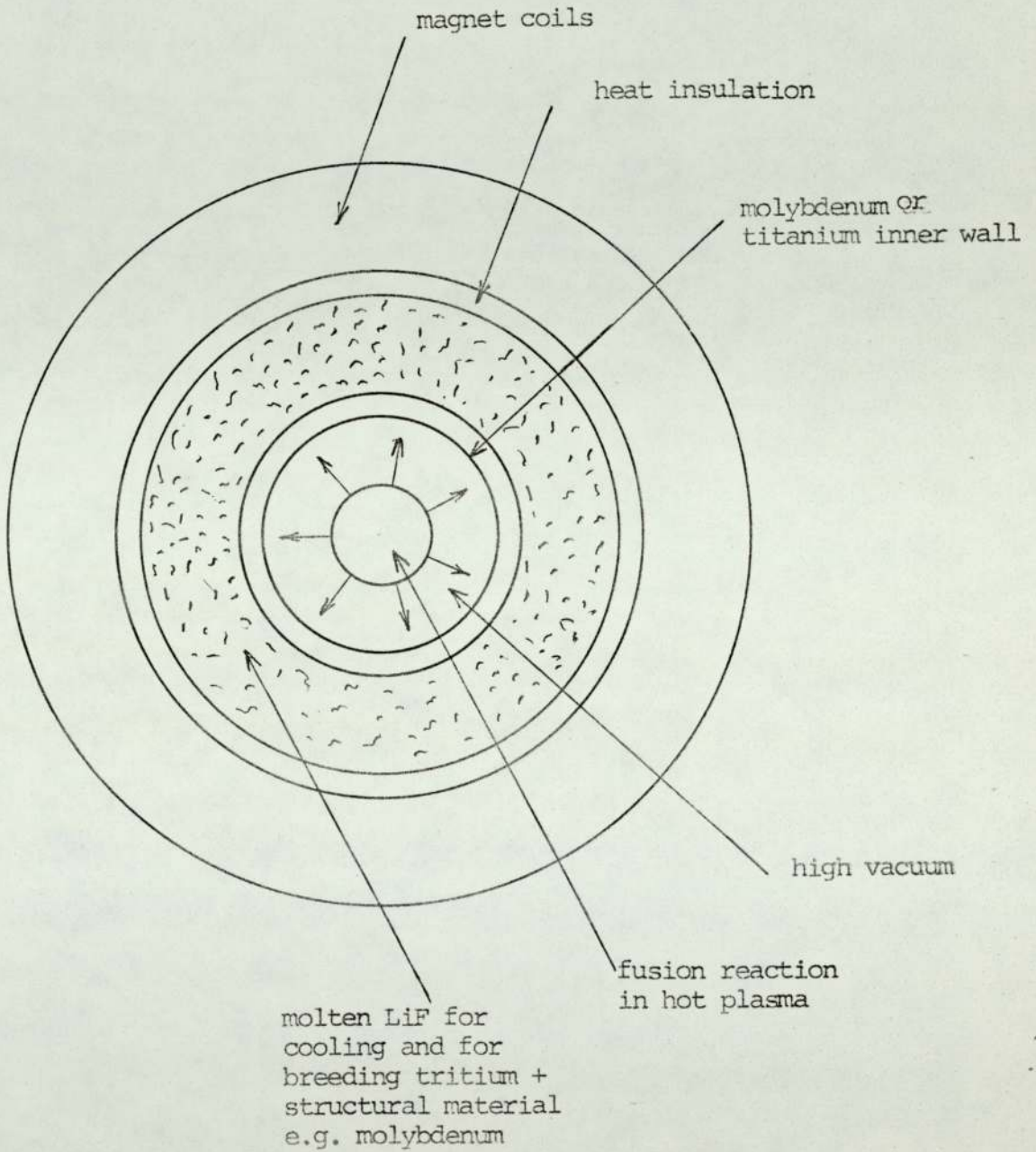


Fig. 1.1 Cross section of a possible fusion reactor

of possible use is the LiF-BeF₂ (colloquially called FLIBE) proposed because of the reaction ${}^9\text{Be} + n \rightarrow {}^4_2\text{He} + 2n - 1.57 \text{ MeV}$ which provides extra neutrons for tritium breeding. Structural materials that are of possible use in future fusion reactors must resist radiation damage and corrosion, and have low vapour pressure. Niobium, molybdenum, titanium and steel are likely candidates as structural materials.

CHAPTER 2

NEUTRON INTERACTION WITH MATTER

2.1 Introduction

The interaction of neutrons in passing through matter is quite different from that of either charged particles or gamma rays. Since neutrons have no charge they can penetrate the electron clouds and collide with the nuclei. The nature of neutron interaction depends on the neutron energy and on the matter through which they pass. Neutrons interact with nuclei in a variety of ways. They may change direction, lose energy, or may be absorbed (⁹). If the nucleus is unchanged in either isotopic composition or internal energy after interacting with a neutron, the process is called elastic scattering and may be written as (n,n) . If the nucleus, still unchanged in composition, is left in an excited state the process is called inelastic scattering (n,n^1) .

In referring to these interactions it is common to say that the incident neutron has been scattered (elastically or inelastically), since a neutron reappears after the interaction, however this term is somewhat misleading since the emerging neutron may not be the same neutron that originally struck the nucleus. Neutrons may disappear as a result of absorption reactions, the most important of which in most nuclei at lower neutron energies is the (n,γ) reaction. This process is called radiative capture since one of the products is γ -radiation. Neutrons also disappear in charged particle reactions such as (n,p) or (n,α) reactions. When neutrons

of high energy strike a nucleus two or more neutrons are emitted. These are (n,2n) or (n,3n) reactions. The (n,pn) reaction may also occur with high-energy incident neutrons. A description of these processes follows.

2.2 Elastic Scattering (n,n)

In this type of scattering kinetic energy is conserved and the energy level of the target nucleus is the same before and after the collision⁽¹⁰⁾. Elastic scattering is the dominant mode of neutron interaction when moderate neutron energies are involved (<10 Mev) in a non-absorbing medium.⁽¹¹⁾ In this reaction the neutron will transfer part of its kinetic energy to the nucleus. The amount of energy transferred will depend upon the angle through which the neutron is scattered and upon the mass of the scattering nucleus.

The relationship between the scattering angle ϕ and the energy of the neutron before and after collision with a nucleus of mass number A may be derived from the conservation laws of energy and momentum. If an incident neutron has an energy E_1 before collision then the neutron energy after collision E_2 is given by ⁽¹²⁾

$$E_2 = E_1 \left| \frac{A^2 + 2A \cos \phi + 1}{(A+1)^2} \right| \quad \text{_____} \quad 2.1$$

Where ϕ is the angle of scattering in C-M system.

If θ is this angle in the lab-system then the relationship between the angle in C-M system and the Lab-system is given by

$$\cos \theta = \frac{1+A \cos \phi}{\sqrt{A^2+2A \cos \phi+1}} \quad \text{_____} \quad 2.2$$

From equation 2.1 and equation 2.2 the neutron energy after collision E_2 in the lab-system is given by

$$E_2 = E_1 \left| \frac{A^2 + 2\sqrt{A^2 - \sin^2 \theta} \cos \theta + \cos 2\theta}{(A+1)^2} \right| \quad \text{_____} \quad 2.3$$

When $\phi = 180^\circ$ $\theta = 180^\circ$ and when $\phi = 0$ $\theta = 0$

But for all other angles θ is less than ϕ .

From equation 2.3 it can be seen that the energy of the scattered neutron is greatest for $\theta = 0^\circ$ that is

$$(E_2)_{\max} = E_1 \quad \text{_____} \quad 2.4$$

i.e. no scatter. The minimum value of E_2 occurs when $\theta = 180^\circ$ that is

$$(E_2)_{\min} = \alpha E_1 \quad \text{_____} \quad 2.5$$

$$\text{where } \alpha = \left(\frac{A-1}{A+1} \right)^2 \quad \text{_____} \quad 2.6$$

The minimum energy of a neutron after an elastic collision depends on the mass of the struck nucleus. For hydrogen with mass $A=1$ a neutron can lose all its energy in one collision. In collisions with heavier nuclei a neutron loses a fraction of its energy so the maximum fractional energy loss in a single collision decreases with the increasing mass of the struck nucleus. Elastic scattering may be potential scattering, which corresponds to an interaction in which the incident neutron is not assimilated by the target to form a compound nucleus and without sharing its energy with nucleons of the target, is scattered much as it would be by a potential well, or it may be resonance scattering in which the neutron is assimilated by the nucleus which subsequently

decays by giving off a neutron with energy equivalent to that carried into the nucleus by the incident neutron.

Neutron angular distributions in the resonance scattering in isotropic in the C-M system. In the potential scattering neutrons are forward peaking and this becomes more pronounced as energy increases (at 14 Mev Li and F have very strongly forward peaked distributions).

2.3 Inelastic Scattering (n, n^1)

(n, n^1) becomes energetically possible when the neutron energy E_n is great enough to raise the nucleus above its first excited level. The excited nucleus may decay to the ground state by the emission of one or more gamma rays and the energy of the emitted neutron E is given as the difference between its incident energy E_n and the energy of the first excited level E_1 , $E = E_n - E_1$.

The minimum or threshold energy which the neutron must have to make the inelastic scattering process energetically possible is given by

$$E_{th} = \frac{A+1}{A} E_{ex}$$

where E_{th} = inelastic threshold energy

A = mass of the target nucleus

E_{ex} = the energy of an excited state of the target nucleus.

The relative spacing of the energy levels of an isotope determines the threshold neutron energy for inelastic scattering, Level spacings are wide in light nuclei and the stable magic nuclei and hence the interaction energy threshold is high and

decay is more likely to be by emission of a small number of high energy γ -rays. As the spacings get closer together (heavier isotopes of high excitation energies) their width may overlap so that the γ -rays emission spectrum essentially forms a continuum.

Neutrons which are inelastically scattered by heavy nuclei can undergo large fractional energy losses until they are scattered below the inelastic thresholds. This energy loss mechanism can be much more effective for high energy neutrons than elastic scattering by light nuclei and can be an important process in designing fast neutron shields.

2.3.1 The $(n,2n)$ and $(n,3n)$ reactions.

When the incident neutron has an energy greater than the binding energy of the last neutron in the nucleus, the emission of two neutrons becomes possible. In the $(n,2n)$ reaction the incident neutron is inelastically scattered by the target nucleus, then if the residual nucleus is left with an excitation energy above the binding energy of its least bound neutrons, this neutron has sufficient energy to escape from the system, that is there is a possibility that a second neutron will appear. The $(n,2n)$ reaction rapidly becomes more probable than the (n,n^1) reaction as the incident neutron energy rises. Therefore the bulk of the inelastic scattering is now included as part of the $(n,2n)$ reaction. The Q value of the $(n,2n)$ reaction is equal to the binding energy of the loosest neutron in the target nucleus and the threshold energy in the Laboratory system is given by

$$E_{th} = \frac{A+1}{A} Q$$

where A is the mass of the target nucleus.

The threshold energy is low for nuclei which contain a loosely bound neutrons, an example being the $(n,2n)$ threshold for ${}^9\text{Be}$ is 1.8 MeV. With most nuclei however the $(n,2n)$ threshold is in the range from about 7 to 10 MeV. In the case of $(n,3n)$ reaction the relationship of the $(n,3n)$ reaction to the $(n,2n)$ reaction is similar to that of the $(n,2n)$ and the (n,n^1) reaction. Thus a third neutron will be emitted if the target nucleus still has sufficient excitation energy after the emission of the second neutron in the $(n,2n)$ reaction to free a further neutron. The $(n,3n)$ cross section therefore rises from the $(n,2n)$ threshold at the expense of the $(n,2n)$ cross section as shown in figure 2.1. The $(n,3n)$ threshold is so high (it ranges from 11 MeV to 30 MeV) that makes this reaction unimportant in fission reactor calculation but it may have some significance for fusion reactors.

2.4 NEUTRON ABSORPTION REACTIONS (n,f) , (n,p) , (n,α) , (n,γ)

Neutrons may disappear as a result of being absorbed by the nuclei of the medium, some of the more common reactions are:

(a) Fission Reaction (n,f)

The type of neutron interaction of immediate interest is the nuclear fission reaction. In the fission process the nucleus absorbs a neutron and the resulting compound nucleus is so unstable that it immediately breaks up into two parts of more or less equal mass called fission fragments⁽¹³⁾. The probability of neutron induced fission is described by

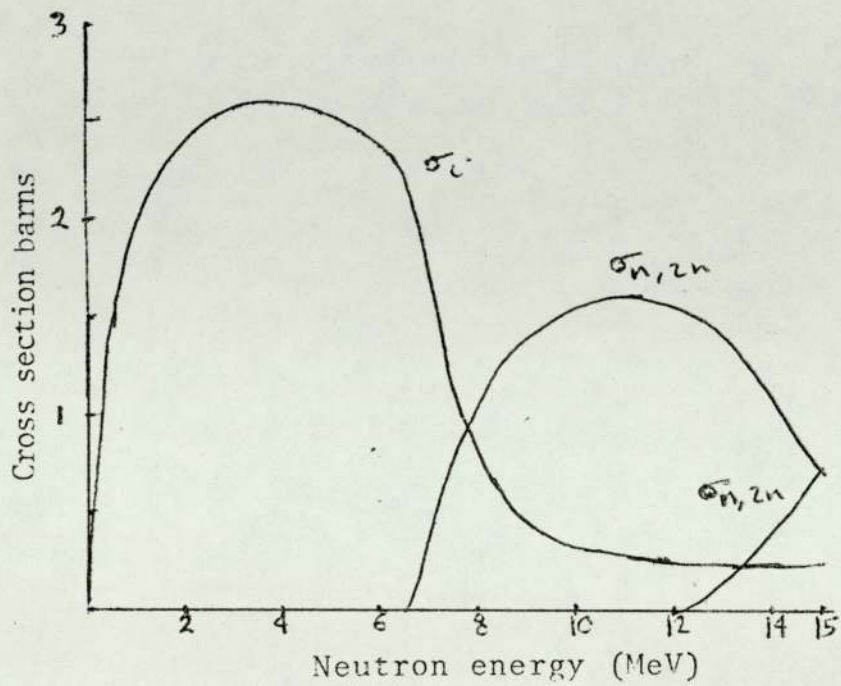
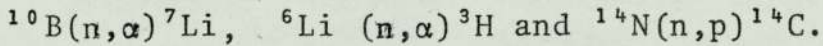


Fig. 2.1 The inelastic (n,2n) and (n,3n) Cross-section of ^{238}U (Lamarsh 1966)

the fission cross section σ_f and it is a function both of the target nucleus and the energy of the incident neutron.

(b) Charged-particle reaction (n,p), (n, α)

These reactions are usually endothermic. However, in the case of few light nuclei they are exothermic, examples of the exothermic reaction are the



An endothermic reaction type is thus $^{16}\text{O}(n,p)^{16}\text{N}$, these reactions are useful in the way they do not give rise to energetic γ -rays after they absorb the neutrons.

(c) Radiation Capture (n, γ)

This process can occur at all neutron energies but it is most probable at low energies (less than 1 KeV). If instead of expelling a neutron the excited compound nucleus formed by the absorption of a neutron emits its excess energy in the form of γ -radiation the process is referred to as radiation capture. The residual nucleus, having an additional neutron, is thus an isotope of the original nucleus but one unit higher in mass number.

The reactions mentioned are not the complete list, (n,d), (n,n α) for example are other possible reactions.

CHAPTER 3

NEUTRON DETECTION

3.1 Introduction

All methods of detecting nuclear particles and radiations are based on the fact that charged particles cause ionization when passing through matter. If the particle of interest is neutral, and does not therefore cause ionization directly, an intermediate process is necessary in which an energetic charged particle is produced. Neutrons differ from other types of radiation considered in that their primary interactions are with the nuclei rather than with the atomic electrons. Being uncharged massive particles they can penetrate the electron clouds and collide with the nuclei. The neutron interactions with nuclei are of two types, scattering or absorption. In the scattering type the neutron collides with the nucleus and a fraction of the neutron energy is transferred to the recoil nucleus. In the absorption type the neutron is absorbed by the nucleus and disappears. The most important scattering process is the elastic scattering of neutrons by proton $H(n,n)H$ reaction. Neutrons are elastically scattered by all nuclei but the energy transfer to the recoil nucleus is a maximum for neutron-proton scattering. Hence this process is the most widely used for the detection of fast neutrons. In many cases the proper selection and use of the detection method depends on the type, purpose, and the environment of the experiment. The detection system has to

take into consideration the following; the energy range of neutrons to be measured, the flux of neutrons and its variation, the detector sensitivity and the energy resolution, and finally the detector sensitivity to the neutrons in the presence of other nuclear radiation.

3.2. Choosing the Detector

A great variety of methods have been used to measure the energy spectra of fast neutrons⁽¹⁴⁾. Then techniques (usually of low efficiency) include nuclear emulsions⁽¹⁵⁾, proton recoil telescopes⁽¹⁶⁾ and ³He filled proportional counters.⁽¹⁷⁾ For the fast neutrons the elastic scattering from hydrogen nuclei which gives rise to detectable recoil protons is the basis for fast neutron detection with organic scintillators which are known to have the highest efficiency for the detection of fast neutrons because of their high hydrogen content, high density compared with gases and the relatively large cross-sections for neutron-proton elastic scattering. Organic materials include plastics, organic liquids and organic crystals such as anthracene or stilbene. The recoil protons produce scintillations which can be detected using a photomultiplier tube, ⁽¹⁸⁾.

A nuclear particle incident on a scintillation detector produces a flash of light in the scintillator and this light is transmitted to the photocathode of the photomultiplier tube.⁽¹⁹⁾ The photoelectrons emitted at the photocathode are multiplied typically 10^6 to 10^8 times by means of the electron-multiplier section of the photomultiplier tube giving a large pulse at

the anode. Some organic crystals, and liquids and plastics with suitable additives emit light when bombarded with nuclear radiation in response to either primary or secondary ionization induced by the radiation. A number of these scintillators have found widespread use in nuclear spectroscopy⁽²⁰⁾ because they possess desirable physical characteristics, exhibit good detection efficiency and their response times allow relatively simple derivation of fast timing signals. Among these different scintillators the ones which have found wide application as neutron detectors in neutron time-of-flight spectrometers⁽²¹⁾ are the following :

1. The liquid organic scintillator type NE-213.

This scintillator consists of specially purified xylene, naphthalene, activators and POPOP spectrum shifter. NE-213 shows good pulse shape discrimination properties, particularly for neutron counting in presence of gamma radiation, ^(22,23), it has reasonably fast response time (3.7ns) and is often used without time-of-flight as fast neutron spectrometer ^(24,25).

2. Polyvinyltoluene based plastic scintillator such as type NE-102A.

With this detector it is possible to reject contributions due to external γ -rays by using an appropriate threshold⁽²⁶⁾. Pulse shaped discrimination cannot be used with NE-102A, but it is proved to be a very useful tool whenever measurements of 14 MeV neutrons were involved which will be discussed in more detail in section 3.4.

3.3 Recoil proton energy Spectrum

In the fast neutron region, elastic scattering by hydrogen (below 10 MeV)⁽²⁷⁾ is isotropic in the centre-of-mass system, hence the energy distribution of the recoil protons from monoenergetic neutrons of energy E_0 is a continuous distribution in energy from zero to E_0 . Consider the elastic scattering of a neutron, mass unity initial energy E_n , by a nucleus of mass A initially at rest. From the kinematics of the collision it can be shown that the maximum energy of the recoil nucleus for a head-on collision is given by

$$E_{\max} = \frac{4A}{(A+1)^2} E_n \quad \text{-----} \quad 3.1$$

Thus for a proton ($A=1$) the entire neutron energy is transferred ($E_{\max} = E_n$) in a head-on collision. While for a carbon nucleus ($A=12$) $E_{\max} = .35 E_n$. For (n,p) scattering equation 2.3 becomes $E_p = \frac{E_n}{n} \cos^2 \theta$

Barshall and Kanner⁽²⁸⁾ have shown that the energy distribution of recoil particles in the lab-system is the same as the angular distribution of neutrons scattered in the centre of the mass system. For neutron-proton collisions, below $E_n = 10$ MeV, it has been found experimentally that the scattering is isotropic, that is, all angles of recoil are equally probable in the C-M-system.⁽²⁹⁾ Hence the energy distribution of recoil protons is uniform from $E_p=0$ to $E_p=E_n$ as shown in figure 3.1. However, in scintillators pulse height distribution is not the same as energy distribution. The upper end of the distribution is unsharp because of straggling

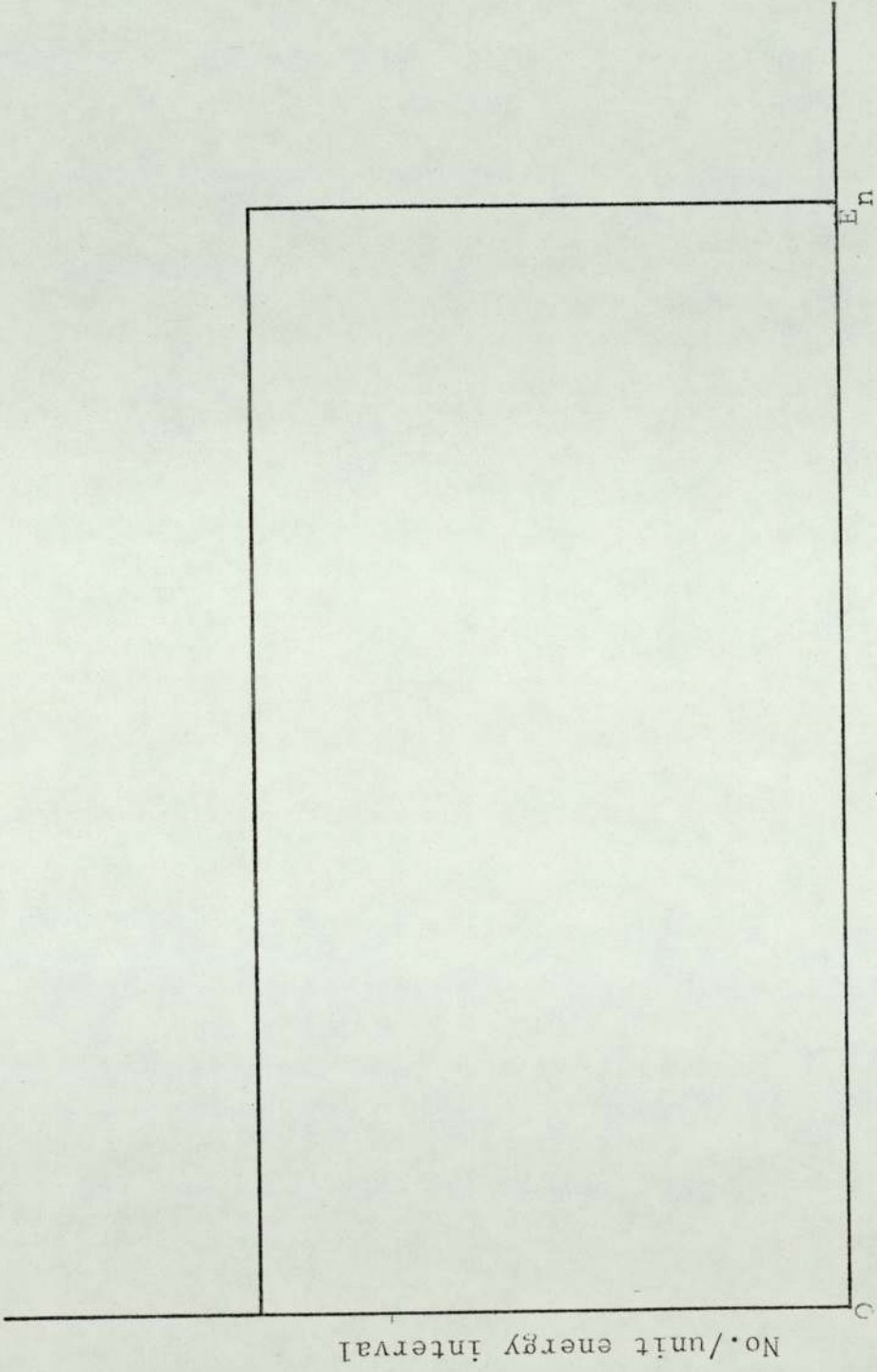


Fig. 3.1 Recoil proton spectrum

in the range of recoil protons and variation in light output per Mev lost.

3.4 NE-102A Scintillator

The scintillator used in this work was a plastic scintillator type NE-102A developed by Nuclear Enterprises Ltd. which has the following desirable physical properties: high light output, good light transmission, good detection efficiency, fast response and decay time. The light output has a rise time = 1ns and an exponential decay with a time constant $t_c = 2.4 \text{ ns}$ (³⁰). With all these properties the NE-102A scintillator is well suited to the fast neutron time-of-flight experiments. In using a thin plastic scintillator, single elastic neutron-proton scattering is the most probable reaction for neutrons. With increasing scintillator thickness the efficiency increases but it will introduce double and multiple scattering besides the timing uncertainty due to the variation in flight times to different detection points within the scintillator.

The time uncertainty is

$$\Delta t_d = \frac{\ell}{\left(\frac{2E_n}{m}\right)^{\frac{1}{2}}}$$

when ℓ = detector thickness

E_n = energy of the incident neutron

m = neutron mass

For the 14 MeV neutrons, $\ell = 5 \text{ cm}$ the detector timing uncertainty = 1ns, for the same scintillator and for 2.5 MeV neutron timing uncertainty = 2.2 ns.

3.5 Scintillator Efficiency

The efficiency of an organic scintillator is defined as the ratio of the number of recoil protons to the number of incident neutrons⁽³¹⁾

$$\epsilon = \frac{\text{number of recoil protons}}{\text{number of incident neutrons}}$$

The efficiency of a scintillator consisting entirely of carbon and hydrogen^(32,33) can be calculated under the assumptions that only single scattering occurs and that edge effects are negligible. The number of recoil protons in a scintillator of length L exposed to a flux of N_0 neutrons all of energy E_0 is

$$N_1(E_0, L) = N_0 n_H \sigma_H L |1 - \exp(-aL)| / aL \quad \text{-----} \quad 3.2$$

Where $a = \sigma_H n_H + \sigma_C n_C$

σ_H = neutron-proton scattering cross section at neutron energy E_0

σ_C = neutron-carbon cross section at neutron energy E_0

which is equal to $\sigma_T(E_0)$

n_H = number of hydrogen atoms/cm³

n_C = number of carbon atoms/cm³

The efficiency for single scattering is then

$$\epsilon(E_0, L) = \frac{N_1(E_0, L)}{N_0} = \frac{\sigma_H n_H}{a} (1 - e^{-aL}) \quad \text{-----} \quad 3.3$$

Figure 3.2 shows the variation of efficiency with neutron energy by applying equation 3.3 to a 5 cm thick NE-102A scintillator.

The n_H and n_C values as quoted by the manufacturers

$$n_H = .0525 \times 10^{24} \quad \text{atoms/cm}^3$$

$$n_C = .0475 \times 10^{24} \quad \text{atoms/cm}^3$$

In the discussion above only single scattering events were considered. Recoil protons can be produced by neutrons which have already been scattered one or more times by carbon or by hydrogen. Double scattering from hydrogen results in the production of two recoil protons of practically the same instant of time. Such events are registered as one proton by the photomultiplier tube and thus the number of recoil protons registered is not affected. However, double scattering from hydrogen does result in a distortion of the output pulse height spectrum of the scintillator. Recoil protons may also be produced by neutrons which have a first collision with carbon and second collision with hydrogen. This results in an increase in the number of recoil protons produced. It is found that organic scintillators are also efficient as detectors of γ -rays. Therefore it was necessary to discriminate the unwanted γ -rays.

3.5.1 Non-linear response of scintillators

The quantity directly recorded in the scintillation method is the pulse height spectrum. Under appropriate conditions the photomultiplier output is directly proportional

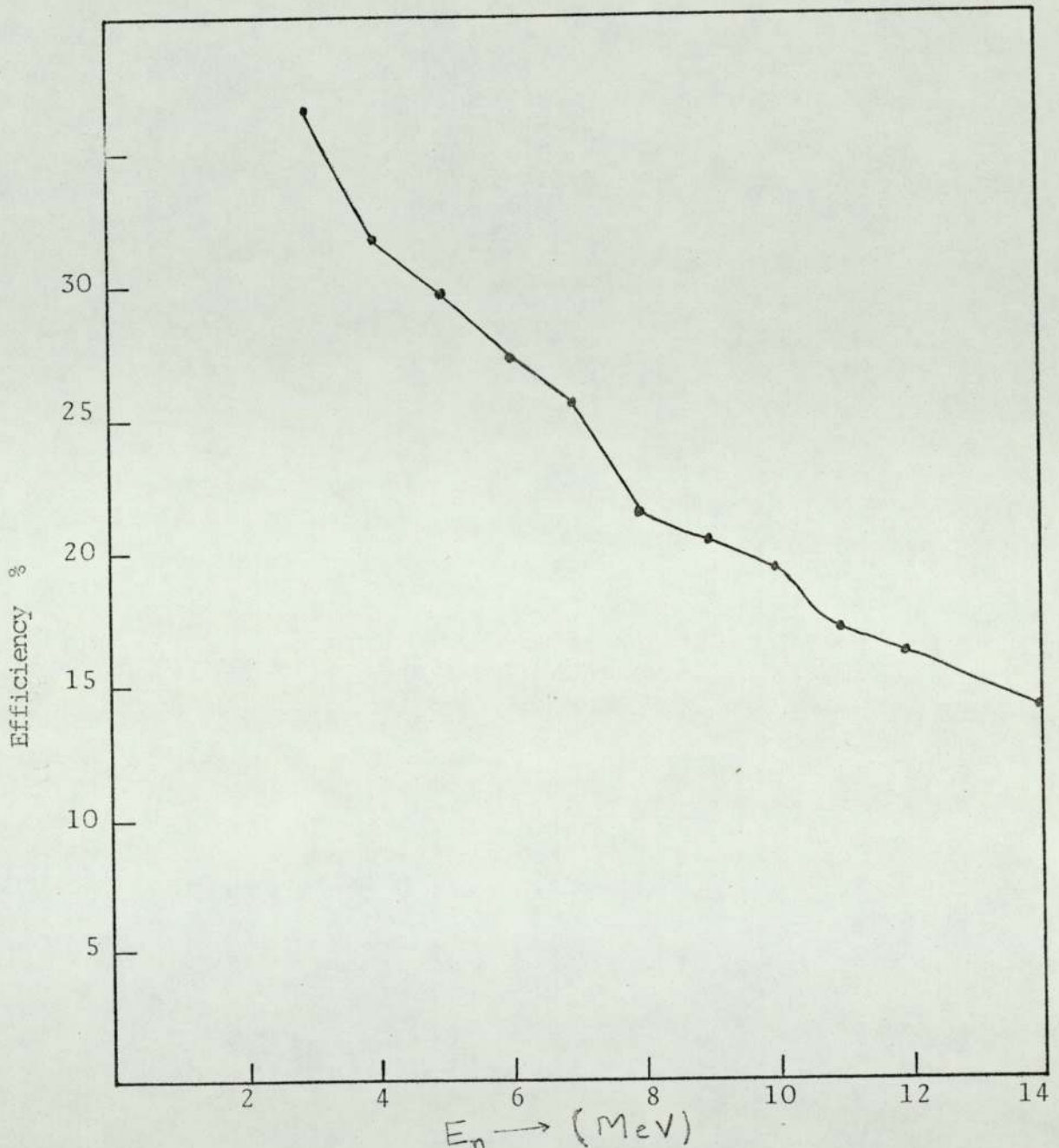


Fig. 3.2. Theoretical efficiency of 50mm. thick NE-102A)

to the luminous output of the scintillator. The luminous output of an organic scintillator for various charged particles is well represented by the semi-theoretical formula of Birks

$$\frac{dS}{dx} = \frac{A \cdot \frac{dE}{dx}}{1 + KB \frac{dE}{dx}} \quad \text{-----} \quad 3.4$$

where S = luminous output of the scintillator

x = path length of the particle in the scintillator

E = particle energy

$\frac{dE}{dx}$ = rate of loss of energy of charged particle

A and KB are constants for a given scintillator.

To avoid dependence on specific units for the measurement of S it is convenient to represent the scintillator output by the variable $p = S/A$ equation 3.4 can be rewritten in terms of $\frac{dp}{dE}$ as follows

$$\frac{dp}{dE} = A^{-1} \frac{dS}{dx} \frac{dx}{dE} = \frac{1}{1 + KB \frac{dE}{dx}} \quad \text{-----} \quad 3.5$$

where p and E have the same units. For electrons⁽³⁴⁾ with energies from a few tens of KeV up to several MeV $\frac{dE}{dx}$ is very small so that $KB \frac{dE}{dx}$ can be neglected then $\frac{dp}{dE} = 1/p = E_e$ where E_e is the electron energy. For protons^(35,36) with energies of a few MeV however $\frac{dE}{dx}$ cannot be neglected. For plastic scintillator type NE-102A Evans and Bellamy⁽³⁷⁾ have shown that the value of KB is $1.0 \times 10^{-2} \text{ gm. cm.}^{-2} \cdot \text{MeV}^{-1}$, taking the energy-range relationship of protons in the plastic to be the same as that for CH given by the tables of Rich and Madey.⁽³⁸⁾ The pulse height for a given proton energy E_p was

then obtained by numerical integration of equation 3.5 since $\frac{dE}{dx}$ is a non-analytic function of proton energy. The resulting pulse height p obtained as a function of proton energy for NE-102A scintillator are listed in table 3.1.

If the number of recoil protons with energies between E and $E+dE$ is written as $dN = N(E)dE$ and the number with pulse height between p and $p+dp$ as $dN = N(p)dp$ then the two spectra are related by $N(E) = N(p) \frac{dp}{dE}$ _____ 3.6

This relationship results from the requirement that the area under the two spectra be the same.

For convenience $N(E)$ was taken as unity in the present calculation, the two spectra are then related by

$$N(p) = \frac{dE}{dp} \quad \text{_____} \quad 3.7$$

Using equation 3.7 and the proton pulse height (p) of table 3.1, then figure 3.3 shows the distortion of the pulse height spectrum by the non-linear response of plastic scintillator NE-102A for neutrons of 14.1 MeV. In practice the pulse height spectrum will take the form shown by the dashed curve. This distortion is due to statistical fluctuation in the scintillator output and the photomultiplier tube.

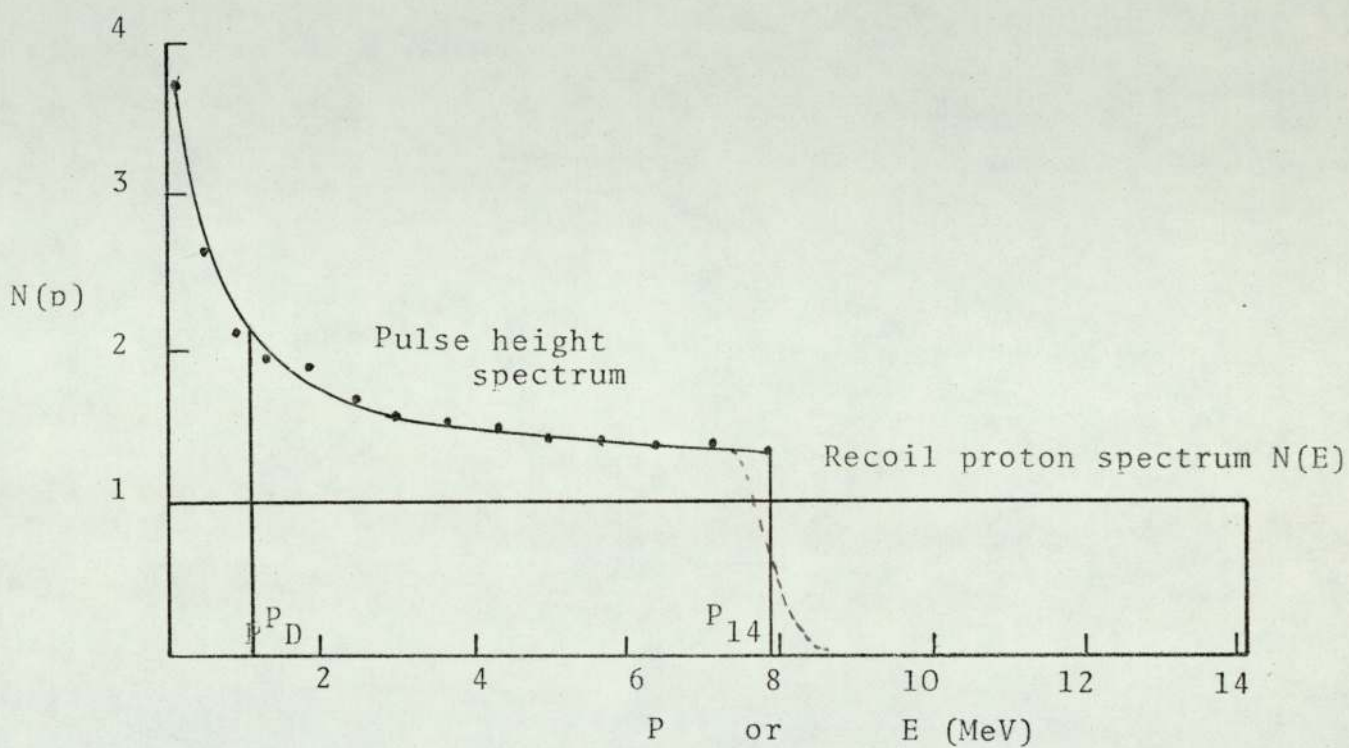


Fig. 3.3. Theoretical pulse height spectrum of fast neutrons in NE-102A.

TABLE 3.1

Proton Energy Ep (MeV)	$\frac{dE}{dx}$ KeVcm ² mg ⁻¹	N(p) = $\frac{dE}{dp}$	p
1	278.8	3.78	1.1675
2	167.6	2.68	.49
3	122.9	2.229	.903
4	98.11	1.98	1.38
5	82.10	1.82	1.908
6	70.86	1.709	2.47
7	62.51	1.626	3.076
8	56.04	1.59	3.705
9	50.86	1.508	4.357
10	46.61	1.466	5.029
11	43.05	1.43	5.72
12	40.03	1.4	6.425
13	37.44	1.37	7.147
14	35.18	1.35	7.88
15	33.20	1.33	8.626

3.5.2 Detector Efficiency with Discrimination

To reduce the background count rate in the neutron detection channel it was necessary to discriminate against pulses arising from photomultiplier noise, low energy background neutrons and γ -rays. This discrimination resulted in the rejection of some recoil proton pulses⁽²³⁾ which have been

included in the calculation of efficiency. With a discriminator ⁽³⁹⁾ set to reject all pulses of amplitude less than P_D , the scintillator efficiency for 14 MeV neutrons is given by

$$\epsilon_{14} = \epsilon_1(14) \frac{A_{14} - A_D}{A_{14}} \quad \text{-----} \quad 3.8$$

where $\epsilon_1(14)$ = 14 MeV efficiency without discrimination

$(A_{14} - A_D)$ = Area under the pulse height spectrum between ordinates P_D and P_{14} (Figure 3.3)

P_D = Discriminator level

P_{14} = pulse height due to 14 MeV protons

A_{14} = total area under pulse height spectrum

= area under recoil proton energy spectrum.

Hence the scintillator efficiency for neutrons of energy E_n can be written as

$$\epsilon(E_n) = \epsilon_1(E_n) \times \frac{A_{E_n} - A_D}{A_{E_n}} = \epsilon_1(E_n) \times \frac{E_n - E_D}{E_n} \quad \text{-----} \quad 3.9$$

since $\int N(E)dE = \int N(p)dP$.

The choice of the discriminator level was such that while rejecting pulses due to low energy neutrons, γ -rays, and photomultiplier noise it was not at such a level as to reject significant scattered neutron pulses. For setting-up reasons it was necessary to fix the discriminator level at a consistently reproducible known pulse height. This condition was met by setting up the discriminator to reject

γ -ray pulses from a source of known energy.⁽¹⁴⁾ The source used was ^{60}Co which emits two γ -rays at 1.17 MeV and 1.33 MeV. In this energy range, γ -rays interact with the plastic scintillator mainly through the production of Compton electrons.⁽⁴⁰⁾ The energies of the recoil electrons in Compton collisions range from zero up to a maximum value E_{max} given by

$$E_{\text{max}} = \frac{E}{1 + \frac{E}{2m_0 c^2}} \quad \text{-----} \quad 3.10$$

where E = the incident γ -ray energy in MeV

$m_0 c^2 = .51$ MeV is the rest mass energy of the electron

E_{max} = the maximum energy of the recoil Compton electrons

Applying equations 3.10 to ^{60}Co γ -rays of energy 1.33 MeV gives $E_{\text{max}} = 1.116$ MeV.

Therefore a discriminator set to reject ^{60}Co γ -ray pulses was equivalent to the rejection of pulses due to 1.116 MeV electrons. In order to relate the pulse height due to 1.116 MeV electrons to the equivalent proton pulse height spectrum it was necessary to consider the luminous output of NE-102A. For electrons consider equation 3.5 for electron energy of 1.116 MeV the term $KB \frac{dE}{dx}$ is small. Hence the pulse height due to electrons is given by $P = E$.

This means that a 1.116 MeV electron produces a pulse of amplitude $P=1.116$ MeV. Interpolation of the proton pulse heights given in table 3.1 showed a pulse of $P=1.116$ MeV to be equivalent to a proton of energy 3.4 MeV.

Therefore setting up the discriminator with ^{60}Co γ -rays as a reference resulted in the rejection of pulses due to neutrons with energy less than 3.4 MeV.

With the discriminator set at a pulse height $P = 1.116$ MeV applying equation 3.9 to figure 3.3 gave the efficiency curve shown in figure 3.4.

3.6 The Scintillator-photomultiplier Coupling

In fast neutron time-of-flight experiments the transit time of the detector pulse through the photomultiplier tube is included in the time interval measured to determine neutron energy, therefore a ^{suitable} photo-multiplier tube should have a fast transit time⁽⁴¹⁾ with low time spread. The photomultiplier tube chosen in the present work was a Philips 56 AVP having an electron transit time spread of 0.5 ns which was an adequate choice for the present work. The 56 AVP tube has 14 stages of amplification giving a gain of 10^8 ^(42,43). This high gain eliminated the need for further amplification of the output pulses. The dynode voltages were supplied by the resistor chain shown in figure 3.5. The current through the dynode chain was 2.3 mA at an operating voltage of 2KV.

Because of the high pulse current in the later stages of the tube, signal decoupling condensers were included across the last four dynode chain resistors; this was effective in preventing fluctuations in the dynode voltages. For good light collection by the photocathode great care must be taken with the optics of the system, the light loss is minimum when the scintillator is coupled directly to the photomultiplier

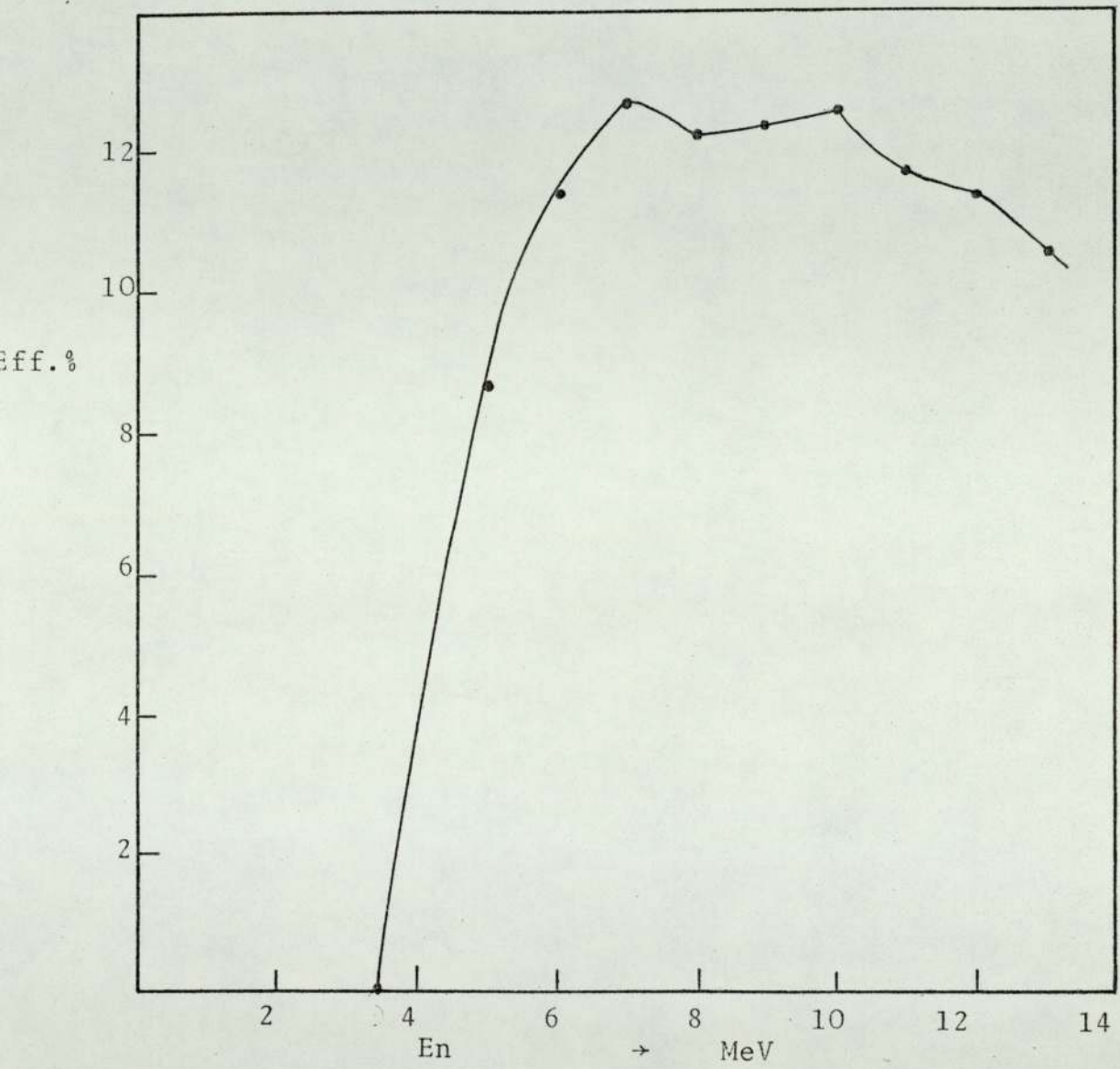


Fig.3.4. Theoretical efficiency of 50mm. thick NE-102A with the discriminator.

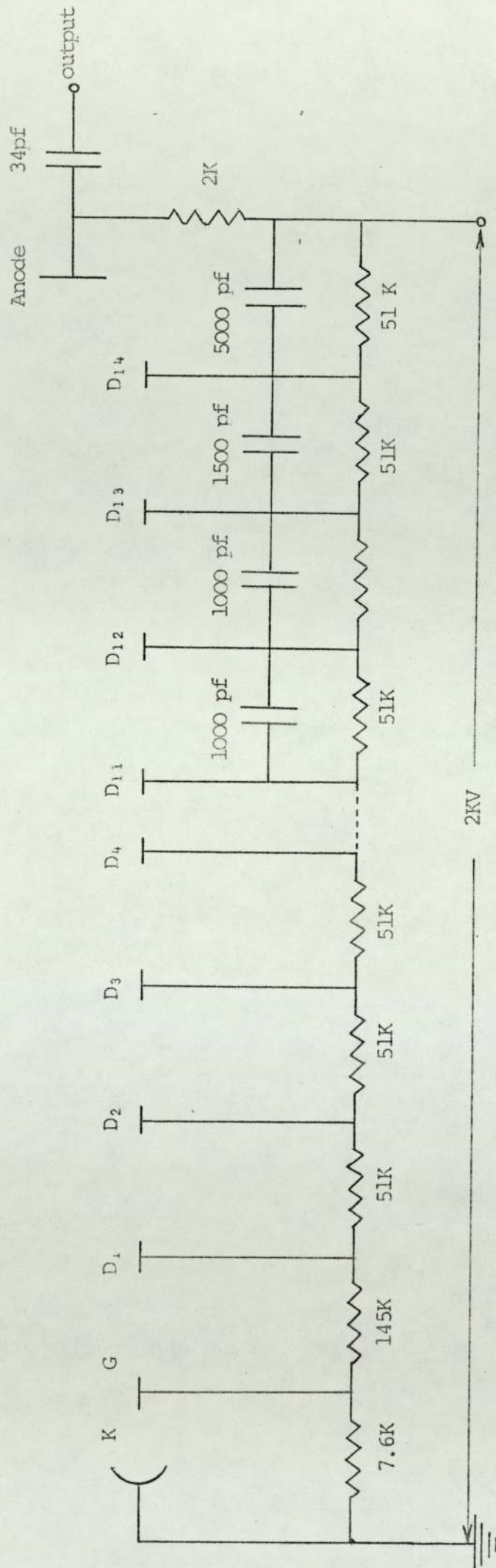


Fig. 3.5 56 A.V.P. photomultiplier dynode resistor chain

tube but as the scintillator used had a larger diameter (10cm) than the photo-multiplier tube (5cm) a truncated conical perspex light pipe of 7cm length was used for size matching purposes.

To ensure effective light transmission between the scintillator and the light pipe they were connected with optical cement type NE580 that has a refraction index ($\mu = 1.58$) which is close to that of the NE-102A scintillator. Optical contact between the light pipe and the photo-multiplier tube was obtained by using non-drying immersion oil. The neutron detector is shown in figure 3.6.

In the time-of-flight experiment the electronics instruments involved were several meters away from the experimental area i.e. the neutron detector is far away from the electronics, so a length of coaxial cable was required to connect the neutron detector to the neutron discriminator. To avoid reflections in this long cable the anode signals were matched into the cable through an emitter follower. Figure 3.7 shows the emitter follower circuit included to match the output impedancy of the photo-multiplier tube to the 75Ω coaxial cable leading to the neutron discriminator.

3.7 Magnetic Field Effect

The performance photo-multiplier tube is sensitive to magnetic fields. In the presence of a magnetic field electron emitted from the photocathode will be deflected away from their

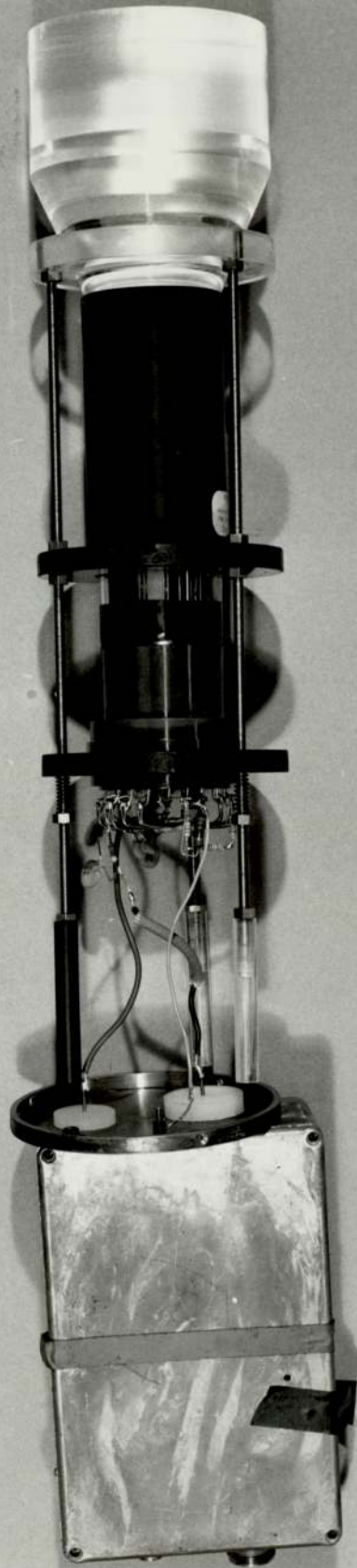
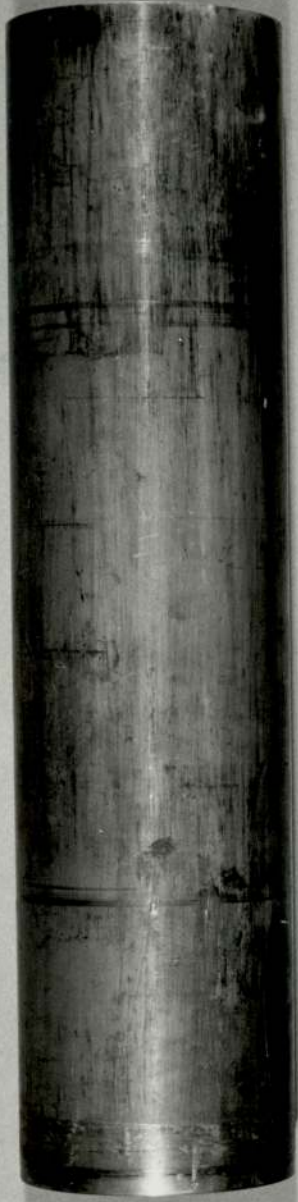


FIGURE 3.6 NEUTRON DETECTOR

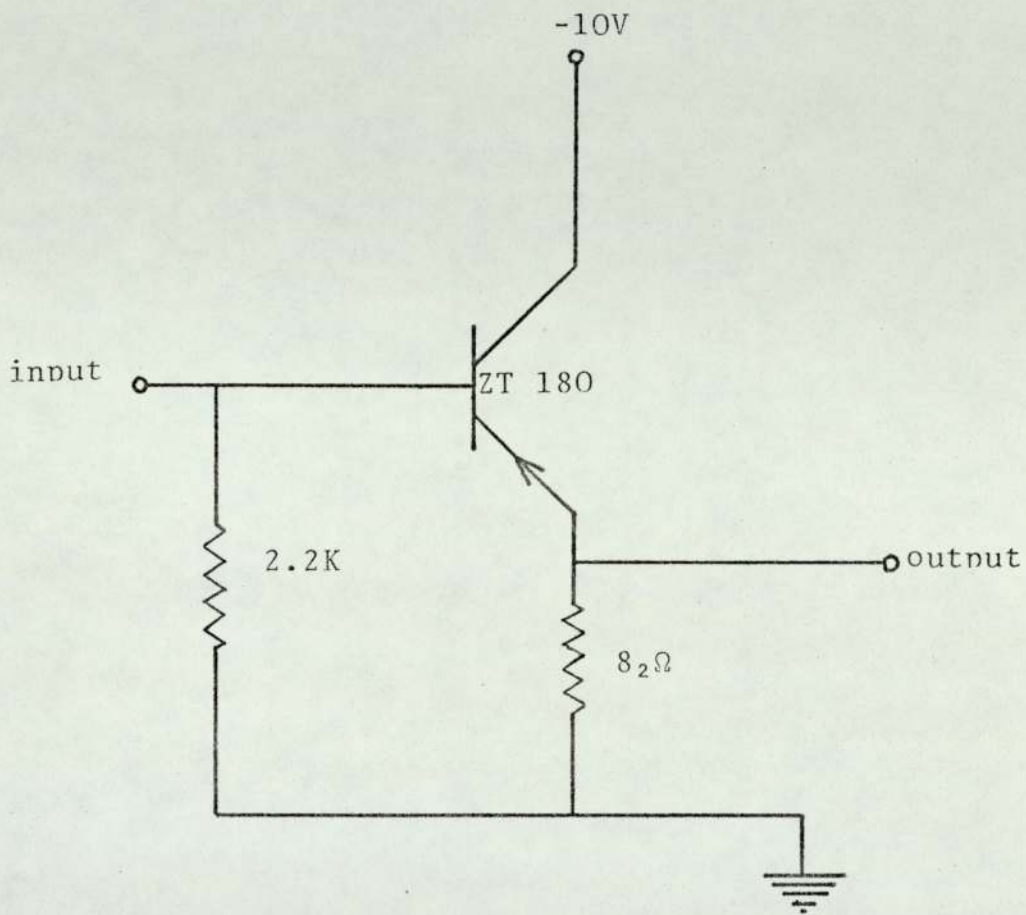


Fig. 3.7 Emitter follower circuit

normal path and may not be collected by the first dynode.⁽⁴⁴⁾ Hence the movement of the photo-multiplier relative to a magnetic field can result in changes of the photomultiplier gain.

The earth's magnetic field is not usually a problem if the tube is operated in a fixed position throughout an experiment, but in the present work it was required to rotate the detector (neutron detector) about the sample position, so shielding from the earth's magnetic field was essential for stable performance. The electron trajectories from the cathode to the first dynode are most sensitive to magnetic fields, the photo-multiplier tube was therefore placed inside a cylindrical mu-metal magnetic shield number 56131 recommended by the manufacturers so that the first dynode stages and the photo-cathode were adequately shielded, the use of a mu-metal shield, besides giving optimum tube gain gives minimum transit time spread.

3.8 Neutron Detector Shielding

The purpose of shielding is basically to reduce background effects caused by undesired neutrons and γ -rays to a reasonably small fraction of the effects due to the neutrons of interest. Neutron scattering experiments require careful shielding of the detector from the neutron source. The shielding usually consists of a shadow bar and a collimator surrounding the detector, the shadowbar used to shield against the direct source of the 14 MeV neutrons that are incident on

the detector while shielding against background caused by neutrons and γ -rays scattered into the detector from the floor and surrounding walls was achieved by placing the detector in a large collimator.

3.8.1 Neutron Shielding Materials

A shield should attenuate fast neutrons producing a minimum of secondary penetrating γ -radiation without causing a build-up of activity in the shielding material and this is achieved by slowing down or moderating the fast neutrons and then absorbing the secondary penetrating γ -rays. The selection of the shielding materials represents a compromise between size, weight and efficiency of the detector. Materials used to shield against neutrons in the MeV region were of two types, heavy materials and hydrogenous materials. The heavy materials like W, Cu, Fe, pb have been used since the elastic differential cross sections for these heavy materials are very sharply forward peaked and for attenuation purposes the entire elastic cross-section may be neglected compared with the non-elastic absorption and inelastic scattering processes. A hydrogenous material is the most efficient fast neutron moderator. The elastic scattering cross-section for hydrogen is relatively large but decreases with increasing neutron energy. Hydrogen, however, provides on the average a 50% energy degradation per elastic collision. Neutrons thermalized in this way give γ -rays with 2.2 MeV produced from ${}^1_1\text{H}(n,\gamma){}^2_1\text{D}$ reaction. Suitable hydrogenous materials are water, paraffin

wax, polyethylene. The use of those materials has been investigated by Hopkins et al⁽⁴⁵⁾ who found that for the 14 Mev neutrons the heavy materials are more effective in terms of attenuation per unit thickness of shield. However, if the weight of the shield is considered the hydrogen moderators are far more effective, paraffin wax being approximately four times as effective as copper. In using paraffin wax scattering by its carbon content produces γ -rays of 4.43 MeV from $^{12}\text{C}(n,n^1\gamma)^{12}\text{C}$ reaction but the cross-section for this reaction is very much less than for elastic scattering by hydrogen and carbon. It is possible to reduce the γ -rays production in paraffin wax by loading the wax with a good slow neutron absorbing materials. Suitable materials are ^6Li and ^{10}B generally used in the form of a compound. Both materials have a large cross-section for the (n,α) reaction but ^6Li is more effective since no γ -rays are emitted in $^6\text{Li}(n,\alpha)^3\text{H}$ reaction. In the $^{10}\text{B}(n,\alpha)^7\text{Li}$ reaction .48 MeV. γ -rays are emitted in about 95% of the interactions.

Mixing a substantial amount of lithium carbonate with paraffin wax to reduce γ -radiation from neutron capture in hydrogen reduces the density of hydrogen in the shield and consequently the neutron shield is less efficient. On the basis of weight effectiveness, cost and ease of fabrication, paraffin wax was used as the major constituent of the shield. The innermost part of the shield consisted of a suitable γ -ray absorbing material, lead layers of 4 cm thickness being

used for this purpose because of its density and high atomic number. This shielded the detector from the γ -rays. A cross-section of the shielding assembly is shown in figure 3.8. The shadow bar and the collimator were fabricated by moulding the paraffin wax in a container of the desired shape. The wax was not loaded with boron or lithium carbonate.

3.8.2 The Shadow bar Position

Correct location of the shadow bar was important in the angular distribution measurements. There are several criteria concerning a proper location for the shadow bar. It should not intercept neutrons between the target and the scattering sample or between the scattering sample and the detector. The entrance of the collimator should not be exposed to the target and the shadow bar face nearest the target and scattering sample should not be visible to the detector. Within these limitations, which may be mutually exclusive at certain very small or very large angles, the shadow bar was very effective in attenuating fast neutrons. Figure 3.9 shows the position of the shadow bar for a scattering angle of 45° .

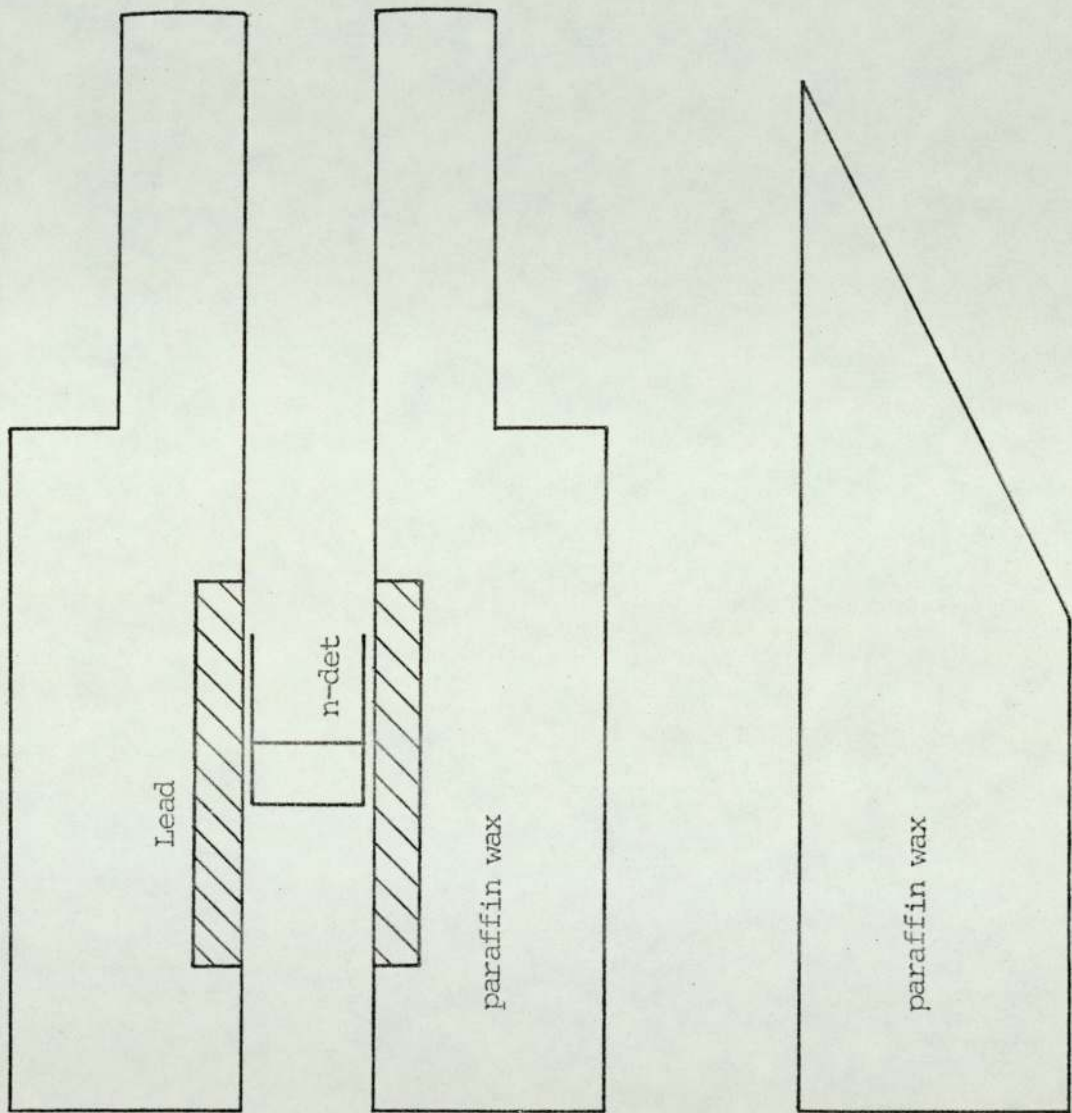


Fig. 3.8 Neutron-detector shielding composed of a collimator and a shadow bar

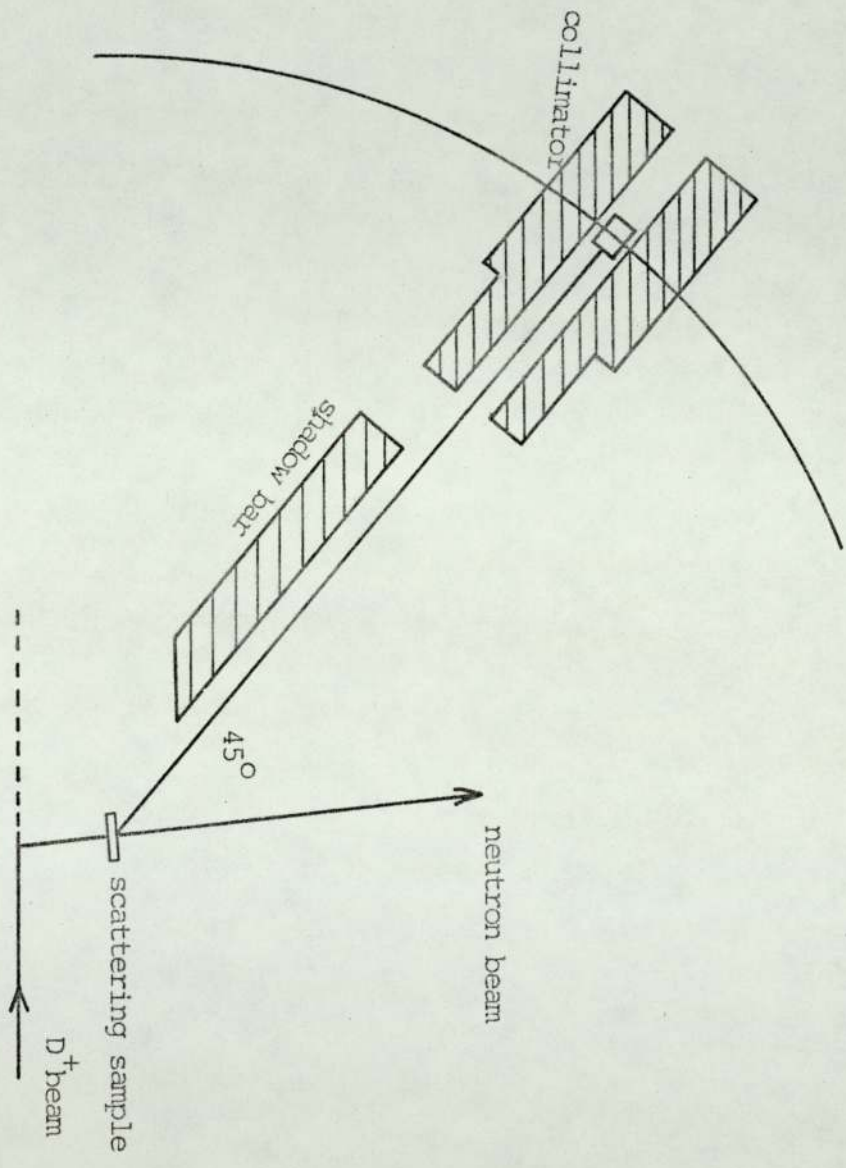


Fig. 3.9 Position of the shadow bar at angle 45°

THE NEUTRON PRODUCTION4.1 Introduction

Neutrons were produced from the $T(d,n)^4\text{He}$ reaction. With a deuteron beam of energy about 150 KeV obtained from using a S.A.M.E.S. type -J accelerator incident on a tritium-titanium target, neutrons of 14.1 MeV can be obtained with a small spread in energy.

4.2 S.A.M.E.S. Accelerators and the Target Assembly

The deuteron beam was accelerated by the S.A.M.E.S. type J accelerator shown in figure 4.1. The accelerating voltage is produced by an electrostatic generator which is housed in a hermetically sealed unit in a hydrogen atmosphere. The generator can deliver 2mA at +150 KV with a stability of $\pm 1\%$.⁽⁴⁶⁾ The target and the other experimental facilities are situated at the far end in the laboratory and they are several metres away from the accelerator. Therefore the deuteron beam has to pass through a 6 metres long evacuated beam tube to reach the far end where the target is situated. Due to the length of the tube an auxillary pumping stage at the target end was necessary to maintain a pressure of less than 10^{-5} mm.Hg, and because of the length of the tube extra beam focusing was required. The deuteron beam is focussed by two electrostatic quadrupole lenses⁽⁴⁷⁾ and a pair of electrostatic deflector plates. The incident deuteron beam on the target was restricted by a vertical slit 10mm. x 1mm. in a brass plate situated across the end of the beam tube. The target

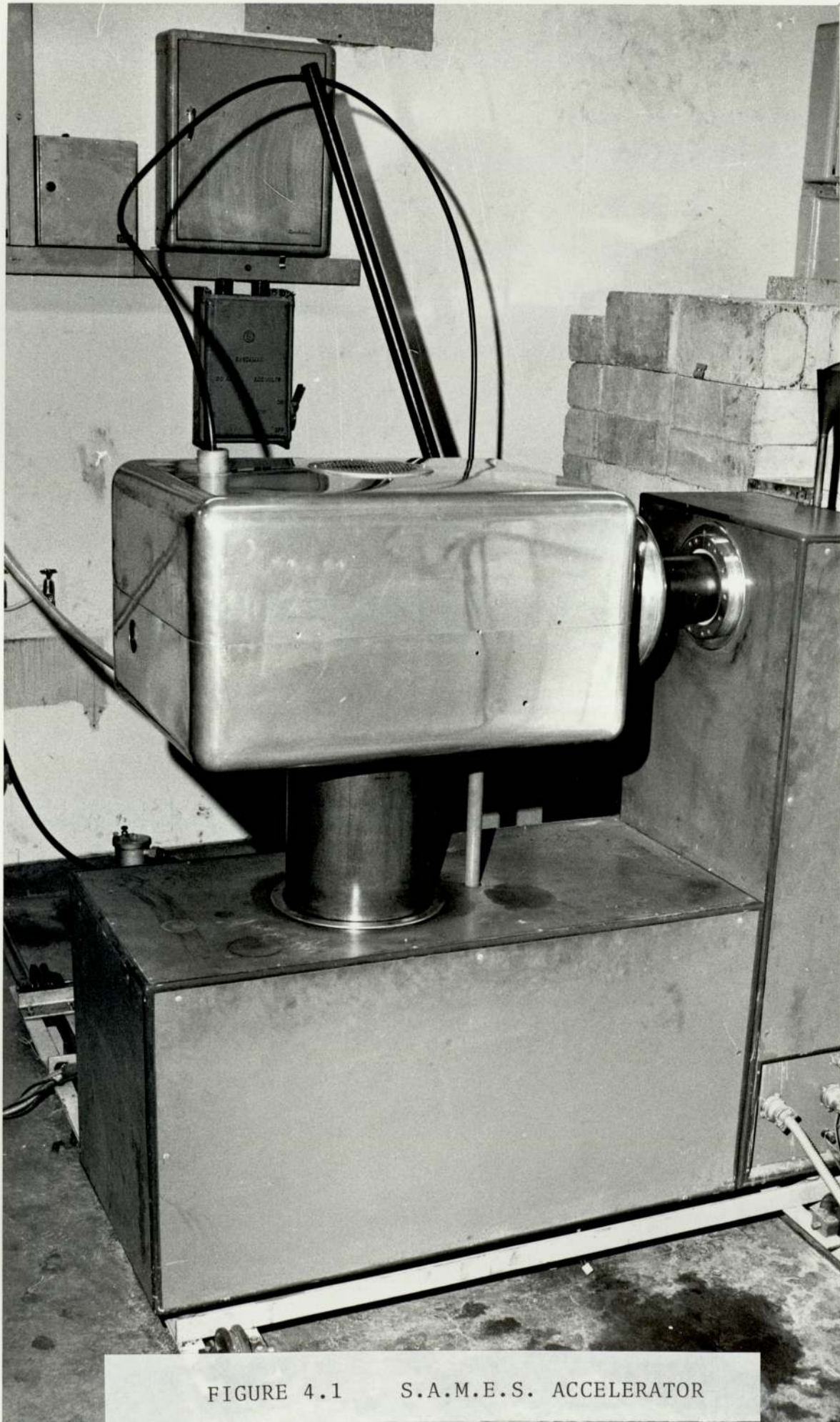


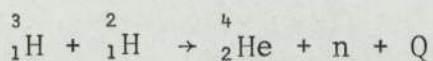
FIGURE 4.1 S.A.M.E.S. ACCELERATOR

assembly was supplied by Multivolt Ltd. and it consists of a disc of copper coated with a thin layer of titanium loaded with tritium, contained in a stainless steel case. The target disc is water cooled, and it has a 90° branch as shown in figure 4.2. Only a small part of the target is struck at any one time by the deuteron beam, and the target can be rotated to expose new areas to the deuterons.

Under positively charged deuteron bombardment electrons are ejected from the target assembly. To prevent these electrons back streaming to the accelerator a suppressor electrode was inserted between the target and the beam tube, and this was maintained at about +150 volts, thus reflecting the secondary electrons back to the target. Araldite spacers insulated the target, suppressor and slit from each other and from the beam tube and target and slit currents were monitored by means of multi-range current meters.

4.3 The T(d,n)⁴He reaction

The nuclear reaction



Which is highly exothermic and has long been used as a source for the production of neutrons with high energy. The Q value which can be calculated from the nuclear masses of the reaction is very high 17.586 MeV⁽²⁵⁾. Because of this high Q value the variation of neutron energy with the incident deuteron beam energy is relatively small. Neglecting the

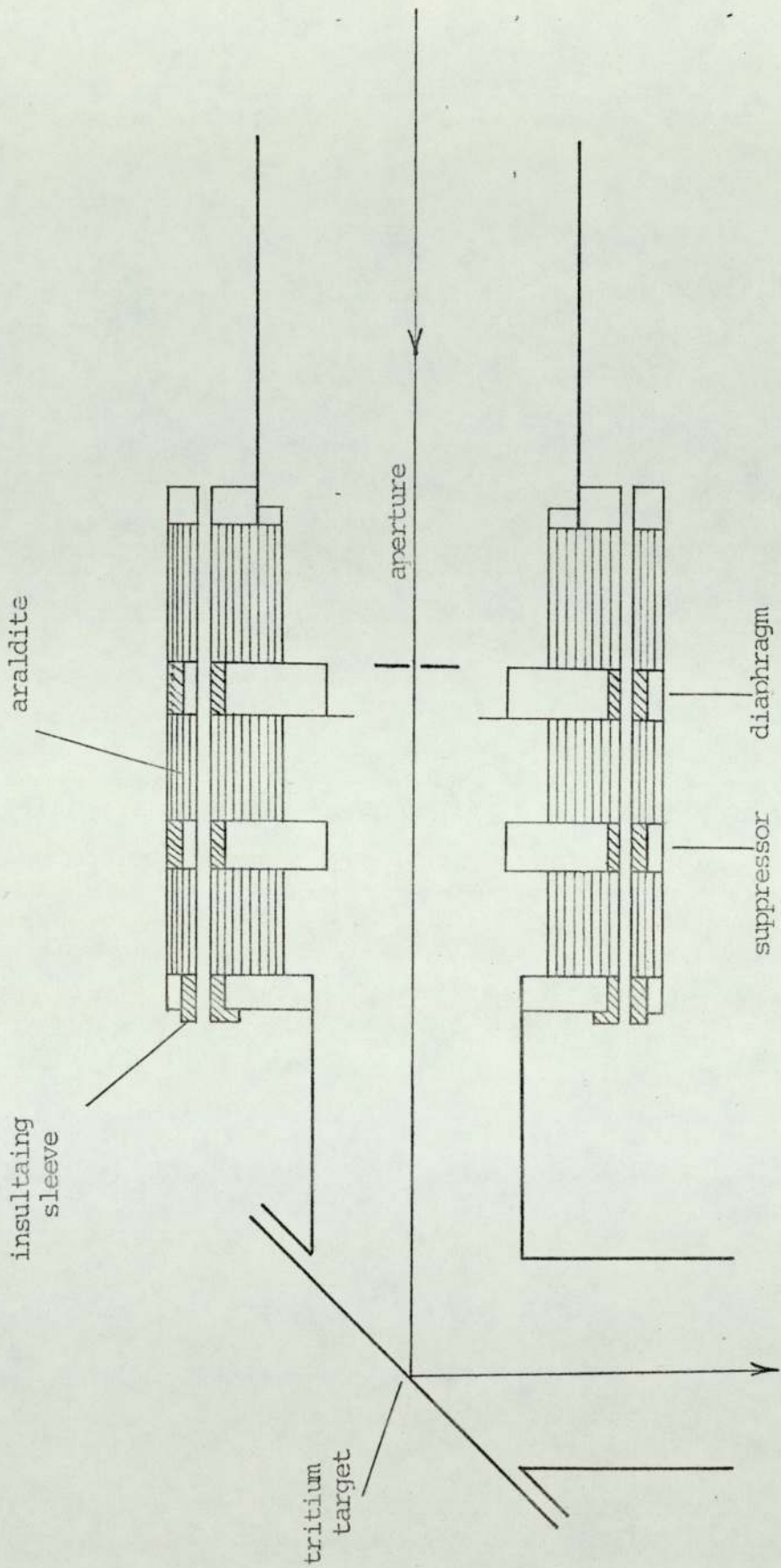


Fig. 4.2 The 90° branched target assembly

kinetic energy of the incident deuteron beam the products will share an energy of 17.586 MeV as the inverse ratio of their masses, ⁽⁴⁸⁾ which gives the neutron $17.586 \times \left(\frac{4}{4+1}\right) = 14.1$ MeV and the alpha particle $17.586 \times \left(\frac{1}{4+1}\right) = 3.5$ MeV.

The cross section for this reaction rises to a peak of 5.1 barn ⁽⁴⁹⁾ at a deuteron energy of 110 KeV as shown in Figure 4.6.

4.3.1 Kinematics of $d(T,n)^4\text{He}$ reaction.

The energies and the angles of the scattered particles from a nuclear collision can be computed using the conservation laws of energy and momentum. In this reaction a particle of mass m_1 (deuteron) is incident on another particle of mass m_2 (triton), which is at rest in the laboratory system. The interaction produces two particles, one of mass m_3 (neutron) and the other of mass m_4 (^4He). Let (θ_3, θ_4) represent the angles of scattering ⁽⁵⁰⁾ of the particles m_3 and m_4 respectively in the laboratory system and (ϕ_3, ϕ_4) represents the angles of scattering of the particles m_3 and m_4 respectively in the C-M system as shown in Figure 4.3.

Then a mathematical expression for the energy of the scattered neutron E_3 as a function of angle which is available in several works ^(51,52) and can be produced here from the laws of momentum and energy conservation, E_3 is then given by the following expression

$$E_3 = (\mu E_1 + Q) \frac{m_4}{m_3 + m_4} + E_1 \frac{m_1 m_3}{(m_1 + m_2)^2} \cos 2\theta$$

$$+ \frac{2\sqrt{m_1 m_2}}{(m_1 + m_2)} \cos\theta \sqrt{\frac{E_1 (\mu E_1 + Q) m_4}{(m_3 + m_4)} - \frac{m_1 m_3}{(m_1 + m_2)^2} E_1^2 \sin^2\theta}$$

4.1

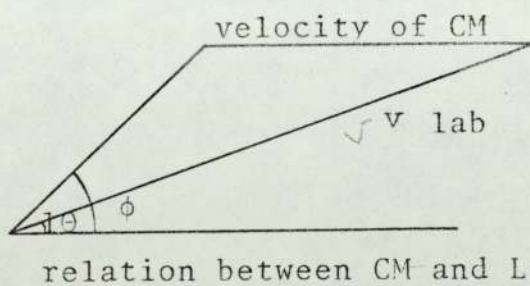
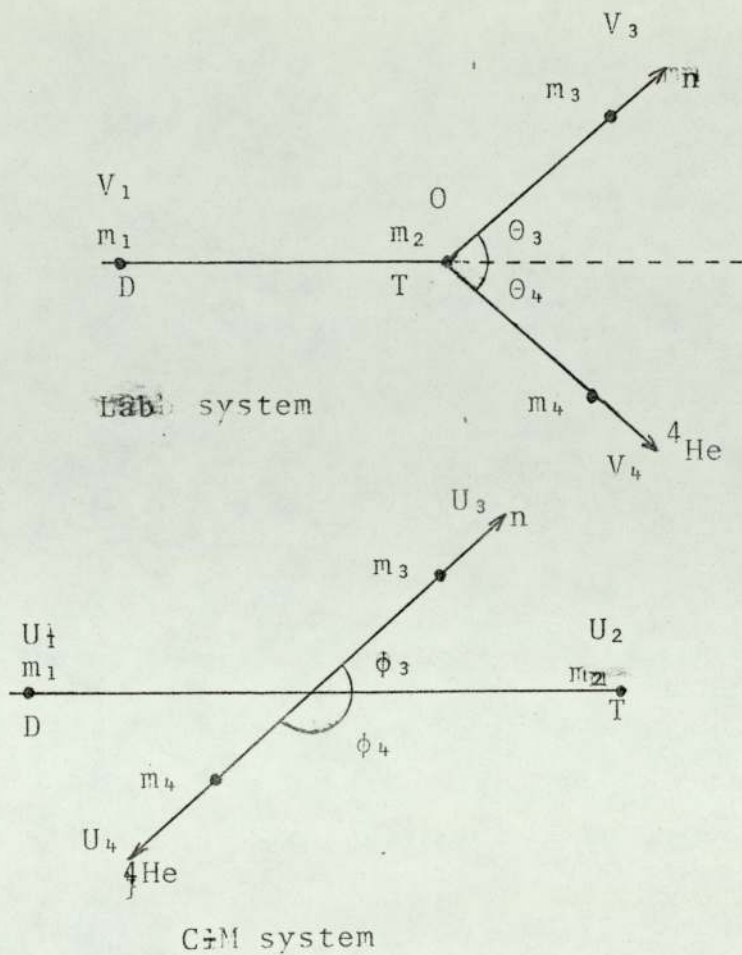


Fig. 4.3 Relation between CM and Lab system

In deriving the above expression for the neutron energy E_3 it is always easier to consider working out the mathematical equations for the conservation of energy and momentum in the C-M system and then transferring them into the laboratory system. To transfer neutron production rate at a particular angle in the C-M system to an equivalent angle the laboratory system it must be multiplied by the anisotropy factor $|A|$ which is the ratio of the solid angle in the laboratory system given as $|A| = \frac{d\Omega_c}{d\Omega_L}$

The derivation of the mathematical equation to find E_3 with the anisotropy factor is given in Appendix 1. The tritium target used was thick compared with the deuteron range as the thickness of the titanium layer was $\sim 1 \text{ mgm cm}^{-2}$ and the range of deuterons of energy between $150 \rightarrow 20 \text{ KeV}$ in titanium is $.4 \text{ mgm cm}^{-2}$ (54). Consequently deuterons of all energies from the bombarding energy to the energy where the cross-section becomes negligible ($\sim 20 \text{ KeV}$) yield neutrons. The variation of neutron energy with the angle of emission is shown in figure 4.4 for different deuteron energies.

4.3.2 Angular relationship of the associated particles.

The angular range of neutrons defined by α -particles emitted at $90 \pm 5^\circ$ to the deuteron beam in the $d(T,n)^4\text{He}$ reaction can be calculated from the reaction kinematics. Equation A 1.10 gives the relationship between the alpha particle angle θ_4 and the neutron angle θ_3 , it can be seen that the relation between the two angles depends on the incident deuteron energy.

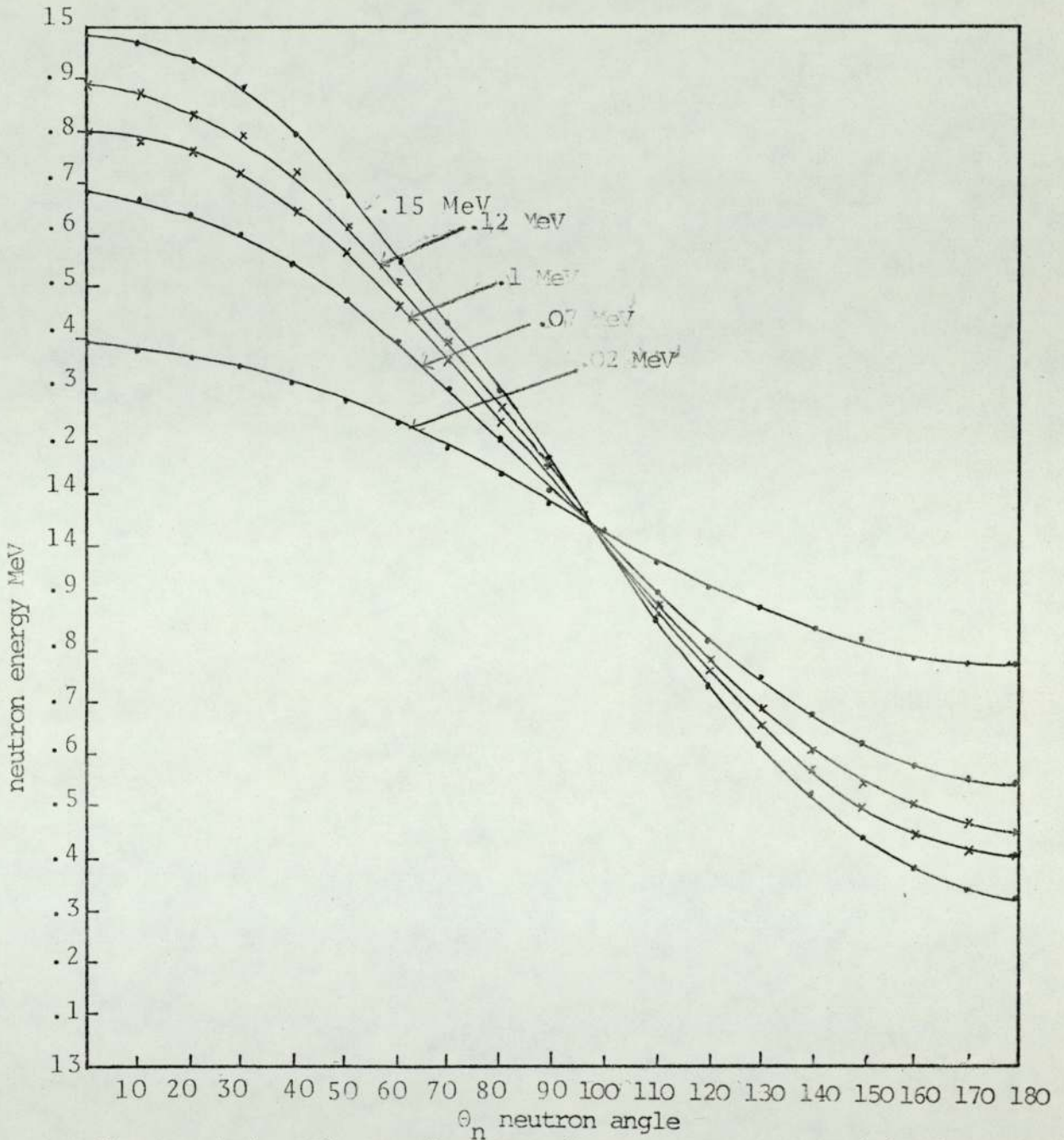


Figure 4.4 The variation of neutron energy with the angle of emission of the T-D reaction

Figure 4.5 shows the relationship between neutron angle and alpha particle angle in the angular range of interest calculated with a computer programme as shown in Appendix 2. The calculation was done for deuteron energies ranging from 150 KeV to 20 KeV. The figure also shows the alpha particles detected at $(90^\circ \pm 5^\circ)$ define a neutron beam over the angular range of $(83^\circ \pm 7^\circ)$

4.4 The Neutron Yield

The reaction probability for a deuteron on passing a distance dx through a target containing N tritium atoms/cm³ is given by $N\sigma dx$, where σ is the cross section for the reaction and is a function of energy. Since deuterons range is not a linear function of energy then

$$\sigma dx = \frac{\sigma}{dE/dx} dE \quad \text{-----} \quad 4.2$$

The angular dependents of the differential cross section for the $T(d,n)^4He$ reaction has been found to be isotropic in the C-M system for deuteron energies up to 200 KeV by Allen and Poole ⁽⁵³⁾ and to 570 KeV by Argo et al ⁽⁵⁵⁾. The total yield of neutrons per incident deuteron of energy E_D is given by

$$Y = \int_0^{E_D} \frac{N \cdot \sigma}{dE/dx} dE \quad \text{-----} \quad 4.3$$

where σ is the total cross section for the $T(d,n)^4He$ reaction at a deuteron energy E . $\frac{dE}{dx}$ is the rate of energy loss of deuterons of energy E in the titanium tritide target.

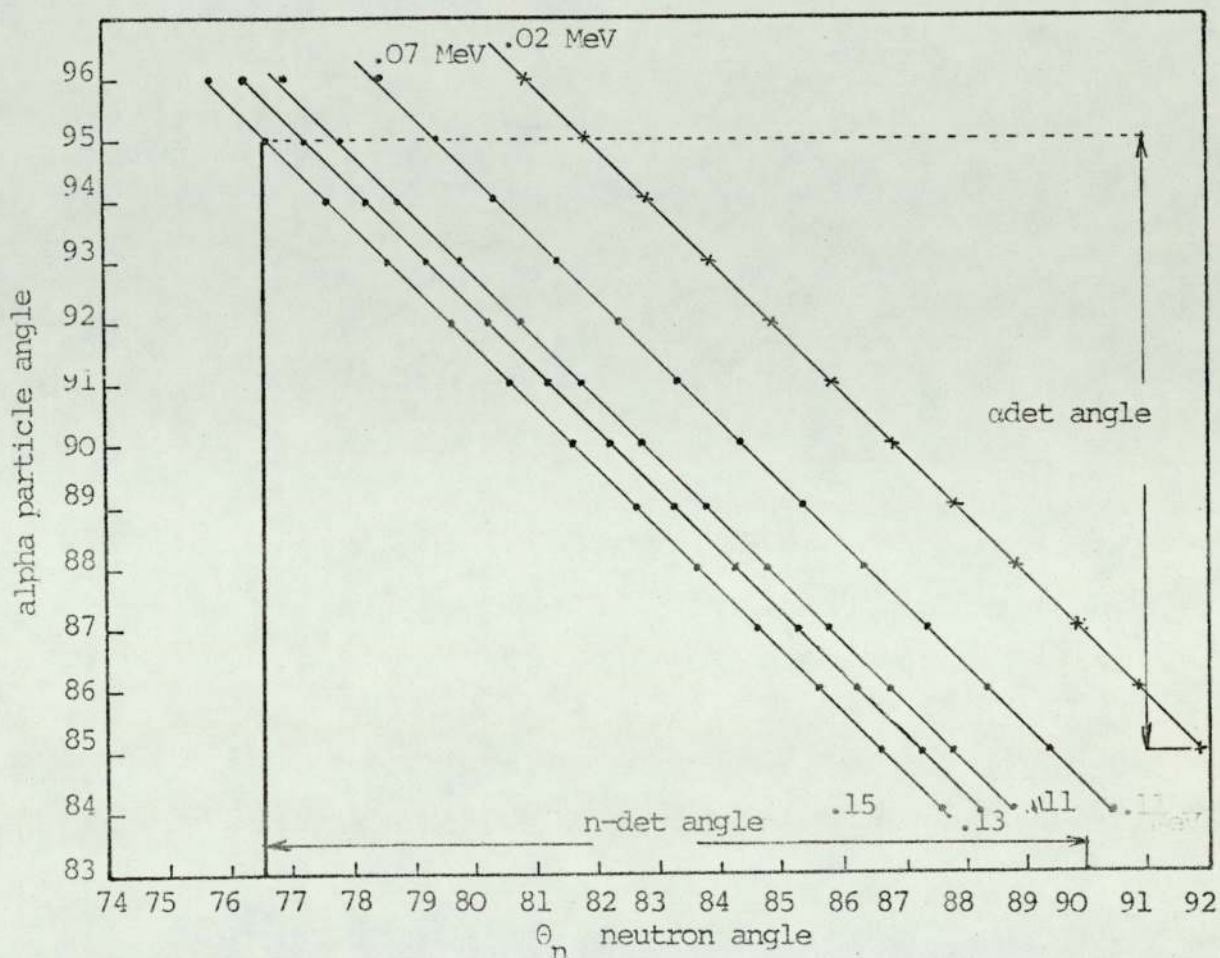


Fig. 4.5 Relationship between neutron and alpha particle angles in the lab-system

To determine the energy loss, the loading factor or number of tritium atoms per titanium atom in the target must be known, a reasonable estimate for this factor is unity⁽⁵¹⁾.

$$N_1 = \frac{\rho_{T_1-T} \times 6.02 \times 10^{23}}{A_{T_1-T}} = \frac{4.1 \times 6.02 \times 10^{23}}{50.9}$$

$$= 4.8 \times 10^{22} \text{ atoms/cm}^3$$

The cross section for the $T(d,n)^4\text{He}$ reaction has been measured by Conner et al⁽⁵⁶⁾ for 10 - 1752 KeV deuterons and by Arnold et al⁽⁵⁷⁾ for 7.5 - 120 KeV deuterons. Figure 4.6 gives the cross section for deuteron energies between 10 KeV to 500 KeV⁽⁵¹⁾.

The rate of energy loss for deuteron in Ti-T is given by

$$\frac{dE}{dx} = \frac{47.9}{47.9+3n} \left(\frac{dE}{dx}\right)_{Ti} + \frac{3n}{47.9+3n} \left(\frac{dE}{dx}\right)_T$$

where $\left(\frac{dE}{dx}\right)_{Ti}$ is the rate of energy loss of deuteron in titanium.

$\left(\frac{dE}{dx}\right)_T$ is the rate of energy loss of deuteron in tritium

n is the number of tritium atoms per titanium atom

(it is assumed $n = 1$)

3 and 47.9 are the atomic weights of tritium and titanium respectively.

To obtain the curve for Ti it is necessary to assume a law relating energy loss with atomic weight⁽⁵⁹⁾.

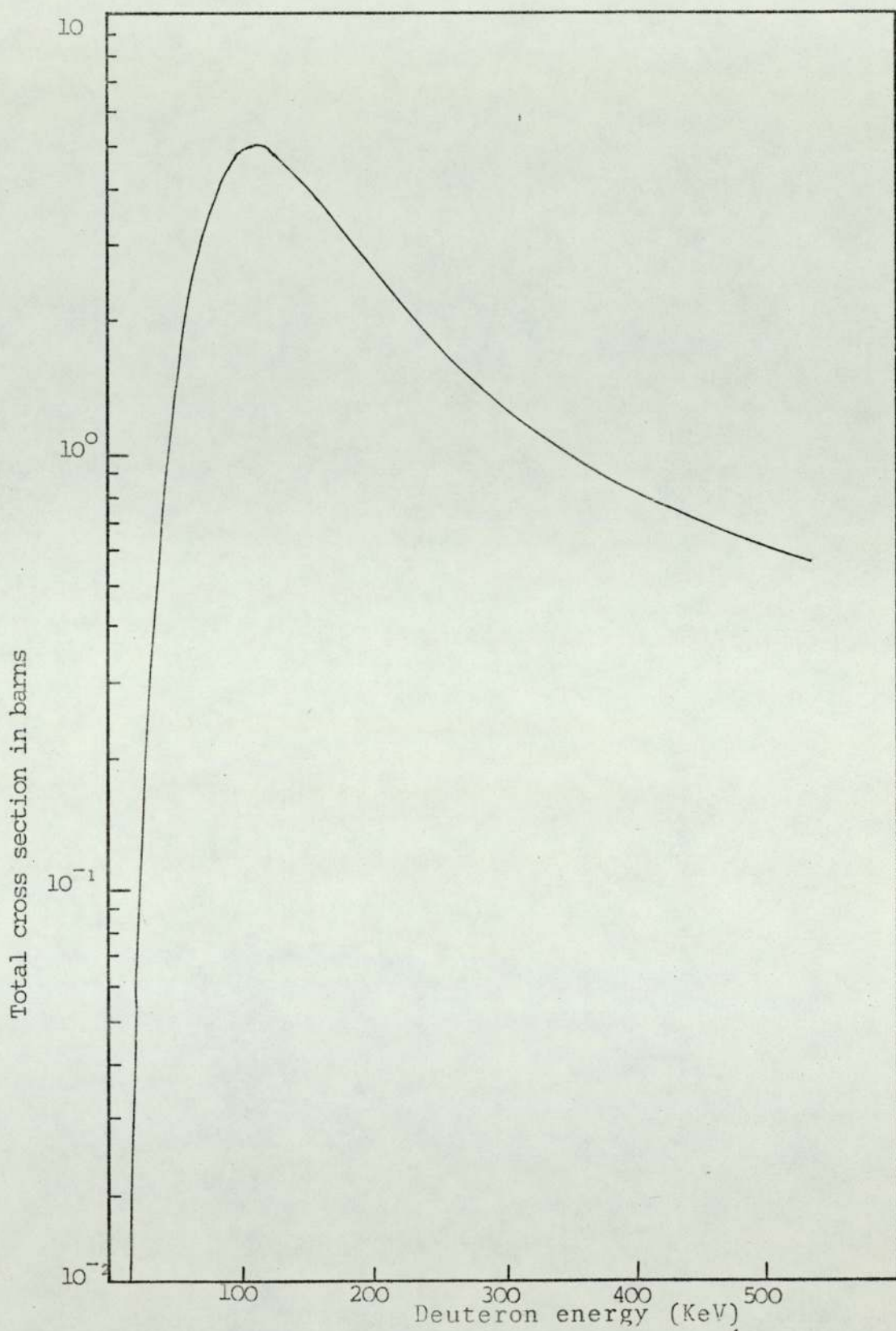


Fig. 4.6 Total cross section for $T(d,n)^4He$ reaction

The usual assumption is $dE/dx \propto A^{-1/2}$ but by taking Warshaw's measured results for the metals quoted the assumption is found only to be valid at higher energies (deuteron energy of 300-400 KeV) and only for materials of low atomic weight (${}_{22}^{47}\text{T}_i$ lies between ${}_{13}^{27}\text{Al}$ and ${}_{29}^{63}\text{Cu}$ in the atomic table).

The stopping power $\frac{dE}{dx}$ has been calculated by Benveniste and Zenger⁽⁵¹⁾. They interpolated the proton stopping power data of Warshaw⁽⁵⁶⁾ for 50 KeV to 350 KeV protons in aluminium and copper with respect to the inverse square root of the mass number to produce a proton stopping power curve in titanium, then by assuming that the rate of energy loss is a function only of the velocity of the particle

$$\left(\frac{dE_p}{dx}\right)_E = \left(\frac{dE_d}{dx}\right)_{2E}$$

a deuteron stopping power curve in titanium was derived. Similarly the rate of energy loss of deuterons in tritium was obtained using the proton data of Reynold⁽⁶⁰⁾. Figure 4.7 shows the rate of energy loss of deuterons in the tritium-titanium target.

With this information the neutron yield per incident deuteron energy E can be calculated by numerical integration of equation 4.3.

4.5 The Alpha-Particle Detector

Alpha particles are heavy and have a positive charge twice that of protons. They do not easily penetrate to the nucleus because their primary interactions are with the electrons and

~~electrostatic forces that~~
~~surrounding~~

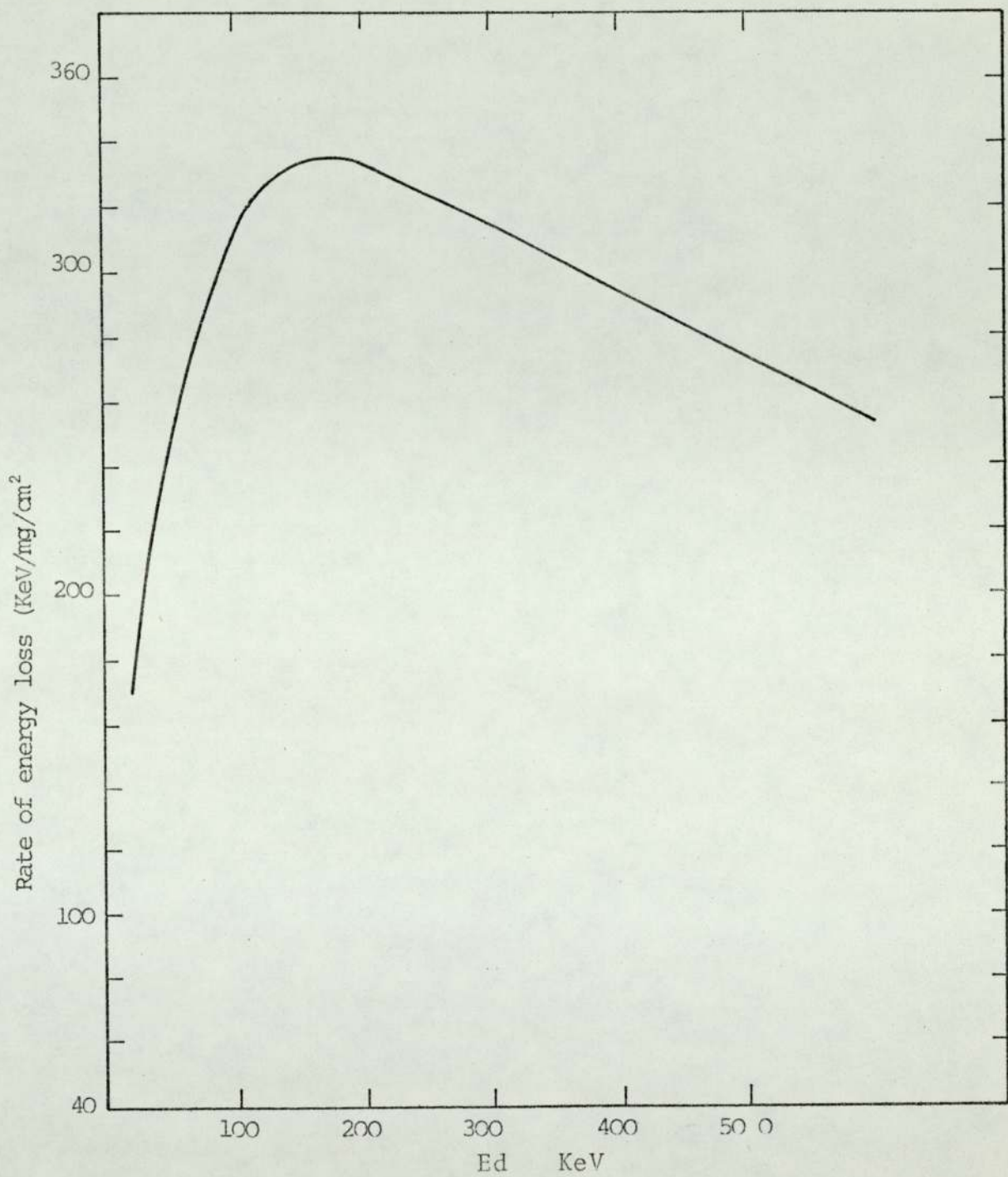


Fig. 4.7 Rate of energy loss of deuteron in tritium-titanium target

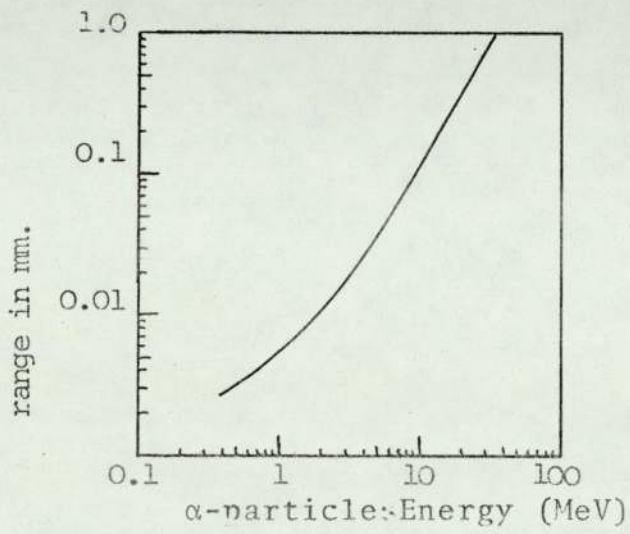


Fig. 4.8 Range of α -particles in NE-102A

electrostatic forces that surround atoms. They lose energy to the surrounding medium primarily through the ionization and because of their highly ionizing properties they can be detected with high efficiency. Alpha particle detector suitable for the present work should have the following properties

- (a) a high detection efficiency (100% if possible) for the 3.5 Mev alpha particle from the $T(d,n)^4\text{He}$ reaction.
- (b) a low neutron and γ -ray detection efficiency
- (c) a fast response time for the nanosecond time-of-flight measurements.

Two types of detectors, an organic plastic scintillator or a semi-conductor detector, closely meet these requirements. A suitable scintillator is Nuclear Enterprise's plastic scintillator type N.E.-102A. It is readily available in thin sheets, thus having a low neutron detection efficiency and being an organic material with low z number it has a low detection efficiency for γ -rays. Plastic scintillator N.E.-102A has been discussed in section 3.4. When used in conjunction with a photomultiplier tube with a small transit time spread it meets the timing requirements for the present work. The silicon surface barrier semi-conductor detector has a low response to both neutrons and γ -rays and has a fast response time (less than 6ns). On comparing these two detectors there are two advantages in using plastic scintillator in preference to the silicon surface barrier detector.

1. The use of a plastic scintillator with a high gain photomultiplier tube is preferred because of the high amplification

required with the semi-conductor detector.

2. The scintillation detector is less sensitive to radiation damage than the semi-conductor detector. Radiation damage in the semi-conductor is mainly due to α -particles which are more damaging than fast neutrons. (61)

For the above advantages the plastic scintillator was chosen for the alpha particle detection in the present work. In the $T(d,n)^4\text{He}$ reaction the alpha particles emitted at 90° to the deuteron beam direction have an energy of approximately 3.5 MeV as discussed in section 4.3.

The range of alpha particles in NE-102A is shown in figure 4.8 (30) which gives a range of .025 mm. for 3.5 MeV alpha particles, so this thickness of plastic scintillator NE-102A would be 100% efficient.

The scintillator used was .5 mm. thick and was coupled to a 56 AVP photomultiplier tube. Figure 4.9. The tube has a transit time spread of less than 0.5 ns making it very good for fast timing work. Since the position of the photomultiplier was fixed with respect to the earth's magnetic field a magnetic shield was not placed around the photomultiplier. The detector was in the form of a square sheet 3.18 x 3.18 cm. When positioned 9 cm from the centre of the target, the detector subtended an angle of $\approx 19^\circ$. This is the maximum angle allowed by the inside diameter of the connecting vacuum tube. By the use of defining apertures, smaller detector areas were selected as required. The short range of the 3.5 Mev alpha particles made it necessary to locate the detector within the vacuum

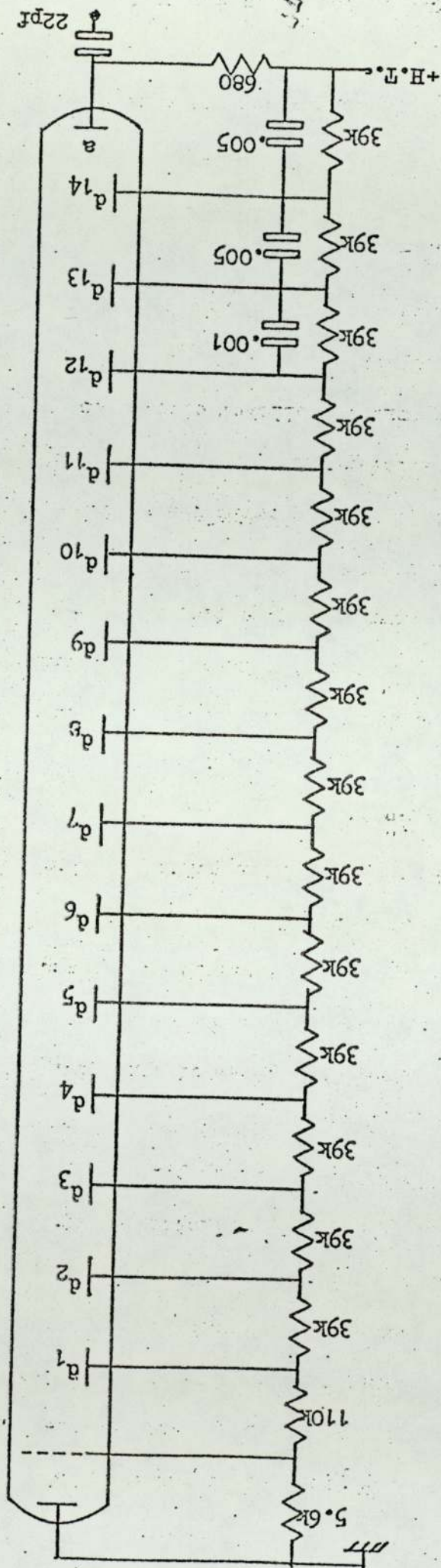


Fig 4.9 Dynode Resistor chain

system, while for reasons of outgassing from the dynode chain, as well as cooling, it was desirable to mount the photomultiplier system outside the vacuum. This was accomplished by mounting the NE-102A scintillator on a perspex light pipe 10 mm. thick which also acted as a vacuum seal. The alpha particle detector is shown in figure 4.10. The scintillator sheet was attached to the perspex light pipe with optical cement type NE.580 to ensure good optical contact in vacuum. The photomultiplier was spring loaded onto the flange using silicone immersion oil to make a good optical contact between the perspex flange and the photocathode.

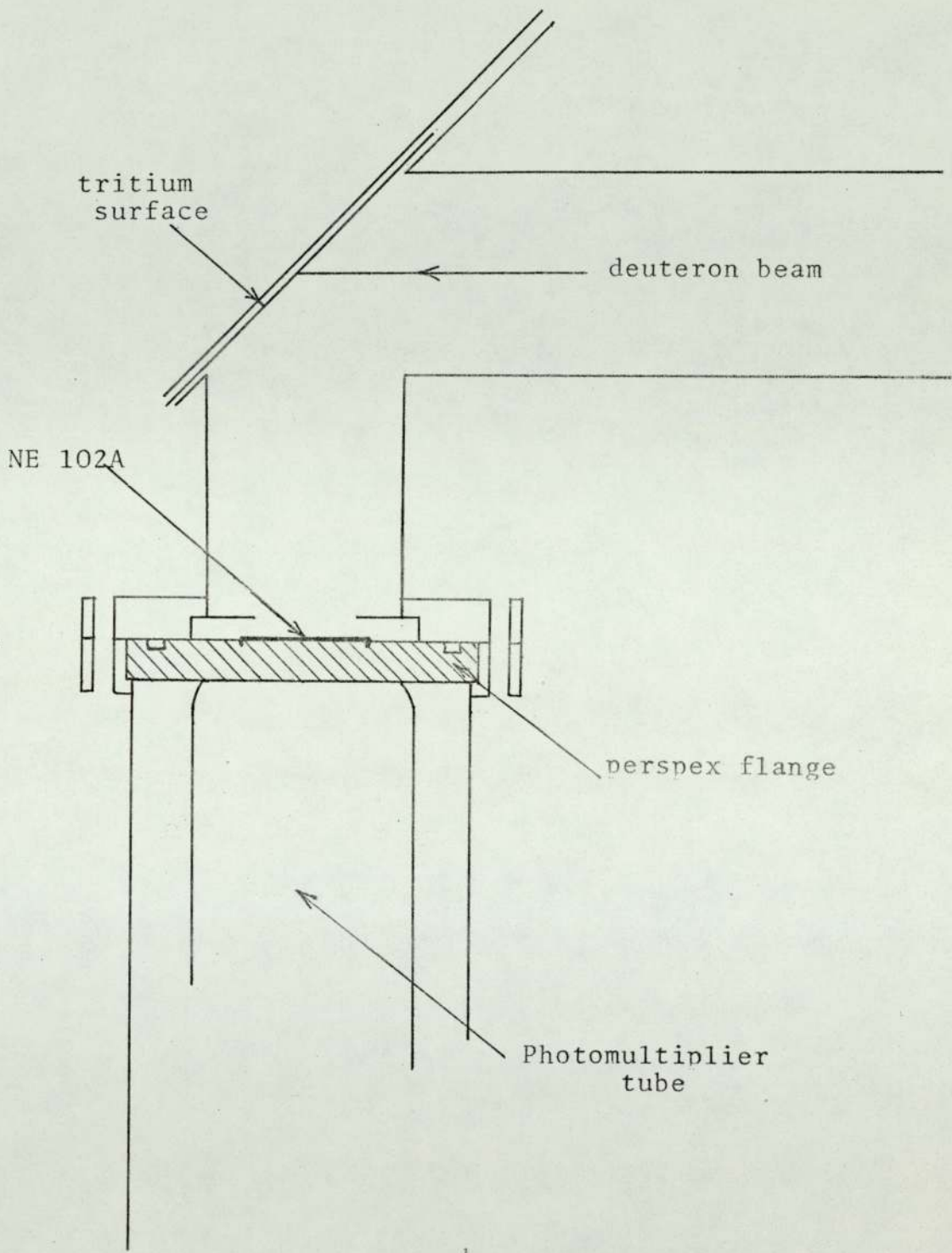
4.6 Alpha-detector Shielding

The alpha-detector had to be shielded from two sources of radiation. These were β -particles emitted by the tritium target and deuterons scattered by the target.

The β -particles were produced by the decay of tritium in the target to ${}^3\text{He}$ with 12.3 year half-life $T \rightarrow {}^3\text{He} + \beta^- + \bar{\nu}$

The decay is not accompanied by γ -rays. The total energy released is 18.6 KeV. The range of 18.6 KeV β -particles in aluminium is .0022mm. ⁽⁶²⁾ so this thickness of aluminium would completely shield the scintillator against β - particles. The deuterons scattered through 90° into the alpha-detector have a maximum energy of 140 KeV, the range of deuterons in aluminium can be obtained by scaling proton range data ⁽⁵¹⁾, the range $R_d(E)$ of a deuteron of energy E and mass m_d is given by

Fig. 4.10 The alpha particle detector assembly



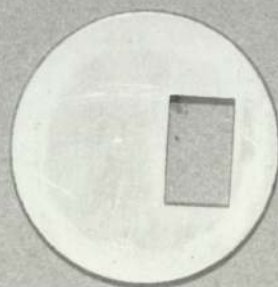
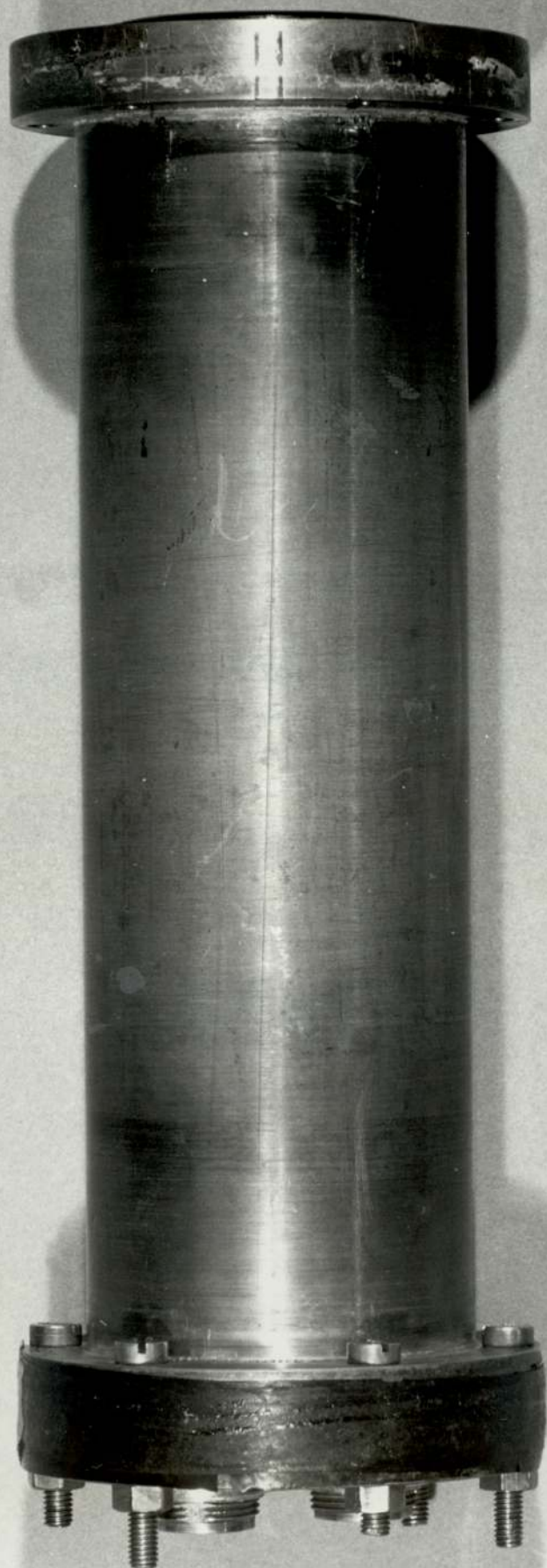
$$R_d(E) = \frac{m_d}{m_p} R_p \left(\frac{m_p}{m_d} E \right)$$

where m_p is the proton mass, R_p is the proton range so the deuteron range is twice the range of a proton with the same velocity. A 100 KeV proton has a range in aluminium of .26 mg/cm² (.001 mm.) so a 200 KeV deuteron has a range in aluminium of .52 mg/cm² (.002 mm.)

The aluminium foil was used to shield the scintillator from both the β -particles and scattered deuterons.⁽⁶³⁾ The foil used was .004 mm. thick which completely shielded the scintillator from β -particles and scattered deuterons, but not the α -particles. The range of 3.5 MeV alpha-particles in aluminium is 4.5 mg./cm² (.016mm).

The exposed area of the alpha-scintillator was defined by an aluminium aperture plate placed directly in front of the scintillator in a slot in the target assembly flange. The aluminium plate had a rectangular hole cut out measuring 1.8 cm. horizontally by 1 cm vertically. This limited the angular acceptance of alpha-particles in the horizontal plane to $90^\circ \pm 5^\circ$. The alpha-detector assembly is shown in Figure 4.11.

FIGURE 4.14 ALPHA PARTICLE DETECTOR



CHAPTER 5

THE TIME-OF-FLIGHT TECHNIQUE AND THE EXPERIMENTAL ARRANGEMENTS

5.1 Introduction

With the development of electronic techniques and scintillation materials with responses in the nanosecond range the time-of-flight technique has become quite a widely used technique in recent years for the energy measurement of fast neutrons. (64)(65)

The time-of-flight over a distance D measured in metres of a non-relativistic neutron of energy E_n (MeV) is given by the equation $t = \frac{72.3 D}{\sqrt{E_n}}$ ns 5.1

with a flight path of one metre the interval of time for neutrons of energies in the range (.5 - 15 Mev) is of the order of a few nanoseconds to 100 ns: (66,67) for 14 MeV neutrons the flight time is 19 ns for a path of 1m.

The neutron energy resolution for a time-of-flight spectrometer is given by the formula

$$\frac{dE}{E} = 2 \frac{dt}{t}$$

The basic problem involved in using the time-of-flight technique for the measurement of a neutron energy can be divided into two parts :

- (a) The production of a signal giving the time zero at the start of the flight of the neutron.
- (b) The production of another signal corresponding to the end of the flight.

The precise determination of the time of origin of the neutron is an essential part of the time-of-flight technique. There are two different methods for the determination of the zero time ⁽⁶⁸⁾ with low energy acceleration and they are

- (i) The pulsed beam method
- (ii) The associated particle method

In the pulsed beam method the neutrons are produced in short bursts which mark the beginning of the neutron flight time and the end of the flight path is marked by a signal from the neutron detector. ⁽⁶⁹⁾ The source is usually a nuclear reaction induced by ion bombardment. The zero time for a neutron originating at the source point can be localized by producing the neutrons in bursts of time duration Δt_b . A certain neutron is then produced at a given point and time with a time uncertainty Δt_b . If the neutrons are produced by positive ions bombarding a target to induce a nuclear reaction it is sufficient to produce the positive ions in bursts of time Δt_b , therefore talking in terms of ion-beam burst duration is in fact talking about neutron burst duration. The pulsing method is more general and can in principle be applied to all types of reactions, hence a wide range of neutron energies can be covered by the use of different charged particle reactions. In the pulse method the burst duration is an important factor in determining the spectrometer resolution so the beam of incident particles which initiates the reaction must be pulsed on the target for a time shorter than the time of

flight of the highest energy neutrons involved and at such a rate that the longest flight time of interest can be measured before the next beam pulse reaches the target.^(70,71)

The associated particle method is not as generally applicable as the pulsed beam method and it is mainly used with the $T(d,n)^4\text{He}$ reaction and sometimes with the $D(D,n)^3\text{He}$ reaction. The helium particle from the reaction which can be detected with 100% efficiency⁽⁷²⁾ by a scintillation or solid state detector is used as the zero time marker, the neutron associated with this alpha particle proceeding to the scatterer when it is scattered towards a second detector that detects the neutron and provides the second time pulse that corresponds to the end of its flight. The angle between the helium particle and the neutron is fixed by the kinematics of the nuclear reaction (section 4.3.1).

The solid angle subtended by the helium particle detector at the target defines a related solid angle into which the associated neutrons are emitted.

The associated particle method has the advantage of being used with a continuous beam and with the scattering sample positioned so that it subtends all of the defined neutron beam and a neutron start pulse is only obtained when a neutron penetrates the sample thus giving a good signal to background ratio resulting from the coincidence requirement.⁽⁷³⁾ For a system employing two detectors the random coincidence rate per analyser channel is $C = N_1 N_2 t$

Where N_1 = count rate in the neutron detector

N_2 = count rate in the alpha detector

t = resolving time/analyser channel

A comparison between these two methods shows that the pulsed beam method can be applied to all types of reactions and gives a zero time independent of the reaction mechanism, which the associated particle method is mostly limited with the D-D and D-T reactions. The pulsed beam method which can give higher neutron intensities enables the flight path of the spectrometer to be <10 metres,⁽⁷⁴⁾ whereas random coincidences exist in the associated particle method due to continuous production of neutrons and their scattering by the surroundings into the neutron detector. Therefore the flight path has to be relatively shorter (<metres⁽⁷⁵⁾) in order to minimize the random coincidence rate compared to the wanted signal. The time resolution with the associated particle method may be slightly better than that with the pulsed beam method because of timing uncertainty caused by the finite pulse length. The production of intense ion bursts in the nanosecond range requires sophisticated equipment which is not required with the associated particle method, so the associated particle method with the $T(d,n)^4\text{He}$ reaction was adopted in the present work.

5.2 Experimental Considerations for the Associated Particle Method

From the kinematics of the $T(d,n)^4\text{He}$ reaction and from the discussion in section 4.3.2 the alpha particles detected at an angle of $90^\circ \pm 5^\circ$ to the incident deuteron beam define a cone of neutrons extending from 76° to 90° to the deuteron beam direction in the laboratory system. The most intense part of the neutron beam was at an angle of 83° to the deuteron beam direction so the scattering sample was centred on this angle. The scattering sample was positioned so that it completely intercepted the neutron beam defined by the associated alpha particles. The scattering sample was positioned 25cm from the target, at this distance the cross-sectional area of the neutron beam defined by the 10° alpha particle detector aperture was 2.65cm high by 5cm wide. The sample stand had a steel base fixed to the laboratory floor, the sample platform was a thin flat steel plate as shown in figure 5.1 due to the limited experimental area available in the laboratory the flight path from the centre of the scattering sample to the face of the neutron detector was fixed at 1.9 metres and the scattering angle was limited to angles between 0° and 100° by the experimental layout as shown in figure 5.2.

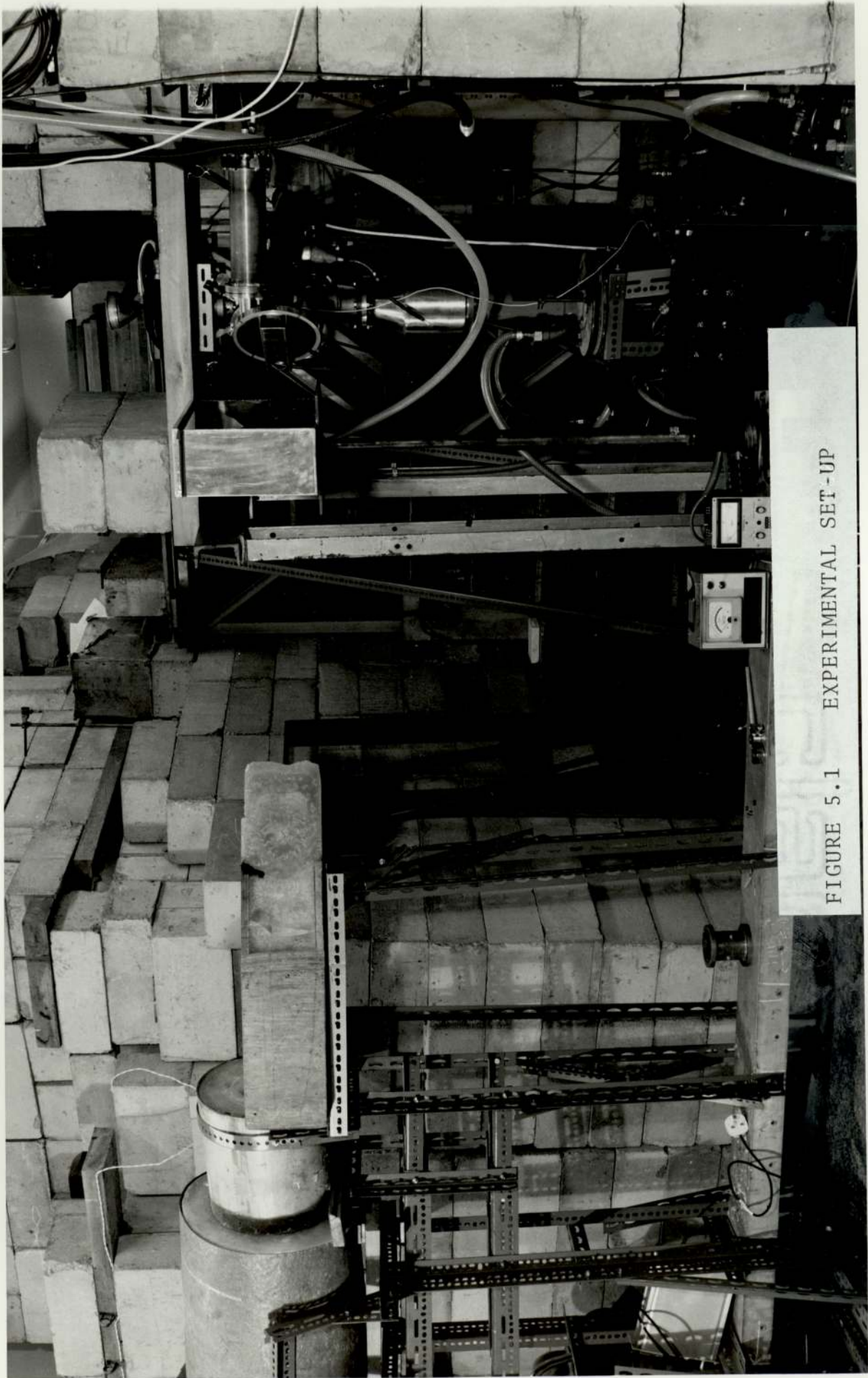
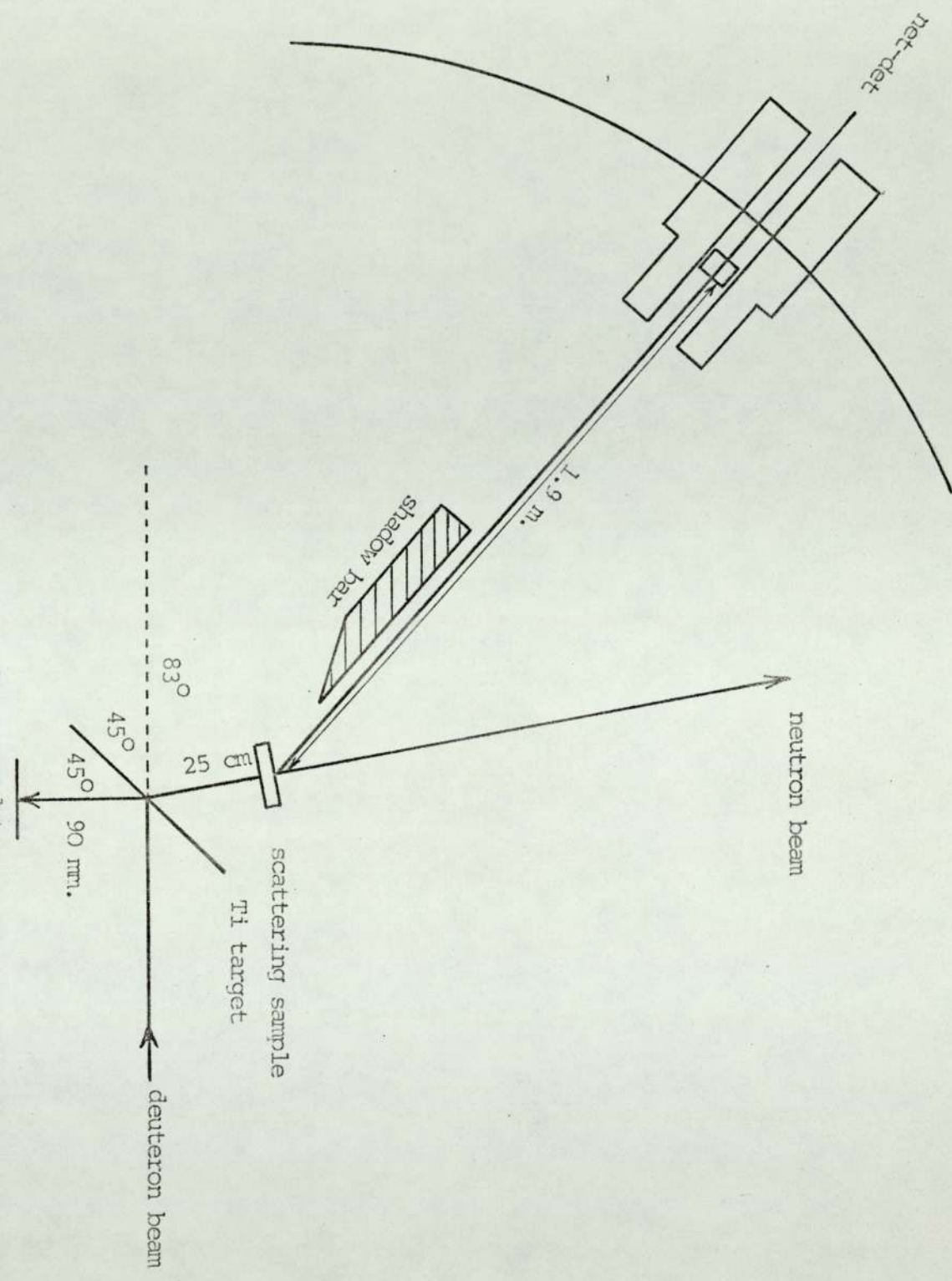


FIGURE 5.1 EXPERIMENTAL SET-UP



5.3 Time-of-Flight Spectrometer Electronics

In the time-of-flight technique the time differences between the start and the stop pulses can be measured by a time-to-pulse height converter whose pulse height output is directly proportional to the time difference of the two pulses arriving at the converter inputs. The pulse height distribution can then be recorded on a multi-channel pulse height analyser. A block diagram of the electronics system is shown in figure 5.3. The negative output pulses from the anode of the neutron photo-multiplier tube are fed into a coaxial cable through an emitter follower designed to provide suitable drive and matching into the coaxial line. From the emitter follower the pulses then go to the 100 MHz discriminator which accepts the pulses only if they exceed a preset amplitude. The negative output of the discriminator is then passed to the "start" input of the time-to-pulse height converter. In the alpha particle detection line the negative output pulses from the anode of the alpha photomultiplier tube are fed through a similar circuit, but because there will be a delay corresponding to the time of flight of the neutron from the target to the detector, so a delay must be estimated and allowed for in the measurement of the neutron flight time, therefore a variable delay unit is included in the alpha line to delay the signal to the "stop" input of the time to pulse height converter. The bipolar output pulse from the time to pulse height converter is fed to a multichannel pulse height analyser.

In choosing the components of the time-of-flight spectrometer it was necessary to ensure that all the units involved had

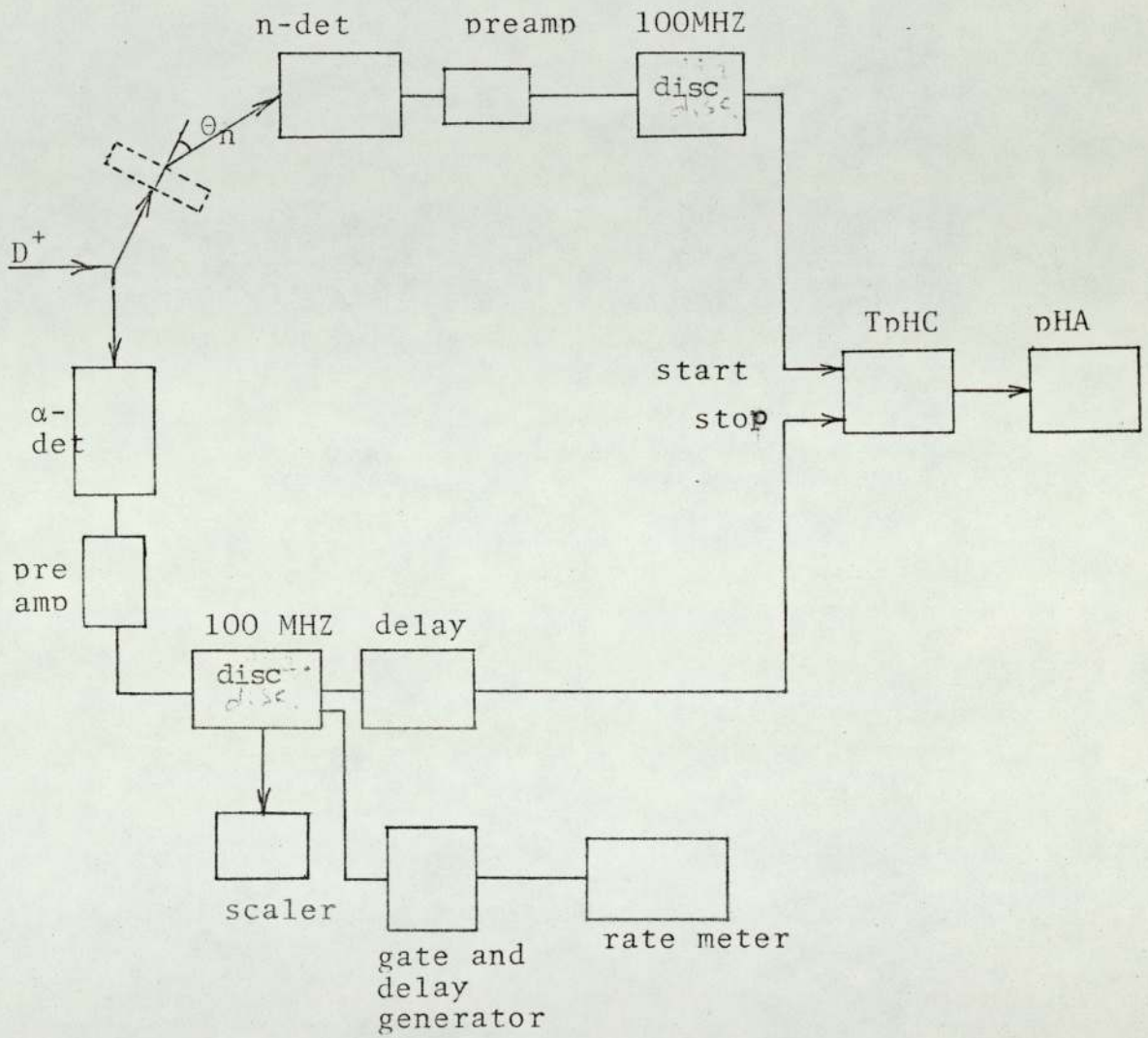


Fig. 5.3 Block diagram of the time-of-flight spectrometer

fast responses in order to match the fast pulses from the plastic scintillators of the neutron and the alpha counters. With the time-to-pulse height converter used the "stop" input could accept a maximum counting rate ten times as high as the "start" input. Consequently as the neutron counting rate was less than the alpha counting rate, the neutron signal was used to start the time-to-pulse height converter. Since the neutron detector was 1.9 metres away from the scatterer, the neutron pulses occur at a later time than the alpha pulses so the alpha pulses then were delayed by a fixed amount of time to use them as the stop signal.

5.4 Discriminators Adjustment

The discriminator used in the neutron line was the ORTEC 436 100 MHz discriminator which is a time derivation unit designed primarily for use with photomultiplier tubes but versatile enough to be used as a timing trigger or pulse shaper with any input signal shape from dc to 100 MHz; the discriminator level control sets a dc bias on the discriminator element which determines at what level of input voltage the unit will trigger⁽⁷⁷⁾. A similar discriminator was used with the alpha line. It was necessary to set the discriminator levels for both the neutron and the alpha particle detectors to discriminate against undesired pulses and to reduce the background from the accidental coincidences as discussed in section 3.5.2. The neutron discriminator was set to just reject pulses from ^{60}Co γ -rays interacting in the neutron detector. The experimental arrangement for setting the neutron discriminator level is shown in figure 5.4.

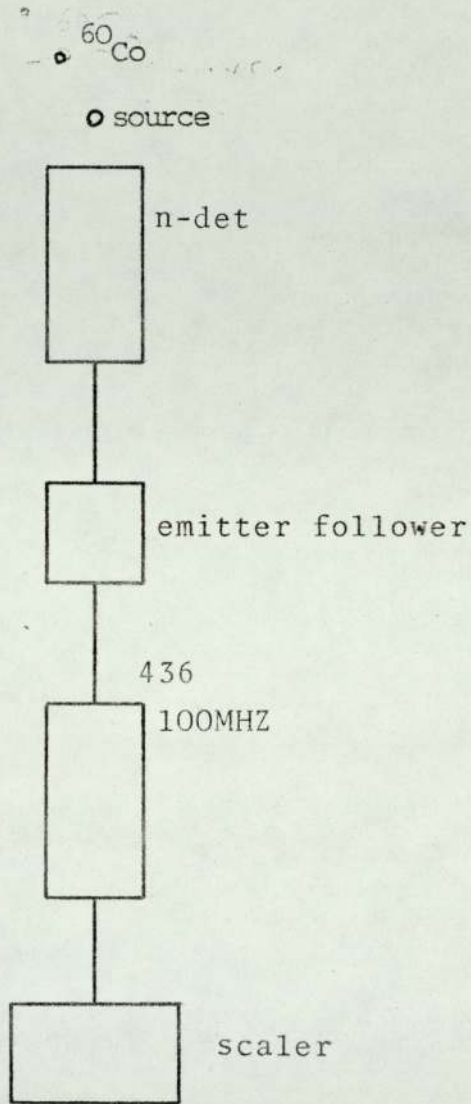


Fig. 5.4 Block diagram for adjusting the discriminator level

With a ^{60}Co γ -ray source placed in front of the neutron detector the count rate was measured as a function of the discriminator level setting (voltage setting). The differential Compton spectrum was obtained by plotting the difference in the number of counts in successive discriminator setting against that interval. This yielded the histogram shown in figure 5.5 which represents the Compton spectrum of the ^{60}Co γ -rays, the Compton edge of the 1.33 MeV γ -rays coinciding approximately with the point at which the count rate fell to one-half of its peak value. This point determined the discriminator level setting for the experiment.

The alpha discriminator level was adjusted in such a way that the time spectrum should have the optimum resolution and that was done by adjusting the discriminator level until the FWHM was the minimum for the time spectrum without distorting the shape of the spectrum, and that adjustment is the proper one by which the low energy noise pulses were eliminated without affecting the pulses of the 3.5 MeV alpha particles from the $\text{T(d,n)}^4\text{He}$ reaction.

5.5 Time-to-Pulse height Converter

In the time-of-flight technique the measurement of the time difference between the start (anode) signal from the neutron detector and the stop (anode) signal from the alpha detector is usually made by converting the time interval into a voltage pulse with amplitude proportional to the time differences between the start and the stop pulses. The time converter used in the present work was the ORTEC 447 time-to-pulse height converter⁽⁷⁸⁾ which provides an output pulse with

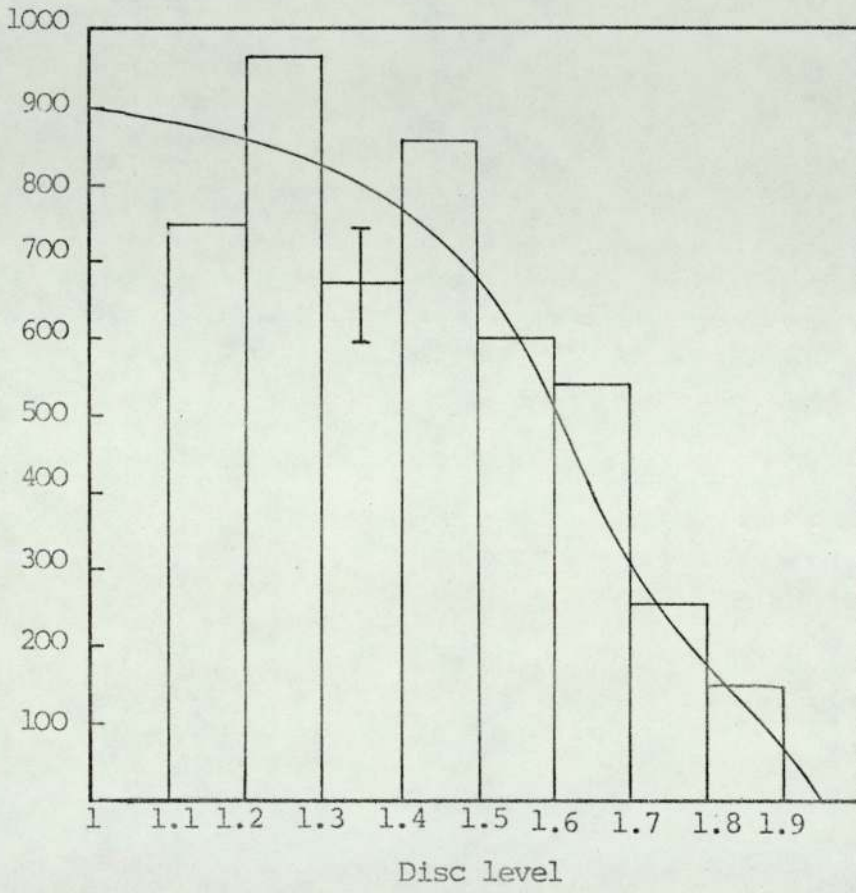


Fig. 5.5 Spectrum from ^{60}Co for discriminator adjustment

an amplitude proportional to the time interval between a start input and its related stop input, the full scale time range is a switch selectable for 3 ranges 50, 250 and 500 ns. A conversion signal is generated only if a stop signal follows an accepted start signal within the selected time range. The output has a signal with an amplitude proportional to the start-to-stop time interval. Full range for the output amplitude is 10V, the output pulses of the time-to-pulse height converter were analysed in a 100 channel pulse height analyser type TMC gammascope 1202.

5.6 The Spectrometer Resolution

The adjustment of the discriminators in the neutron and alpha lines was made to give optimum resolution for the time-of-flight spectrometer, the time resolution of the spectrometer was measured by observing the direct neutron beam which was at angle 83° to the incident deuteron beam direction. Figure 5.6 shows the FWHM of the spectrometer to be approximately 3.5ns. It was found that the resolution of the spectrometer to be dependent on the repetition rate in the alpha particle channel. The FWHM of the spectrum increases with the increase of the repetition rate in the alpha channel and a shift of the peak to lower channel number was also observed. There are several time uncertainties in the measurement of the start-to-stop time interval in the time-of-flight technique which will affect the time resolution of the spectrometer. The time resolution is the folding together of all contributing time uncertainties in production and detection of an event. With

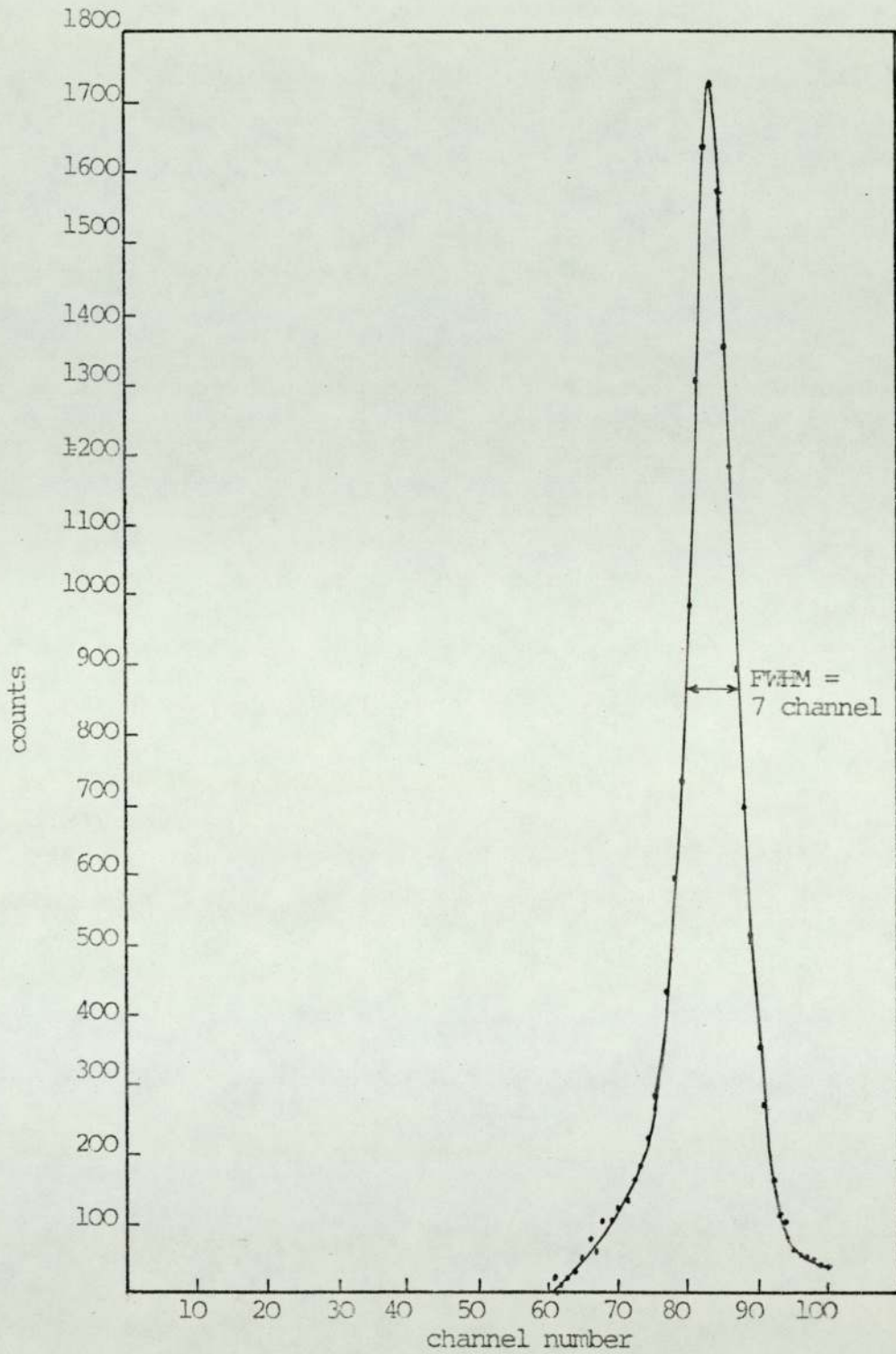


Fig. 5.6 Resolution of the time-of-flight spectrometer

the associated particle method the time uncertainties which affect the time resolution of the spectrometer may be due to the following

- (a) The spread in the flight path of the neutrons owing to the thickness of the detector.
- (b) The finite solid angles introduce a small spread in the flight path.
- (c) The spread in the energy of the neutrons and the α -particles which is due to
 - i. the solid angle of the α -detector with respect to the target
 - ii. the scattering and slowing down of deuterons and α -particles inside the target
 - iii. the $T(d,n)^4He$ reactions occur at different deuteron energies due to the thickness of the tritiated titanium target
- (d) The time uncertainties in the electronics.

Alpha particles of 3.52 MeV had a small energy spread of approximately 60 KeV, due to the 10° angular range subtended by the alpha detector. However, alpha particles produced inside the target by lower energy deuterons lose energy in escaping the target and the effective alpha particle energy range was 3.28 MeV to 3.58 MeV. The transit time in the neutron scintillator was 1ns for the 14 MeV neutrons and 2ns for the 3.5 MeV neutrons (section 3.4). The time resolution of 3.5 ns as represented by the FWHM corresponds to an energy resolution of 3.47 MeV in the 14 MeV neutron range.

5.7 Experimental Efficiency of the Neutron Detector

In the time-of-flight technique the precise detection of the start and the stop of an event is an essential part in the determination of the neutron energy. Also the efficiency

of the detectors involved must be determined in order to obtain a neutron energy spectrum from the time of flight data. The efficiency of the alpha particles detector was assumed to be 100% and counting losses in the alpha channel were ignored. No error should result from this assumption because the spectra were normalized to a constant number of alpha-particle pulses and neutrons associated with lost alpha particles would not be recorded⁽⁶⁷⁾.

The efficiency of the neutron detector was shown in section 3.5.2 to be variable with the neutron energy. The energy of neutrons elastically scattered in the laboratory system by LiF and Iron nuclei varies with the mass of the scattering nucleus and the scattering angle, therefore affecting the efficiency of the neutron detector so that it was necessary to determine experimentally the efficiency of the neutron detector as a function of the energy of the scattered neutron. The efficiency was measured as follows:-

The efficiency of the neutron detector for the 14.1 MeV neutron was measured using the direct beam; the circuitry used is shown in figure 5.7. The neutron-detector was 1.9 metres from the sample, with the discriminators set up as described in section 5.4 and with the count rate maintained as low as possible in the alpha channel. A coincidence spectrum was taken, the efficiency of the neutron detector was then given by the ratio of the total number of coincidences to the total number of neutrons incident on the detector as defined by the alpha particles detector count. The efficiency was given by

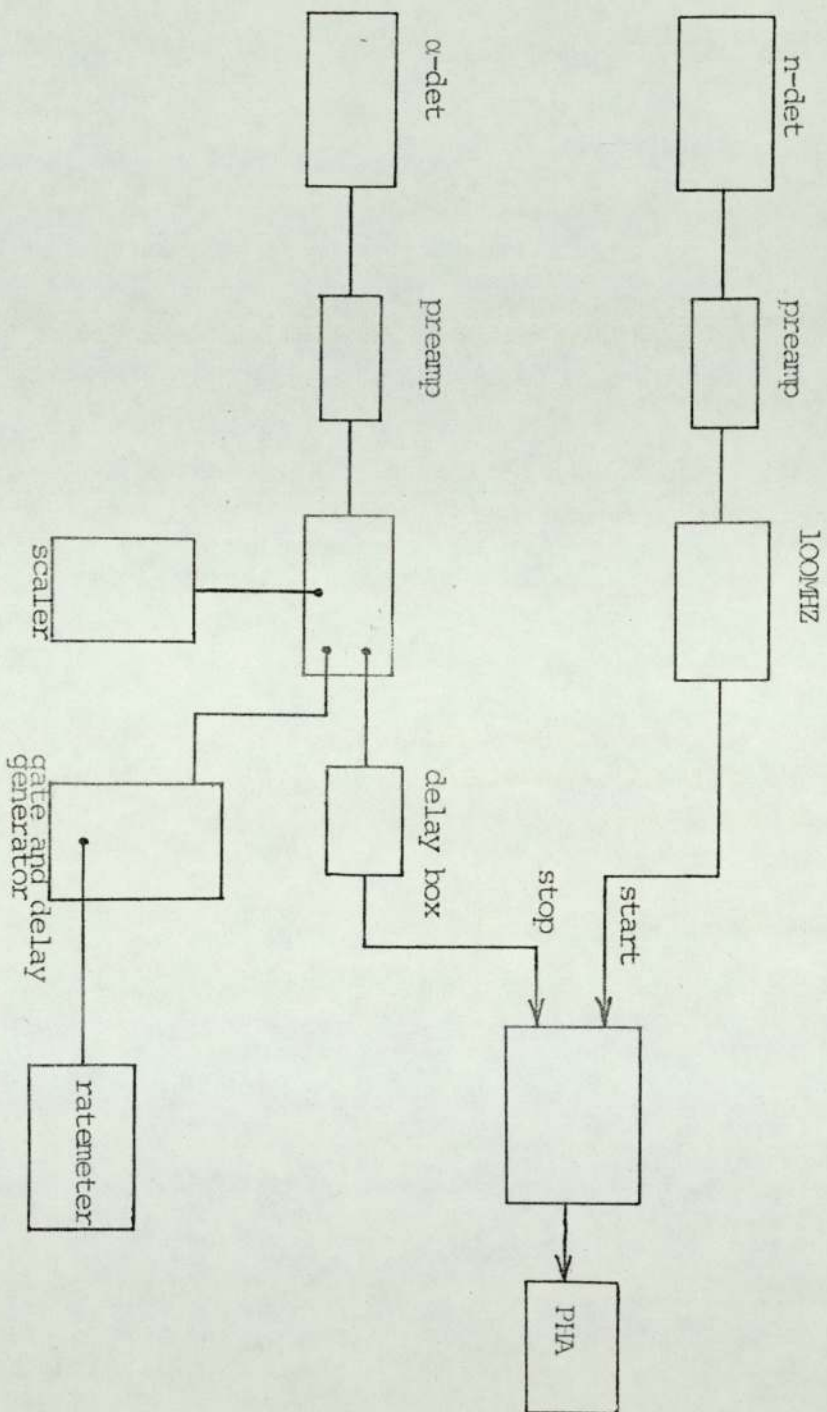


Fig. 5.7 Block diagram used in taking the efficiency measurement

$$\epsilon_{14} = \frac{n_t \times \Omega_\alpha}{n_\alpha \times \Omega_n}$$

where n_t = total number of coincidences

Ω_α = solid angle subtended by the α -detector with respect to the aperture

n_α = total number of alpha counts recorded in the scaler

Ω_n = solid angle subtended by the neutron detector and the sample

The efficiency of the neutron detector obtained from the above method was 5.2%. For neutrons of other energies the efficiency was determined by scattering primary neutrons from hydrogen which is in the form of a thin slab of polyethylene $(CH_2)_n$ at known angles. The incident neutrons of 14 MeV scattered from hydrogen as a function of scattering angle as calculated by equation 2.3 is shown in figure 5.8.

Elastically scattered neutrons from the hydrogen content of the polyethylene was found to overlap with those neutrons scattered by the carbon content of the polyethylene at certain angles. Therefore it was necessary to subtract from the polyethylene spectra the contribution due to neutron scattering from the carbon content of the polyethylene by replacing the polyethylene sample with a suitable graphite sample during the background subtraction mode. The thickness of the graphite sample is equivalent in thickness to the carbon content present in the polyethylene, making due allowance for neutron

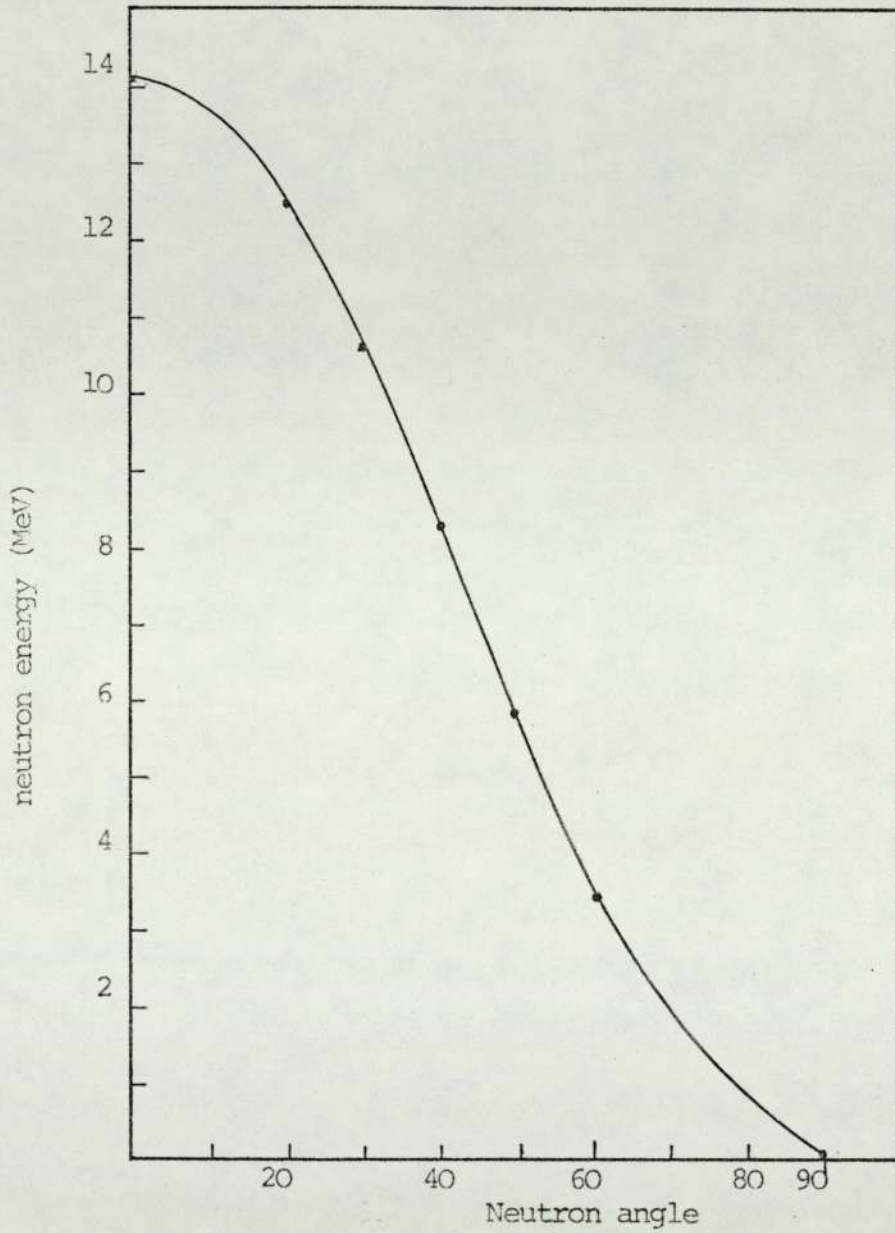


Fig. 5.8 Variation of neutron energy with angle after scattering from hydrogen

absorption. Therefore the graphite sample thickness depends on the thickness of the polyethylene sample, and since the distance a neutron travels in the polyethylene sample is varying with the angle at which the neutron is detected, the thickness of the graphite sample is also a variable with the angle of detection. The thickness of graphite required was calculated as follows:

Assuming single scattering the number of neutrons scattered by the carbon in the polyethylene sample at angle θ is given by

$$n_1(\theta) = \phi N_2 \frac{d\sigma s_2}{d\Omega} \Delta\Omega \left[\frac{e^{-\frac{(N_1\sigma_{t_1}^1 + N_2\sigma_{t_2}^1)\ell}{\cos\theta}} - e^{-(N_1\sigma_{t_1} + N_2\sigma_{t_1})\ell}}{(N_1\sigma_{t_1} + N_2\sigma_{t_2}) - \frac{(N_1\sigma_{t_1}^1 + N_2\sigma_{t_2}^1)}{\cos\theta}} \right] \quad 5.2$$

For the same incident neutron flux ϕ the number of neutrons scattered from a graphite sample of thickness ℓ^1 at the same angle θ is given by

$$n_2(\theta) = \phi N_2^1 \frac{d\sigma s_2}{d\Omega} \Delta\Omega \left[\frac{e^{-\frac{N_2^1\sigma_{t_2}^1\ell^1}{\cos\theta}} - e^{-N_2^1\sigma_{t_2}^1\ell^1}}{N_2^1\sigma_{t_2} - \frac{N_2^1\sigma_{t_2}^1}{\cos\theta}} \right] \quad 5.3$$

Equations 5.2 and 5.3 must be equal for exact subtraction of the scattering contribution due to carbon i.e. $n_1(\theta) = n_2(\theta)$

$$\therefore N_2 \left[\frac{e^{-\frac{(N_1\sigma_{t_1}^2 + N_2\sigma_{t_2}^1)\ell}{\cos\theta}} - e^{-(N_1\sigma_{t_1} + N_2\sigma_{t_2})\ell}}{(N_1\sigma_{t_1} + N_2\sigma_{t_2}) - \frac{N_1\sigma_{t_1}^1 + N_2\sigma_{t_2}^1}{\cos\theta}} \right] = N_1 \left[\frac{e^{-\frac{N_2^1\sigma_{t_2}^1\ell^1}{\cos\theta}} - e^{-N_2^1\sigma_{t_2}^1\ell^1}}{N_2^1\sigma_{t_2} - \frac{N_2^1\sigma_{t_2}^1}{\cos\theta}} \right] \quad 5.4$$

where N_2 = number of carbon atoms/cm³ in polyethylene

N_1 = " " H " /cm³ " "

$\sigma_{t_1}^1$ = x-section for H for neutrons that have been scattered by carbon at that angle

$\sigma_{t_2}^1$ = x-section for carbon for neutrons that have been scattered by graphite at that angle

σ_{t_1} = cross section for H at 14.1 MeV neutrons

σ_{t_2} = " " " C " " " "

N_2^1 = number of carbon atoms/cm³ in graphite

l^1 = thickness of polyethylene

l^1 = " " graphite

θ = neutron detector angle

therefore the thickness of the graphite sample l^1 can be calculated from equation 5.4

In using a thin polyethylene sample of 2 cm thickness so that the multiple scattering is minimum the equivalent thickness of the graphite sample was found to be 7.97 mm., 7.95 mm., 7.87 mm. and 7.72 mm. for the following angles respectively $\theta=20^\circ$, 30° , 40° , and 50° . For these angles the 14.1 MeV neutrons scattered from hydrogen have the following energies respectively 12.45 MeV, 10.57 MeV, 8.27 MeV and 5.82 MeV.

The efficiency measurements.

Times of flight spectra were obtained for laboratory scattering angles 20° , 30° , 40° and 50° with the neutron detector face positioned 1.9 metres from the centre of the scattering sample using the electronics set up as shown in figure 5.7.

The counting for the accumulation of the time-of-flight spectrum was done with several runs. Each run was performed by alternating the polyethylene sample (addition mode) and the graphite sample to correct for the carbon contribution (subtraction mode) each run corresponding to an alpha monitor count of 5×10^8 . The time of flight spectra obtained are shown in figures 5.9, 5.10, 5.11 and 5.12. The efficiency of the detector as a function of energy was calculated as follows

$$\epsilon = \frac{\text{total number of coincidence counts}}{\text{number of scattered neutrons reaching detector}}$$

The number of neutrons scattered from the polyethylene sample coming in to the unit solid angle around the neutron detector at an angle θ is given by

$$\frac{dn(\theta)}{dw} = n_{\alpha} \left(\frac{d\sigma_H}{dw} \right)_{\theta} \times N_H \left[\frac{-(N_H \sigma_H^1 + N_e \sigma_c^1) \ell}{\cos \theta} - \frac{-(N_H \sigma_H + N_c \sigma_c) \ell}{\cos \theta} \right] \quad 5.5$$

where

n_{α} = number of neutrons incident on scatterer = total number of alpha particles for the whole number of runs

$\left(\frac{d\sigma_H}{dw} \right)_{\theta}$ = differential cross section for hydrogen
 $= \frac{\sigma_H}{4\pi} \cos \theta$

N_H = number of hydrogen atoms/cm³ in the polyethylene sample

N_e = " " carbon " " " " " "

σ_H^1 = hydrogen cross section at neutron energy that has been scattered through angle θ by hydrogen

$\theta = 20^\circ$

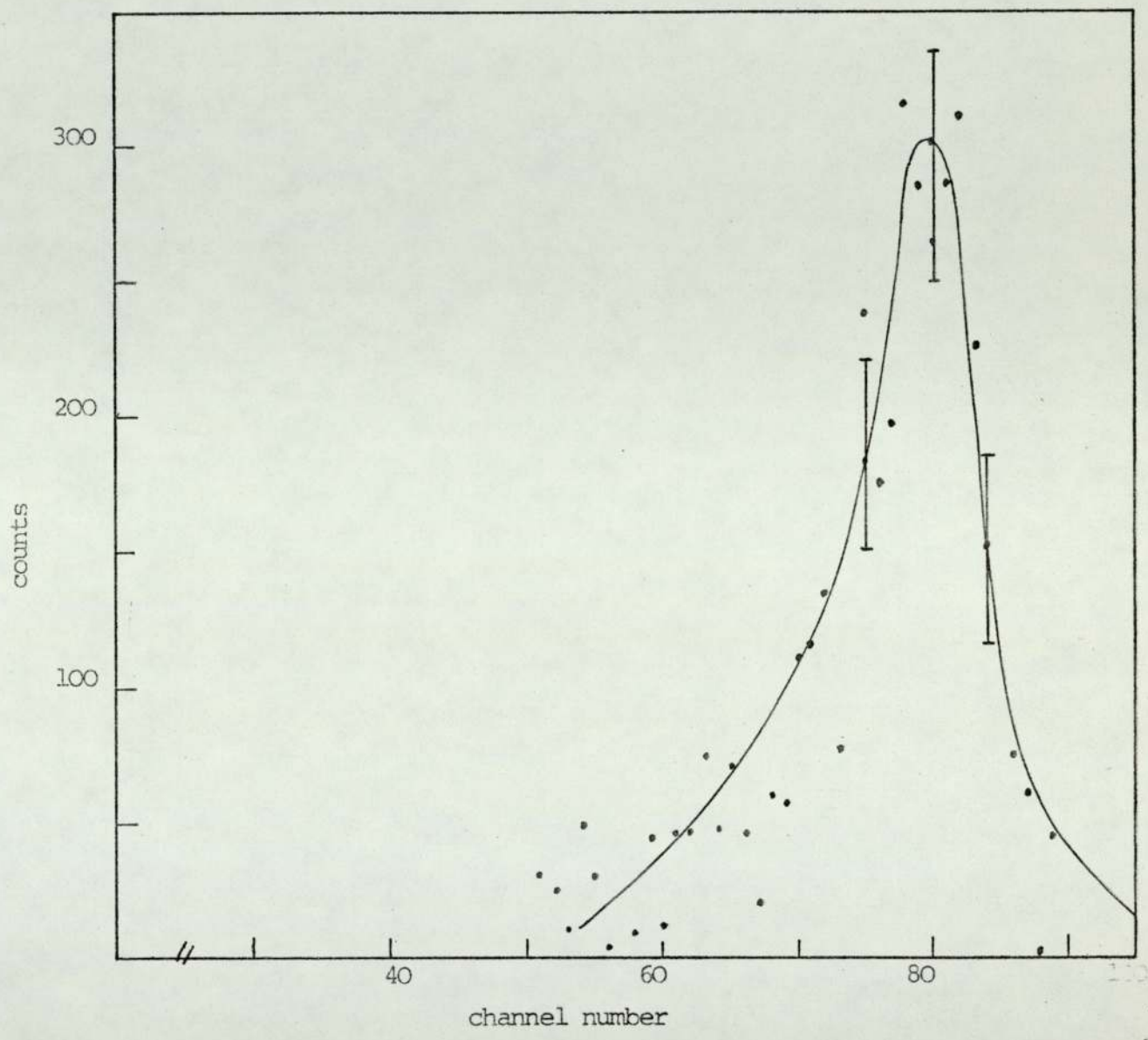


Fig. 5.9 Time-of-flight spectrum from hydrogen at a scattering angle of $\theta = 20^\circ$ in the lab-system

$\theta = 30^\circ$

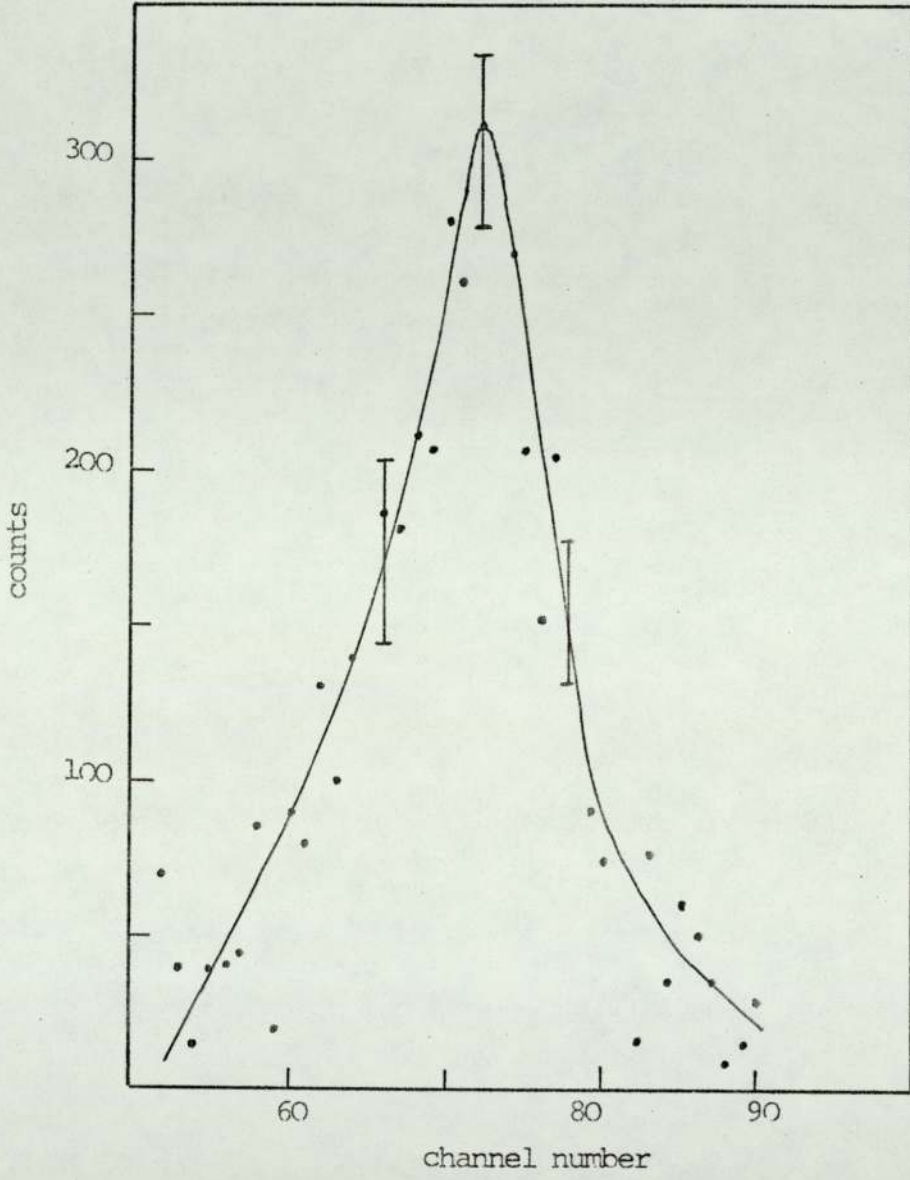


Fig. 5.10 Time-of-flight spectrum from hydrogen at a scattering angle of $\theta=30^\circ$ in the lab-system

$\theta = 40^\circ$

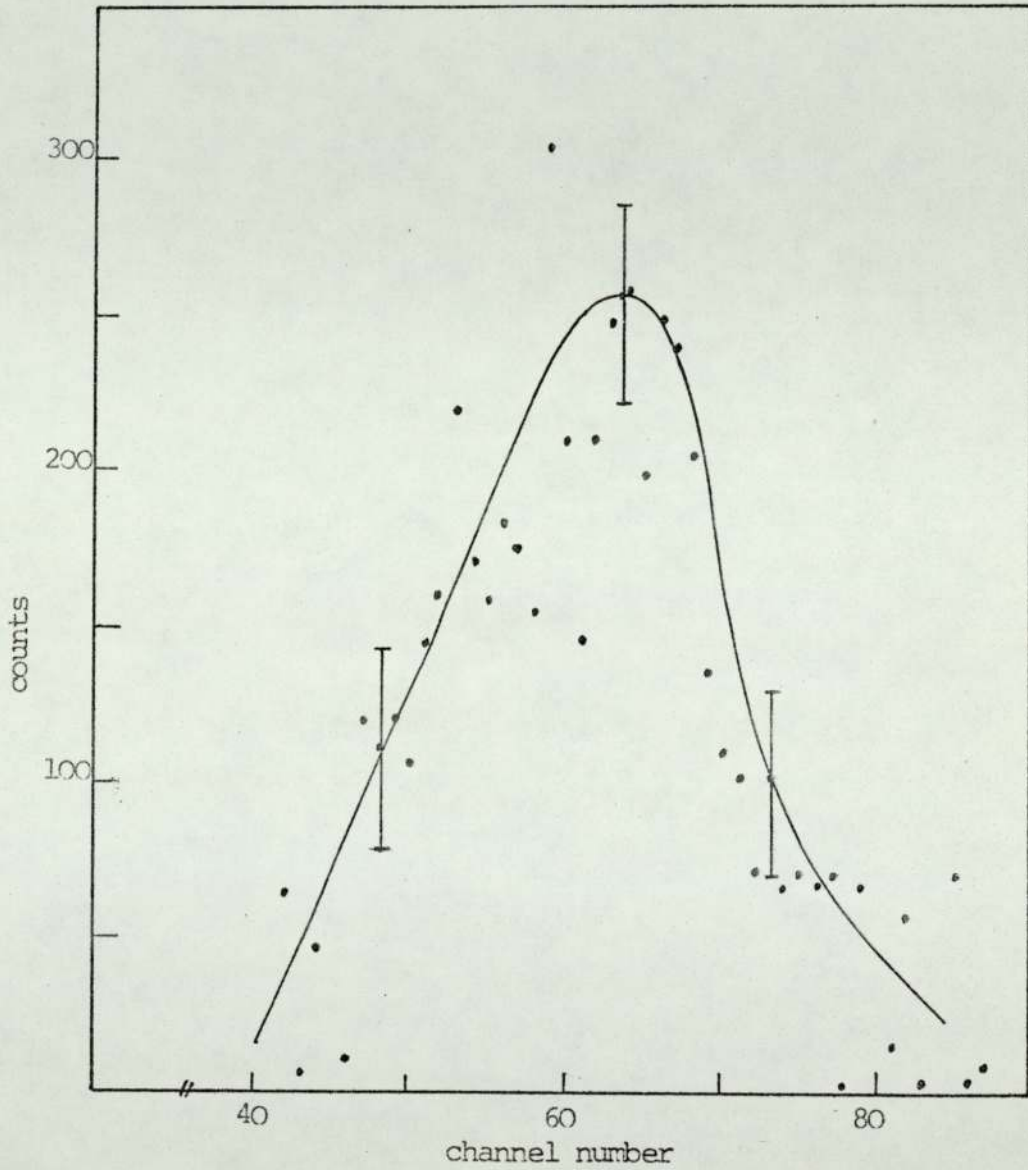


Fig. 5.11 Time-of-flight spectrum from hydrogen at a scattering angle of $\theta=40^\circ$ in the lab-system

$\theta = 50^\circ$

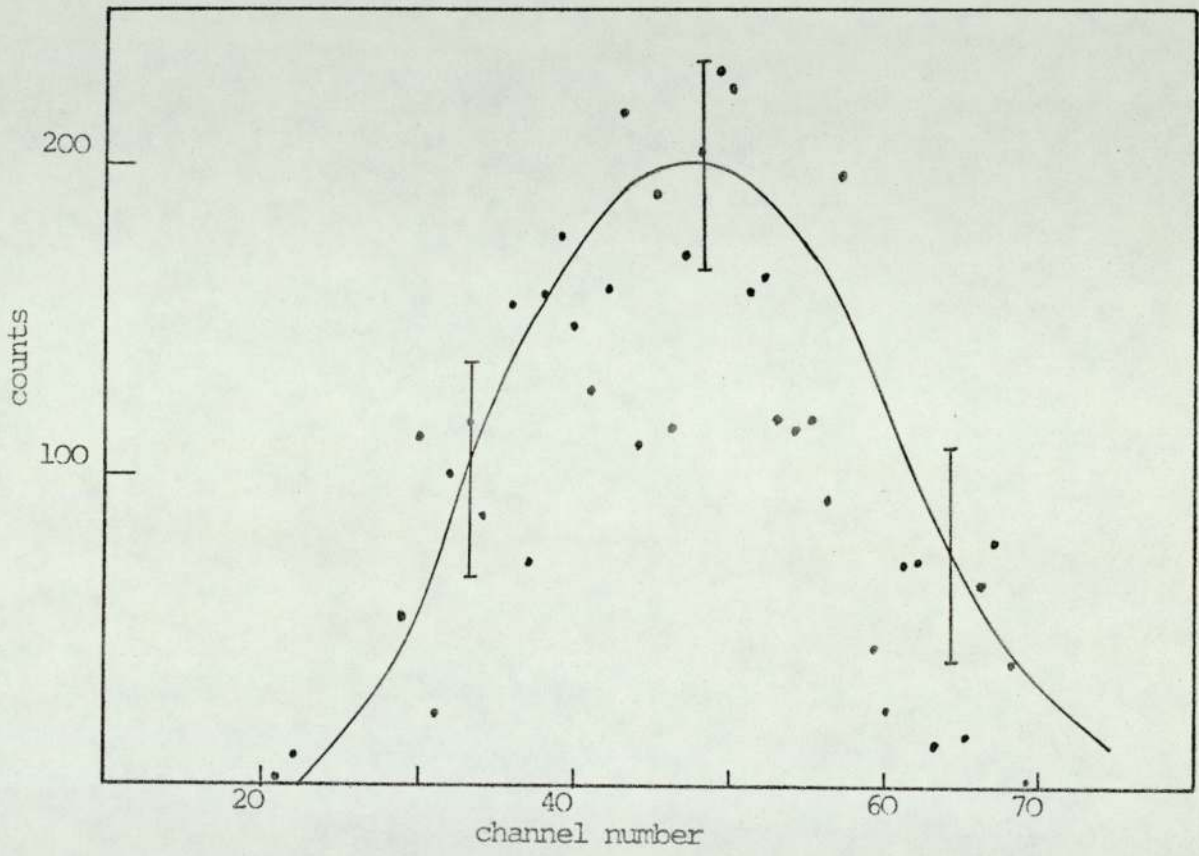


Fig. 5.12 Time-of-flight spectrum from hydrogen at a scattering angle of $\theta=50^\circ$ in the lab-system

σ_H = hydrogen cross section for 14.1 MeV neutrons

σ_C = carbon cross section for 14 MeV neutrons

θ = the neutron detector angle

l = thickness of polyethylene sample

The total number of coincidences is the area under the peak of the time spectrum for that angle. The experimental efficiency of neutron detector and the calculated efficiency of the detector with the discriminator is shown in figure 5.13.

From figure 5.13 it can be shown that the experimental efficiency is only about 50% of theoretical efficiency. This was because of the neutron absorption and scattering in the target due to the presence of copper, water, stainless steel in the way. There is also the very probable misalignment of the wax collimator which appears to be partly masking the detector.

5.8 Energy Calibration of the Spectrometer

Before starting to take any experimental measurements, it was necessary to determine the energy calibration of the spectrometer. Two main things have to be taken into consideration in the energy calibration of the spectrometer. These were first the energy range of the neutrons involved in the experiment and second, the γ -ray interference in the presence of neutrons.

The electronics set up used was the one shown in figure (5.7). The time-to-pulse height converter was set on 50 ns range so

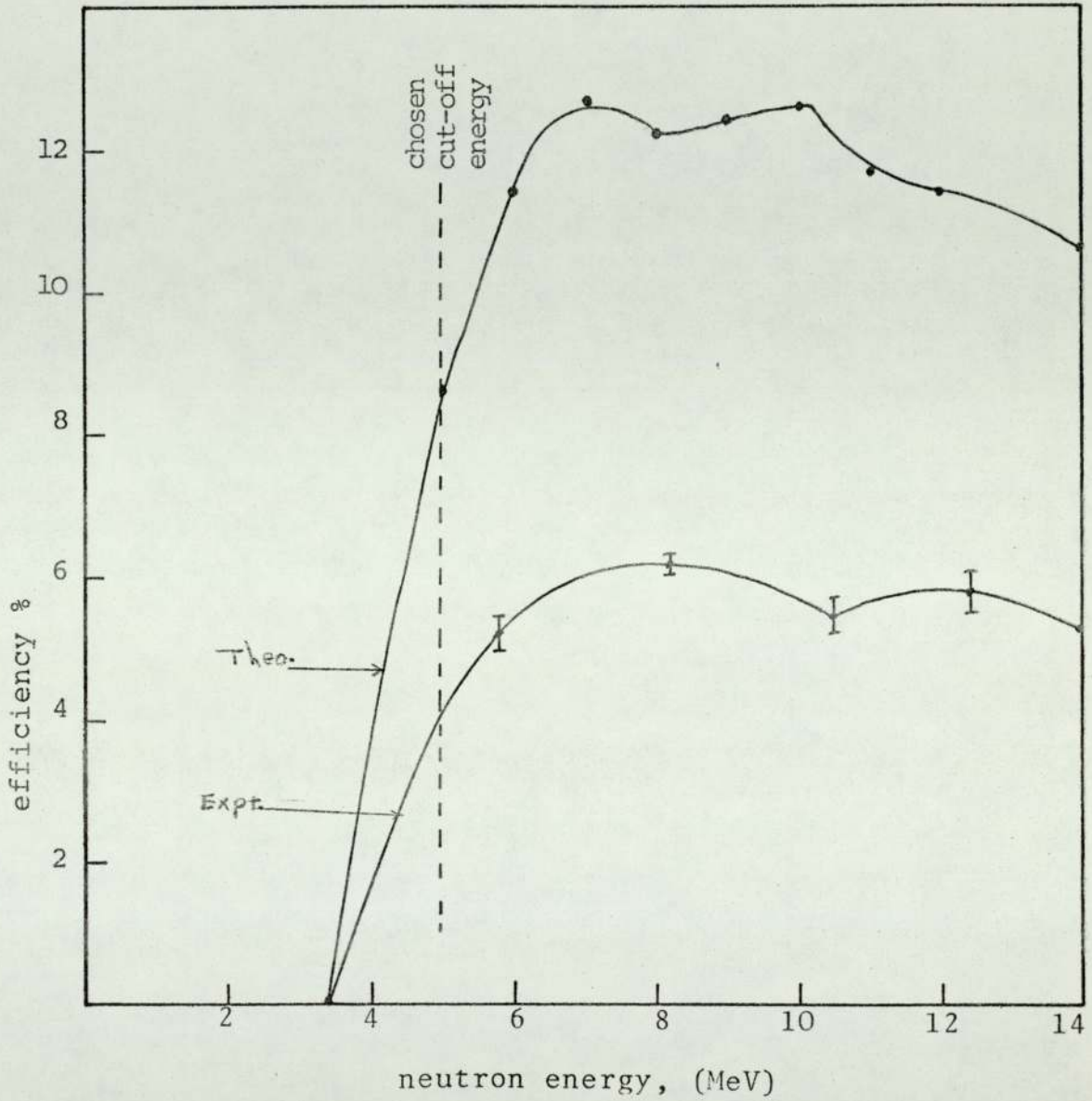


Fig. 5.13 Experimental and theoretical efficiency for the NE-102A 5cm thick neutron detector

that each channel of the multichannel pulse height analyser had a width of .5 ns. The maximum energy involved in this experiment was 14 MeV and the lowest measured efficiency was at 5.82 MeV (section 5.6). This set the lower limit for reliable spectral measurements as the efficiency fell rapidly below this energy, reaching zero at 3.4 MeV (figure 5.13).

By adjusting the position of the peak of the time spectrum of the 14 MeV neutron to be at the far end of the 100 channels the peak of the time spectrum of the 5.82 MeV was located at a position down the scale of the 100 channel as can be seen later.

The interference of the γ -rays has been eliminated in the following way. For a flight path of 2 metres the time taken by γ -rays to travel that distance is 7 ns and the time for the 14 MeV neutrons is 38 ns, so there is a difference of 31 ns between neutrons and γ -rays. Therefore there is a difference of 62 channels between the position of the peaks of γ and neutrons and since the γ -rays are faster than the 14 MeV neutrons the peak of the time spectrum of the γ appears earlier than the 14 MeV neutrons. By arranging the variable delay unit so that the peak of the time spectrum of the 14 MeV neutrons to appear in the higher channels of the multichannel analyser the γ peak can be eliminated. The spectrum which is being considered here is the time spectrum. To convert the time spectrum to energy spectrum the following is considered.

Let the flight path be ℓ metres and the time for a 14.1 MeV neutron to travel one metre be 19.25 ns.

Let the time spectrum peak of 14.1 MeV neutrons be at channel A.

$$v = \frac{\lambda}{t} = \frac{\lambda}{[19.25\lambda + (A-N) \times 0.5]} \times 10^{-9} \text{ m/sec}$$

$$E = \frac{1}{2}mv^2 = \frac{1}{2} m \left[\frac{\lambda^2}{19.25\lambda + (A-N) \times 0.5} \right]^2 \times 10^{-18}$$

For 14.1 MeV neutrons $E = \frac{1}{2} m \frac{1}{(19.25\lambda)^2} \times 10^{-18}$

Therefore the neutron appearing in channel number N has an energy

$$E = \frac{14.1}{\left[1 + \frac{(A-N) \cdot 0.5}{19.25\lambda} \right]^2} \text{ MeV} \quad 5.6$$

knowing the peak channel of the time spectrum for 14.1 MeV neutrons. Then using equation 5.6 the energy at each channel could be calculated. Figure 5.14 shows the energy versus the channel number for 14.1 MeV neutron in channel 81. The 5.82 MeV neutron therefore appears at channel 40.

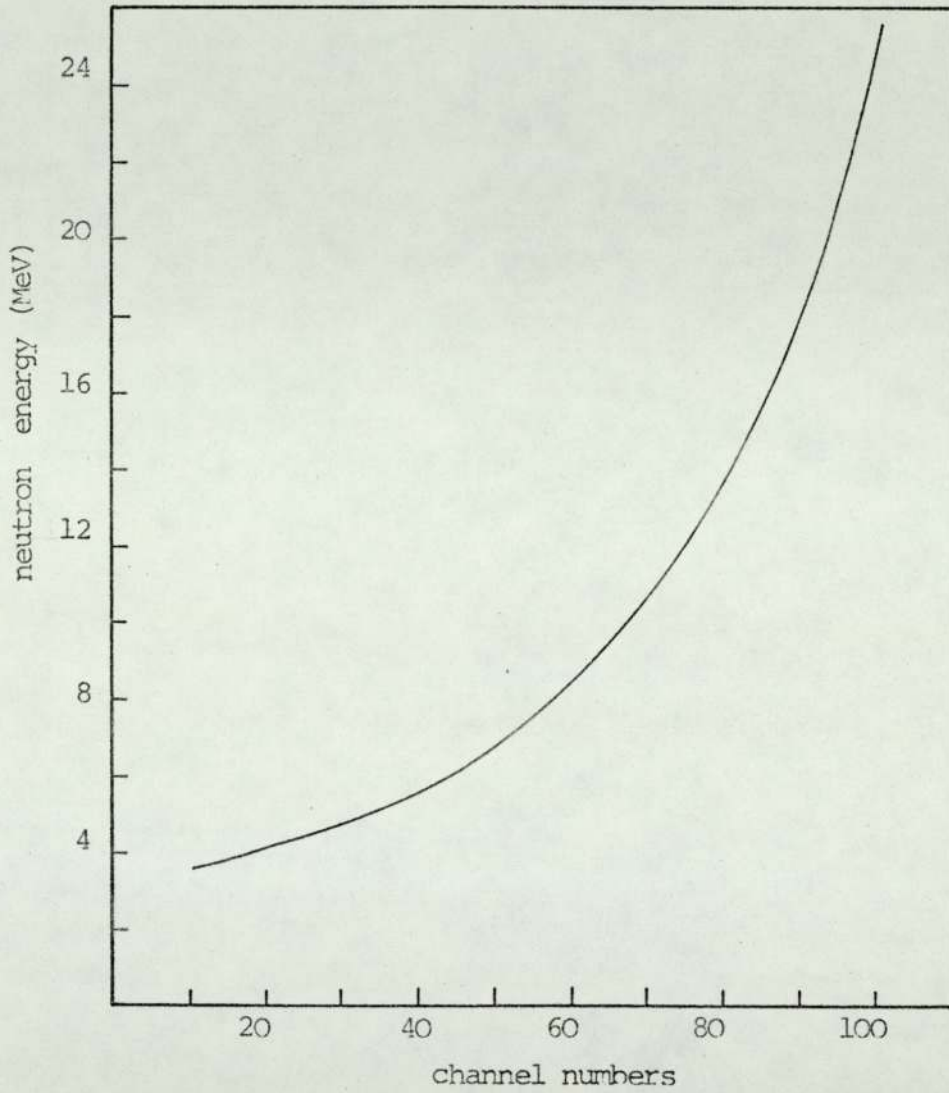


Fig. 5.14 Energy calibration of the multichannel analyser

THEORETICAL CONSIDERATIONS

CHAPTER 6

6.1 INTRODUCTION

The determination of neutron behaviour in a medium is a very complex problem. It can be formulated mathematically by considering the production and collision of neutrons of a particular velocity moving in a particular direction and integrating overall directions and all velocities. The problem is similar to that of motion of molecules in a gas and leads to the same equation, the Boltzmann transport equation. This approach is known as transport theory. The mathematical derivation of the transport equation has been discussed in many text books.⁽⁷⁹⁻⁸⁹⁾ The transport equation represents a neutron balance in a homogenous and isotropic medium, considering neutrons having designated specifications for vector, position, angular direction, speed or lethargy, and time. The neutron balance yields an integro-differential equation. The transport equation is so complicated that solutions have been found only for rather simplified physical models such as the spherical harmonic expansion, the discrete ordinate technique and the moments method.

Another way of determining the neutron behaviour through matter is by Monte Carlo methods⁽⁹⁰⁾ which are applicable to problems involving a series of random events. In these problems the histories of a large number of neutrons are

followed from collision to collision. In going from one collision to another the problem is to determine the distance travelled before the next collision takes place, the type of collision which takes place and the energy and direction of the neutron after the collision, that is the distribution of the neutron in space according to their energies could be determined. With the use of large high speed computers Monte Carlo method has become a powerful tool for detailed study of shielding and reactor design. However, the Monte Carlo method has some limitations due to the time needed to build up accuracy and the large computer core size needed which makes the method less attractive for common use.

6.2 Consideration of possible reactions to be seen.

In studying the reaction of the 14 MeV neutrons with extended samples of LiF and Fe it is necessary to find out from the cross-section data and the energy distribution probability data what reactions will contribute to the emerging neutron flux so as to take those neutrons producing reactions into consideration when setting up a theoretical calculation model for computing the emerging neutron flux. The cross-section and the probability distributions data for the 14 MeV neutrons for the ${}^6\text{Li}$, ${}^7\text{Li}$, ${}^{19}\text{F}$ and Fe nuclei were prepared from the (U.K.N.D.L)* files. Table 6.1 contains the cross-section data for the neutron producing reactions for the following nuclei ${}^6\text{Li}$, ${}^7\text{Li}$, ${}^{19}\text{F}$ and Fe.

* United Kingdom Nuclear Data Library.

⁶Li

From Table 6.1 and from the comparison of the values of the cross-section it can be seen that the elastic scattering cross-section has the highest value and is therefore the predominant reaction for 14 MeV neutrons with ⁶Li. Figure 6.1 shows the energy of a 14 MeV neutron scattered through $\theta = 0^\circ$ to $\theta = 180^\circ$.

The next most important reaction with probable contribution to the emerging flux is the (n,n α) reaction. Figure 6.2 shows the energy distribution for the probability of the scattered 14 MeV neutrons. It can be seen that there is a continuous energy distribution of the scattered neutrons with maximum energy from 12.5 MeV down to energies below the threshold energy of the neutron detector. The threshold energy is taken to be 5 MeV. From Fig. 5.13 the efficiency is zero at 3.4 MeV (the discriminator level set at 3.4 MeV) but the efficiency is dropping sharply below 6 MeV reaching zero at 3.4 MeV and that is the reason why the threshold energy is taken at 5 MeV as seen on Fig. 5.13 by the dotted line. Therefore the contribution from the (n,n α) reaction below the threshold energy indicated by the dotted line on Fig. 6.2 is not going to be detected. There will still be a significant contribution in the neutron region 5 to 12.5 MeV.

The contribution from the (n,2n α) reaction as seen from Table 6.2 is going to appear in the low energy region of the spectrum below the primary elastically scattered neutron

region. From the table the first emerging neutron has its highest energy at approximately 3 MeV; the second neutron has its highest value at 4.79 MeV. The energy distribution probability for both neutrons is below the threshold energy of the neutron detector. Therefore this reaction has no practical contribution in the energy range considered in this work.

The (n,2n) reaction as seen from Table 6.1 is not a possible reaction as it would lead to the formation of the highly unstable ${}^5\text{Li}$.

The inelastic reaction (n,n¹) to the first excited level only is given in the U.K.N.D.L. file and its angular energy distribution is shown in Table 6.3. This has a narrow but sharp contribution to the emerging spectrum which appears at an average energy of 9.5 MeV.

2. ${}^7\text{Li}$

The predominant reaction of the 14 MeV neutrons with ${}^7\text{Li}$ nuclei is also elastic scattering (Fig. 6.1). The (n,n α) reaction, Fig. 6.3 shows the energy distribution probability of the scattered 14 MeV neutrons from the (n,n α) reaction for ${}^7\text{Li}$. It can be seen that there is a continuous energy distribution of the scattered neutrons with a maximum energy of 11.5 MeV down to energies below the threshold energy, therefore the contribution from this reaction to the flux will also appear at energies lower than the primary elastically scattered neutrons.

The $(n,2n\alpha)$ reaction, energy distribution is given in Table 6.4. It will be seen that the first emerging neutron has a highest energy of 1.31 MeV and the second neutron has a highest energy of 2.10 MeV.

The energy distribution probability for both neutrons is below the threshold energy of the neutron detector and therefore this reaction has no contribution in the energy range measured.

For the $(n,2n)$ reaction as seen from Table 6.5, the first emerging neutron has a highest energy of 2.39 MeV and the second neutron has a highest energy of 3.95 MeV. The energy distribution probability for both neutrons is therefore below the threshold energy of the neutron detector and this reaction makes no contribution in the energy range measured.

The inelastic reaction (n,n^1) is given to the first excited level only in the UKNDL file and its angular energy distribution is shown in Table 6.6. The contribution from this reaction appears in a narrow energy band at an average energy of 12.25 MeV.

3. ^{19}F

The predominant reaction of the 14 MeV neutrons with ^{19}F nuclei is again the elastic scattering reaction (Figure (6.1)).

The inelastic reaction (n,n^1) has a probable contribution to the emerging flux. Figure 6.4 shows the energy distribution probability for the inelastically scattered 14 MeV neutrons, showing only a low contribution for this reaction in the measured region because the energy distribution probability of the scattered neutrons is high below 5 MeV and

decreases sharply above that energy.

For the (n,2n) reaction, as seen from Table 6.7 the highest energies of the first and second neutrons are below the threshold energy and consequently they make no contribution to the observed flux.

4. Fe

The predominant reaction of the 14 MeV neutrons with Fe nuclei is the elastic scattering reaction as can be seen from Table 6.1. The energy change is small, see Fig. 6.1.

Figure 6.5 shows the energy distribution probability of the (n,2n) reaction for the 14 MeV neutrons. There is a continuous energy distribution of the scattered neutrons with a maximum energy from 14 MeV down to low energies. The majority of the neutrons produced appear below the detector threshold but there is still a significant contribution in the measured region.

Figure 6.6 shows the energy distribution probability for the inelastically scattered 14 MeV neutrons, the figure shows a low contribution from this reaction in the measured energy range and a high contribution below this.

In conclusion the reaction of the 14 MeV neutrons with ${}^6\text{Li}$, ${}^7\text{Li}$, ${}^{19}\text{F}$ and Fe nuclei that have the highest contribution to the emerging flux which are to be considered are the following ones. For ${}^6\text{Li}$, ${}^7\text{Li}$, ${}^{19}\text{F}$ and Fe nuclei the elastic scattering is the predominant reaction and makes the highest contribution to the emerging flux. The peak of the spectrum is due entirely to this reaction. For

${}^6\text{Li}$, ${}^7\text{Li}$ the $(n,n\alpha)$ reaction is the next most important reaction while for iron the $(n,2n)$ is the next most important. Finally the (n,n^1) reaction produces the lowest contribution for all the nuclei considered. Therefore the computing method should include those reactions that have the highest contribution to the flux and neglect those reactions that have little or no contribution to the flux.

TABLE 6.1

MICROSCOPIC CROSS SECTIONS (in barns) at 14MeV

Nucleus	σ_{el}	$\sigma_{n,n\alpha}$	$\sigma_{n,2n}$	$\sigma_{n,2n\alpha}$	σ_{n,n^1}
${}^6\text{Li}$	0.97	0.367	-	0.073	0.02
${}^7\text{Li}$	0.98	0.335	0.022	0.033	0.08
${}^{19}\text{F}$	0.87	-	0.06	-	0.59
Fe	1.124		0.59	-	0.45

TABLE 6.2

ENERGY DISTRIBUTION PROBABILITY OF THE 14MeV NEUTRONS

FROM (n,2n α) REACTION FOR ${}^6\text{Li}$

	E_n (MeV)	p(E)
first neutron	1.20	.25
	1.80	.25
	2.39	.25
	2.99	.25
second neutron	2.99	.25
	3.59	.25
	4.19	.25
	4.79	.25

TABLE 6.3

ANGULAR ENERGY DISTRIBUTION OF THE 14MeV NEUTRONS FROM
(n,n¹) REACTION TO THE FIRST LEVEL OF ⁶Li

θ_{Lab}	E_n (MeV)
30	9.84
45	9.39
60	8.50

TABLE 6.4

ENERGY DISTRIBUTION PROBABILITY OF THE 14MeV NEUTRONS
FROM (n,2n α) REACTION FOR ⁷Li

	E_n (MeV)	p(E)
first neutron	.52545	.25
	.52545	.25
	1.0509	.25
	1.31365	.25
second neutron	1.31365	.25
	1.57635	.25
	1.85659	.25
	2.10180	.25

TABLE 6.5

ENERGY DISTRIBUTION PROBABILITY OF THE 14 MeV NEUTRONS
FROM THE (n,2n) REACTION FOR ${}^7\text{Li}$

	E_n (MeV)	P (E)
first neutron	.96	.25
	1.44	.25
	1.92	.25
	2.39	.25
second neutron	2.39	.25
	2.87	.25
	3.35	.25
	3.95	.25

TABLE 6.6

ANGULAR ENERGY DISTRIBUTION OF THE 14MeV NEUTRONS FROM
(n,n¹) REACTION TO THE FIRST LEVEL OF ${}^7\text{Li}$

θ_{Lab}	E_n (MeV)
30	12.99
45	12.4
60	11.7

TABLE 6.7

ENERGY DISTRIBUTION PROBABILITY OF THE 14MeV NEUTRONS
FROM THE (n,2n) REACTION FOR ^{19}F

<u>E_n (MeV)</u>	<u>P(E)</u>
.75	1
1.5	1

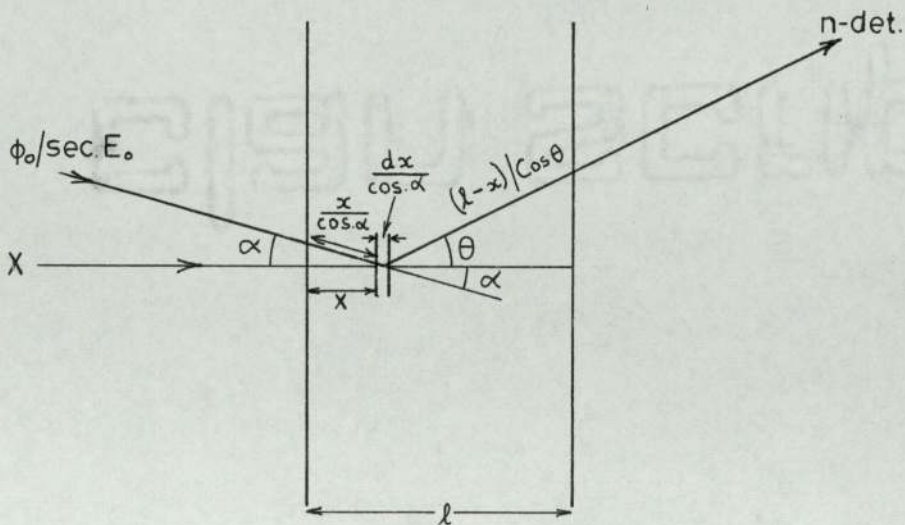
6.3 Single and secondary scattering

In scattering experiments designed to evaluate cross section multiple interactions of particles in the scattering samples are important even in thin samples and an accurate evaluation of these processes is needed to correct the experimental data. Usually the proper assessment of multiple scattering phenomena requires a theoretical study adapted specifically to the particular experimental situation at hand. Many studies have been made of secondary and multiple scattering under circumstances in which simplified theoretical models are applicable. (91-98)

The work described here uses samples up to about two mean free paths thick and second scatter makes an important contribution to the measured flux. In the present work mathematical derivation of the neutron behaviour through matter after suffering first and second scatters has been mathematically derived in order to set up a calculation model for the external flux. The mathematical derivation of both first and second scatters of neutrons has been carried out

as follows:

1. First Scatter



Let the number of neutrons of energy E_0 incident on a sample of thickness l be ϕ_0/sec

number of interactions between x and $x+dx$

$$= \phi_0 e^{-\frac{\Sigma_{t0} x}{\cos \alpha}} \Sigma_{t0} \frac{dx}{\cos \alpha}$$

consider an interaction producing a scattered neutron of energy E_1 at angle $(\theta+\alpha)$

\therefore probability of producing such a neutron is

$$= \phi_0 e^{-\frac{\Sigma_{t0} x}{\cos \alpha}} \Sigma_{t0} \frac{\Sigma_0}{\Sigma_{t0}} p(\theta+\alpha) \cdot \frac{dx}{\cos \alpha}$$

This neutron has to travel through a distance $\frac{(l-x)}{\cos \theta}$

before emerging and therefore the fraction emerging is $e^{-\Sigma_{t1} \frac{(l-x)}{\cos \alpha}}$

∴ Total number emerging

$$= p(\theta+\alpha) \int_0^l \phi_0 e^{-\Sigma_{t0} \frac{x}{\cos\alpha}} \Sigma_{t0} \left(\frac{\Sigma_0}{\Sigma_{t0}} \right) e^{-\Sigma_{t1} \left(\frac{l-x}{\cos\theta} \right)} \cdot \frac{dx}{\cos\alpha}$$

$$\therefore n(\theta+\alpha) = \frac{p(\theta+\alpha)\phi_0 \Sigma_0}{\cos\alpha} e^{-\frac{\Sigma_{t1} l}{\cos\theta}} \int_0^l e^{-\left(\frac{\Sigma_{t0}}{\cos\alpha} - \frac{\Sigma_{t1}}{\cos\theta} \right) x} \cdot dx$$

$$= \phi_0 \frac{p(\theta+\alpha)\Sigma_0}{\cos\alpha} e^{-\frac{\Sigma_{t1} l}{\cos\theta}} \left[\frac{-e^{-\left(\frac{\Sigma_{t0}}{\cos\alpha} - \frac{\Sigma_{t1}}{\cos\theta} \right) x}}{\frac{\Sigma_{t0}}{\cos\alpha} - \frac{\Sigma_{t1}}{\cos\theta}} \right]_0^l$$

$$= \phi_0 \frac{p(\theta+\alpha)\Sigma_0}{\cos\alpha} e^{-\frac{\Sigma_{t1} l}{\cos\theta}} \left[\frac{1 - e^{-\left(\frac{\Sigma_{t0}}{\cos\alpha} - \frac{\Sigma_{t1}}{\cos\theta} \right) l}}{\frac{\Sigma_{t0}}{\cos\alpha} - \frac{\Sigma_{t1}}{\cos\theta}} \right]$$

$$p(\theta+\alpha)\Sigma_0 = \left(\frac{d\Sigma_s}{d\Omega} \right) (\theta+\alpha)$$

$$= \phi_0 \left(\frac{d\Sigma_s}{d\Omega} \right) (\theta+\alpha) \frac{1}{\cos\alpha} \left[\frac{e^{-\frac{\Sigma_{t1} l}{\cos\theta}} - e^{-\frac{\Sigma_{t0} l}{\cos\alpha}}}{\frac{\Sigma_{t0}}{\cos\alpha} - \frac{\Sigma_{t1}}{\cos\theta}} \right]$$

where

ϕ_0 = neutron beam intensity

$\left(\frac{d\Sigma_s}{d\Omega} \right) (\theta+\alpha)$ = differential scattering cross section at energy E_0 into unit solid around angle $(\theta+\alpha) = p(\theta+\alpha) \cdot \Sigma_1$

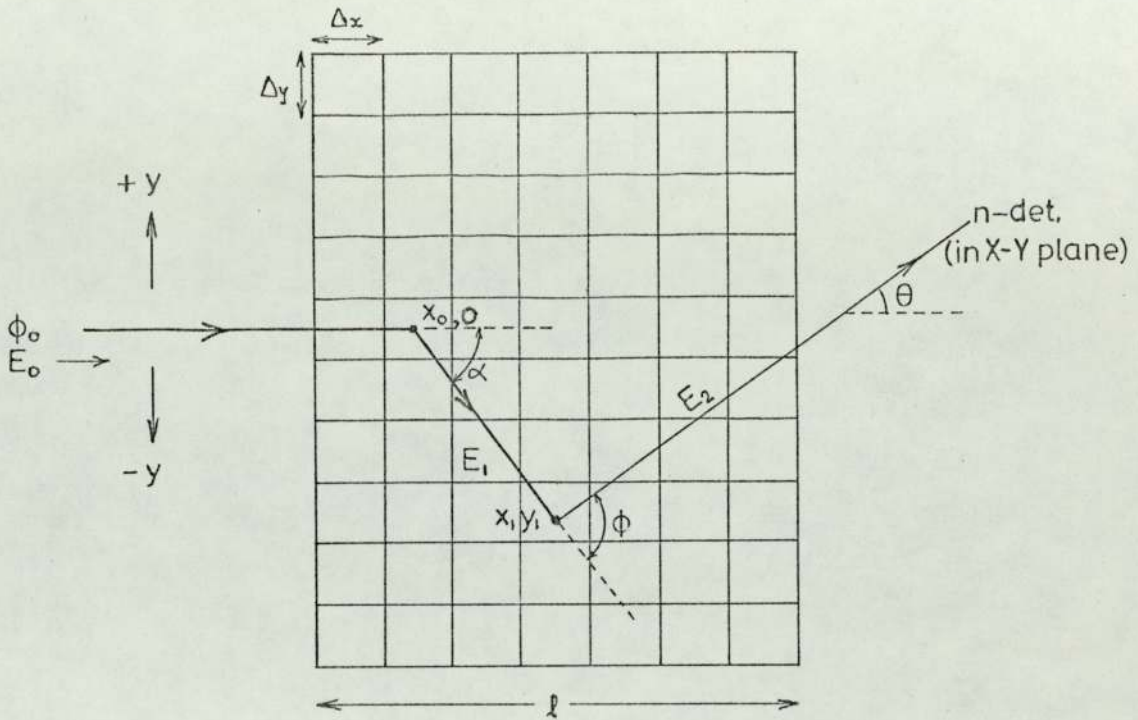
Σ_0 = total scattering cross section at energy E_0

Σ_{t1} = total cross section of the scatterer after one collision

l = thickness of the scatterer

θ = the neutron detector angle

Σ_{t0} = total cross section of the scatterer before collision



2. Second Scatter

Consider the following two-dimensional treatment.

Total number scattered at $x_0 = \phi_0 e^{-\Sigma t_0 x_0} \Sigma_{t_0} \Delta x$

let the angle of scattering be α

$\cos \alpha_x = \frac{X}{\sqrt{X^2 + y_1^2}}$ where $X = (x_1 - x_0)$

Neutron after having been scattered through an angle α its energy becomes E_1 .

The scattered intensity leaving $x_0 = \phi_0 e^{-\Sigma t_0 x_0} \Sigma_0(\alpha) \Delta x$

Neutron travels $\sqrt{X^2 + y_1^2}$ to (x_1, y_1) suffer attenuation

by $e^{-\Sigma_1 t \sqrt{X^2 + y_1^2}}$

Number of neutrons scattered through angle ϕ at $(x_1, y_1) =$

$\phi_0 e^{-\Sigma t_0 x_0} \Sigma_0(\alpha) \Delta x e^{-\Sigma_1 t_1 \sqrt{X^2 + y_1^2}} \Sigma_1(\phi) \frac{\Delta x \Delta y}{X^2 + y_1^2}$

where the final term allows for the finite size of the scattering cell and the solid angle it subtends from the point of first scatter.

Finally, further attenuation by a factor of $e^{-\Sigma_2 t_2 \frac{(l-x_1)}{\cos \theta}}$

∴ Total scattered intensity reaching the detector =

$$n(\theta) = \underbrace{}_{x_0} \underbrace{}_{x_1} \underbrace{}_{y_1} \phi_0 e^{-\Sigma_{t0} x_0} e^{-\Sigma_{t1} \sqrt{x^2 + y^2}} \Sigma_0(\alpha) \Delta x$$

$$\Sigma_1(\phi) = \frac{\Delta x \Delta y}{x^2 + y^2} e^{-\Sigma_{t2} \frac{(\lambda - x_1)}{\cos \theta}}$$

where

$\Sigma_0(\alpha)$ = neutron scattering cross section into unit solid angle for neutrons of energy Σ_0 to be scattered through angle α and its energy becomes Σ_1

Σ_{t1} = total cross section at energy Σ_1

$\Sigma_1(\phi)$ = neutron scattering cross section into unit.

Solid angle for neutron of energy Σ_1 to be scattered through angle α and its energy becomes Σ_1

Σ_{t1} = total cross section at energy Σ_1

$\Sigma_1(\phi)$ = neutron scattering cross section into unit

Solid angle for neutron of energy Σ_1 to be scattered through an angle ϕ and its energy becomes Σ_2

Σ_{t2} = total cross section at energy Σ_2

$$\cos \phi = \frac{x \cos \theta}{\sqrt{x^2 + y_1^2}} + \frac{y_1 \sin \theta}{\sqrt{x^2 + y_1^2}}$$

In three dimensions this becomes

$$n(\theta) = \sum_{x_0} \sum_{x_1} \sum_{y_1} \sum_{z_1} \phi_0 e^{-\Sigma_{t_0} x_0} e^{-\Sigma_{t_1} \sqrt{x^2 + y_1^2 + z_1^2}}$$

$$e^{-\Sigma_{t_2} \frac{(l-x_1)}{\cos \theta}} \Delta \rho \Sigma_0(\alpha) \Sigma_1(\phi) \frac{\Delta x \Delta y \Delta z}{x^2 + y_1^2 + z_1^2}$$

$$\cos \alpha = \frac{x}{\sqrt{x^2 + y_1^2 + z_1^2}}$$

$$\cos \phi = \frac{x \cos \theta}{\sqrt{x^2 + y_1^2 + z_1^2}} + \frac{y_1 \sin \theta}{\sqrt{x^2 + y_1^2 + z_1^2}}$$

6.4 Flux Computing Programmes

Computer programmes have been written to compute the flux of the scattered 14 MeV neutrons from LiF and Fe samples at different laboratory angles using the first and second scatter models of section 6.3. The neutron producing reactions from ${}^6\text{Li}$, ${}^7\text{Li}$, ${}^{19}\text{F}$ and Fe nuclei are the only reactions that are contributing to the emerging flux. Reactions included are those selected in section 6.2. Therefore the following computer programmes have been written.

1. A computer programme for computing the flux of the primary elastically scattered neutrons as shown in Appendix 3.
2. A computer programme for computing the flux of the secondary elastically scattered neutrons as shown in Appendix 4.
3. A computer programme for computing the primary scattered flux from each one of the following reactions $(n,n\alpha)$, (n,n^1) and $(n,2n)$ as shown in Appendix 5. Since these had a relatively small contribution to the flux compared with elastic scattering, no attempt was made to allow for second scatter of neutrons from these reactions.

The programme of the primary scatter model for the elastically scattered neutron has been checked by comparing the flux from this LiF sample (14 cm thick) computed at angle $\theta=60^\circ$ with the individual fluxes from ${}^6\text{Li}$, ${}^7\text{Li}$ and ${}^{19}\text{F}$ nuclei of the same LiF sample at the same angle as shown in Figure 6.7 computed by the primary scatter model. The sum of the fluxes from ${}^6\text{Li}$, ${}^7\text{Li}$ and ${}^{19}\text{F}$ nuclei has exactly the same value as that of the flux from LiF sample, showing that the programme is handling the three scattering nuclei correctly.

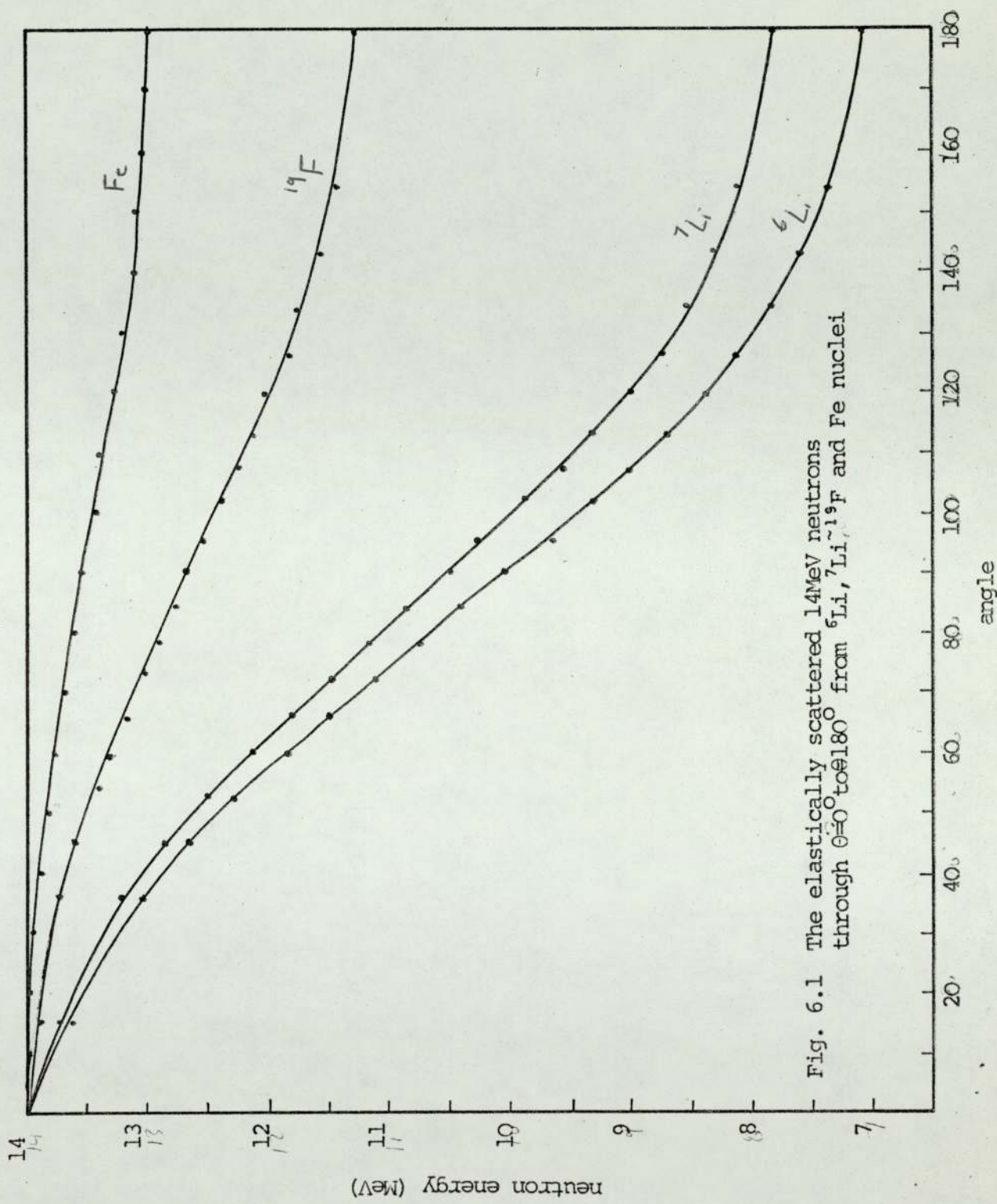


Fig. 6.1 The elastically scattered 14MeV neutrons through $\theta=0^\circ$ to 180° from ^6Li , ^7Li , ^{19}F and Fe nuclei

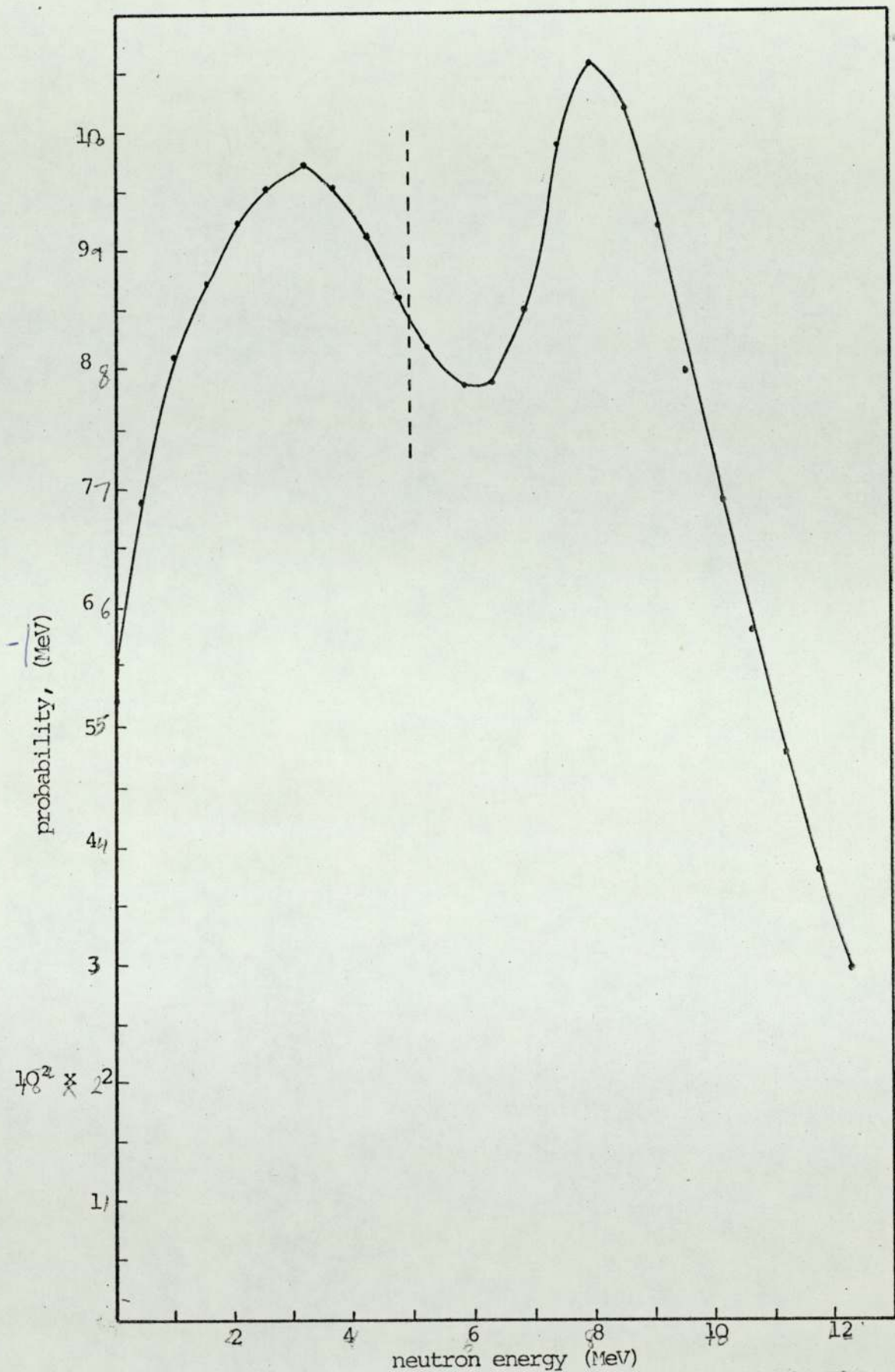


Fig. 6.2 Energy distribution probability of the scattered 14 MeV neutrons from ${}^7\text{Li}$ nuclei by the (n, α) reaction

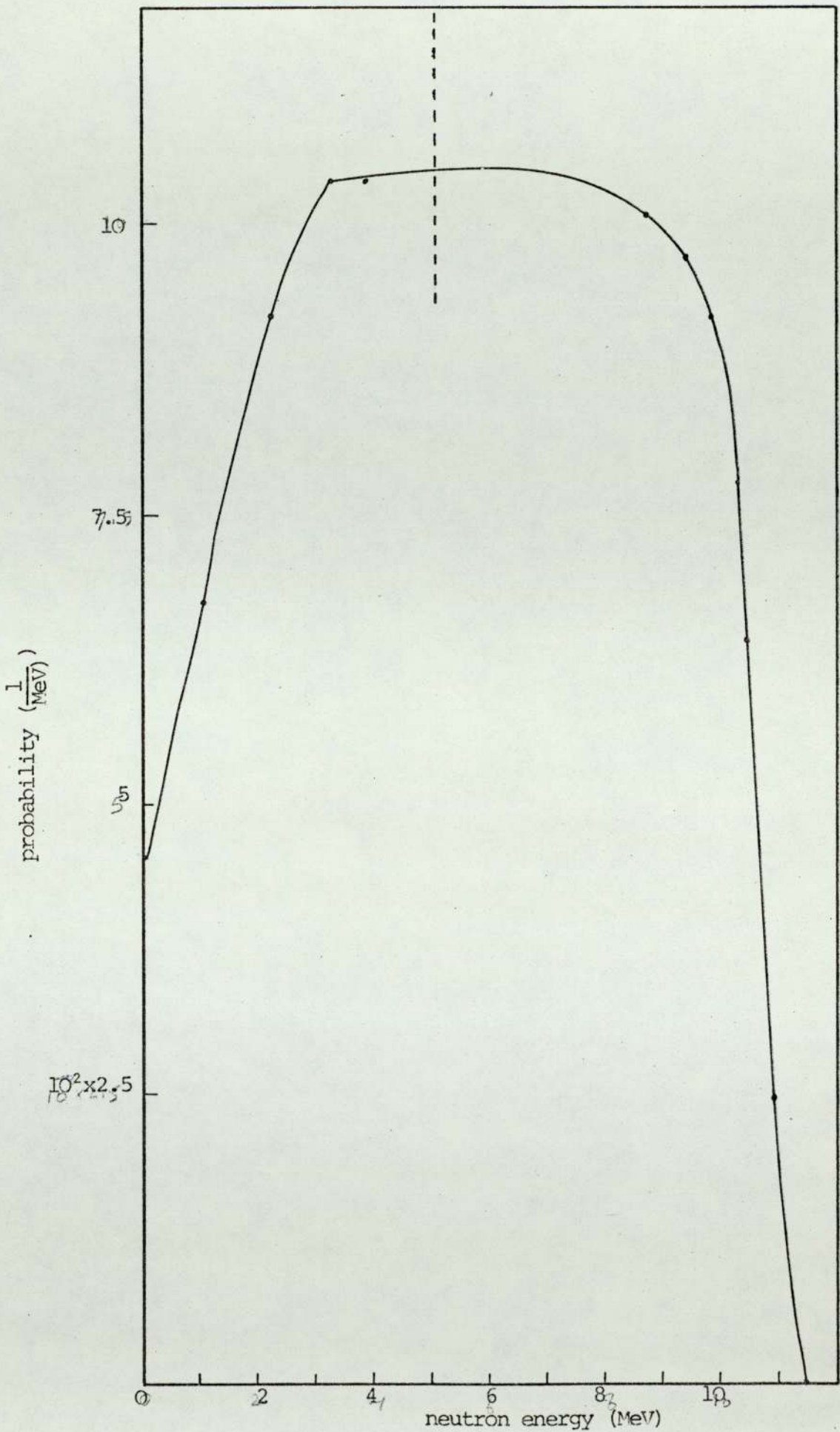


Fig. 6.3 Energy distribution probability of the scattered 14MeV neutrons from ${}^7\text{Li}$ nuclei by the (n,α) reaction

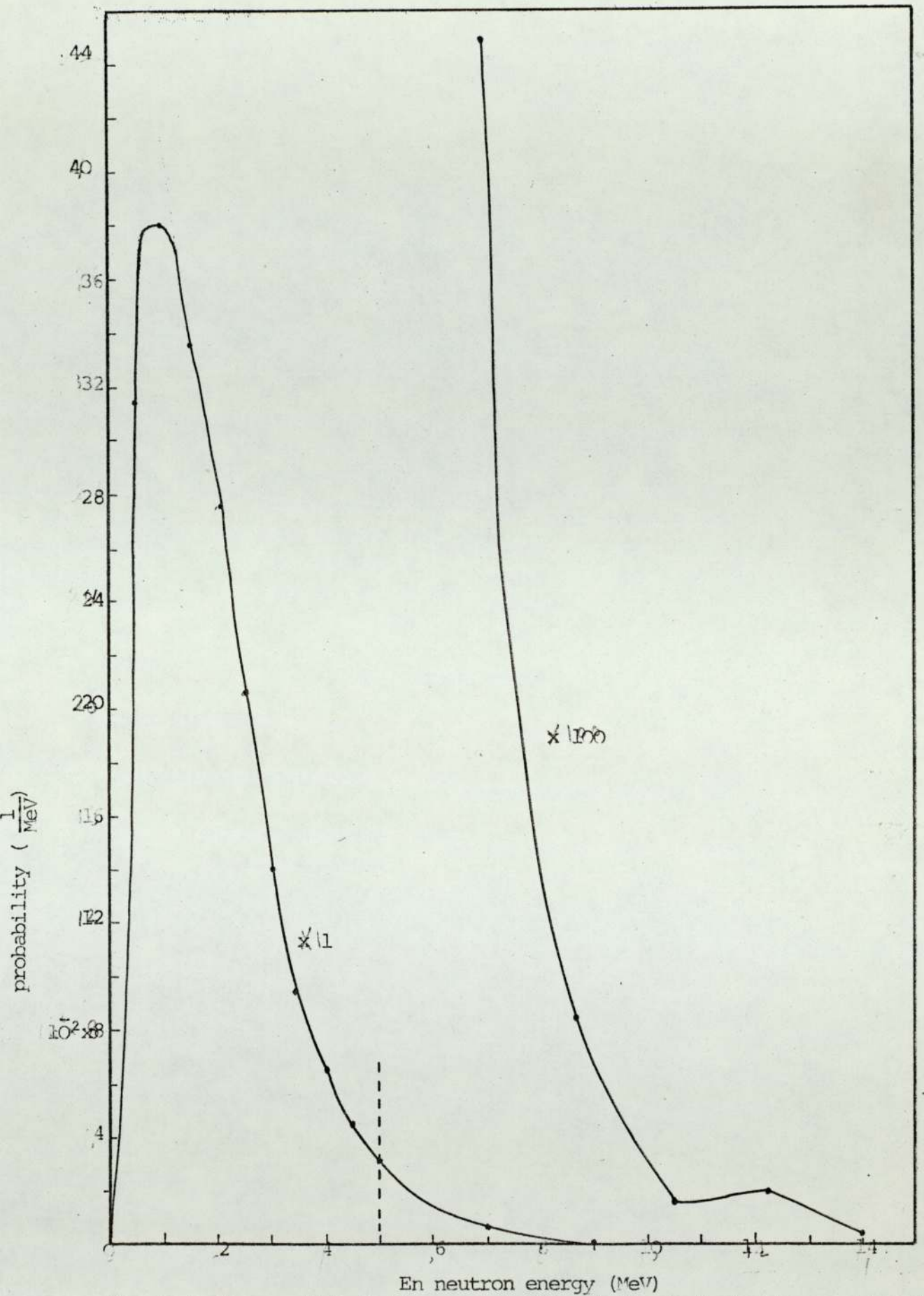


Fig. 6.4 Energy distribution probability of the inelastically scattered 14MeV neutrons from ^{19}F nuclei

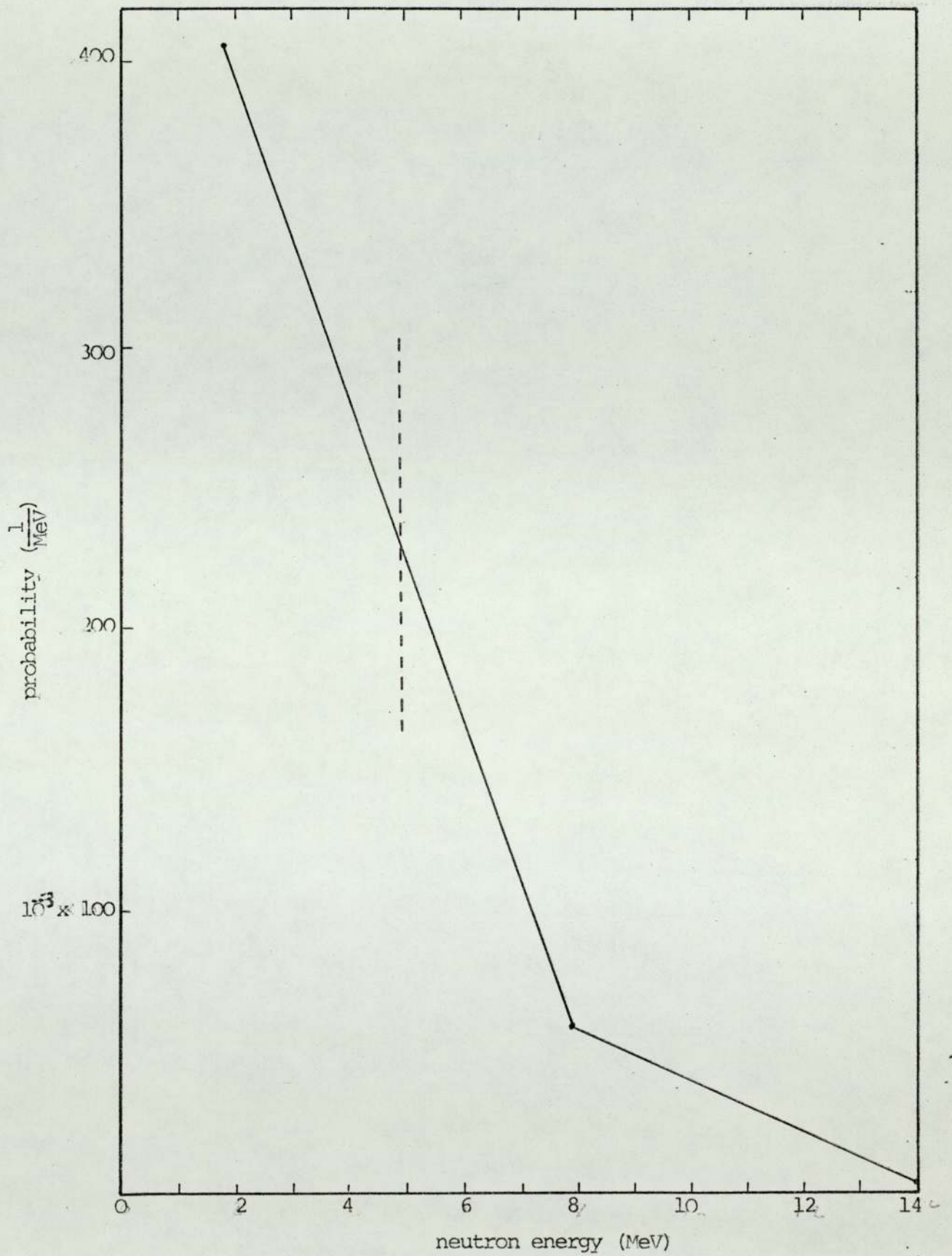


Fig. 6.5 Energy distribution probability of the (n,2n) reaction of the 14 MeV neutrons from Fe nuclei.

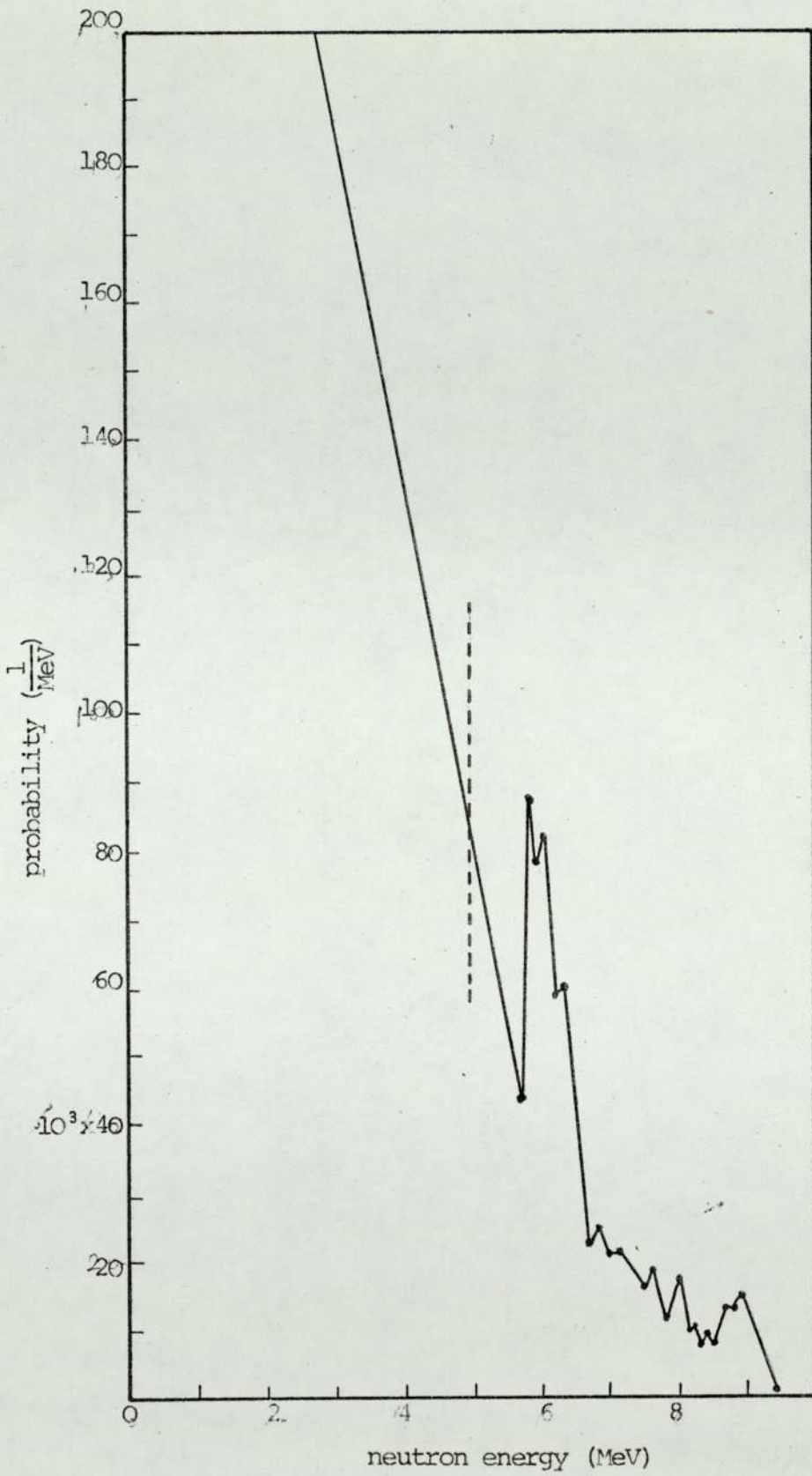


Fig. 6.6 Energy distribution probability of the inelastically scattered 14MeV neutrons from Fe nuclei

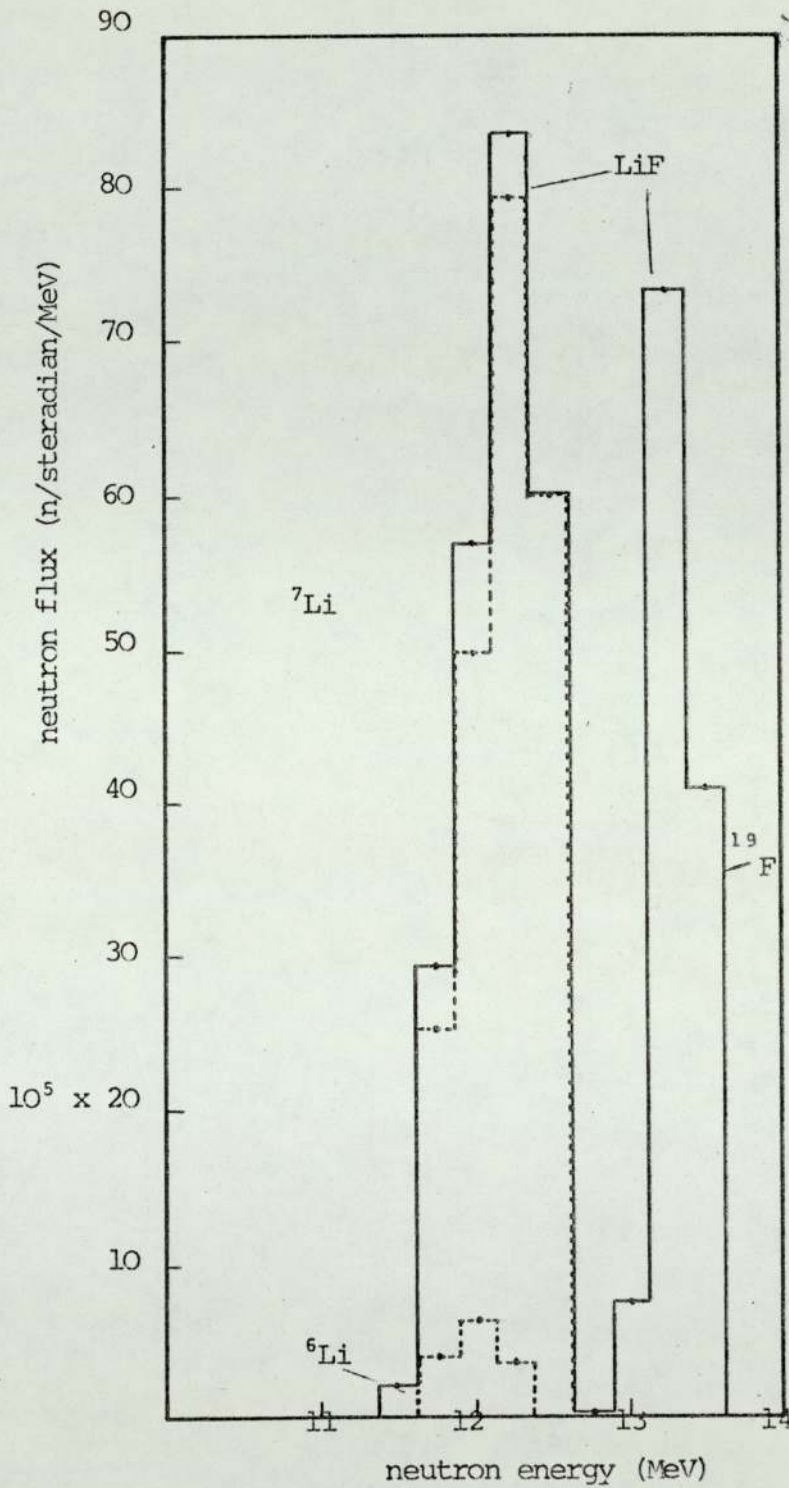


Fig. 6.7 Elastic spectrum from LiF (14cm thick) at angle $\theta=60$ from primary scatter (checking the programme)

CHAPTER 7

EXPERIMENTAL AND THEORETICAL RESULTS

7.1 INTRODUCTION

The experimental results for fast neutron spectra after emerging from different thicknesses of LiF and Fe samples are presented and discussed in this chapter. Also the theoretical results obtained from both the primary scatter and secondary scatter models are compared with those obtained experimentally. The LiF samples were in powder form enclosed in a thin-walled stainless steel container, the sample dimensions were (29 x 32 x 14cm) and (20.32 x 38.1 x 6.35cm) (height x width x thickness).

Identical empty stainless steel containers were used for background subtraction purposes and consequently it was not necessary to allow for the containers in the calculations. The Fe samples were composed of layers of steel sheets, the first sample had dimensions of (31 x 32 x 7.62cm). The second sample had dimensions (14.2 x 30.6 x 3.6 cm.). For background subtraction the sample was totally removed from the neutron beam. The samples were positioned 25 cm from the neutron producing target, the positioning was kept as accurate as possible while doing the alternate runs.

The neutrons were produced in a cone related to the cone of the associated α -particles from the $T(d,n)^4\text{He}$ reaction. With the extended sample used in the present work the

scattering sample completely subtended the neutron beam defined by the associated alpha particles and as the scattering sample was much wider than the defined neutron beam, then a small error in the lateral positioning of the sample had a very small effect on the intensity of scattered neutrons.

Before taking time-of-flight spectral measurements it was necessary (for energy calibration purposes, section 5.7) to determine the direct 14 MeV neutron time spectrum peak in order to find the channel corresponding to 14 MeV. This was achieved by taking the time spectrum of the direct 14MeV neutrons at $\theta=0^\circ$ and observe the peak at which channel falls. The peak should be kept in the same position throught the whole accumulation time for that spectrum.

The experimental procedure for accumulating time-of-flight spectra was as described in Section 5.6. Alternate runs were made with the LiF sample in position (addition mode) and with the empty stainless steel container to subtract the background contribution (subtraction mode), in the case of Fe sample the subtraction mode was done when the sample was removed from the neutron beam. The counting for the spectrum accumulation was performed in cycles as follows

1. With sample (addition mode)
2. Without sample (subtraction mode)
3. Without sample (subtraction mode)
4. With sample (addition mode)

each cycle was for an integrated count of 5×10^7 alpha particles, the accumulation time was about 20 hours per spectrum.

Time-of-flight spectra of the emerging fast neutrons from the different thicknesses of LiF and Fe samples were obtained at different laboratory angles.

Significant multiple scatterings have been reported for thicknesses even less than 0.1 mean free path since the mean free path for the 14MeV neutrons in LiF is about 17 cm. and 4.7 cm. Fe. Therefore with the dimension of the LiF and Fe samples mentioned earlier, multiple scattering can occur quite easily. It has been noticed that with increasing sample thickness the accumulation time for a spectrum at the same angle increases quite considerably compared with the time needed to accumulate to the same number of counts for thinner samples due to the attenuation of the neutrons in travelling through a further distance. The data for each spectrum at each angle for each sample were accumulated for several hours. The larger the angle from the direct neutron beam the longer the time needed for accumulation to reach the same number of counts for the same sample compared to smaller angles.

All spectra measurements were taken with the time-of-flight spectrometer using the associated particle method, the fast neutrons were detected with the use of a plastic scintillator type NE-102A. The primary and secondary scattering calculation

models were used to calculate the neutron energy spectra of the emerging neutron fluid from LiF and Fe samples for the following laboratory angles $\theta=30^\circ$, 45° and 60° . The cross section data for the neutron producing reactions that contribute to the emerging flux that were used in the theoretical calculation models were taken and prepared from U.K.N.D.L. All the measured and calculated spectra were normalised to a source strength of 10^9 neutrons total. The results obtained are in good agreement within the experimental errors within the theoretical predictions.

7.2 CONVERSION OF PULSE HEIGHT ANALYSER SPECTRA TO ENERGY SPECTRA

The spectrum that appears on the pulse height analyser is the time spectrum of the scattered neutrons and this must be converted to an energy spectrum as follows. From Section 5.8, equation 5.6 gives the relationship between the energy and the channel number.

$$E_N = \left(\frac{14.1}{1 + \frac{(A-N) \times 0.5}{19.25 \ell}} \right)^2 \text{ MeV}$$

Differentiating this equation gives

$$\frac{dE_N}{dN} = \frac{-2 \times 14.1}{\left(1 + \frac{(A-N) \times .5}{19.25 \ell}\right)^2} \times \frac{-0.5}{19.25 \ell} \times \frac{1}{\left(1 + \frac{(A-N) \times .5}{19.25 \ell}\right)}$$

$$\frac{dE_N}{dN} = E_N \frac{1}{19.25 \ell \sqrt{14.1}} E_N^{\frac{1}{2}}$$

Therefore the required conversion factor is given by

$$\left(\frac{1}{dE_N} \right) = \frac{19.25 \ell \sqrt{14.1}}{E_N^{3/2}}$$

which converts counts per channel to counts per unit energy (MeV).

Figure 7.1 shows the correction factor $(\frac{1}{dE_N})$ as a function of channel number.

$$\text{Since } n(v)dV = n(E)dE$$

where $n(v)dV = \text{count per channel}$

Therefore the equation by which the data of the time spectrum is converted to energy spectrum is given by

$$n(E) = \frac{n(v)dV}{dE} = (\text{count/channel}) \times \frac{19.25 \& \sqrt{14.1}}{(E_N)^{3/2}} \quad (7.2)$$

The experimental data have to be corrected for both detector efficiency and solid angle. That is, they have to be multiplied by $(\frac{1}{\Omega_n} \times \frac{100}{\epsilon})$ where $(\frac{1}{\Omega_n})$ is the correction for the neutron detector solid angle, $(\frac{100}{\epsilon})$ is the correction for the detector experimental efficiency. A curve of the correction factor $(\frac{1}{\Omega_n} \times \frac{100}{\epsilon})$ versus neutron energy is shown in Figure 7.2. Therefore the data of the time spectrum has to be multiplied by the correction factor of Figures 7.2 as well as the conversion factor of Figure 7.1 then finally it has to be normalised to a total count of 10^9 in order to be compared with the spectrum obtained from the theory, which calculates the number of neutrons scattered into unit solid angle around a detector angle θ for a total number input of 10^9 neutrons.

7.3 THE MEASURED SPECTRA FROM LiF SAMPLES

The measurement of the emerging flux of the 14 MeV neutrons after being scattered from two samples of LiF has been taken with the use of the spectrometer shown in Figure 5.7. at different laboratory angles. The first sample measured 29cm x 32 cm and was 14 cm thick. The second sample measured 20.32 cm x 38.1cm and was 6.35 cm thick. The spectra for the first sample were taken at angles $\theta = 30^{\circ}, 45^{\circ}$. A typical time-of-flight spectrum for the elastically scattered 14 MeV neutrons from the first LiF sample (14 cm thick) at angle $\theta = 30^{\circ}$ in the laboratory system is shown in Figure 7,3 Using the energy conversion factor of Section 7.2 the time spectrum in Figure 7.3 could be converted to an energy spectrum. Figure 7.4 shows the corresponding spectrum of Figure 7.3 after being converted to energy spectrum. Figure 7.5 shows the corresponding energy spectrum of Figure 7.4 after being normalised to a total count of 10^9 and after being corrected for the detector experimental efficiency and solid angle.

Figures 7.6 and 7.7 are the normalised energy spectrum for the first LiF sample at angle $\theta = 45^{\circ}$ and 60° respectively. Similarly, Figures 7.8, 7.9 show the measured energy spectra after normalisation for the second LiF sample (63.5 mm.thick) at angles $\theta = 30^{\circ}, 45^{\circ}$ respectively. The energy spectra from the two LiF samples shown in Figures 7.5 - 7.9 show that the measured neutron flux of the 14 MeV neutrons after being scattered by different thicknesses of LiF samples is due almost entirely to the neutrons that have been elastically

scattered by ${}^6\text{Li}$, ${}^7\text{Li}$, and ${}^{19}\text{F}$ nuclei.

However, there is a contribution shown in the lower energy region of the spectrum which is due to neutrons being scattered by the $(n,n\alpha)$ reaction. This reaction has a broad distribution merging with the lower energy tail of the elastic peak. The small contribution of all reactions except elastic scattering agrees with the conclusions that have been derived from the cross section data and the energy probability distribution which were discussed in Section 6.2. In comparing the heights of the peaks of Figures 7.5, 7.6 and 7.7 it can be seen that the peak of Figure 7.5 is three times higher than the peak of Figure 7.6 and four times higher than the peak of Figure 7.7. Similarly the peak of Figure 7.8 is four times the peak of Figure 7.9.

Therefore it can be deduced that the scattering of the 14 MeV neutrons from the LiF sample shows a forward peak and that agrees with the trend of the angular probability distribution data (taken from U.K.N.D.L.) file for the ${}^6\text{Li}$, ${}^7\text{Li}$ and ${}^{19}\text{F}$ nuclei.

7.4 THE MEASURED SPECTRA FROM IRON SAMPLES

The time-of-flight spectra was measured for the two samples of iron. The first sample measured 31 cms x 32 cm and was 7.62 cm thick, the second sample measured 14.2 cm x 30.6 cm and was 3.6 cm thick.

A typical time-of-flight spectrum for the elastically scattered 14 MeV neutrons from the first iron sample at angle $\theta = 30^\circ$ is shown in Figure 7.10. The converted energy spectrum is shown in Figure 7.11. The normalised energy spectra at angles $\theta = 30^\circ$, 45° and 60° are produced in the same way as discussed in section 7.3 and they are presented in Figures 7.12, 7.13 and 7.14 respectively, for the first sample (7.63 cm thick). For the second sample (316 cm thick) the spectra are presented in Figures 7.15, 7.16 for angles $\theta = 30^\circ$ and 45° respectively. From Figures 7.13 - 7.16 it can be seen that the spectra are almost entirely due to the elastic scattering reaction. Fast neutrons scattered by iron tend to show a forward peak which is in agreement with the general trends of the angular distribution for elastic scattering at this energy.

7.5 RESULTS OF COMPUTER PROGRAMMES

14 MeV neutrons incident on extended samples of LiF and Fe will suffer primary and secondary scatter and even higher orders of scattering. All these forms of scatter will contribute to the final flux. The spectra from different thicknesses of LiF and Fe samples were calculated at different laboratory angles by using the primary and secondary scatter models only and the computation was done with the help of the computer programmes listed in Appendices 3, 4, and 5.

Spectra from LiF samples

The neutron producing reactions from LiF samples that are contributing to the emerging flux (section 6.1) are the elastic, $(n,n\alpha)$ and (n,n^1) reactions. For the first LiF sample (14cm thick) the spectra were computed for the following laboratory angles $\theta = 30^\circ$, 45° and 60° . A typical spectrum at angle $\theta = 30^\circ$ is produced from adding up the contribution of the above mentioned reactions computed as follows

- a. The primary elastically scattered neutron spectrum as shown in Figure 7.17 computed by using the computer programme of Appendix 3.
- b. The secondary elastically scattered neutron spectrum as shown in Figure 7.18 computed by using the computer programme of Appendix 4.
- c. The primary spectrum from the $(n,n\alpha)$ reaction as shown in Figure 7.19 and the primary spectrum from the (n,n^1) reaction as shown in Figure 7.20 as both computed by using the computer programme of Appendix 5.

Therefore the total flux emerging from LiF sample at angle $\theta = 30^\circ$ as shown in Figure 7.21 is the sum of Figures 7.17 - 7.20. The spectra at angles $\theta = 45^\circ$ and 60° for the same LiF sample were produced in the same way and

shown in Figures 7.22 and 7.23 respectively. The spectra for the other LiF samples of 6.35 cm thickness were similarly produced and shown in Figures 7.24 and 7.25 for the angles $\theta=30^\circ$ and 45° respectively.

From the results shown in the figures, the highest contribution to the emerging flux comes from the elastic reaction but there is some contribution from the $(n,n\alpha)$ and the (n,n^1) reactions that appear in the lower energy region of the spectrum, the contribution from both reactions being far lower than the contribution from the elastic reaction, indicating that the elastic reaction is predominant. In comparing the intensity of the peaks of Figures 7.20, 7.21 and 7.22 it can be seen that the peak intensity of Figure 7.20 is three times that of Figure 7.31 and thirteen times that of Figure 7.22. This results from the strong forward peaking of the angular distribution data used.

Spectra from Fe samples.

The neutron producing reactions from Fe samples that are contributing to the emerging flux (section 6.1) are the elastic, (n,n^1) and $(n,2n)$ reactions. For the first Fe sample (7.62 cm thick) the spectra were computed for the following laboratory angles $\theta=30^\circ$, 45° and 60° . A typical spectrum at angle $\theta=30^\circ$ is produced from adding up the contribution of the above-mentioned reactions computed as follows:

- a. The primary elastically scattered neutron spectrum as shown in Figure (7.26) computed by using the computer programme of Appendix 3.

- b. The secondary elastically scattered neutron spectrum as shown in Figure (7.27) computed by using the computer programme of Appendix 4.
- c. The primary spectrum from the (n,n^1) reaction as shown in Figure (7.28) and the primary spectrum from the $(n,2n)$ reactions as shown in Figure (7.29) as both computed by using the computer programme of Appendix 5.

Therefore the spectrum at angle $\theta=30^\circ$ as shown in Figure (7.30) is the sum of Figures 7.26 - 7.29. The spectra at angles $\theta=45^\circ$ and 60° for the same Fe sample were produced in the same way and shown in Figures 7.31 - 7.32 respectively. The spectra for the other Fe samples (3.6 cm thick) were similarly produced and shown in Figures 7.33 and 7.34 for the angles $\theta=30^\circ$ and 45° respectively.

From the results shown in the figures it is clear that the elastic scattering reaction is the predominant one.

The contribution from the (n,n^1) and the $(n,2n)$ reactions appear in the lower energy region of the spectrum and their contribution to the flux is very small compared to that of the elastic contribution.

The strong forward peaking results from the angular distribution data used.

7.6 COMPARISON OF EXPERIMENT AND COMPUTER RESULTS

The experimental and theoretical results of the spectra of the scattered 14 MeV neutrons from different thicknesses of LiF and Fe samples at different laboratory angles were obtained and discussed in sections 7.4 and 7.5. The spectra were plotted as neutrons per steradian per MeV versus neutron energy in MeV. The comparison between the theoretical and experimental spectra is well explained by plotting the experimental spectrum and the theoretical spectrum on the same figure for each angle to each sample. The experimental spectra have a broad elastic peak due to the different time uncertainty factors involved in the experimental measurements (see section 5.7), while the theoretical spectra have a rather sharp peak. Therefore the best way of comparison is achieved by comparing the area under the peaks of the two spectra in each figure as discussed below for LiF and Fe samples.

a) LiF samples

The comparison between the theoretical and experimental spectra for LiF sample (14 cm thick) at angles $\theta=30^\circ$, 45° and 60° are shown in Figures 7.35, 7.36 and 7.37. For the LiF sample (6.36 cm thick) the comparison is shown in Figures 7.38 and 7.39 for the angles $\theta=30^\circ$ and 45° respectively. The area under the peak for the comparison purposes are listed in Table 7.1. From the table it can be seen that within the experimental errors the results of the experiment agree fairly well with what the theory predicted. From the figures it can be seen that the position of the elastic peak

of the theory is almost in the same position of the experiment which shows a proper agreement between the experiment and the theory.

b. Fe samples

Similarly the experimental and theoretical results for Fe samples are shown in the same way. For Fe (7.62 cm thickness) the comparison is shown in Figures 7.40, 7.41 and 7.42 for angles $\theta=30^\circ$, 45° and 60° respectively. For Fe (3.6 cm thickness) the comparison for angle $\theta=30^\circ$ and 45° is shown in Figures 7.43 and 7.44 respectively. Table 7.1 shows the area under the peak for the experiment and the theory.

The comparison between experimental and theoretical results has shown that the primary and secondary scatter models are able to predict with a fairly good accuracy the angular energy distribution of the scattered 14 MeV neutrons from both LiF and Fe samples. The agreement is very good for small angles of scatter, however for large angles of scatter the experimental results show higher values than the theoretical and that is due to the contribution from the third, fourth scatters, etc. which become more significant at large angles of scatter.

A comparison between the theoretical intensities from the primary and secondary scatter models for LiF samples at different angles is shown in Figures 7.45, 7.46 and 7.47 for LiF (14 cm thickness) at angles $\theta=30^\circ$, 45° and 60° respectively

and for LiF (6.32 cm thickness) is shown in Figures 7.48 and 7.49 for angles $\theta=30^\circ$ and 45° respectively. It can be seen that the intensity from the secondary scatter is small compared with the intensity from the primary scatter. Therefore it can be deduced that the contribution from neutrons that have been scattered three or four times is even lower, and therefore neglecting higher orders of scatter would not produce serious error.

The comparison for Fe samples is shown in Figures 7.50, 7.51 and 7.52 for Fe (7.62 cm thickness) at angles $\theta=30^\circ, 45^\circ$ and 60° respectively and for Fe (316 cm thickness) is shown in Figures 7.53 and 7.54 at angles $\theta=30^\circ$ and 45° respectively. The intensity of the secondary scatter is higher at higher angles than that of the primary scatter and that is because Fe has a very sharply forward peaked angular distribution for elastic scattering which is reducing very rapidly at the angle used for measurement, whereas the intensity of multiply scattered neutrons is less dependent on the form of angular distribution.

TABLE 7.1

THE VALUES OF THE AREA UNDER THE PEAK OF BOTH THE
EXPERIMENTAL AND THEORETICAL SPECTRA AT DIFFERENT
ANGLES FOR ALL SAMPLES

	θ Lab	Theoretical values	Experimental values
LiF (14cm thick)	30	100.3×10^6	$(103.5 \pm 1.3) 10^6$
	45	395.9×10^5	$(402 \pm 6.3) 10^5$
	60	1407.1×10^4	$(1997.5 \pm 39.6) 10^4$
LiF (6.35cm thick)	30	79.5×10^6	$(83 \pm 2.6) 10^6$
	45	306.0×10^5	$(382 \pm 11.9) 10^5$
Fe (7.62cm thick)	30	5770.1×10^4	$(5850 \pm 77) 10^4$
	45	942.5×10^4	$(1035 \pm 25) 10^4$
	60	318.7×10^4	$(334.5 \pm 21.3) 10^4$
Fe (3.6cm thick)	30	6699.6×10^4	$(5410 \pm 247.7) 10^4$
	45	1132.1×10^4	$(1300 \pm 59.54) 10^4$

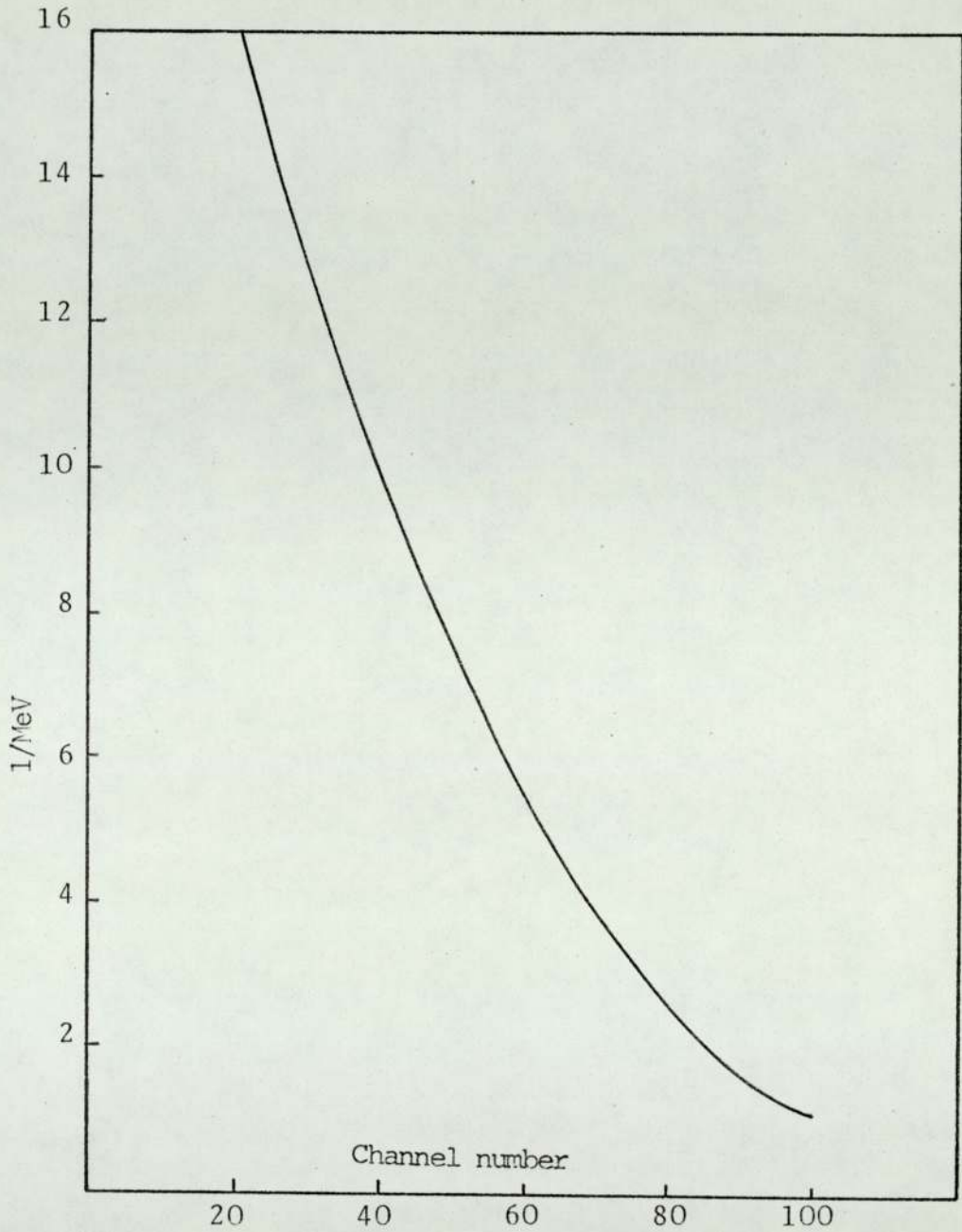


Fig. 7.1 The correction factor for correcting time to energy spectrum

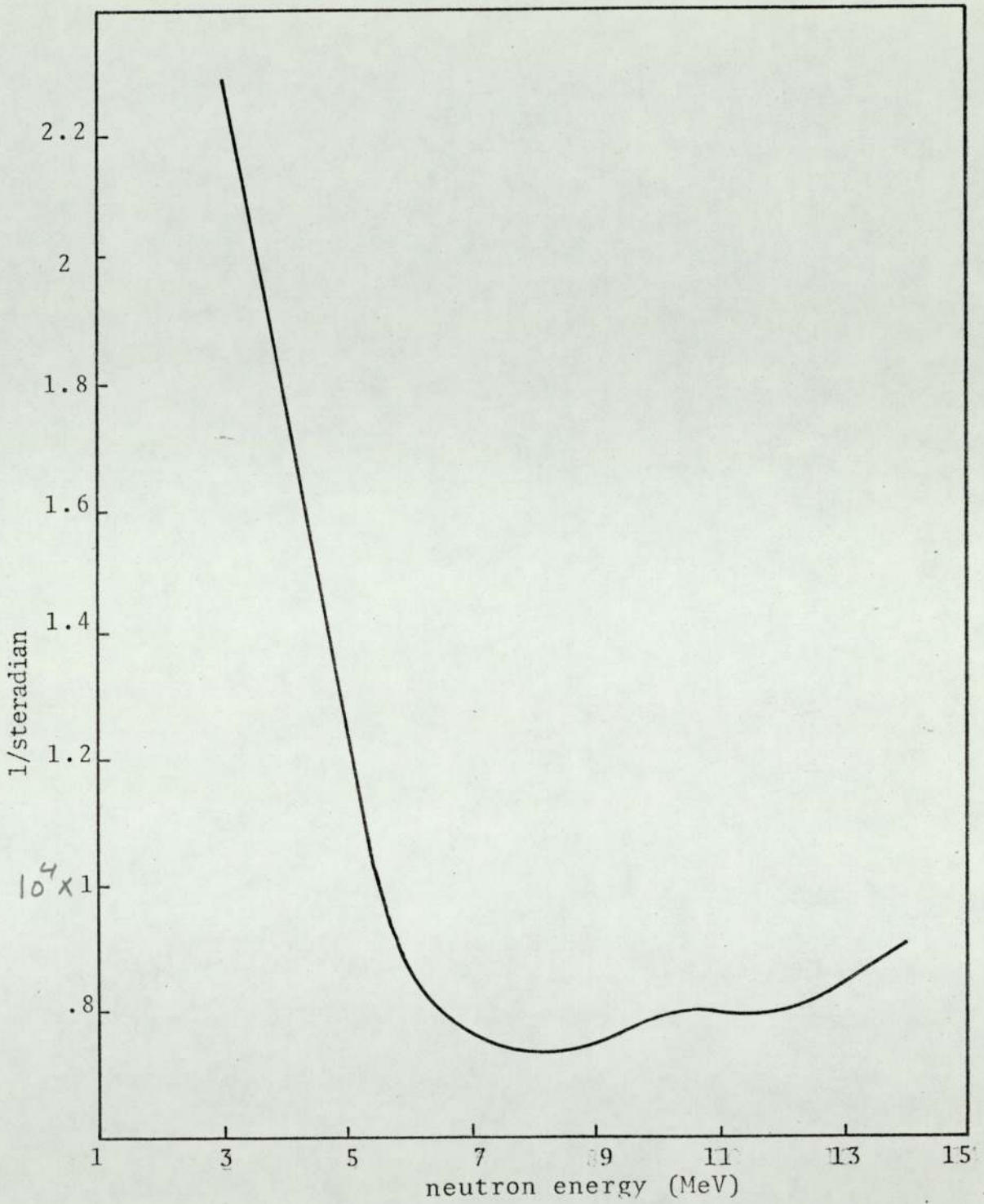


Fig. 7.2 The correction factor for the efficiency of the detector and the solid angle

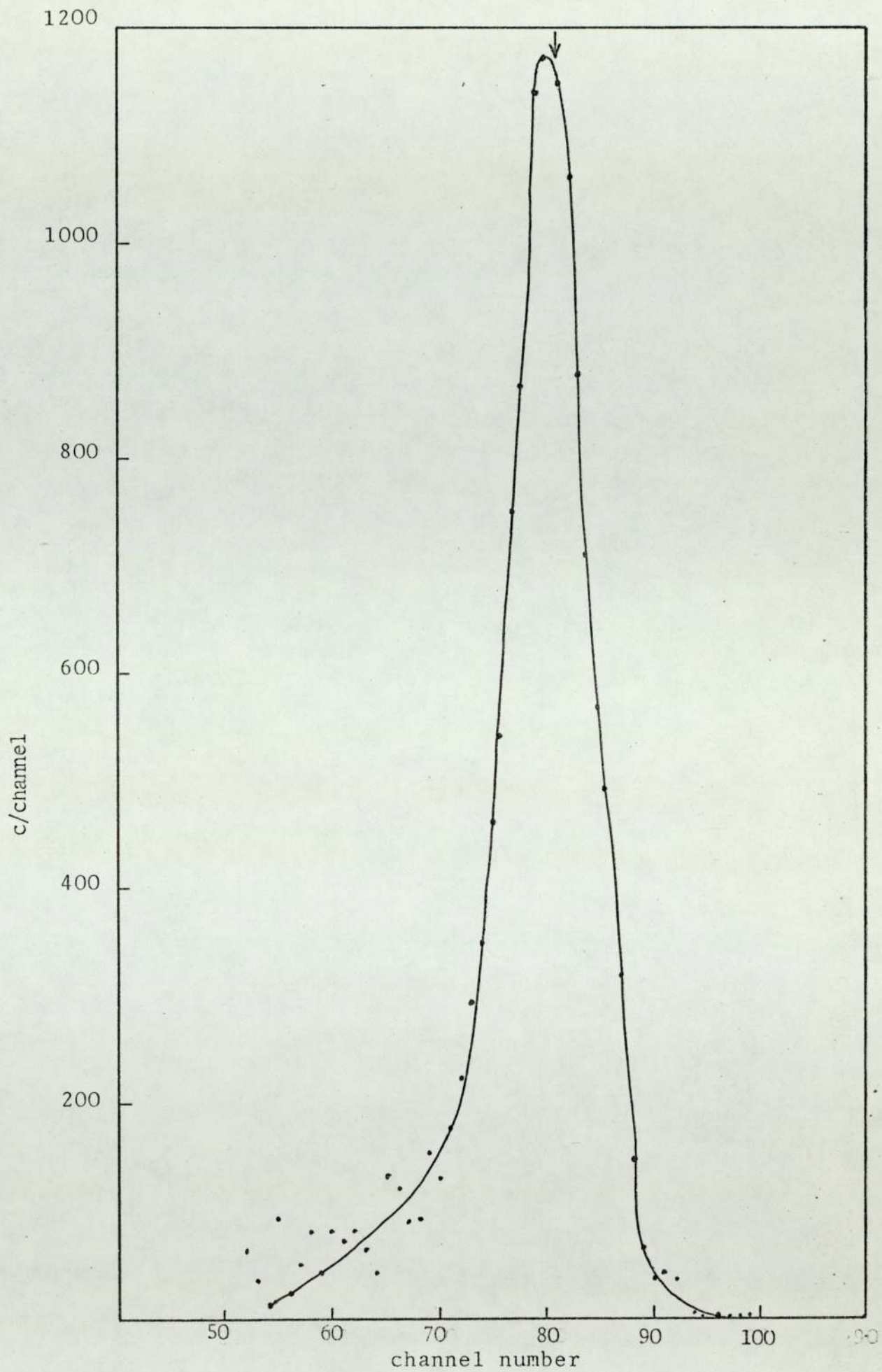
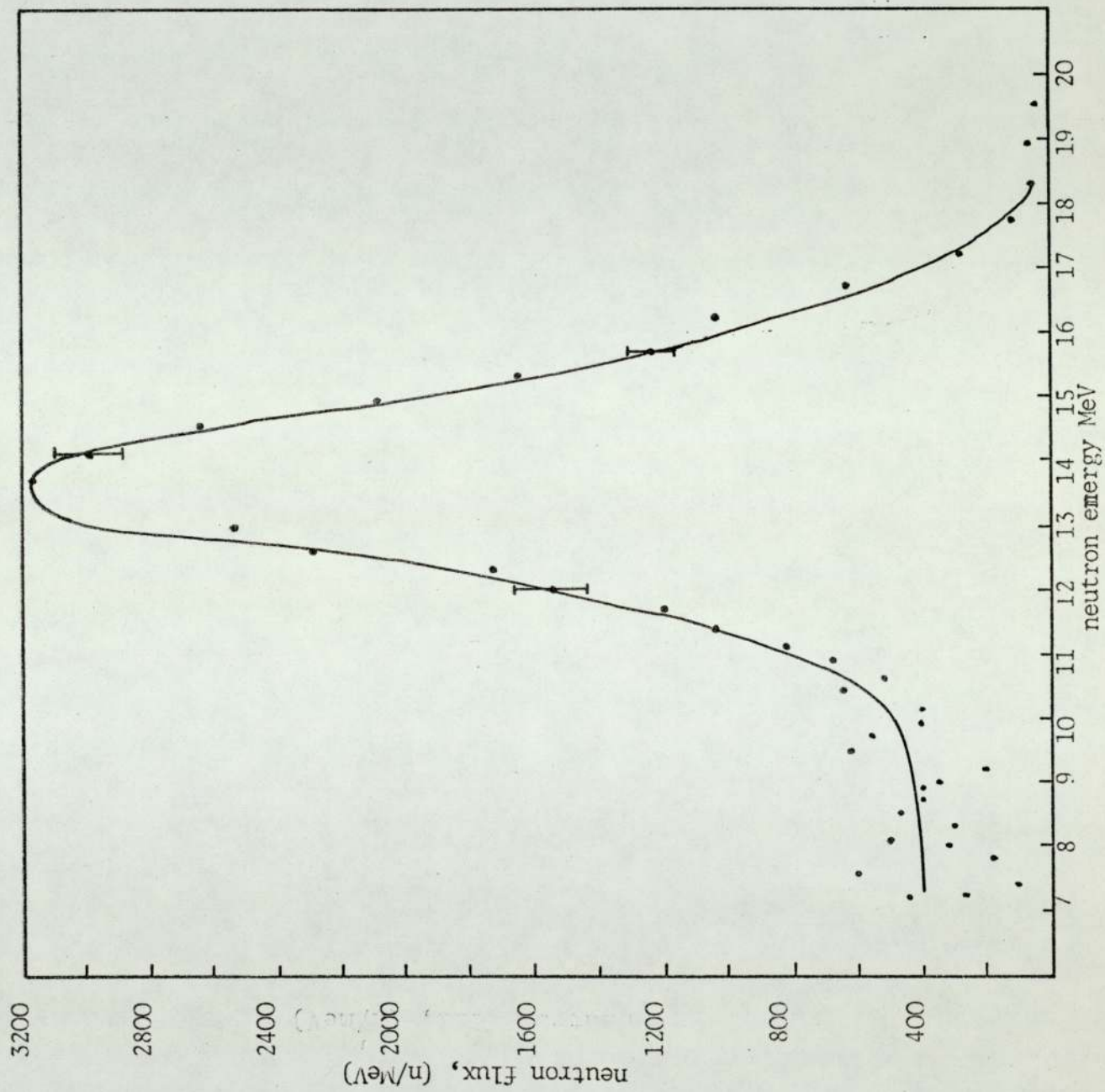


Fig. 7.3 Time-of-flight spectrum of LiF sample (14cm thick) at angle $\theta=30$

Fig. 7.4 Energy Spectrum
of LiF sample
(14cm thick)
at angle $\theta=30$



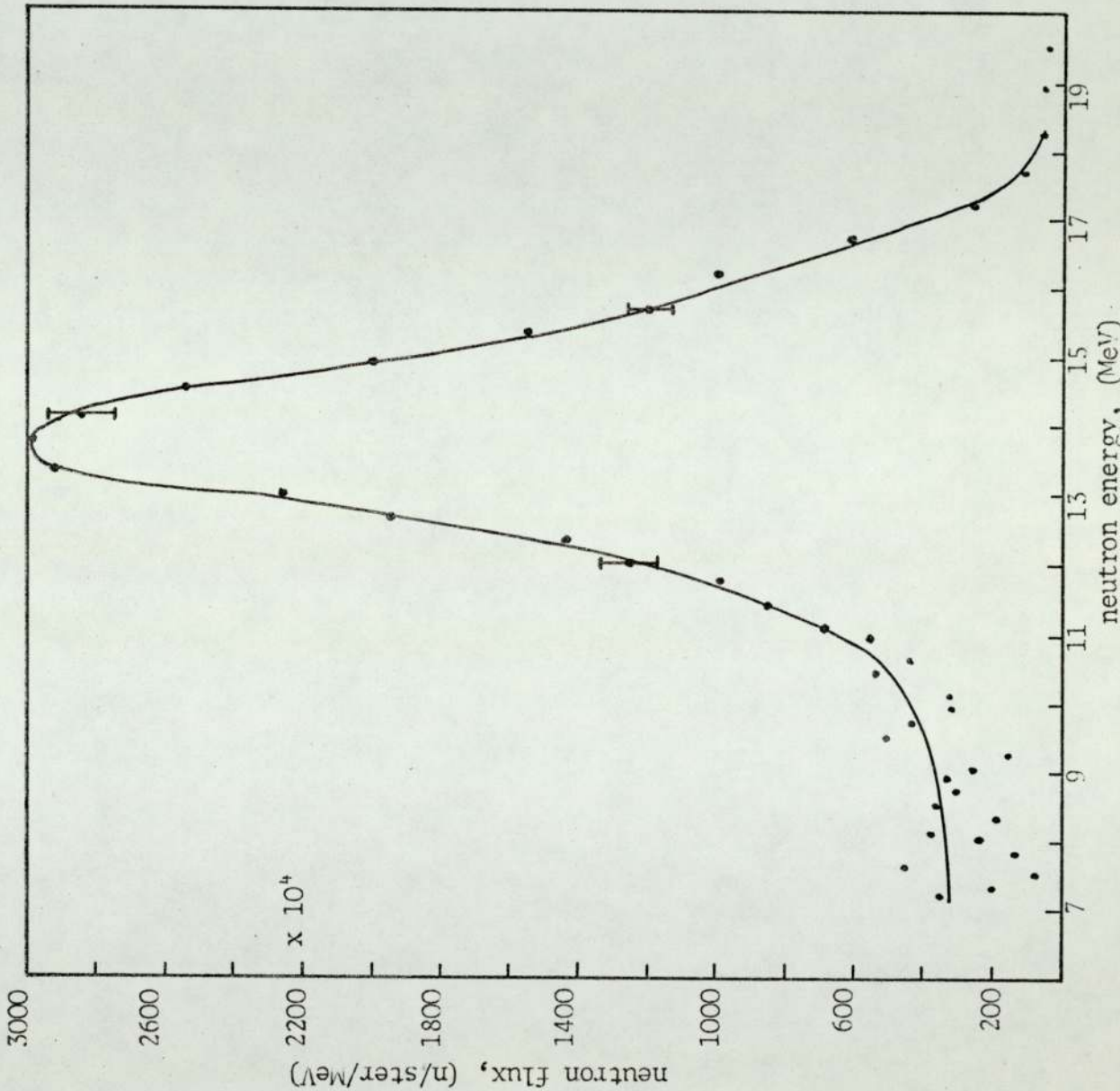


Fig. 7.5 Normalised energy spectrum of LiF (14cm thick) at angle $\theta=30$

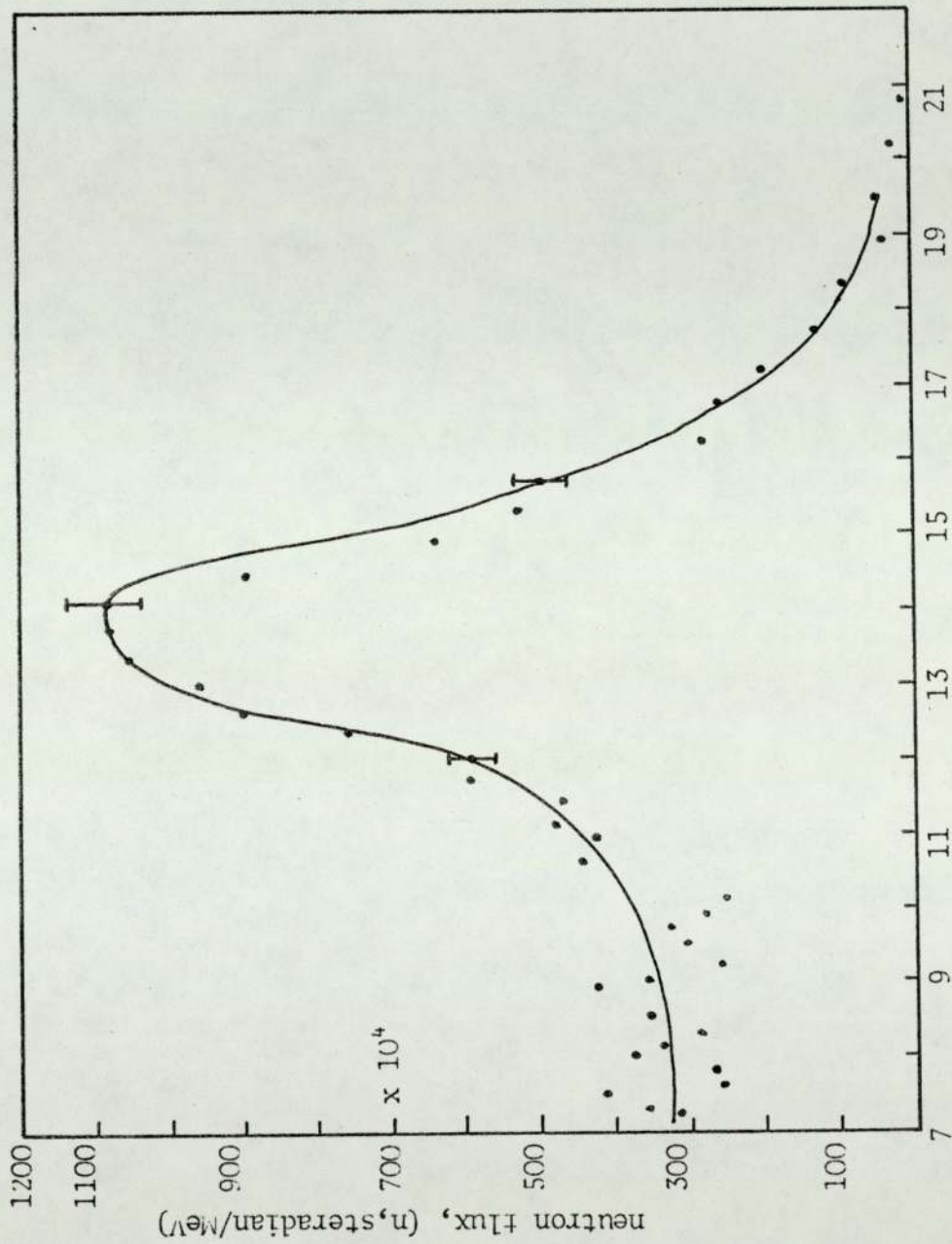


Fig. 7.6 Normalised energy spectrum of LiF (14cm thick) at angle $\theta=45$

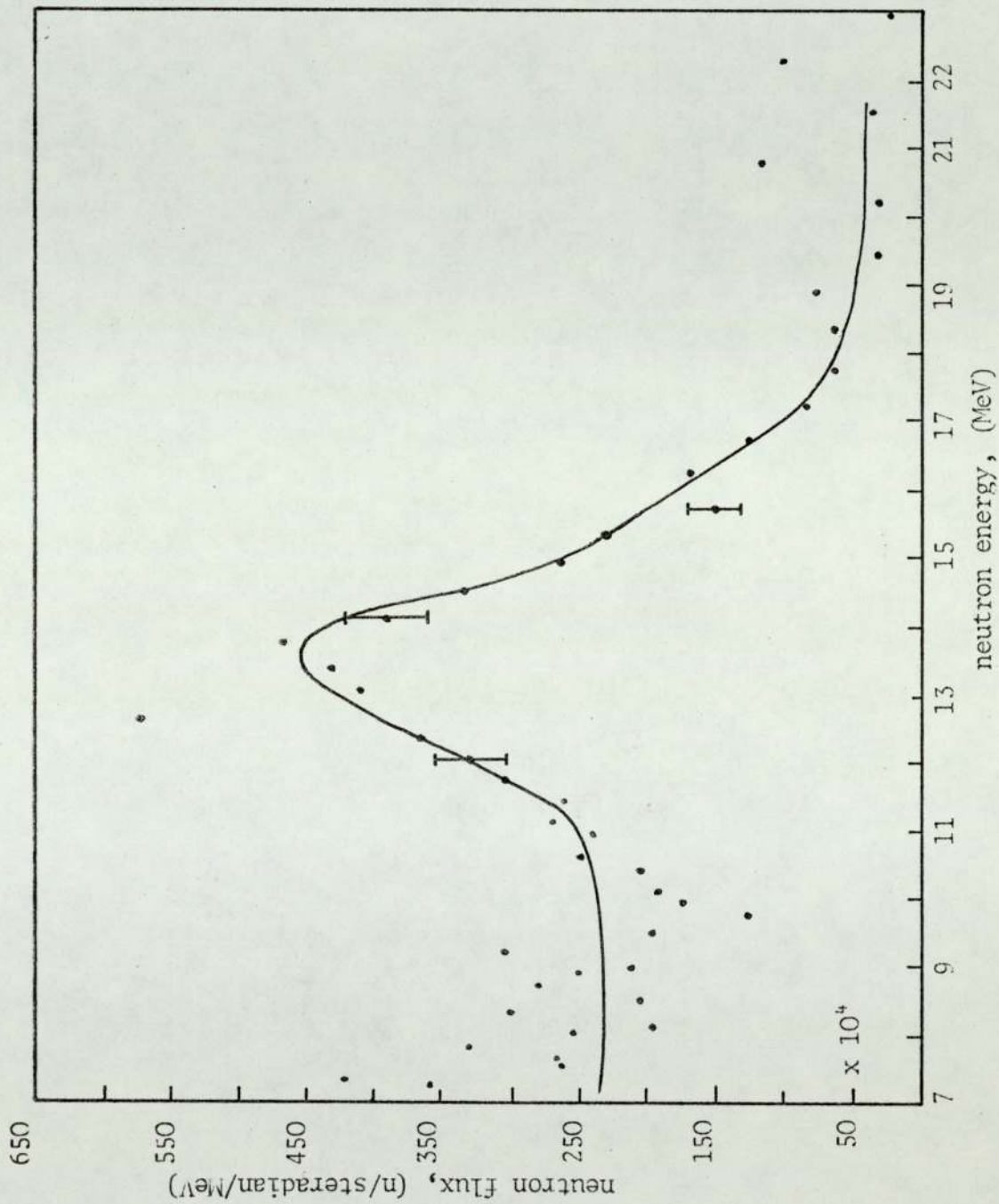


Fig. 7.7 Normalised energy spectrum of LiF (14cm thick) at angle $\theta=60$

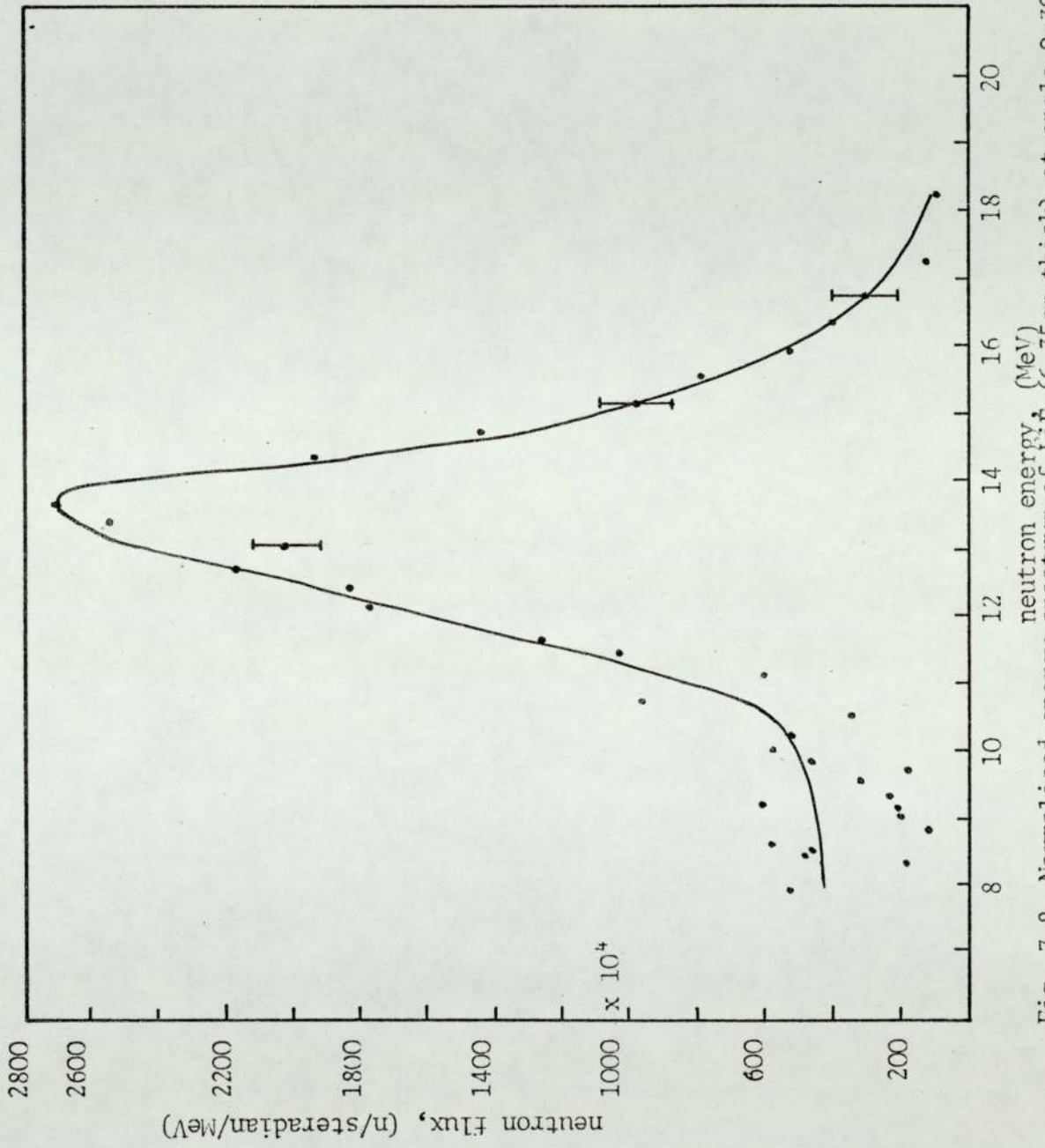


Fig. 7.8 Normalised energy spectrum of LiF (6.35cm thick) at angle $\theta=30$

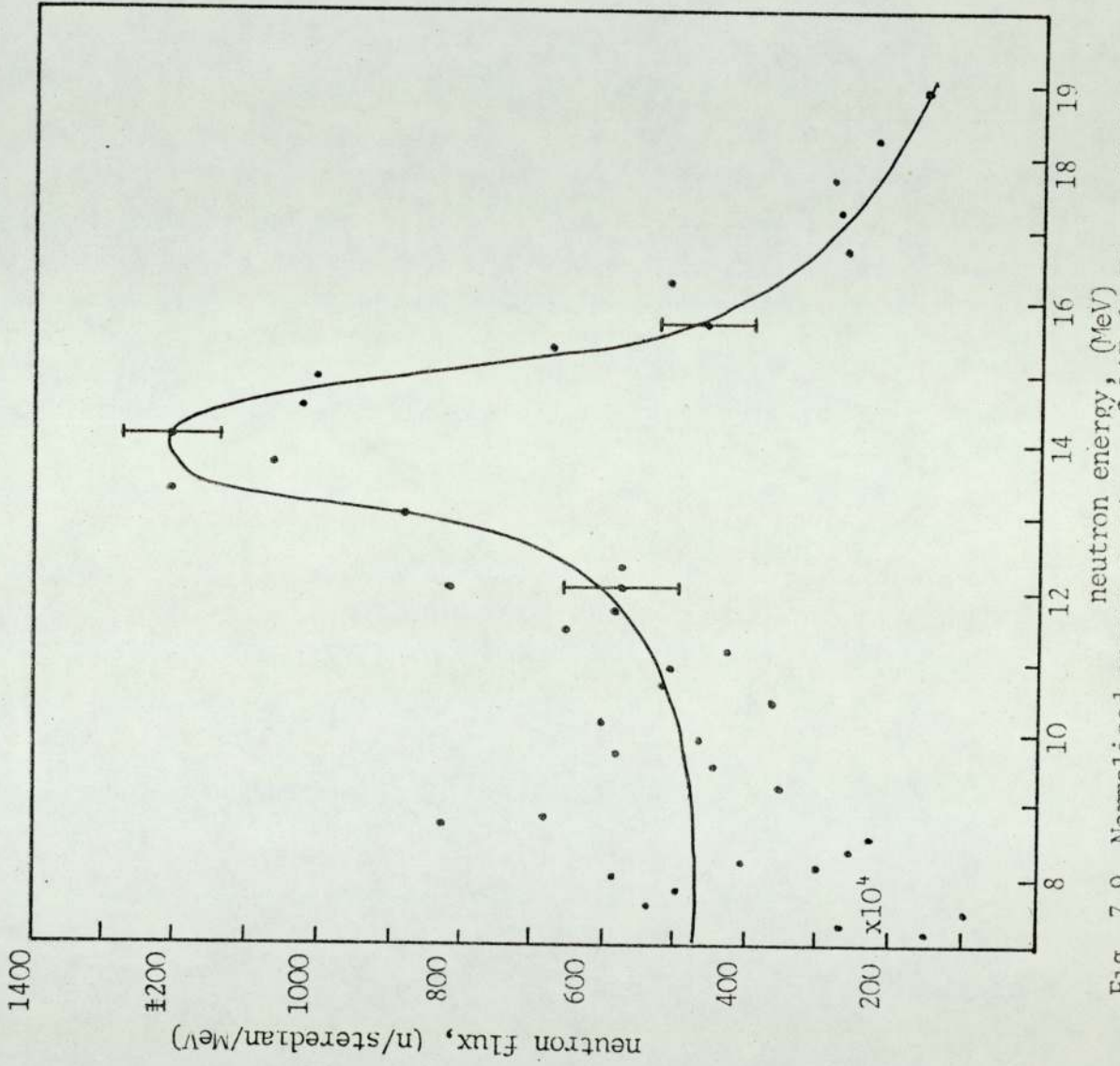


Fig. 7.9 Normalised energy spectrum of LiF (6.35 cm thick) at angle $\theta=45$

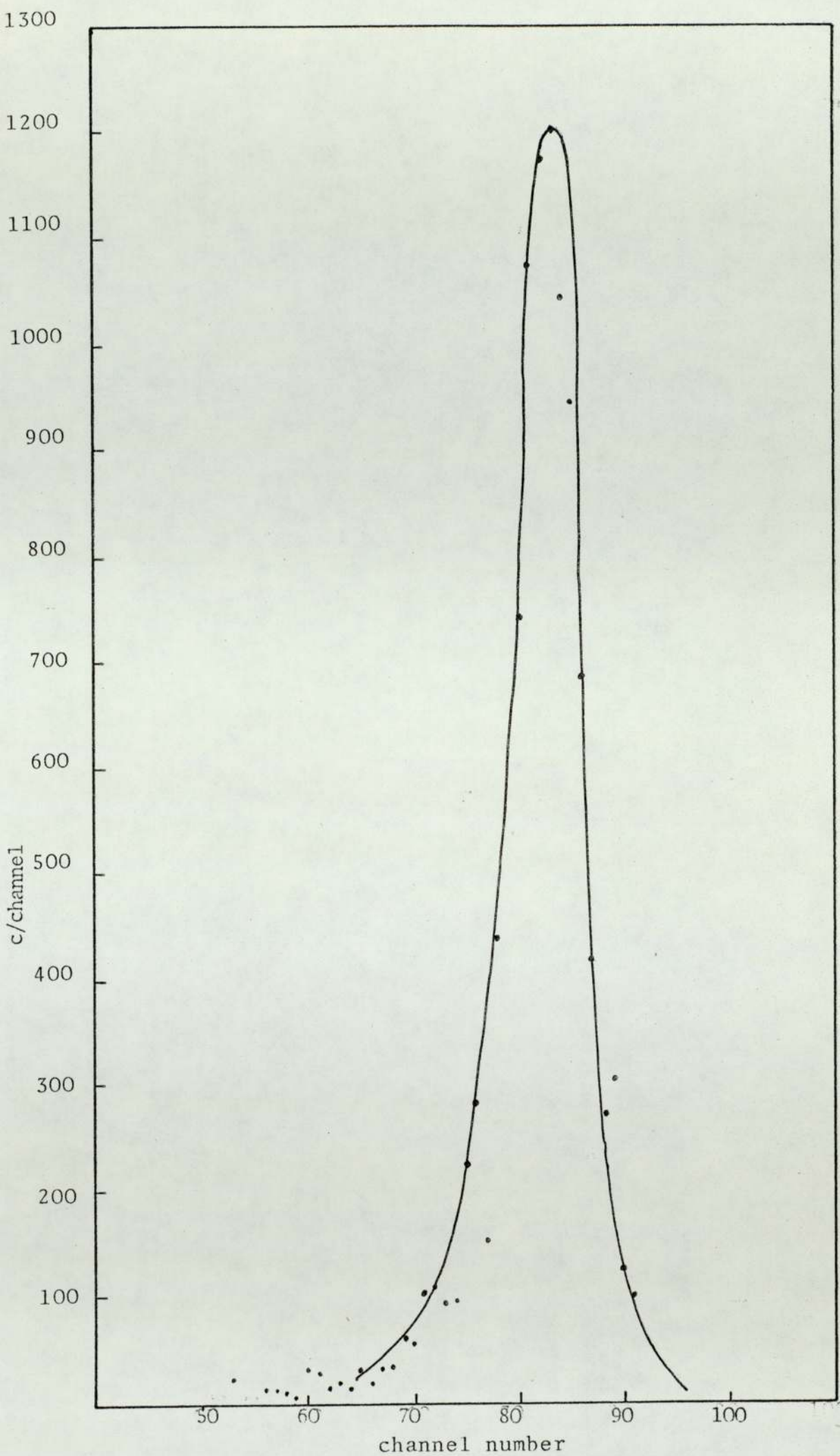


Fig. 7.10 Time-of-flight spectrum of Fe sample (7.62 cm thick) at angle $\theta=30$

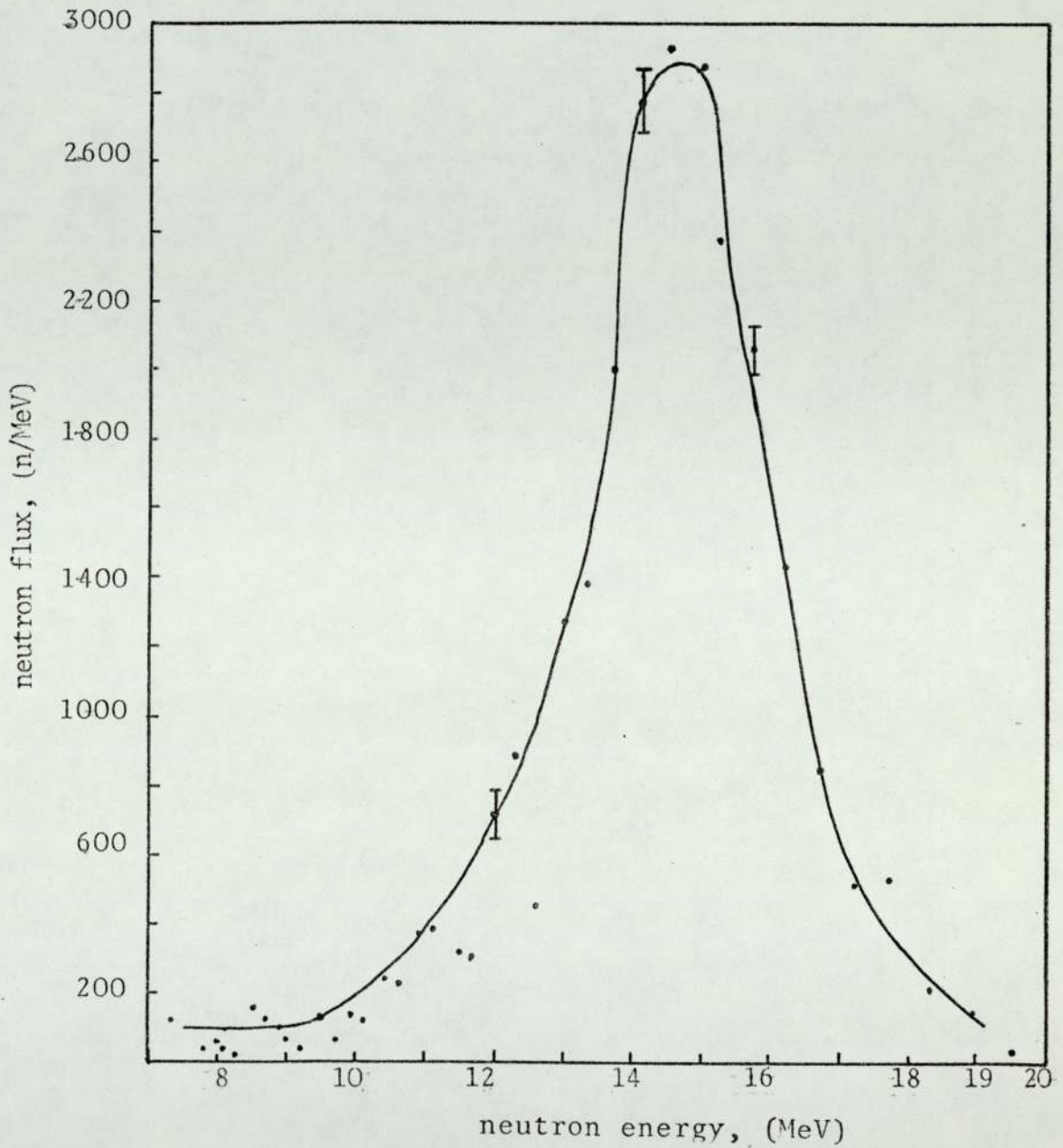


Fig. 7.11 Energy spectrum of Fe sample (7.62cm thick) at angle $\theta=30$

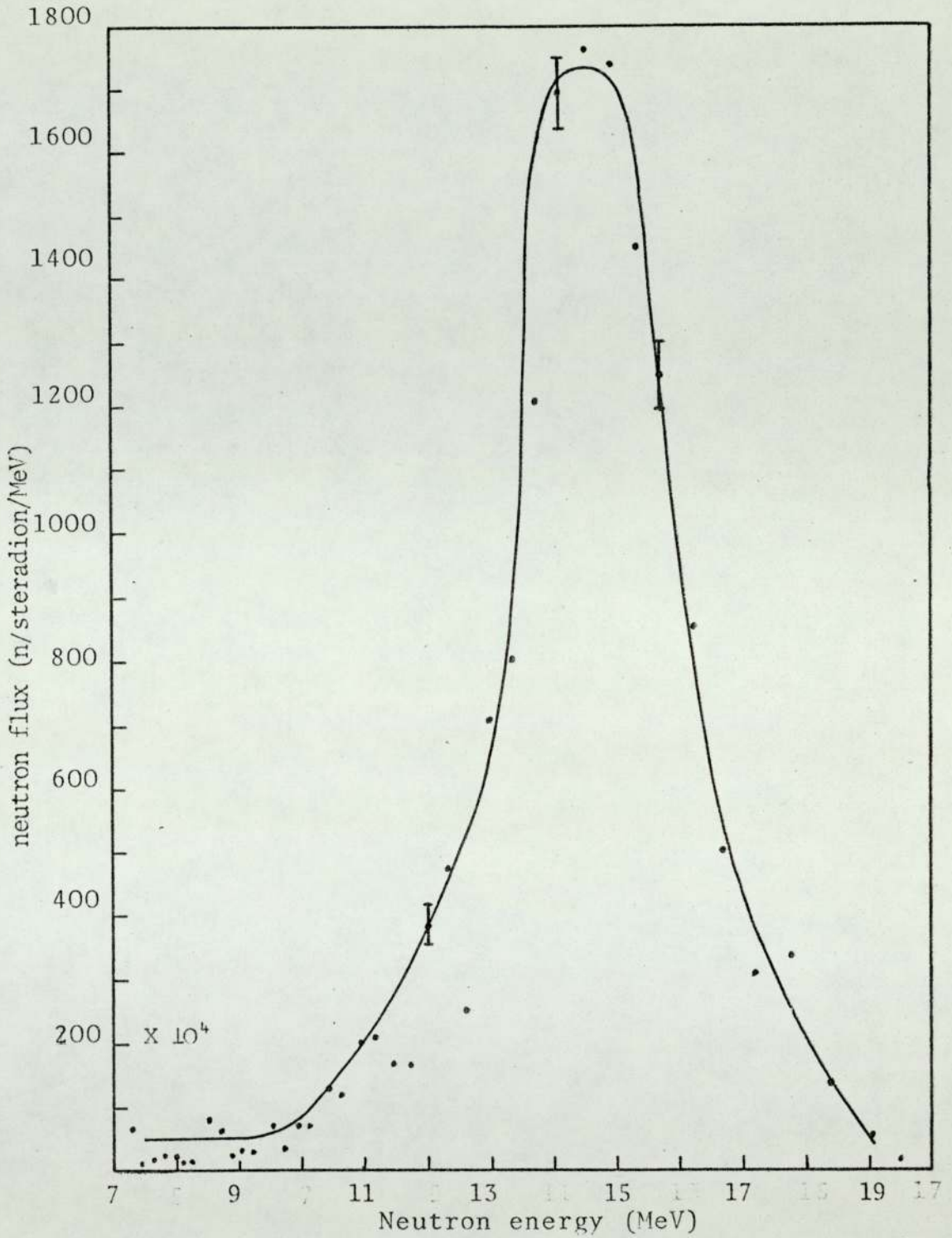


Fig. 7.12 Normalised energy spectrum of Fe (7.62 cm thick) at angle $\theta=30^\circ$.

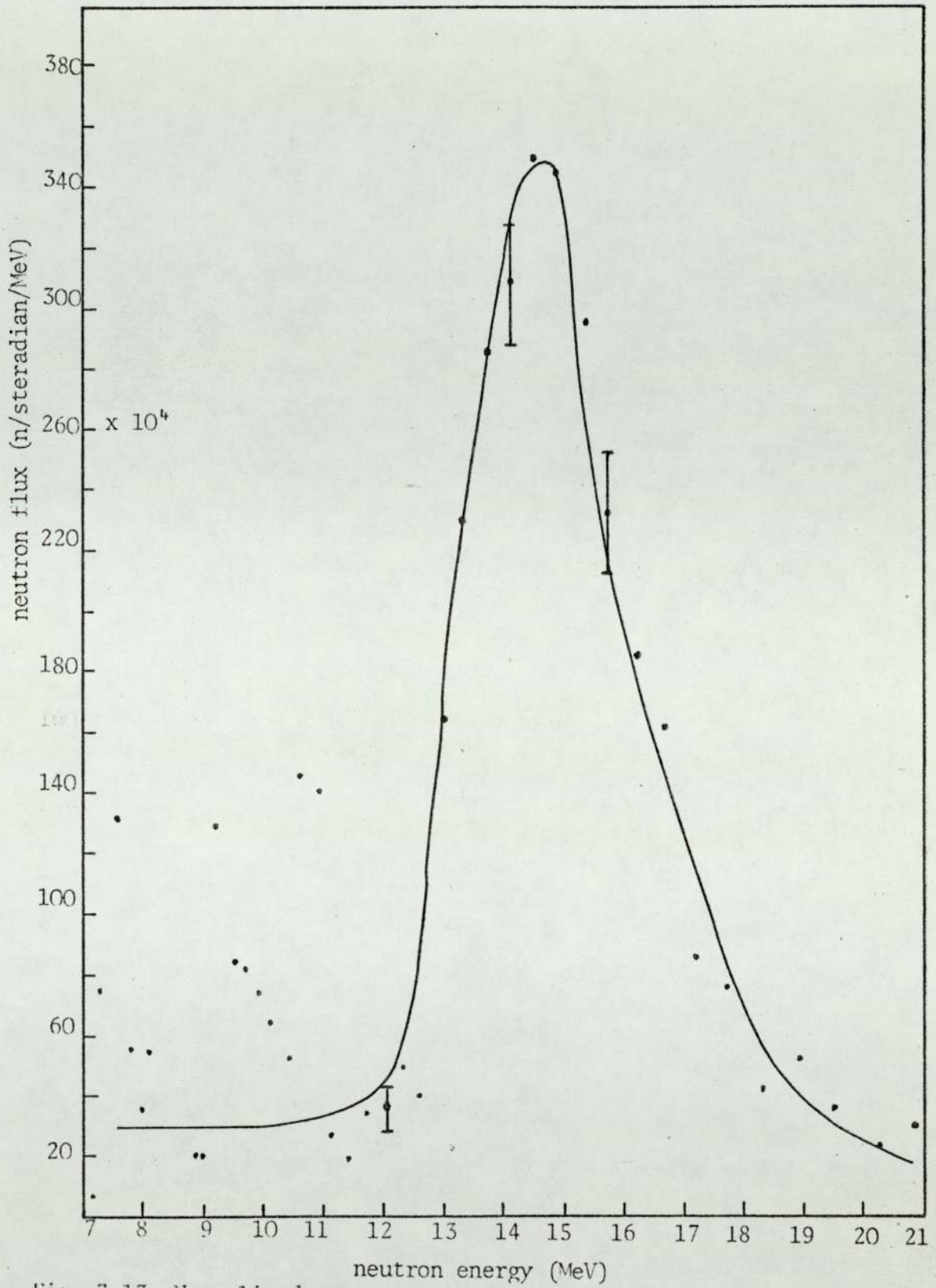


Fig. 7.13 Normalised energy spectrum of Fe (7.62cm thick) at angle $\theta=45$

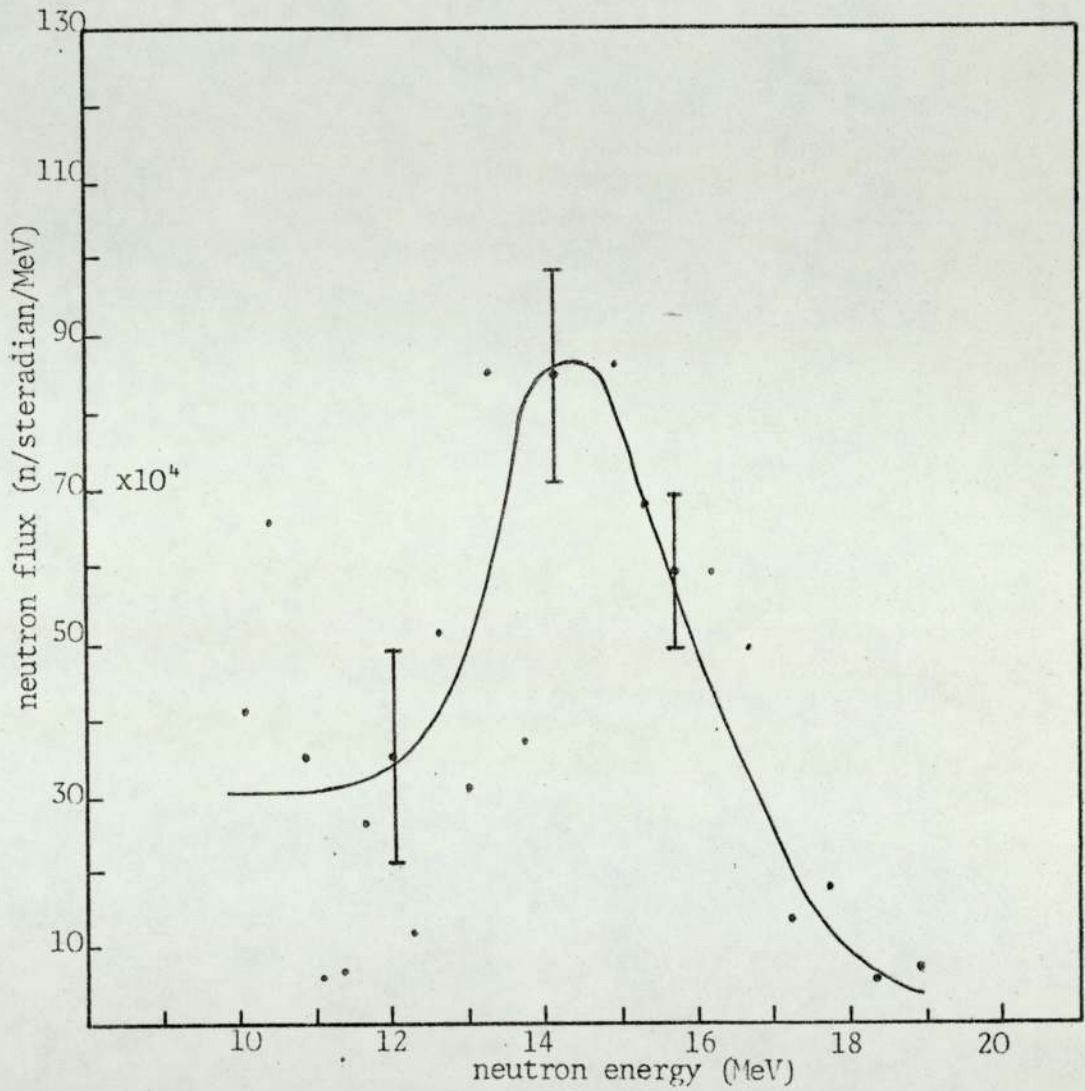


Fig. 7.14 Normalised energy spectrum of Fe (7.62cm thick) at angle $\theta=60$

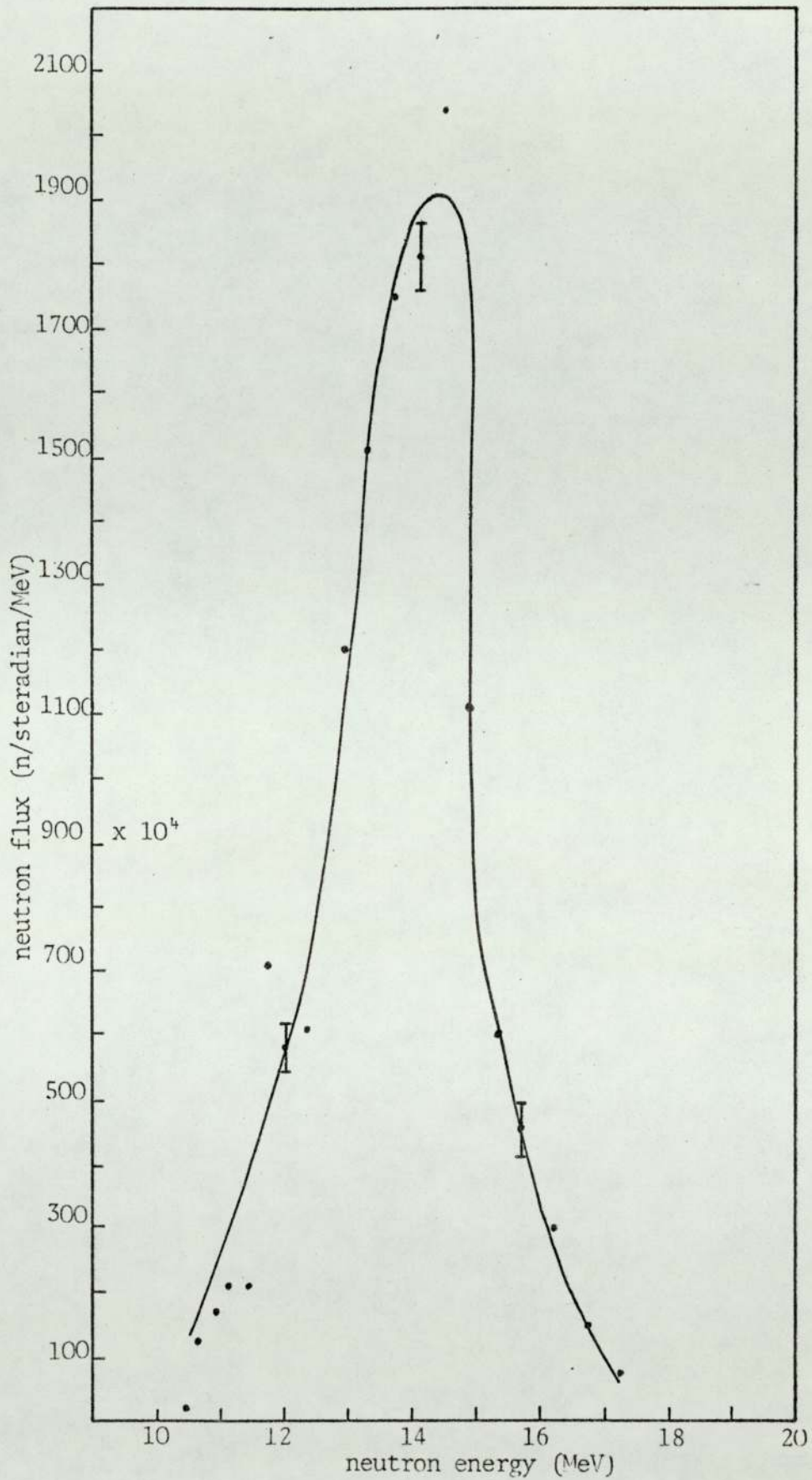


Fig. 7.15 Normalised energy spectrum of Fe (3.6cm thick) at angle $\theta=30$

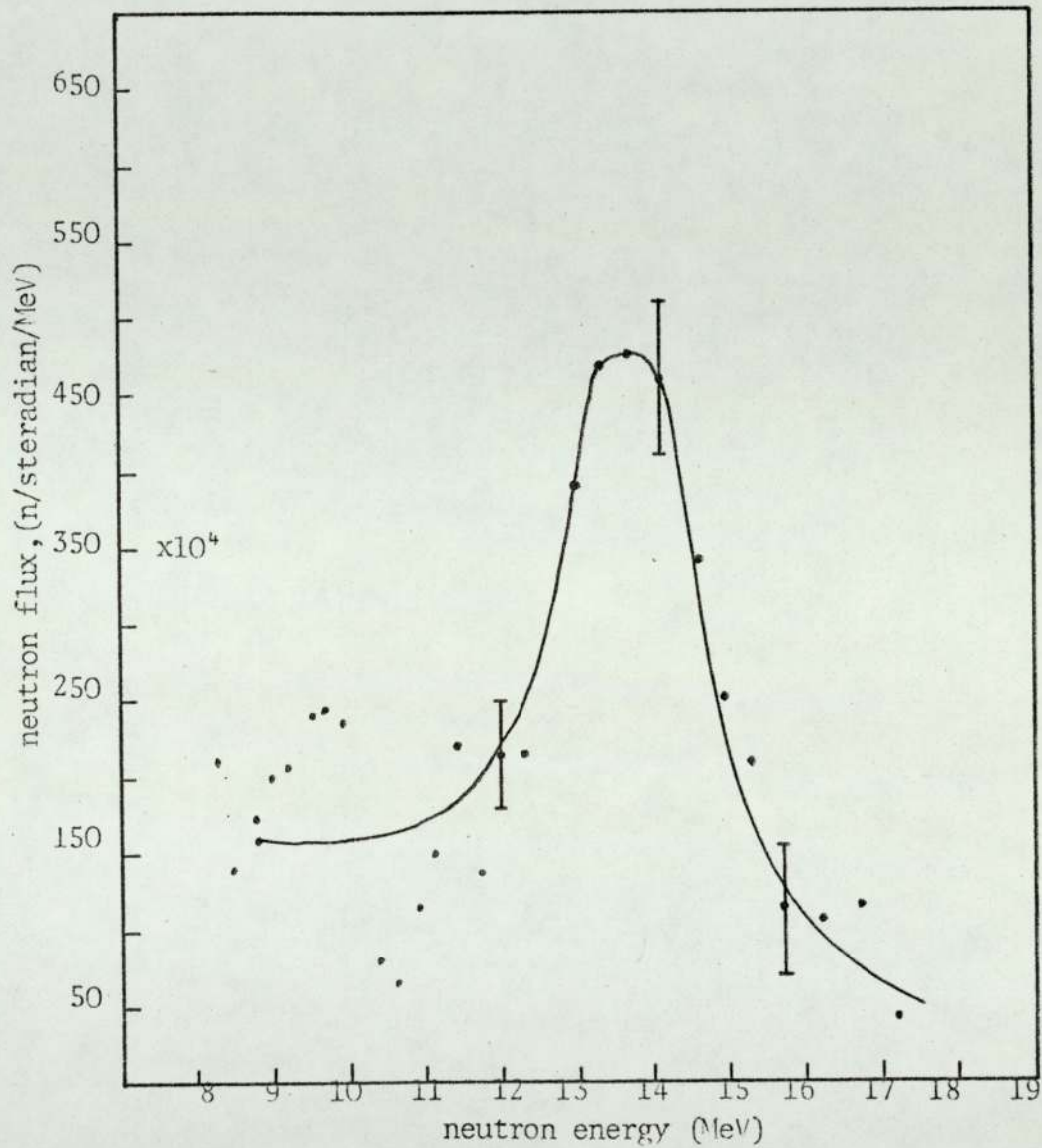


Fig. 7.16 Normalised energy spectrum of Fe (3.6cm thick) at angle $\theta=45$

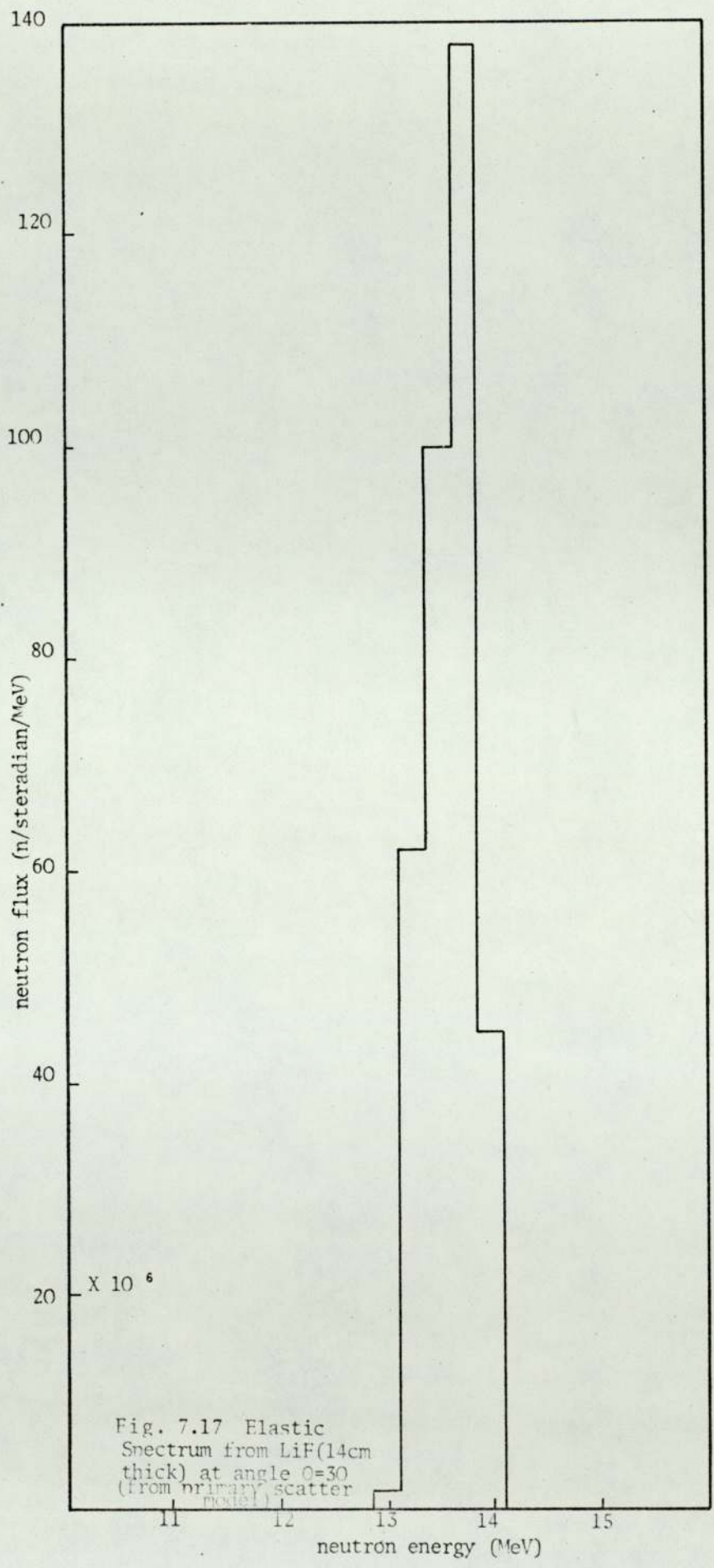
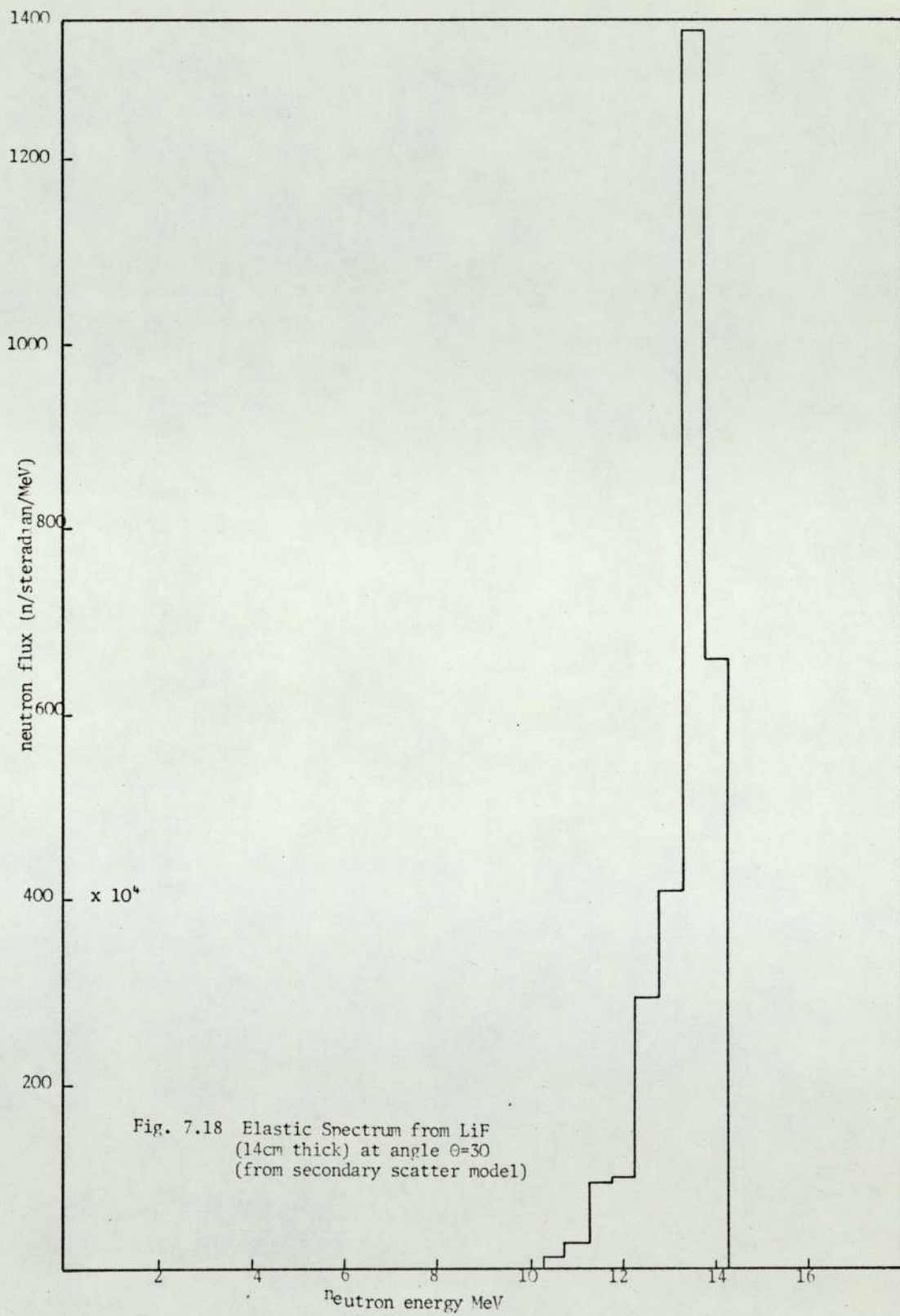


Fig. 7.17 Elastic Spectrum from LiF(14cm thick) at angle $\theta=30^\circ$ (from primary scatter model)



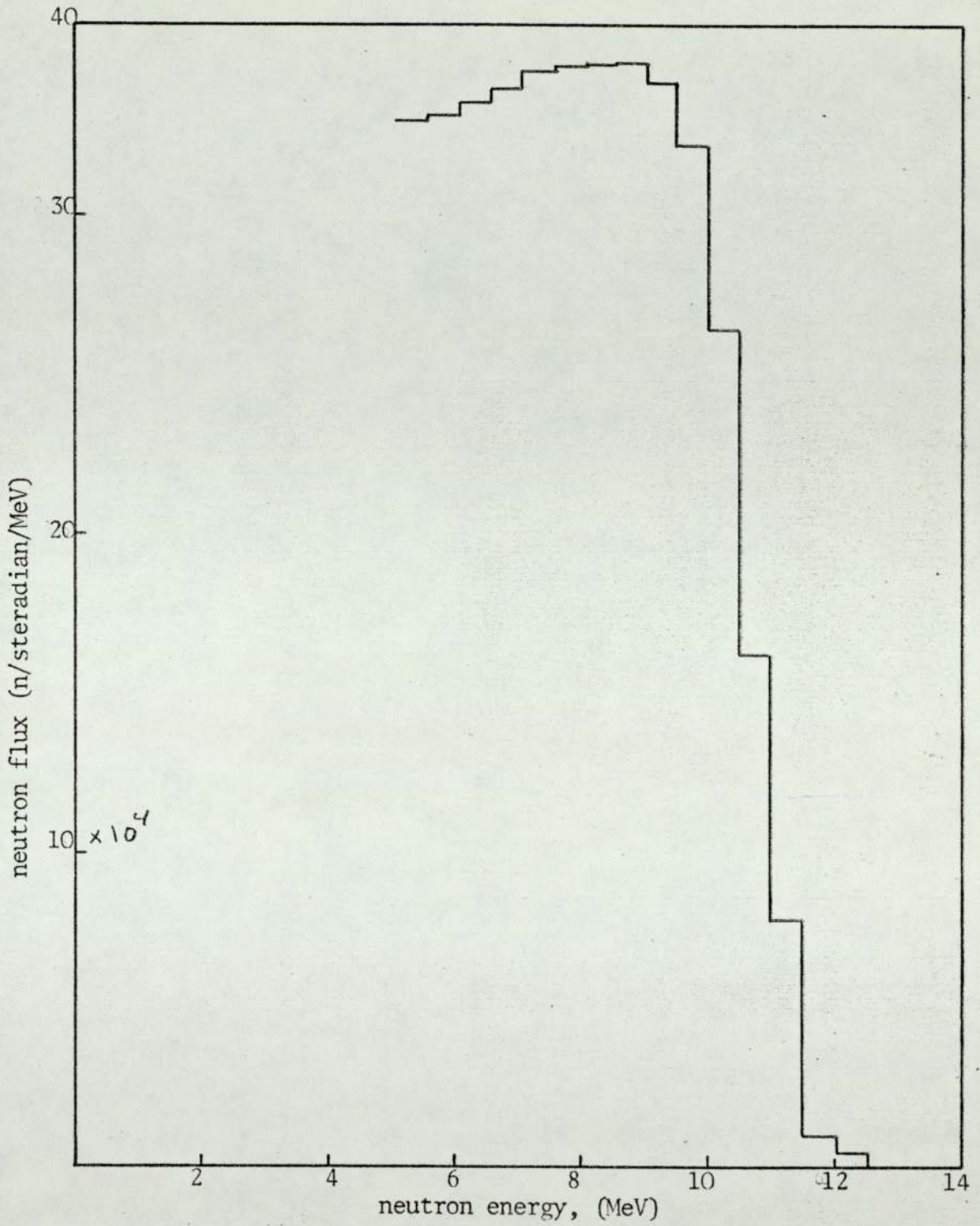


Fig. 7.19 (n, nd) reaction spectrum from LiF (14 cm thick) at angle $\theta=30$ (from primary scatter model)

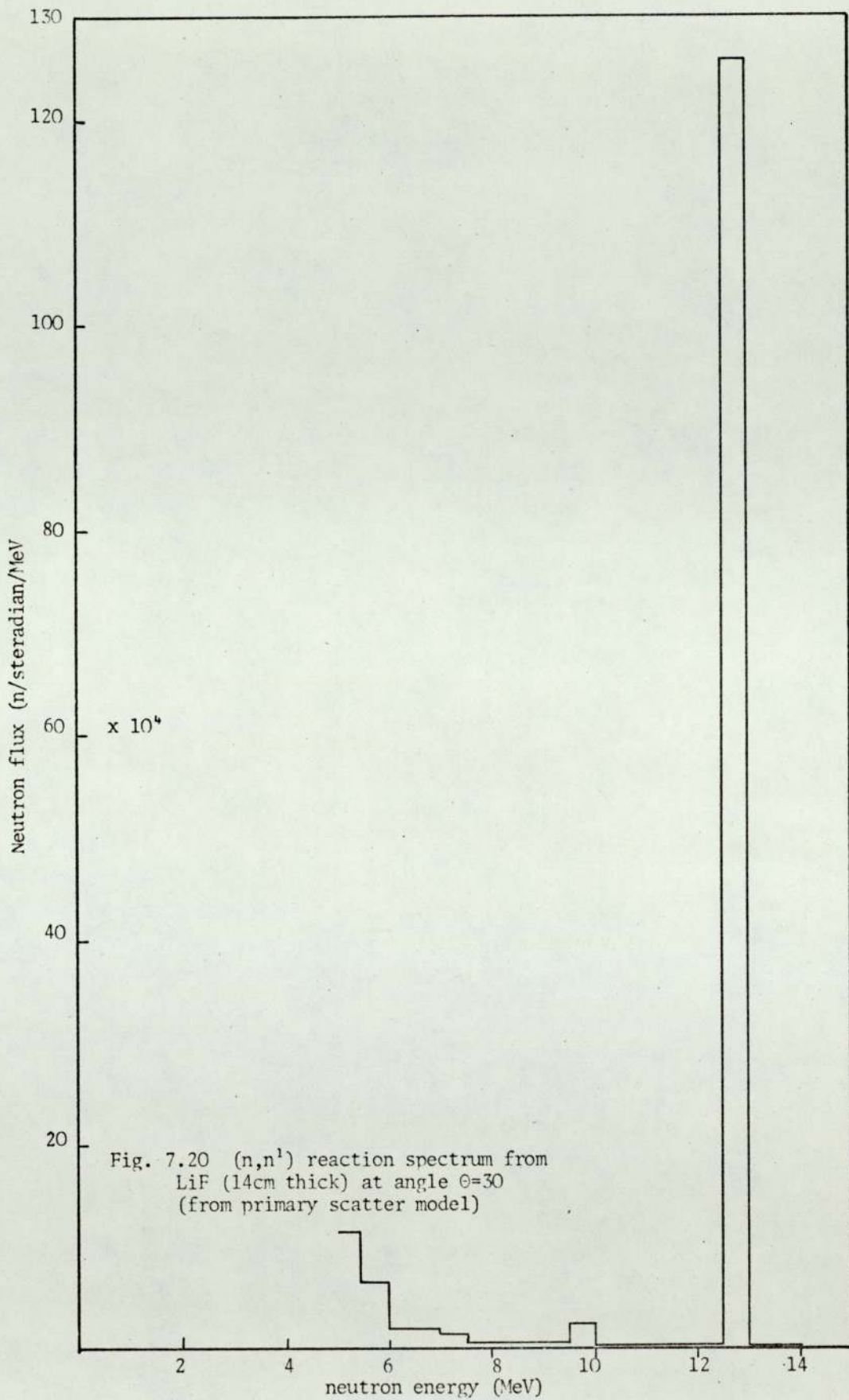


Fig. 7.20 (n,n') reaction spectrum from LiF (14cm thick) at angle $\Theta=30$ (from primary scatter model)

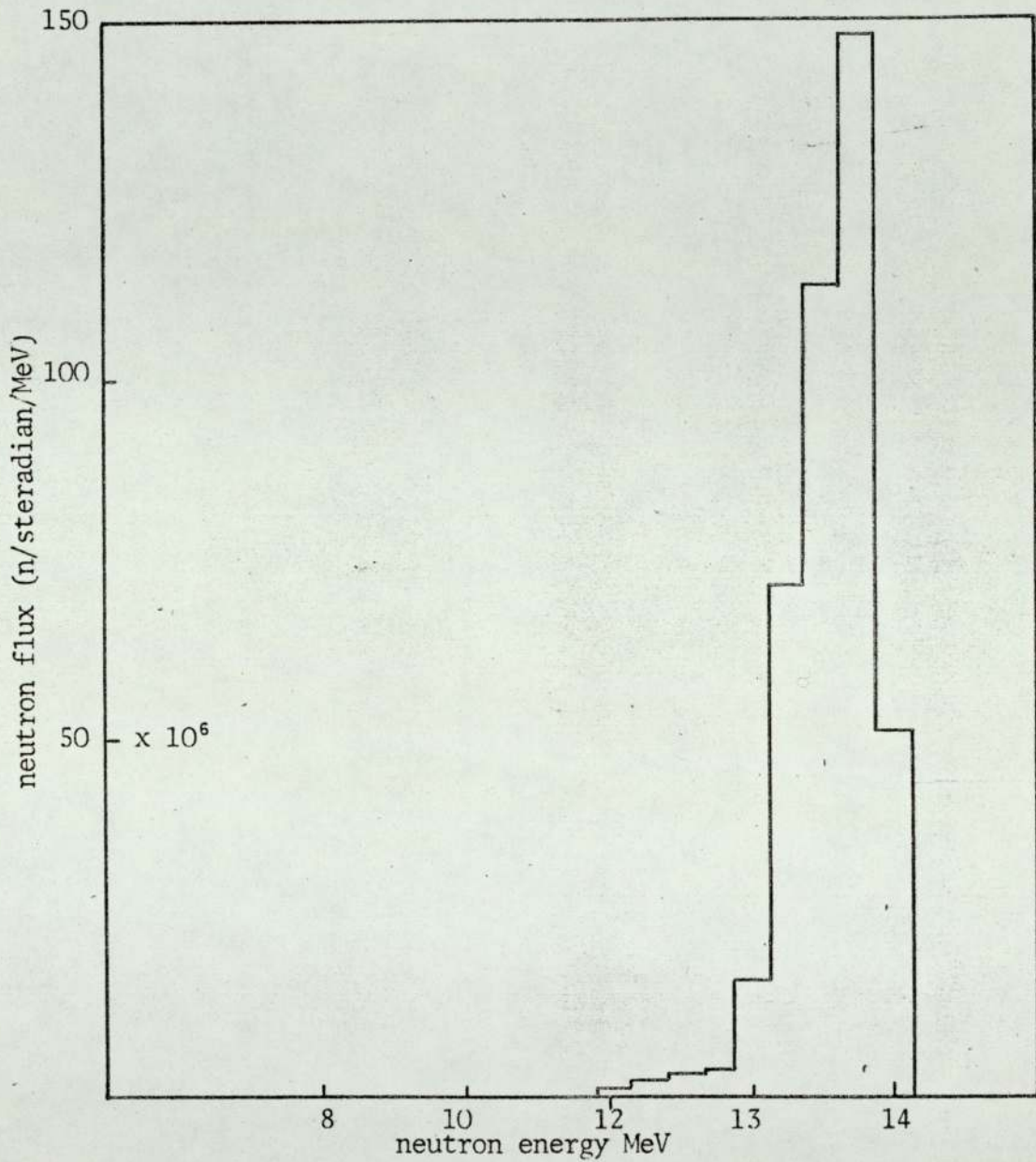


Fig. 7.21 Total flux from LiF (14cm thick) at angle $\theta=30$

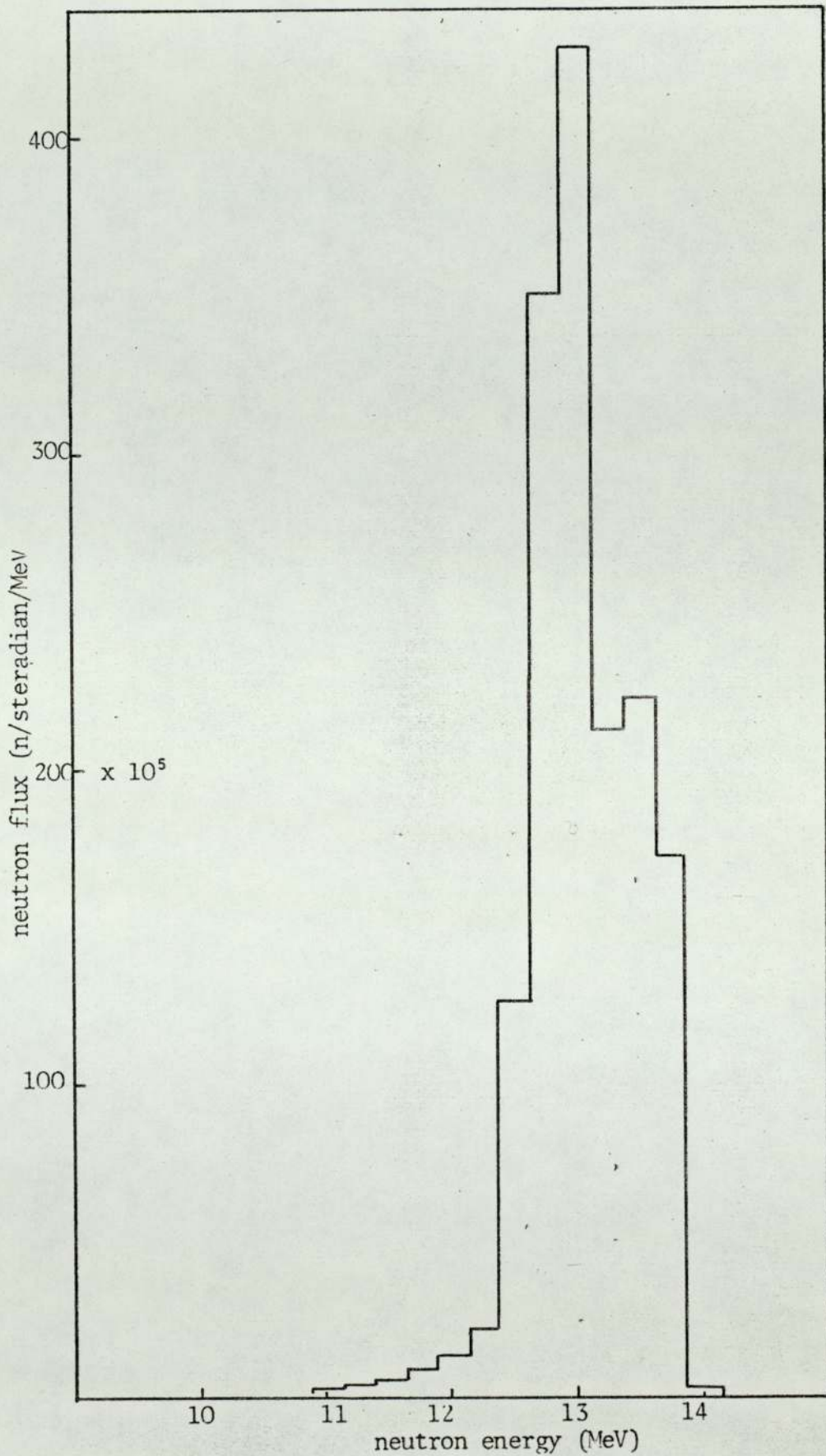


Fig. 7.22 Total flux from LiF (14cm thick) at angle $\theta 45$

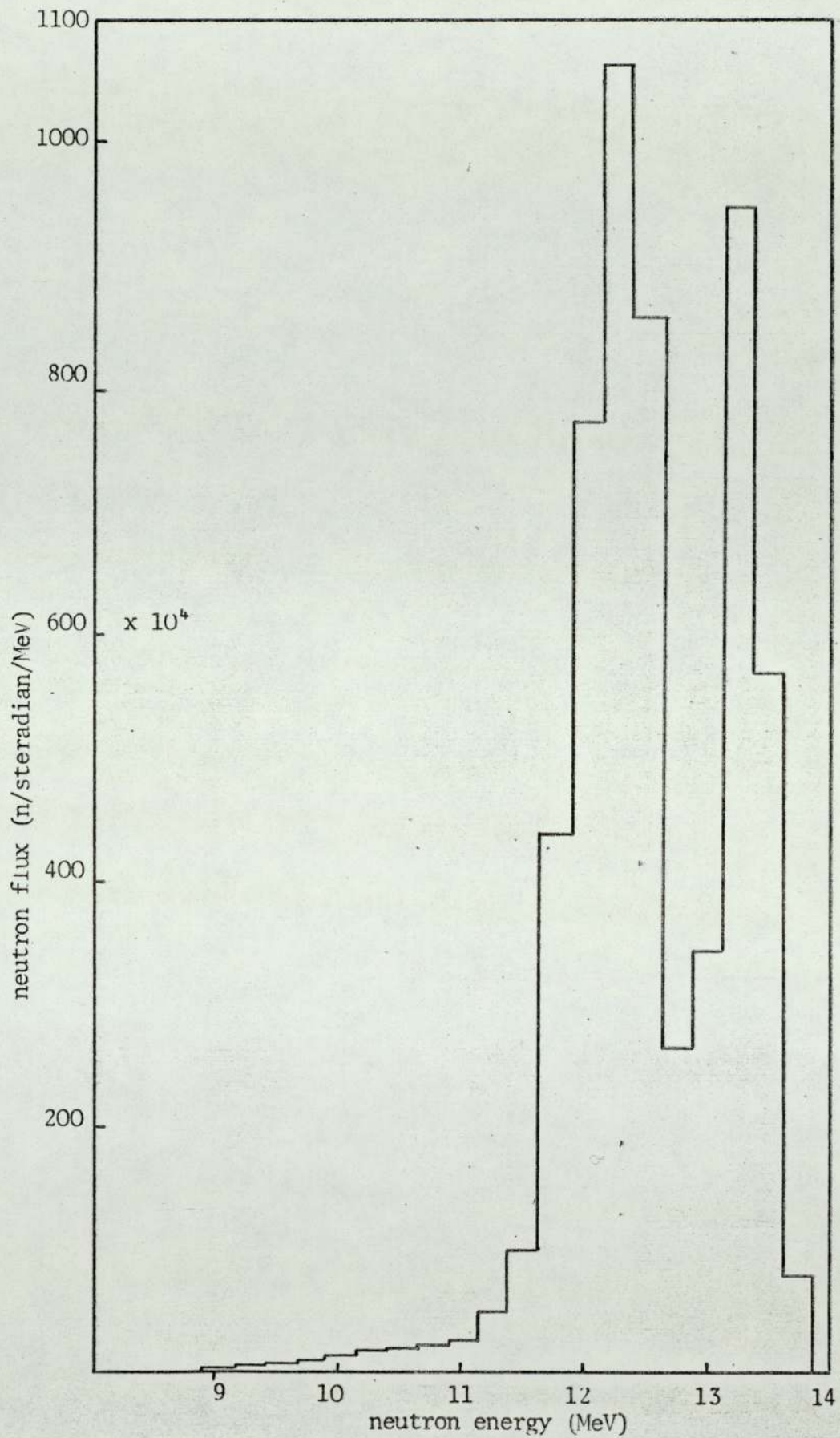


Fig. 7.23 Total flux from LiF (14cm thick) at angle 60

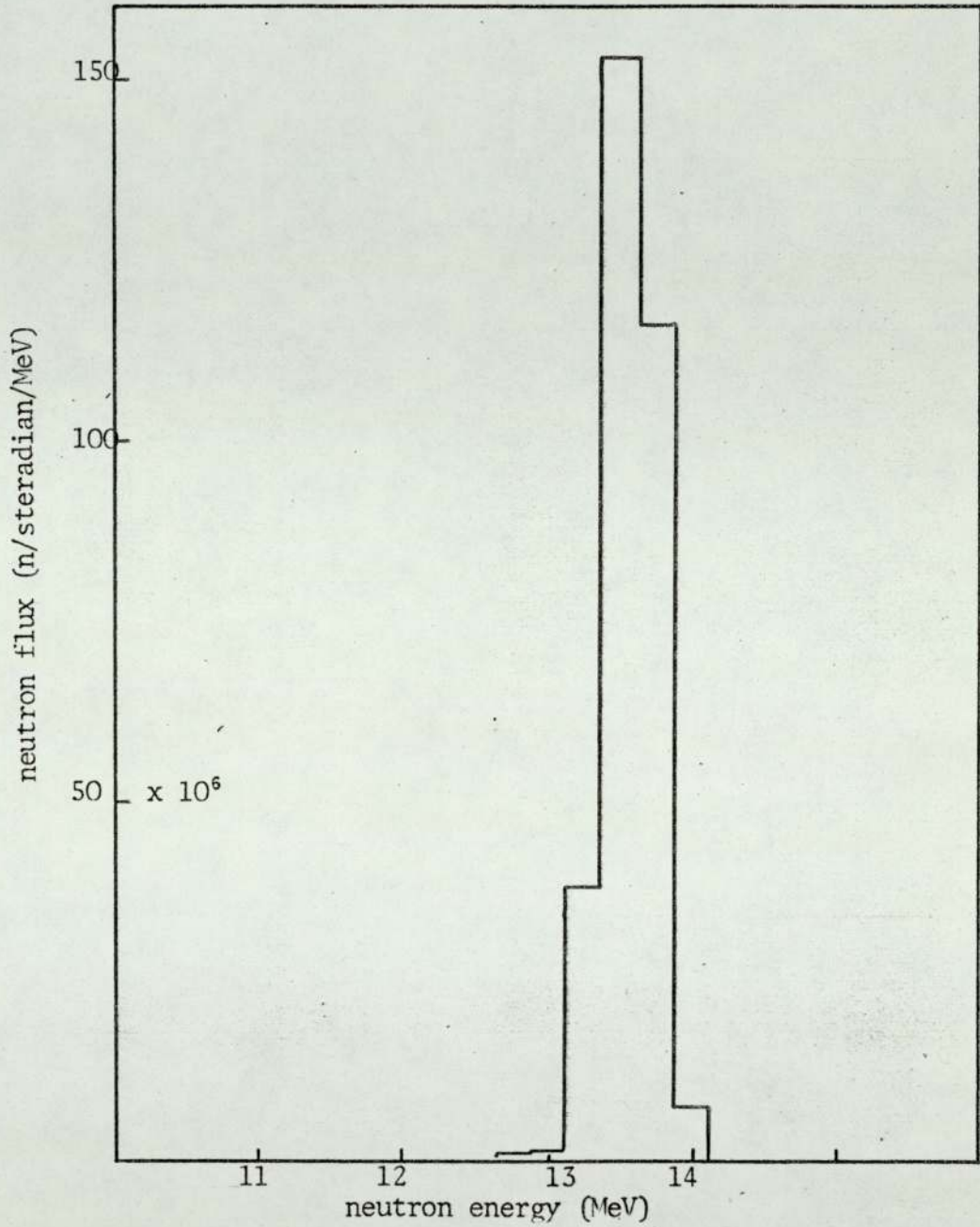
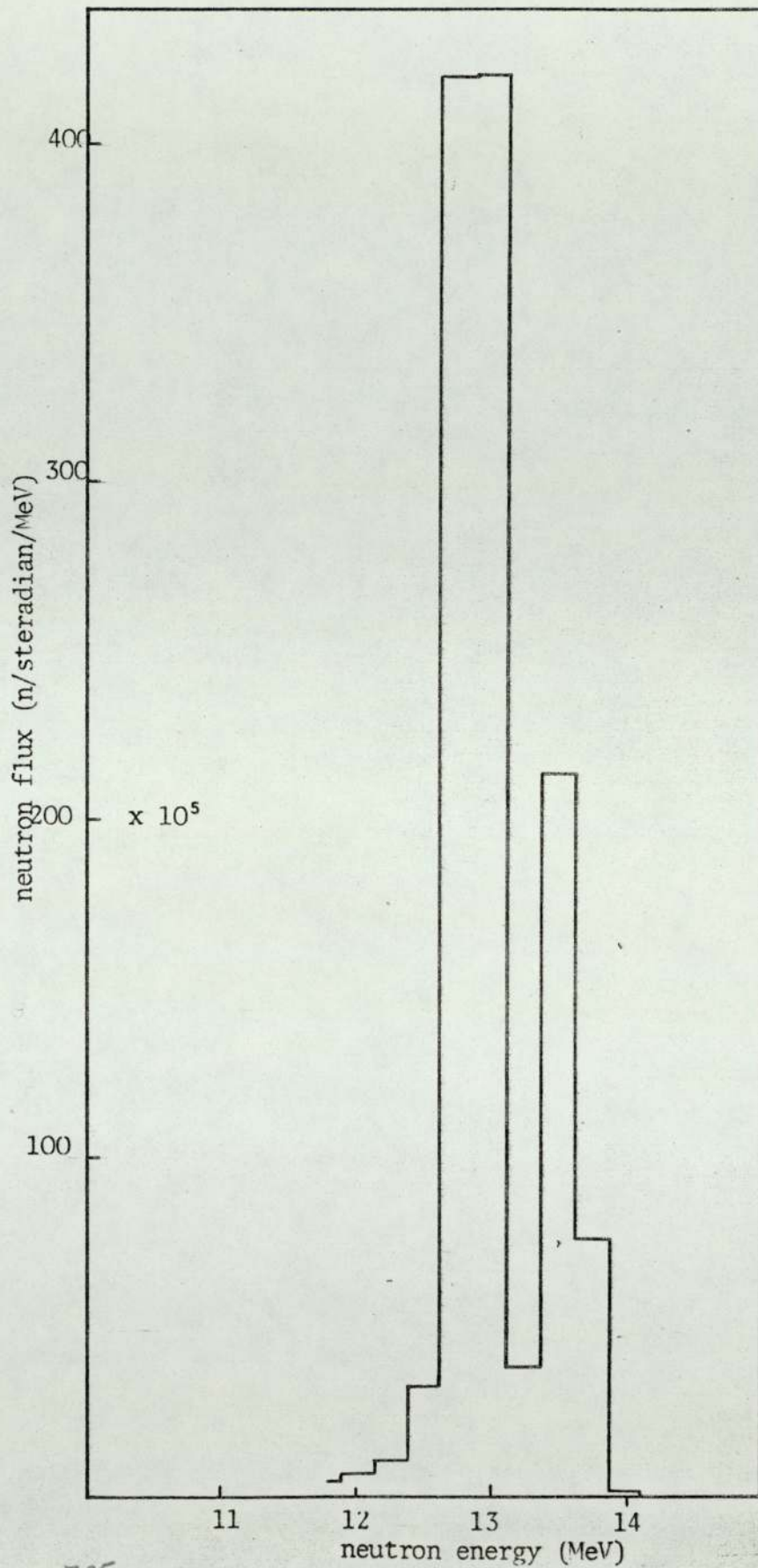


Fig. 7.24 Total flux from LiF (6.35cm thick) at angle $\theta 30$



7.25
 Fig. Total flux from LiF (6.35cm thick) at angle $\theta=45$

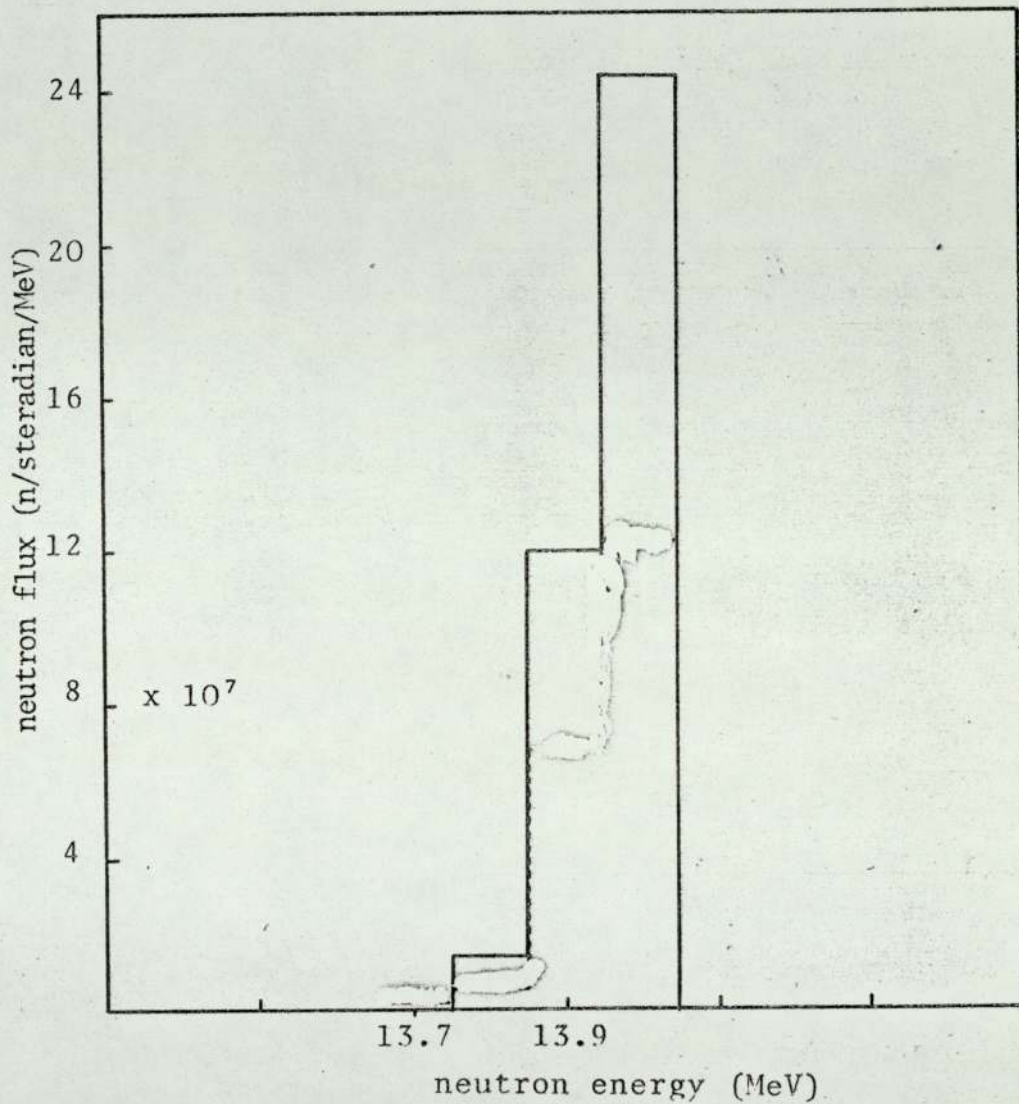


Fig. 7.26 Elastic spectrum from Fe (7.62cm thick) at angle $\theta=30$ (from primary scatter model).

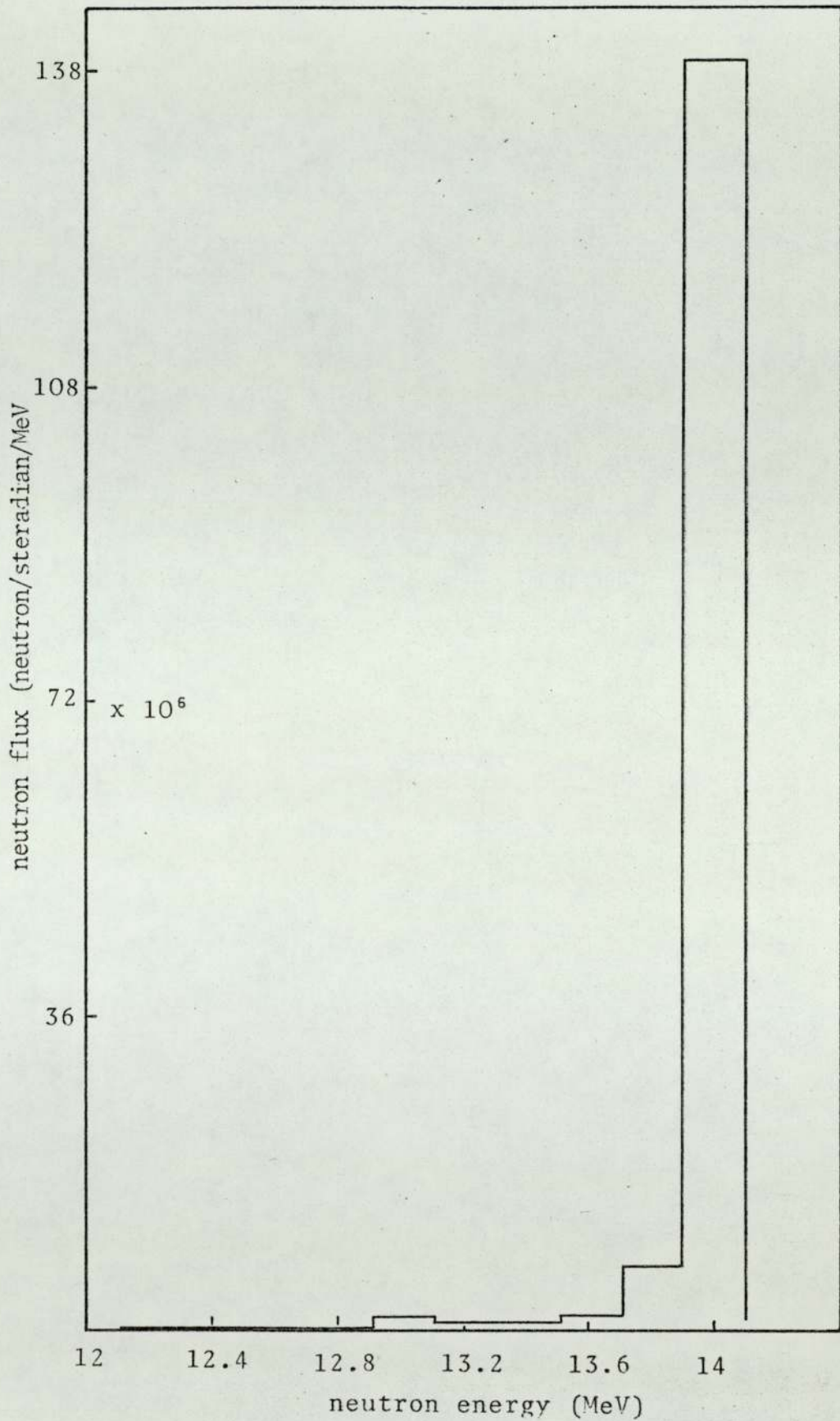


Fig. 7.27 Elastic spectrum from Fe (7.62cm thick) at angle $\theta=30$ (from secondary scatter model)

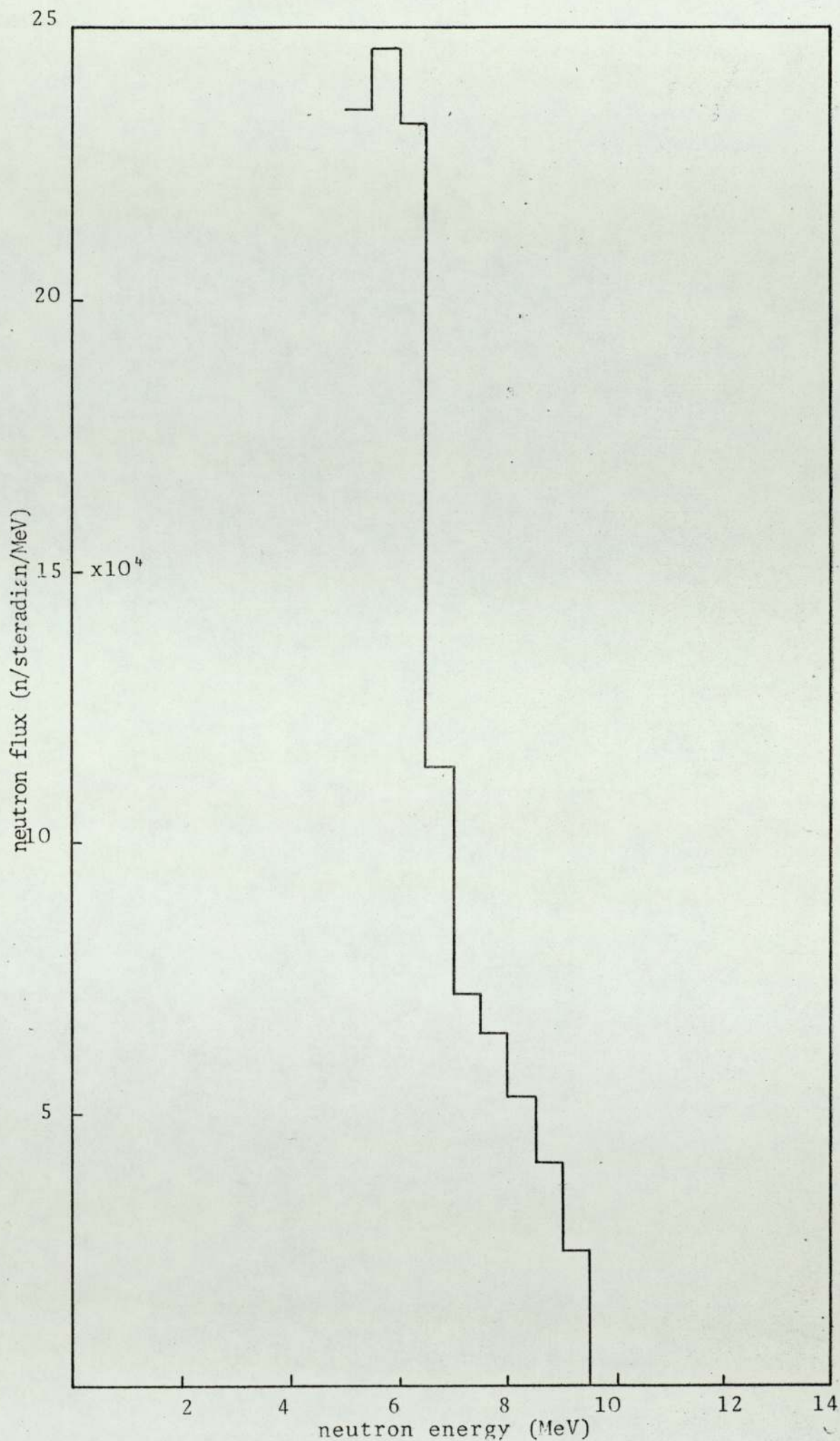
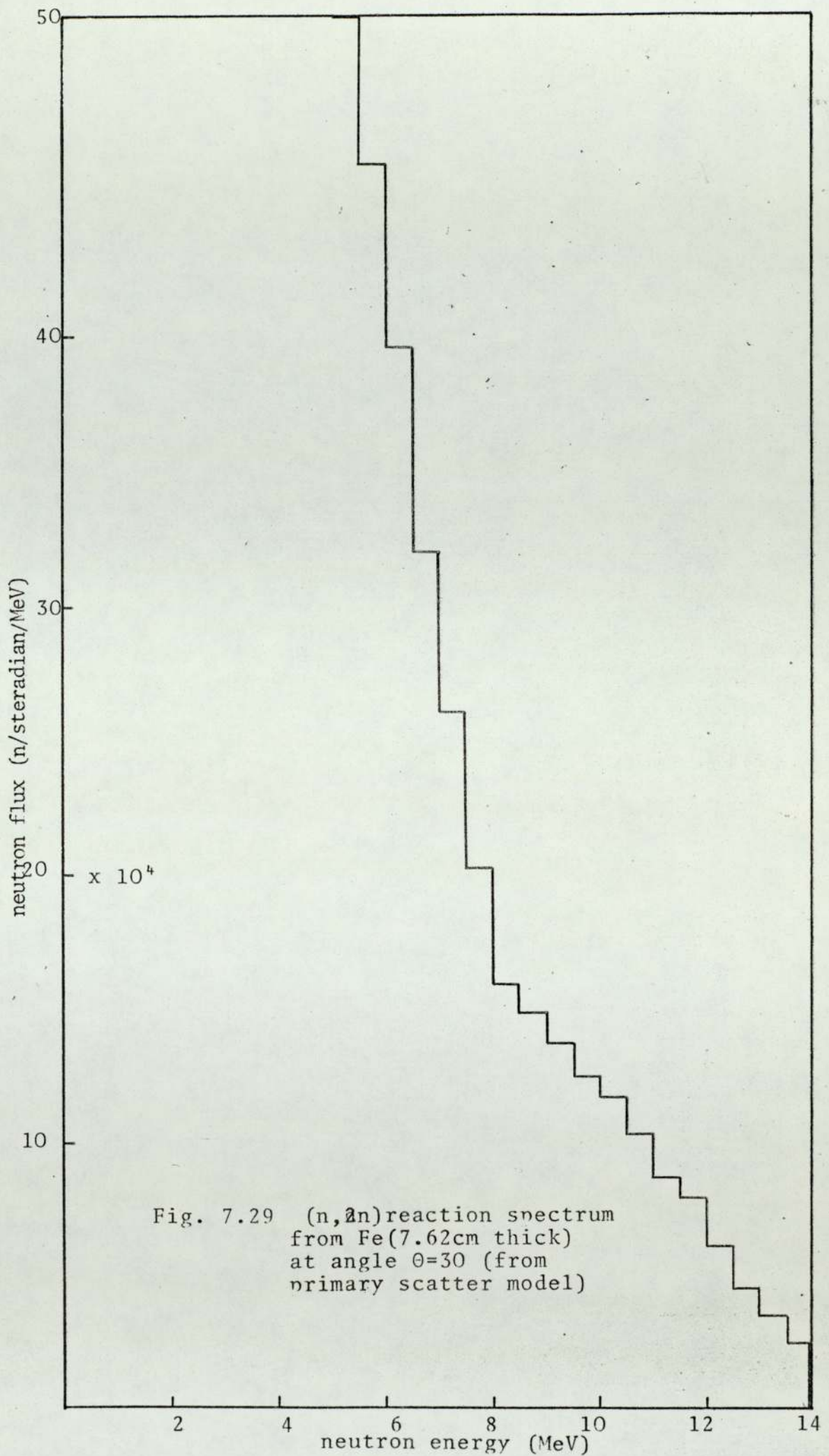


Fig. 7.28 (n, n') reaction spectrum from Fe (7.62 cm thick) at angle $\theta = 30^\circ$ (from primary scatter model)



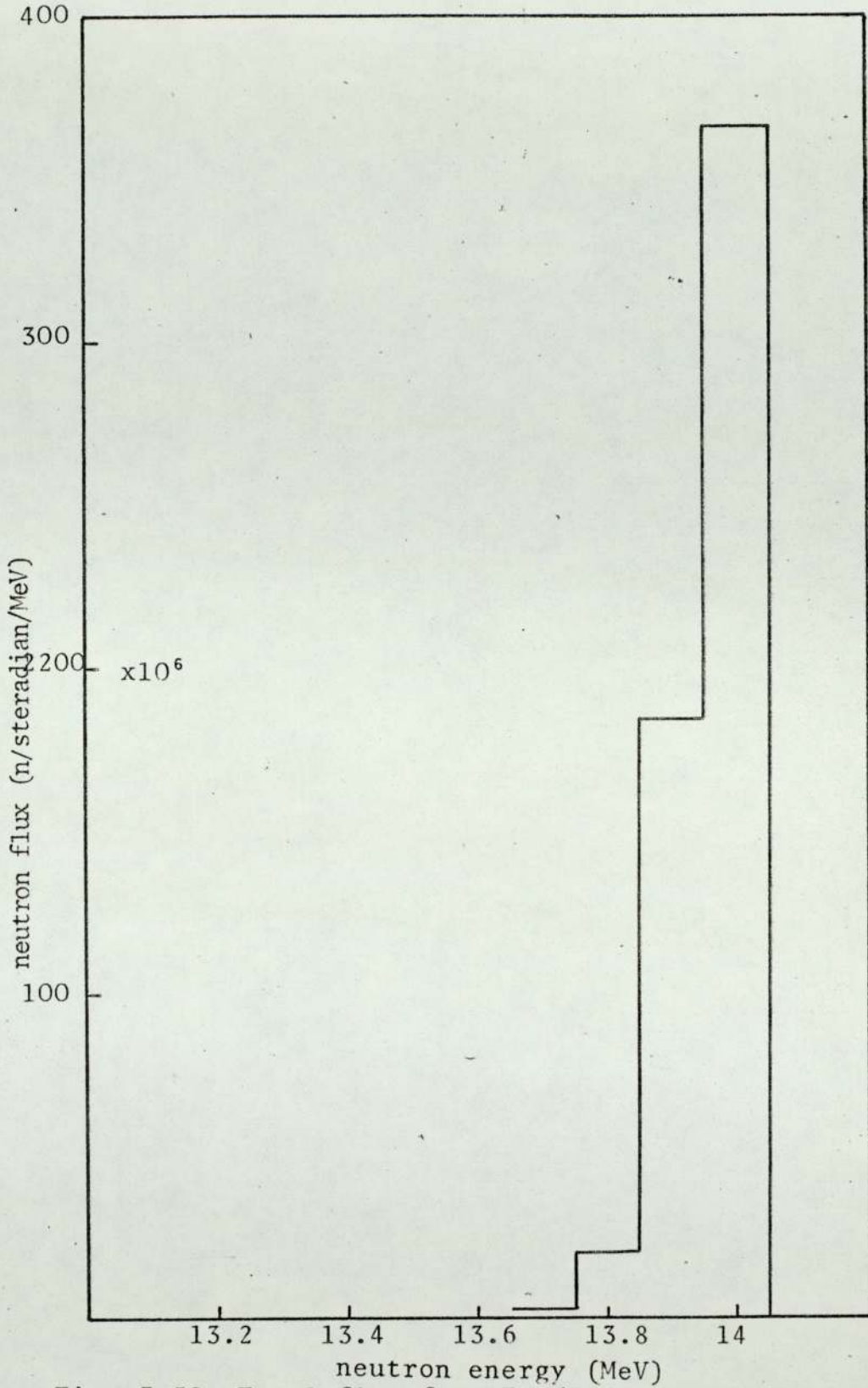


Fig. 7.30 Total flux from Fe (7.62cm thick) at angle $\theta=30$

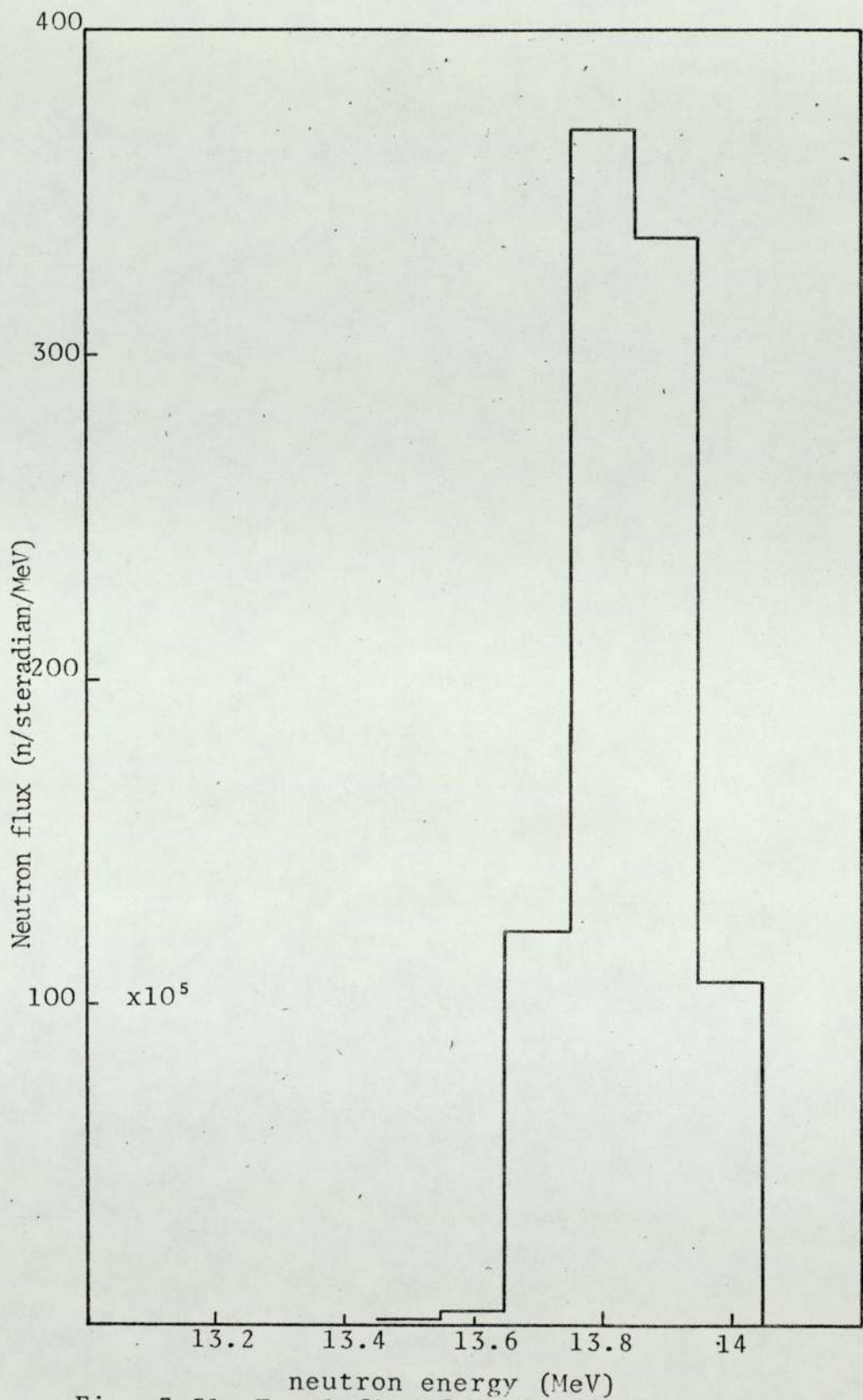


Fig. 7.31 Total flux from Fe (7.62cm thick) at angle $\theta=45$

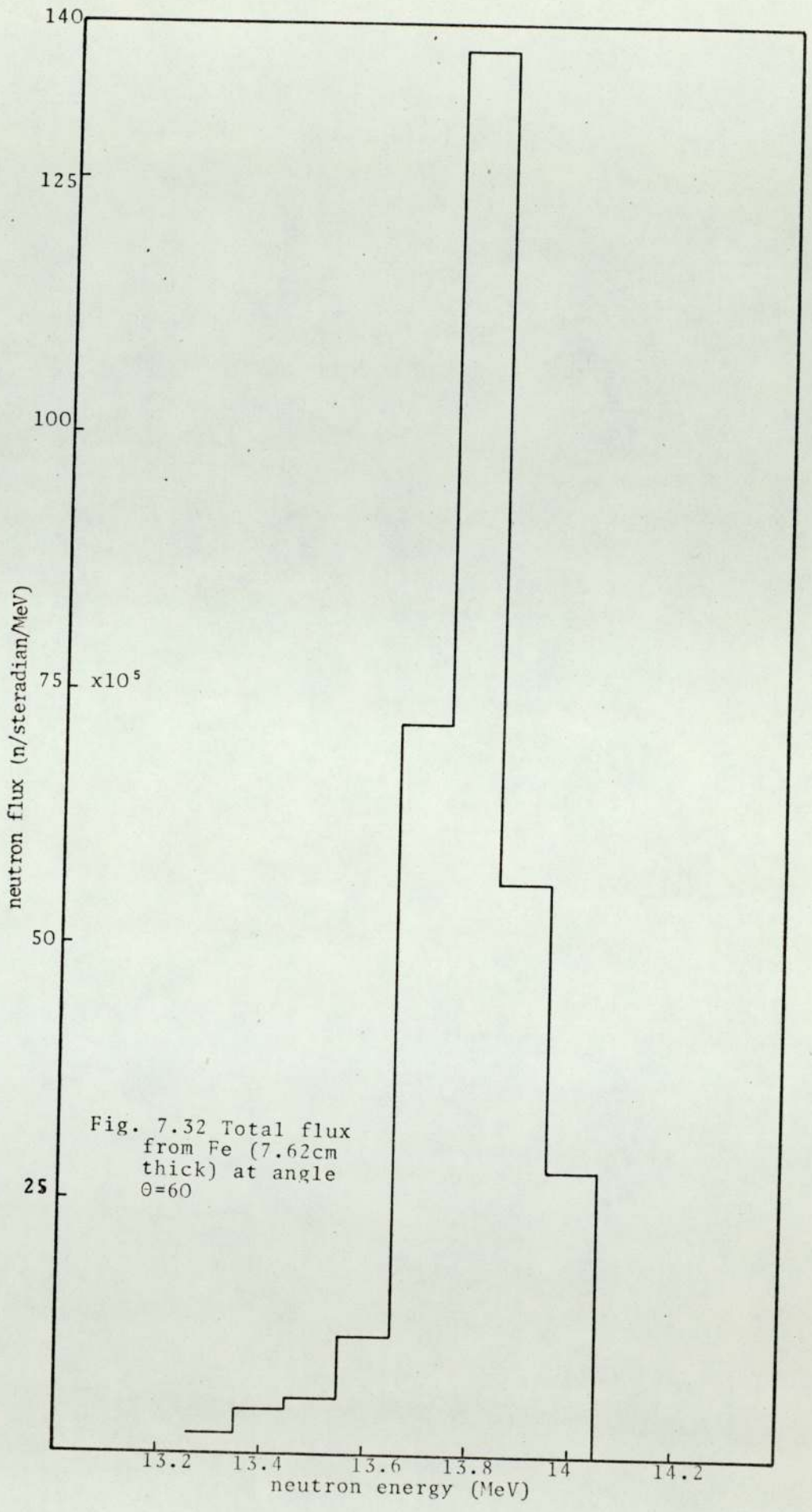


Fig. 7.32 Total flux from Fe (7.62cm thick) at angle $\theta=60$

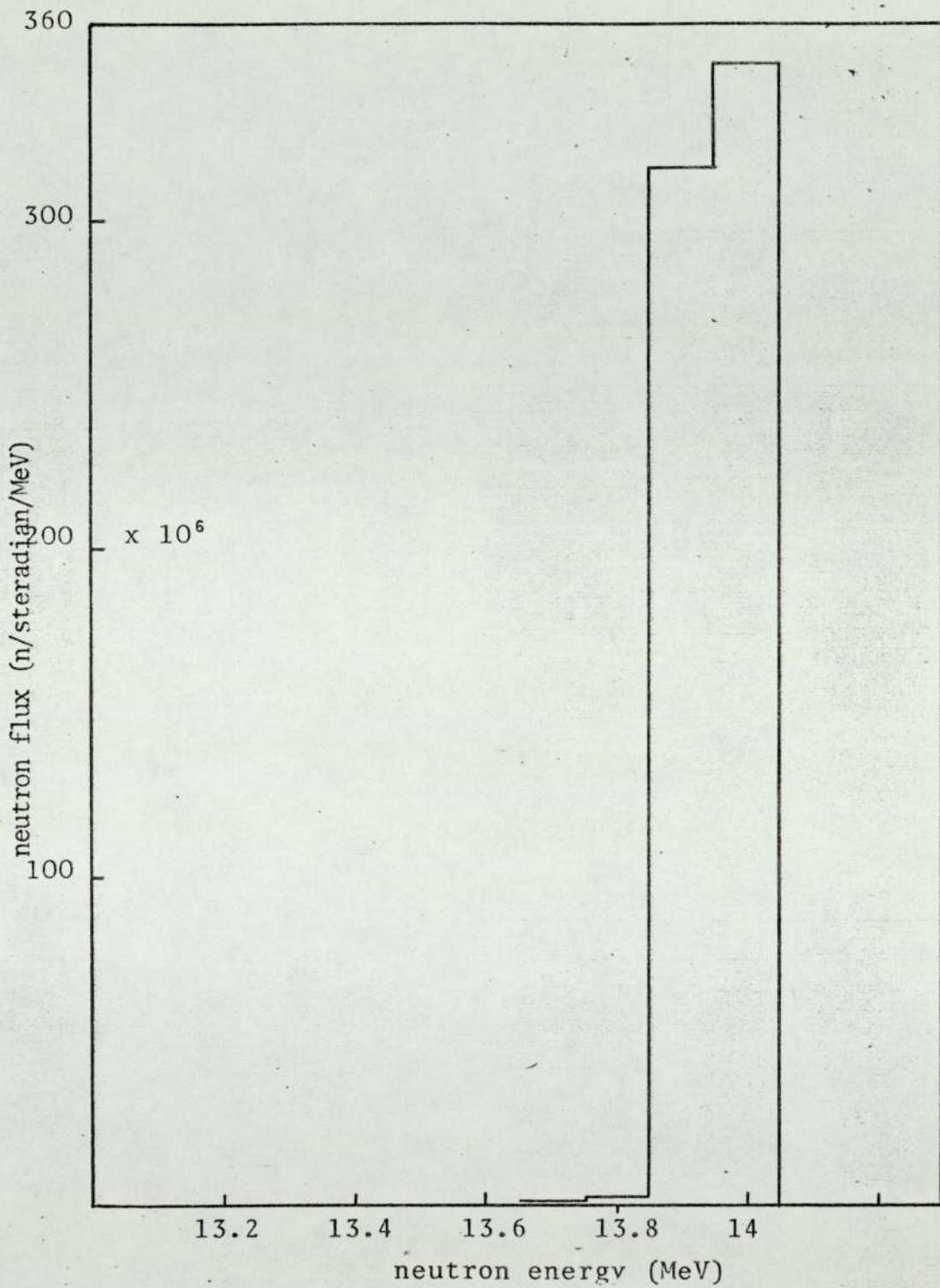
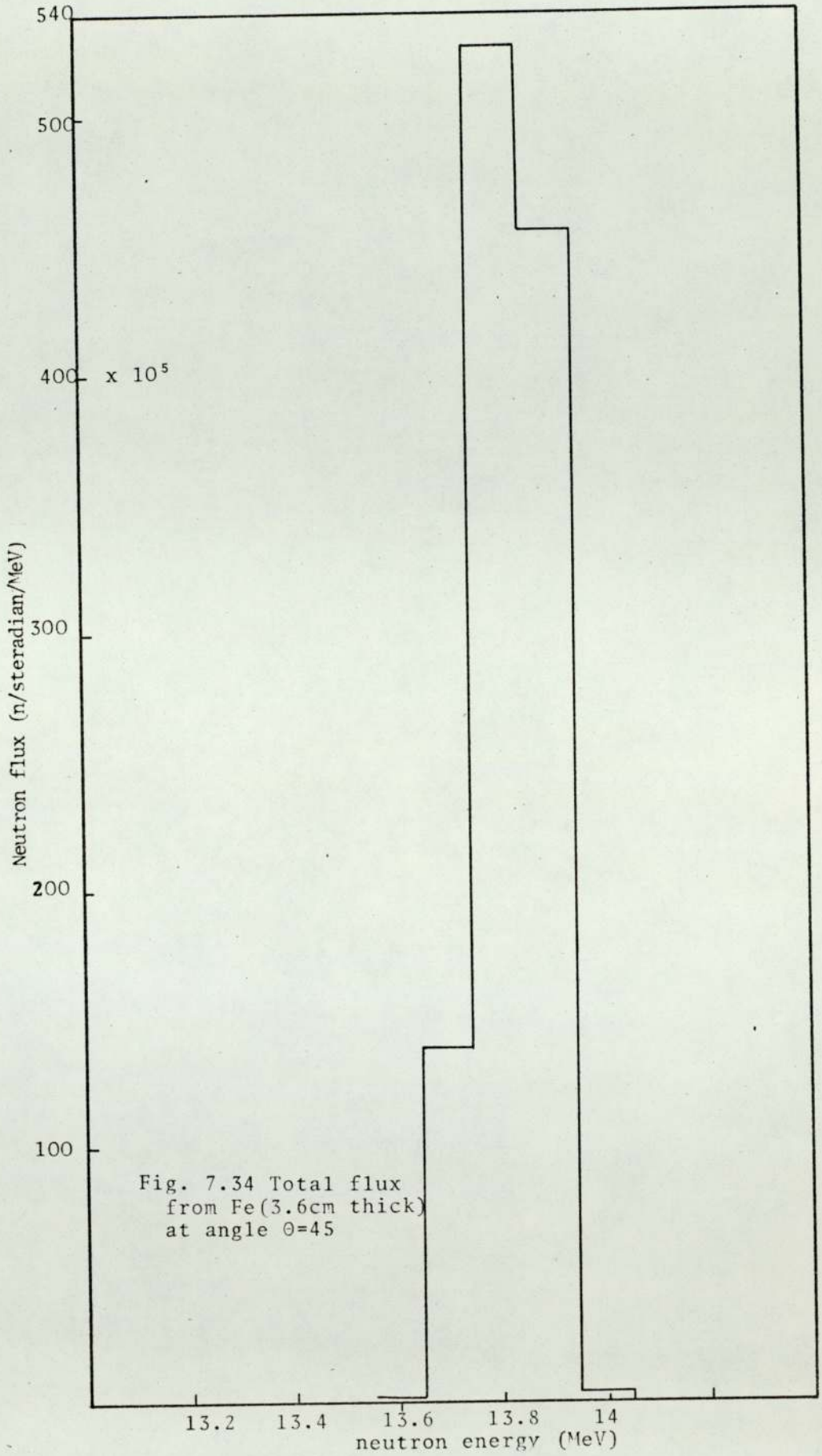


Fig. 7.33 Total flux from Fe (3.6cm thick) at angle $\theta=30$



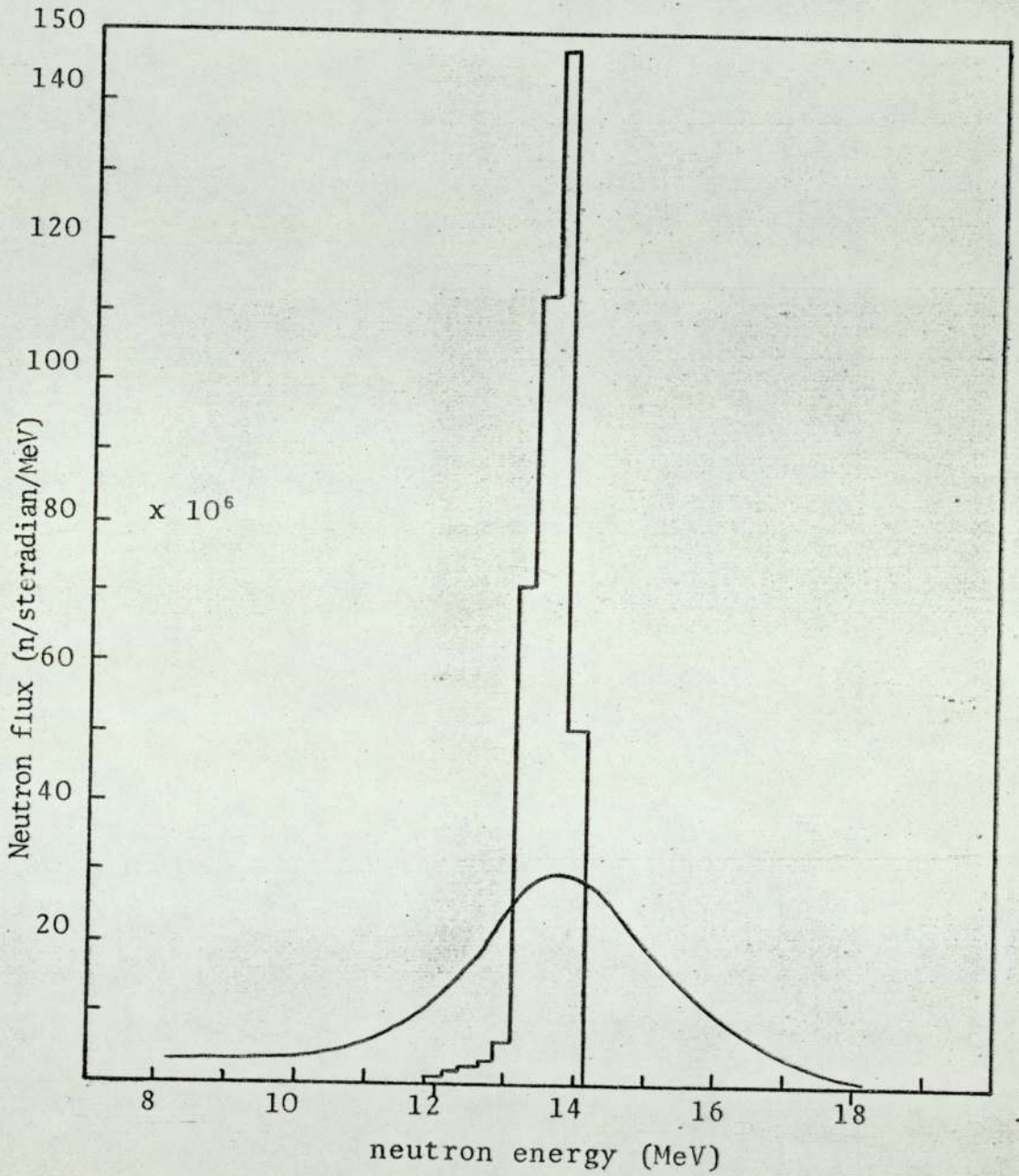


Fig. 7.35 Theoretical and experimental spectra from LiF (14cm thick) at angle $\theta=30^\circ$

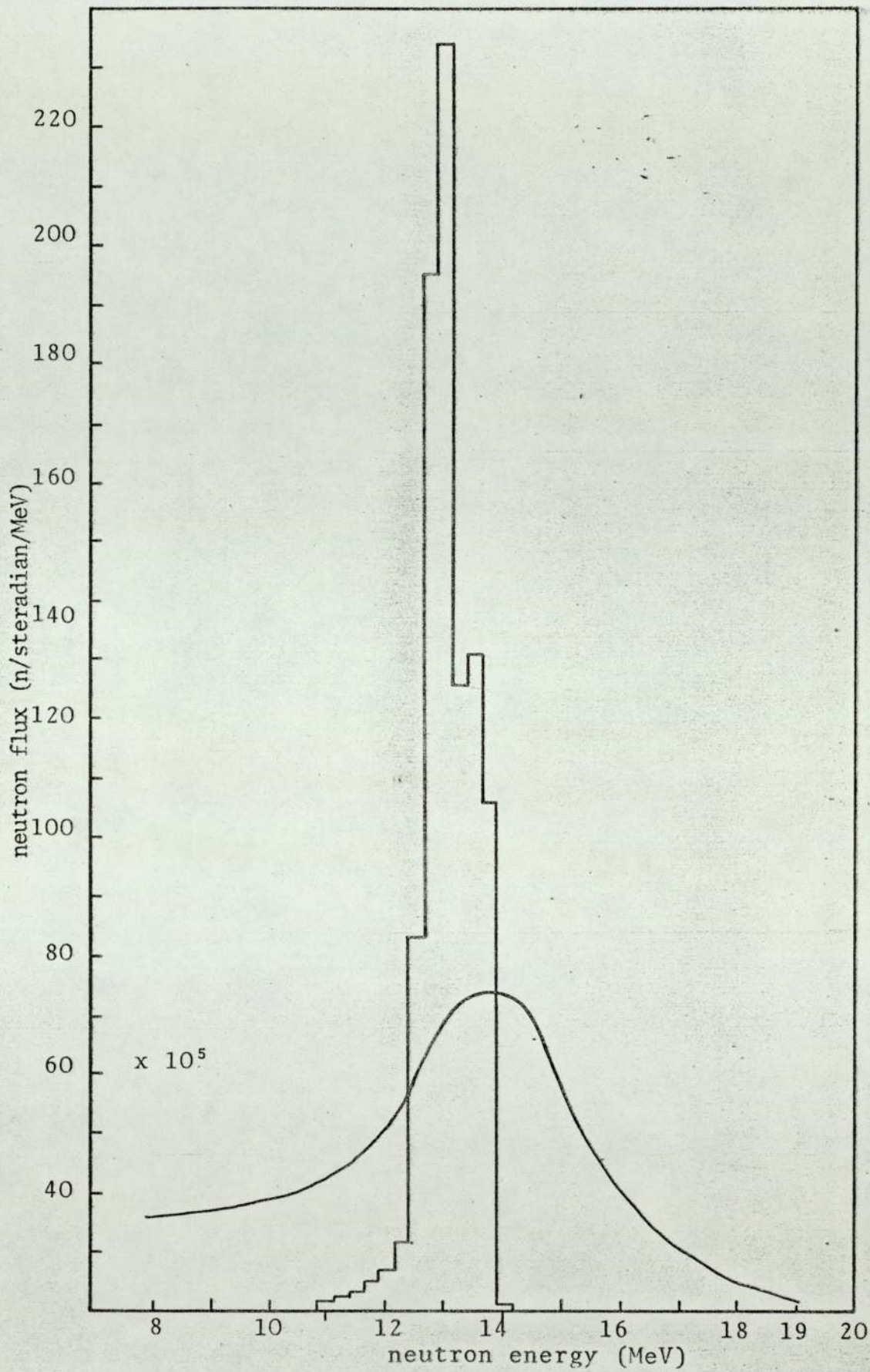


Fig. 7.36 Theoretical and experimental spectra from LiF (14cm thick) at angle $\theta=45^\circ$

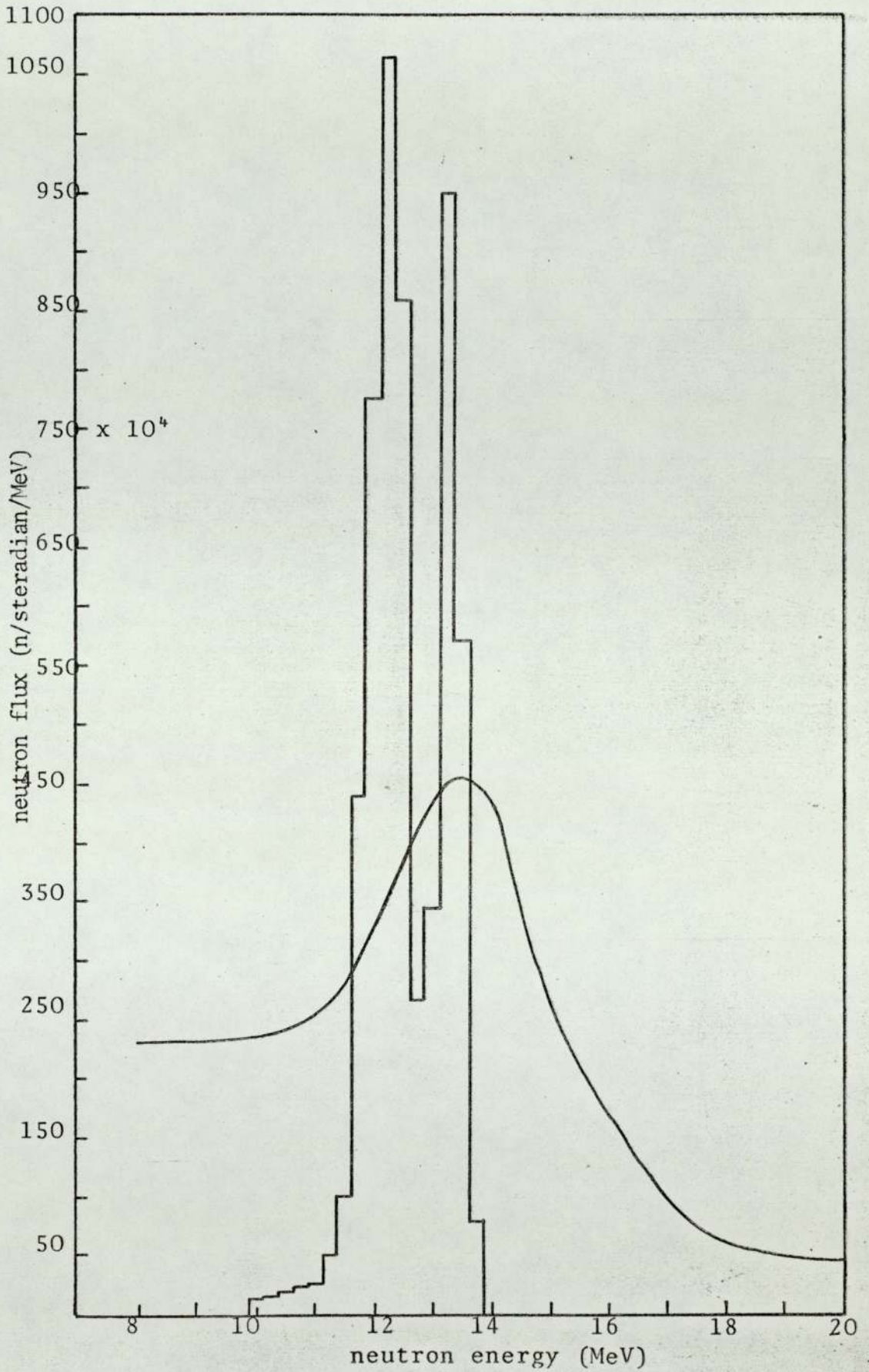


Fig. 7.37 Theoretical and experimental spectra from LiF (14cm thick) at angle $\theta=60$

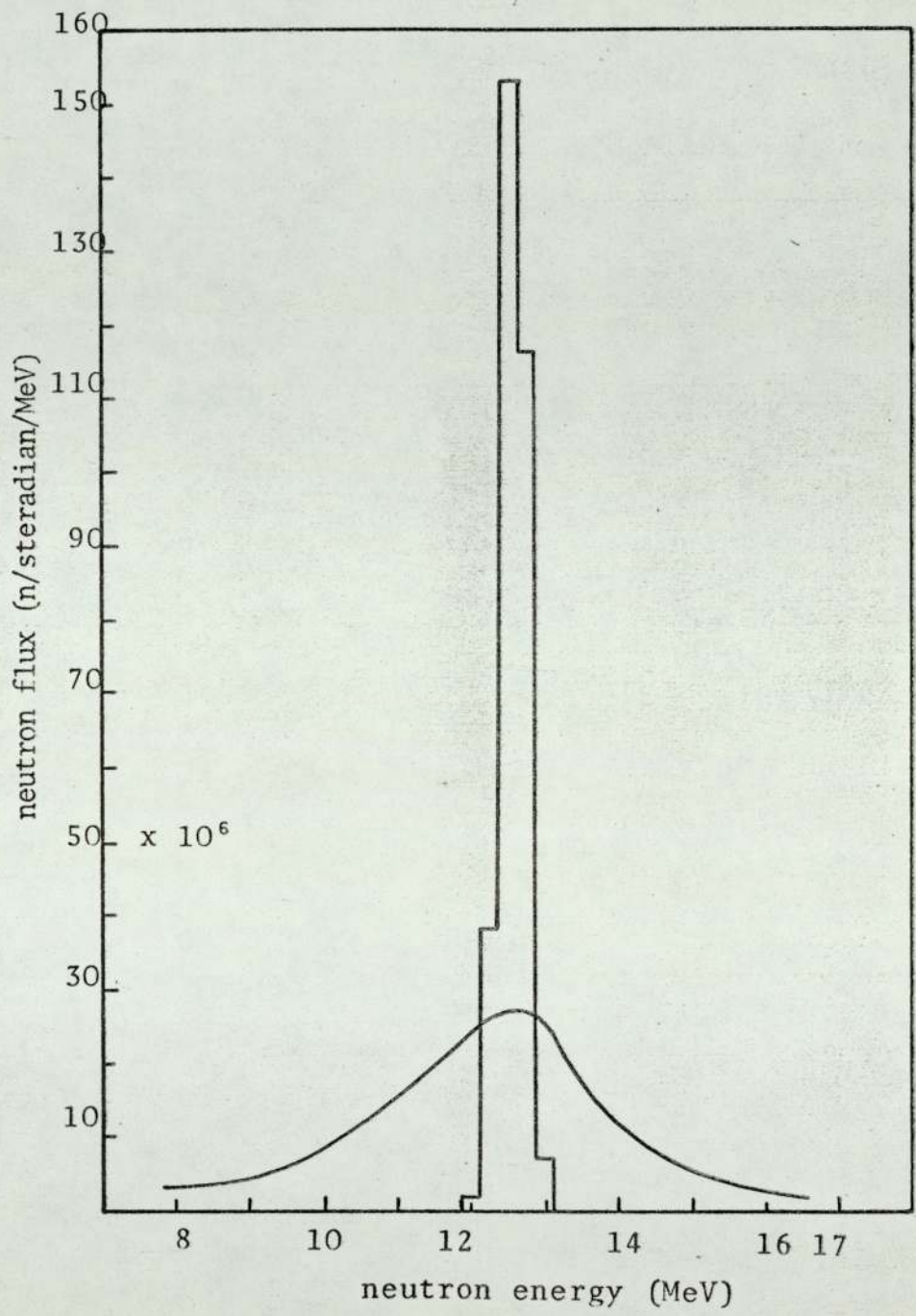


Fig. 7.38 Theoretical and Experimental spectra from LiF (6.35cm thick) at angle $\theta=30$

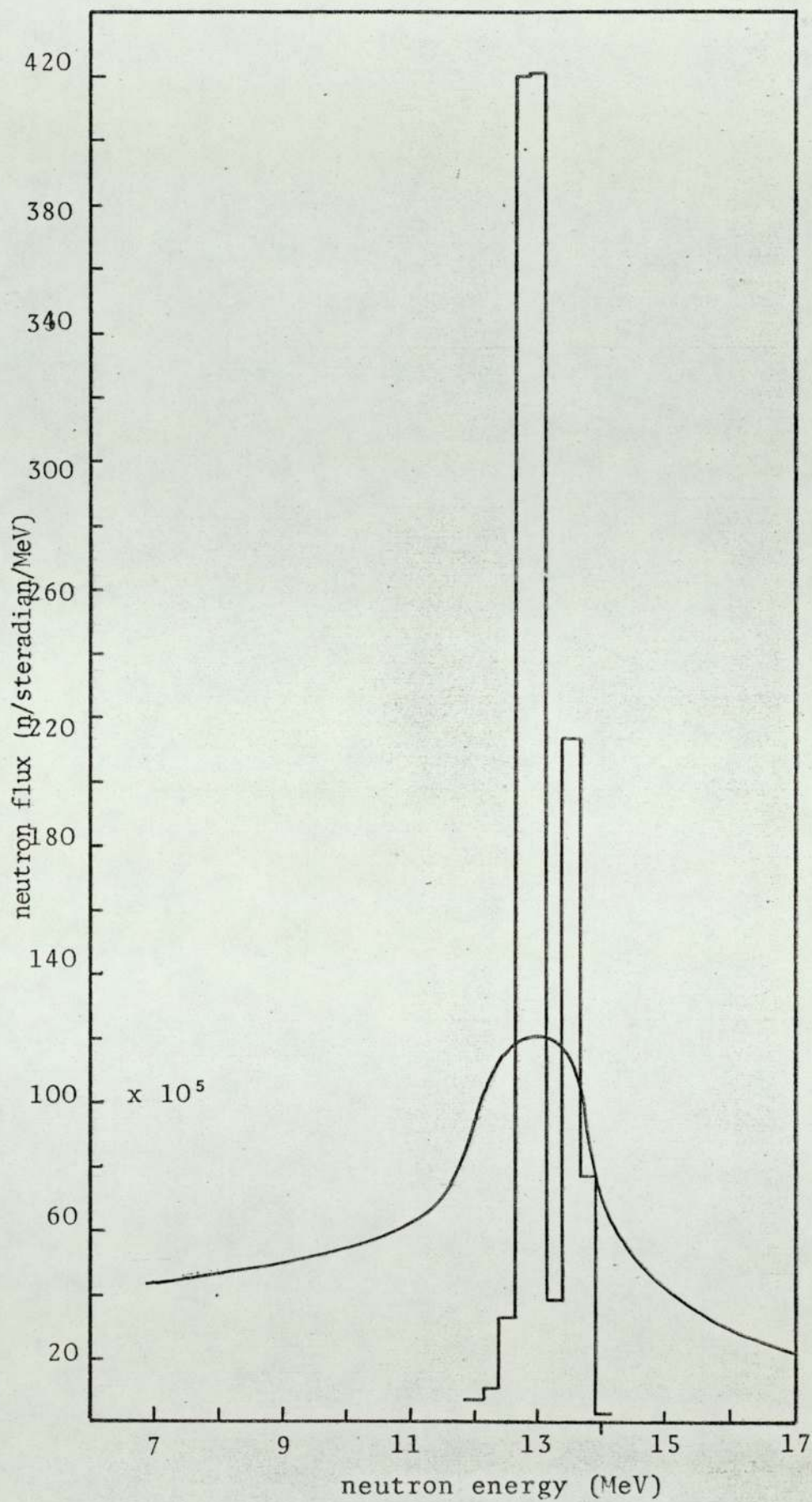


Fig. 7.39 Theoretical and experimental spectra from LiF (6.35cm thick) at angle $\theta=45$

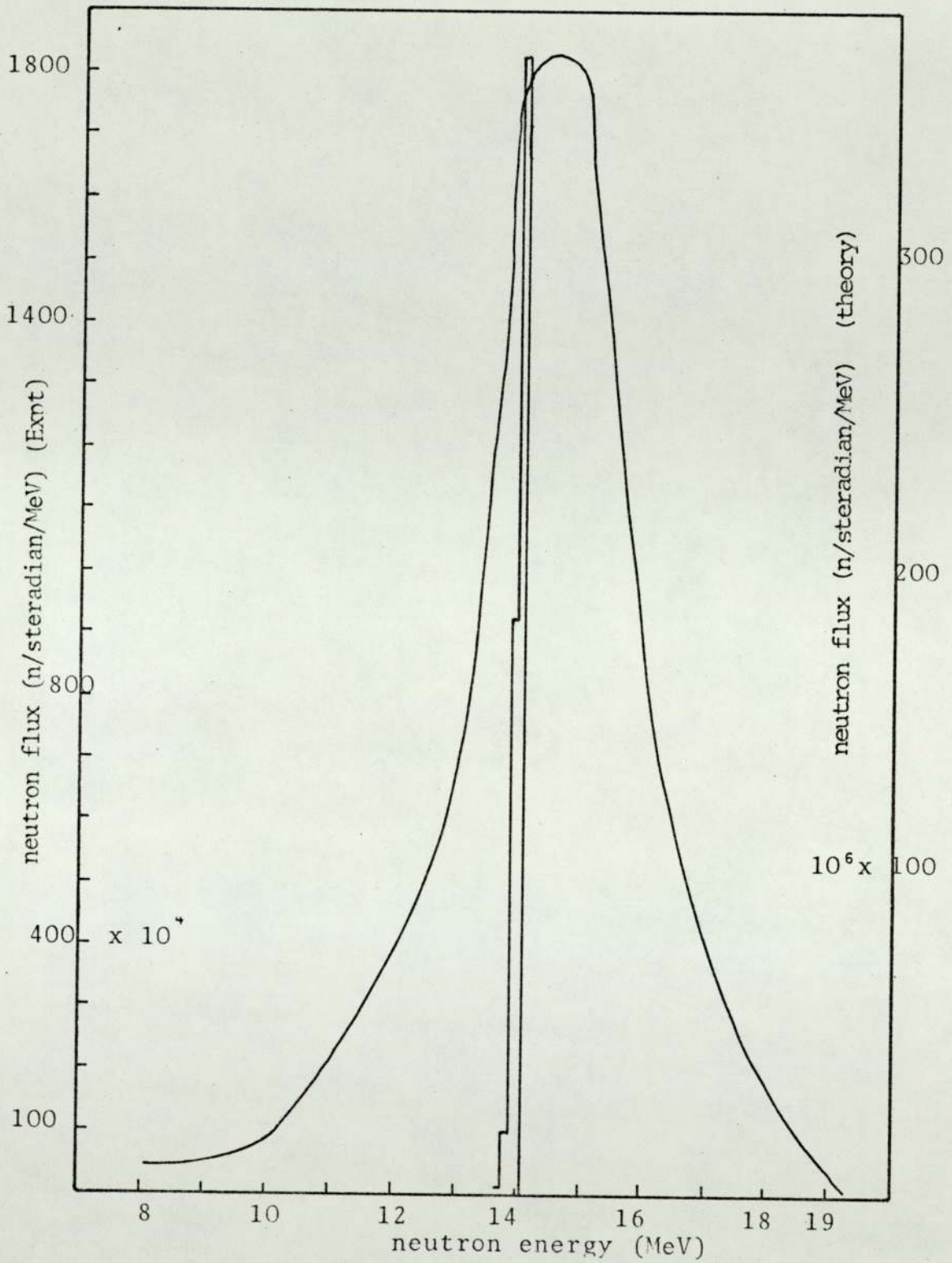


Fig. 7.40 Theoretical and experimental spectra from Fe (7.62)cm thick) at angle $\theta=30$

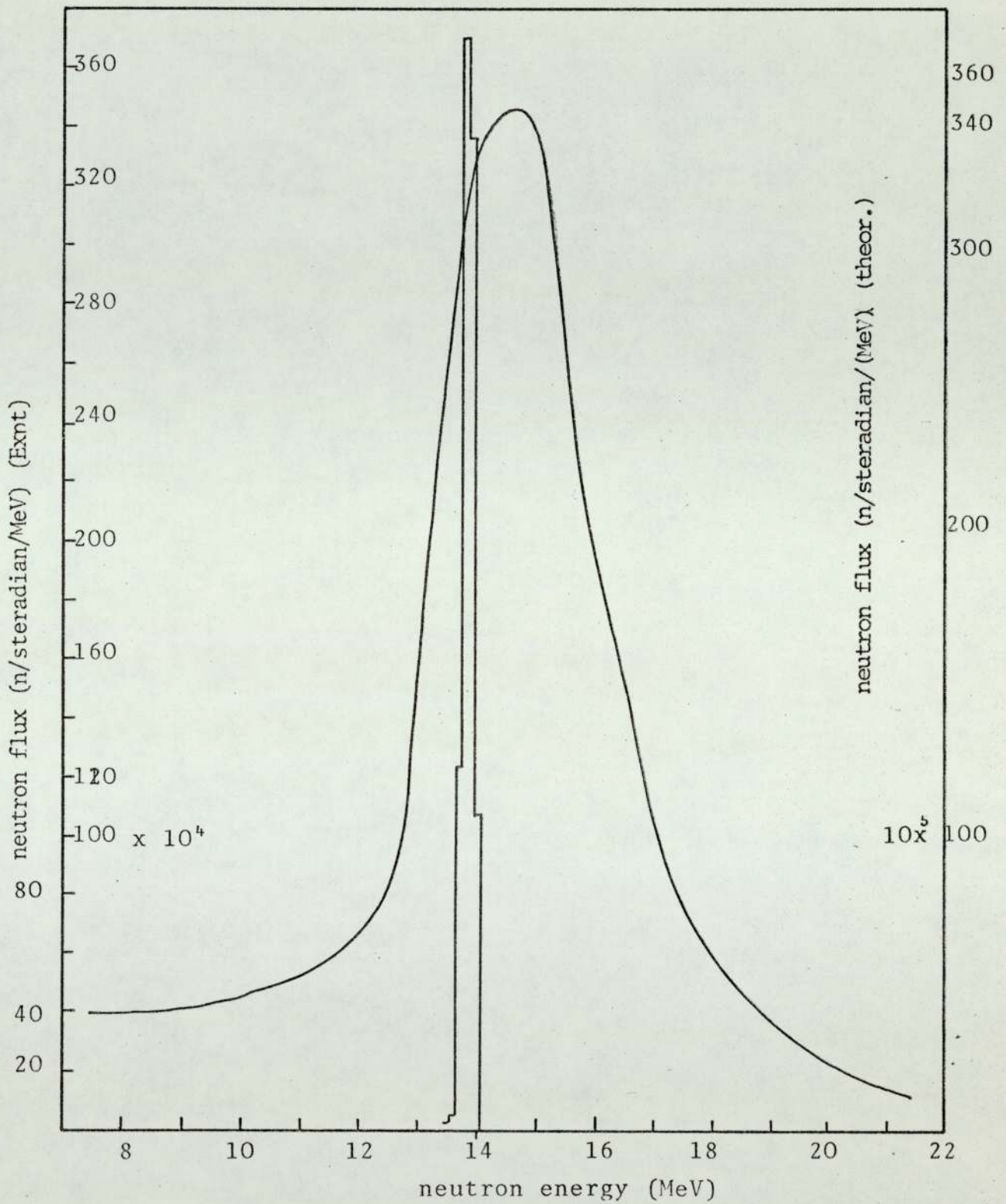
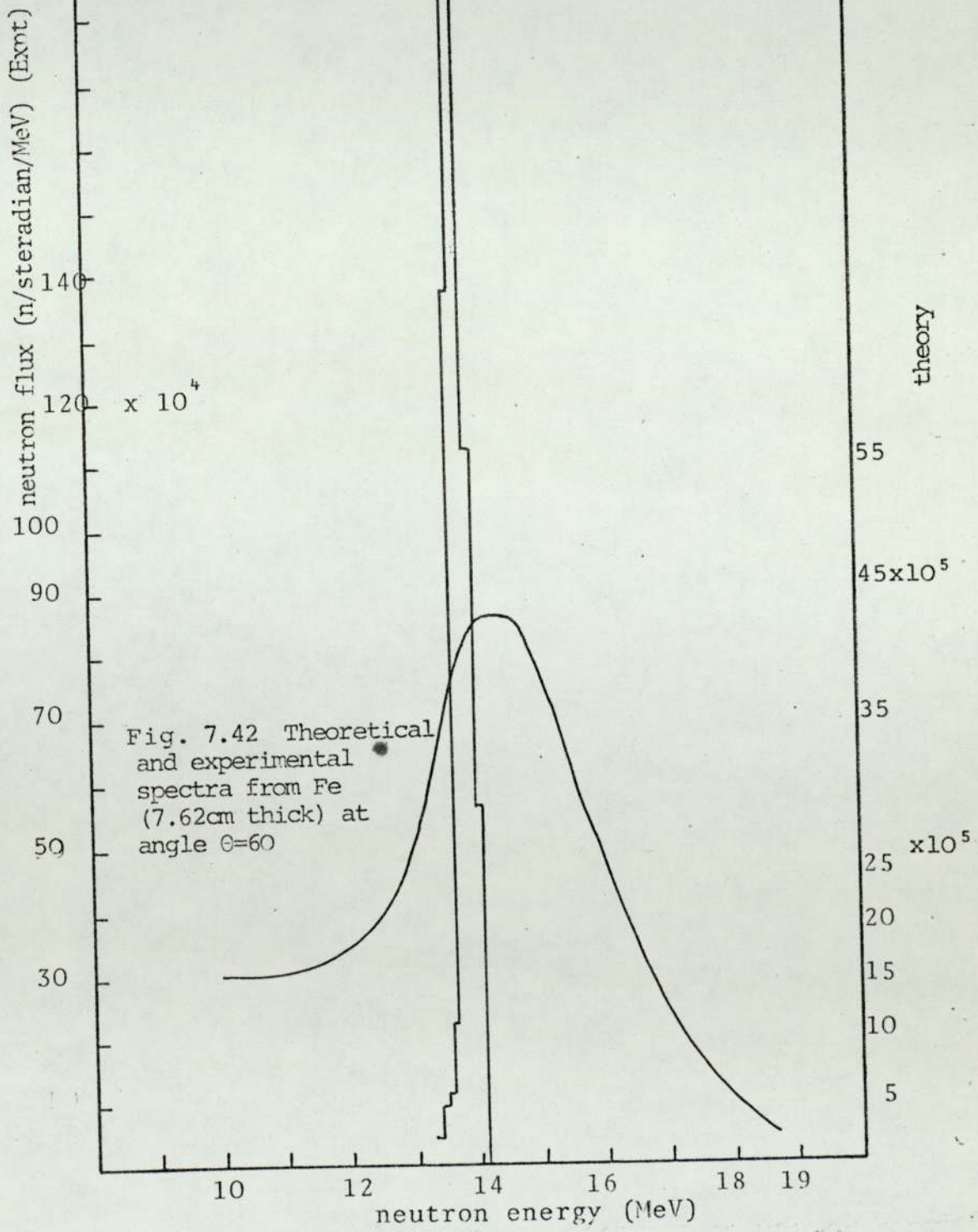


Fig. 7.41 Theoretical and experimental spectra from Fe (7.62cm thick) at angle $\theta=45^\circ$



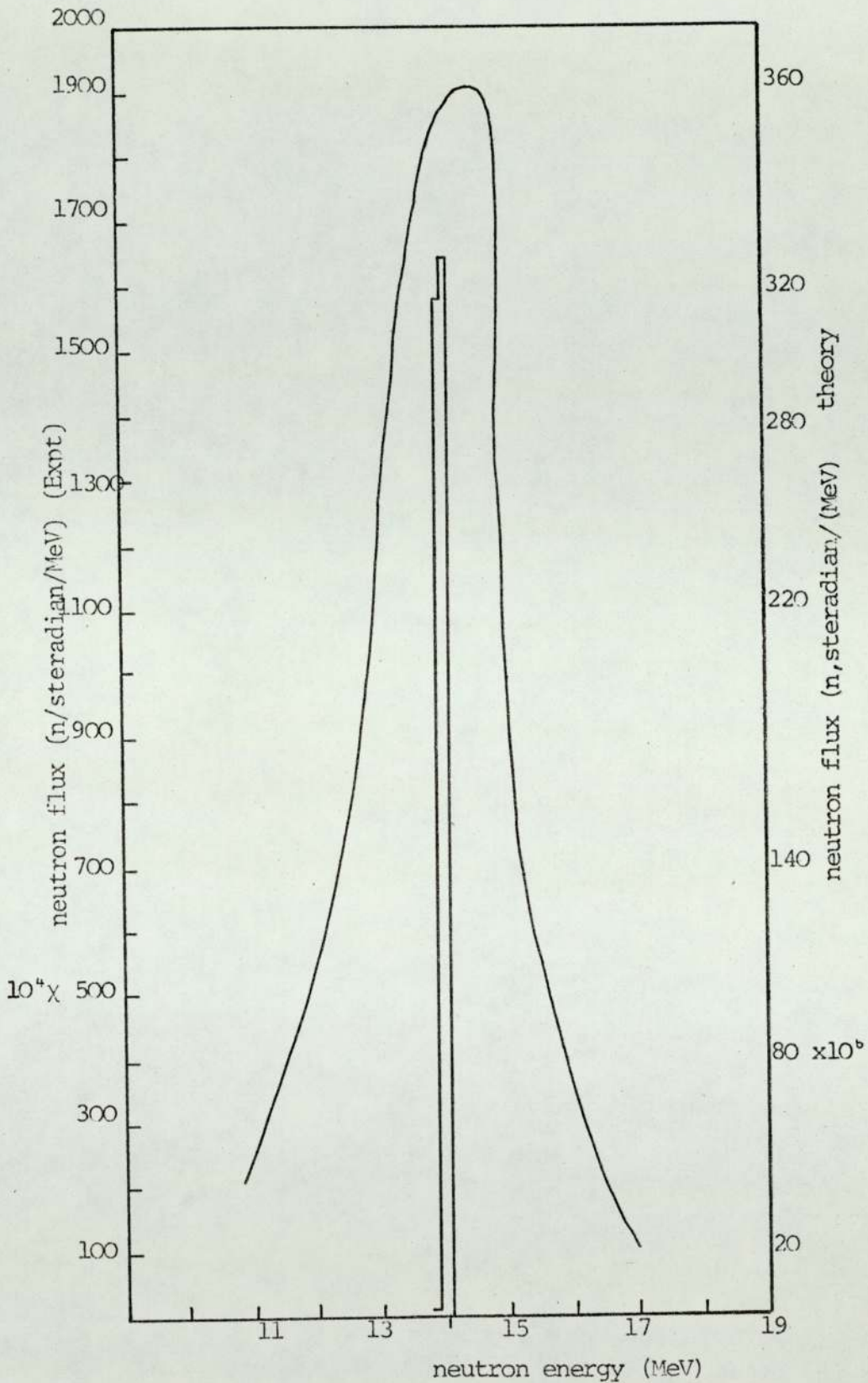
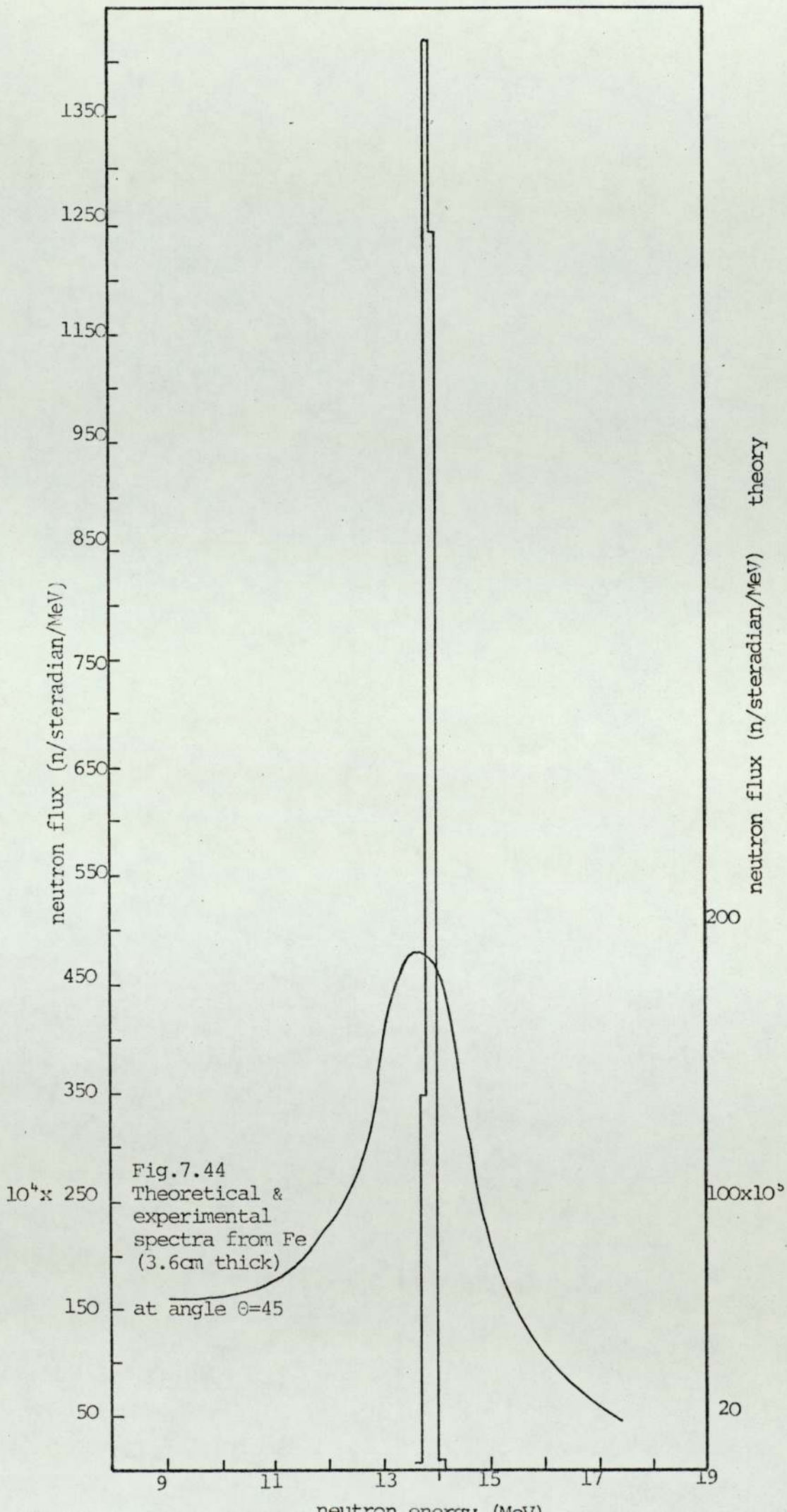


Fig. 7.43 Theoretical and experimental spectra from Fe (3.6cm thick) at angle $\theta = 30$



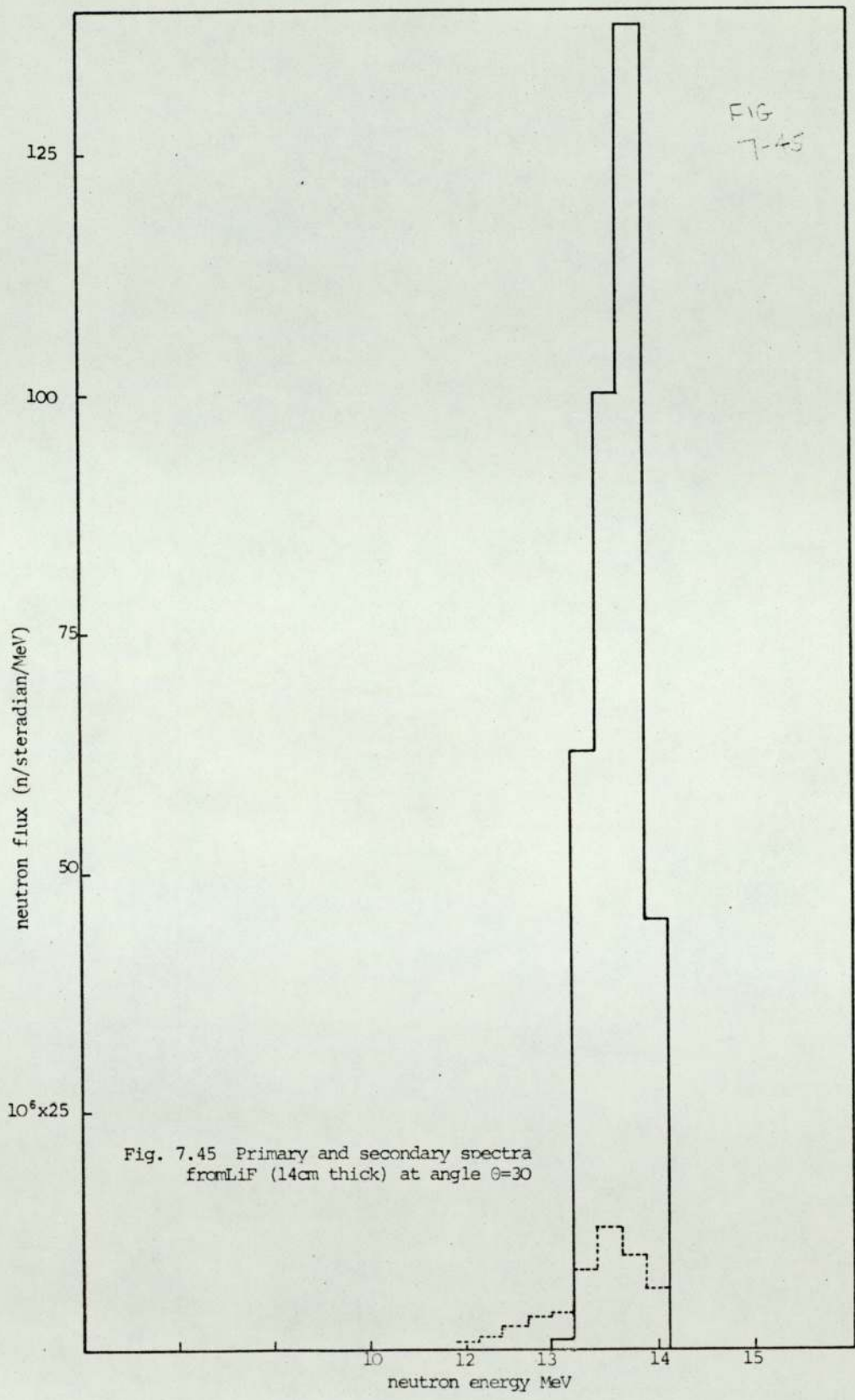


FIG
7-46

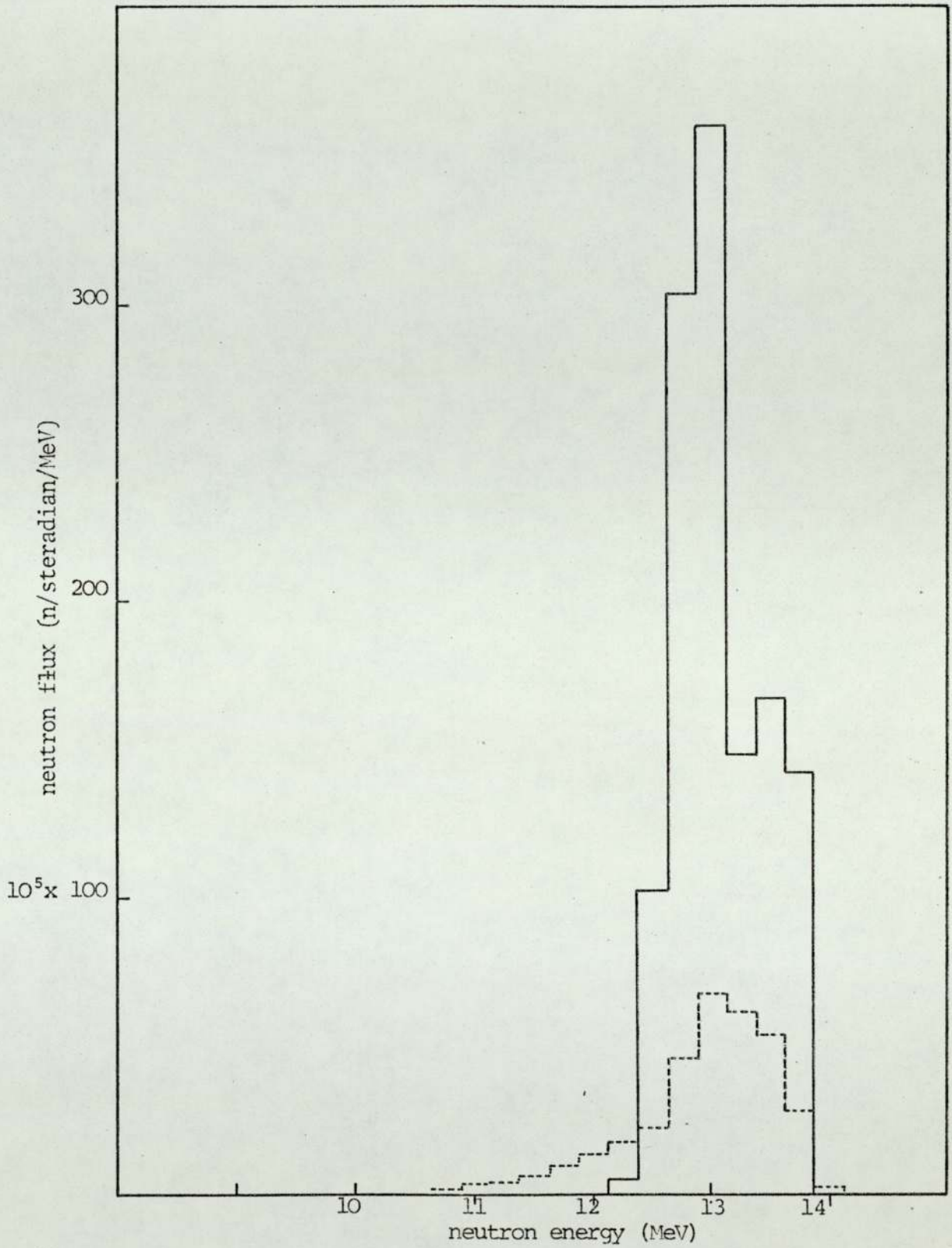


Fig. 7.46 Primary and secondary spectra from LiF (14cm thick) at angle $\theta=45$

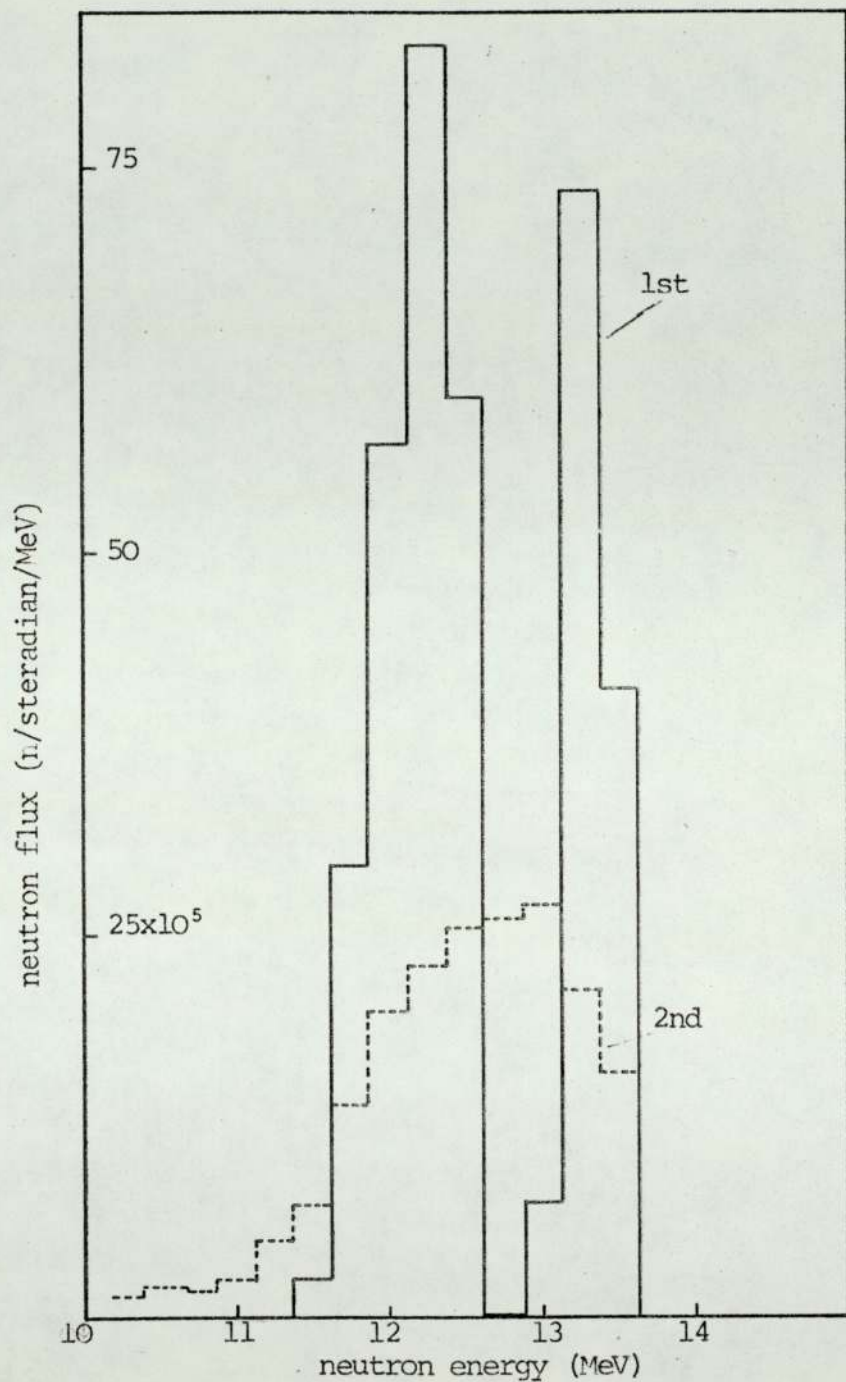


Fig. 7.47 Primary and secondary spectra from LiF (14cm thick) at angle $\theta=60$

FIG
7-48

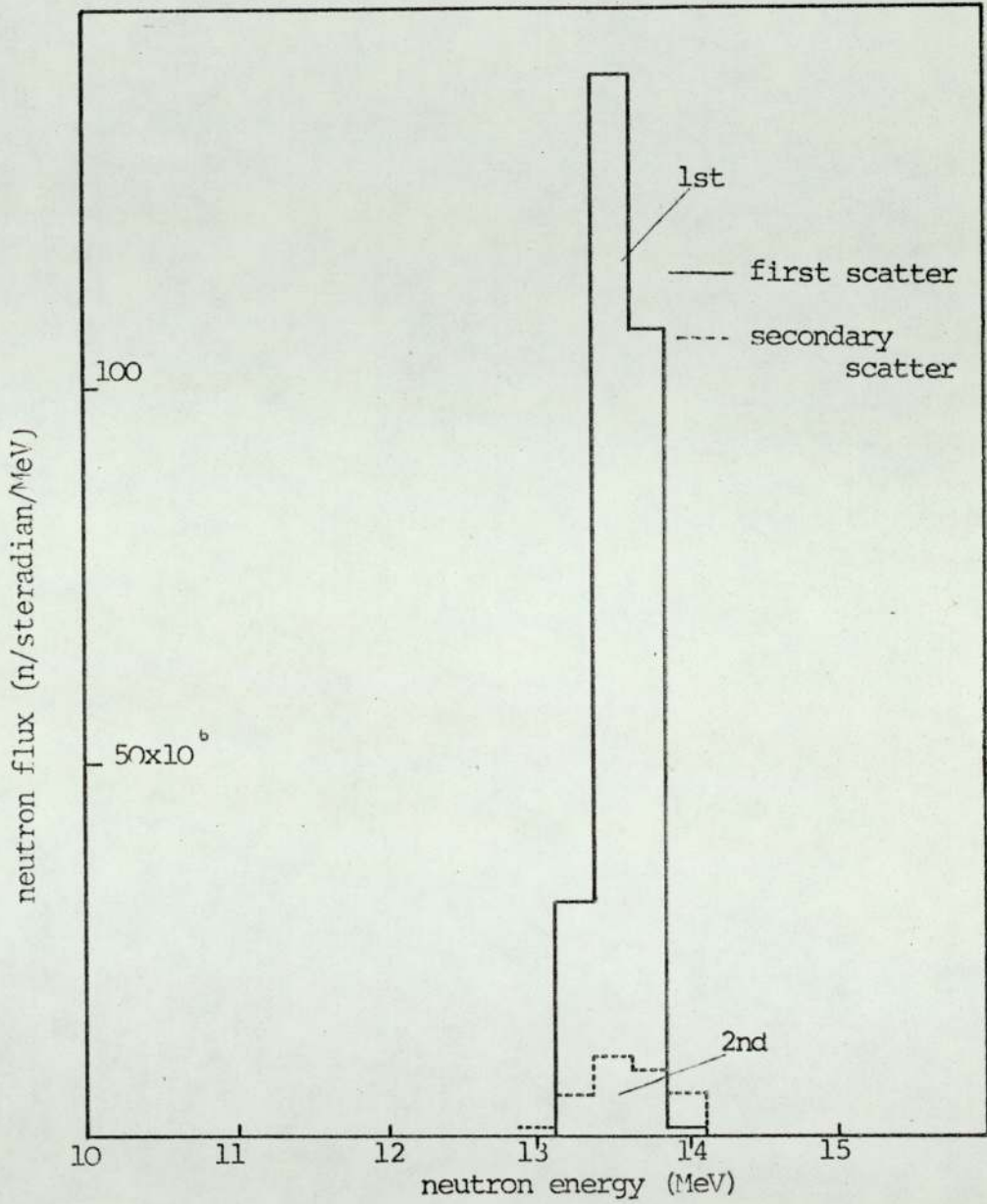


Fig. 7.48 Primary and secondary spectra from LiF (6.35cm thick) at angle $\theta=30$

FIG 7-49

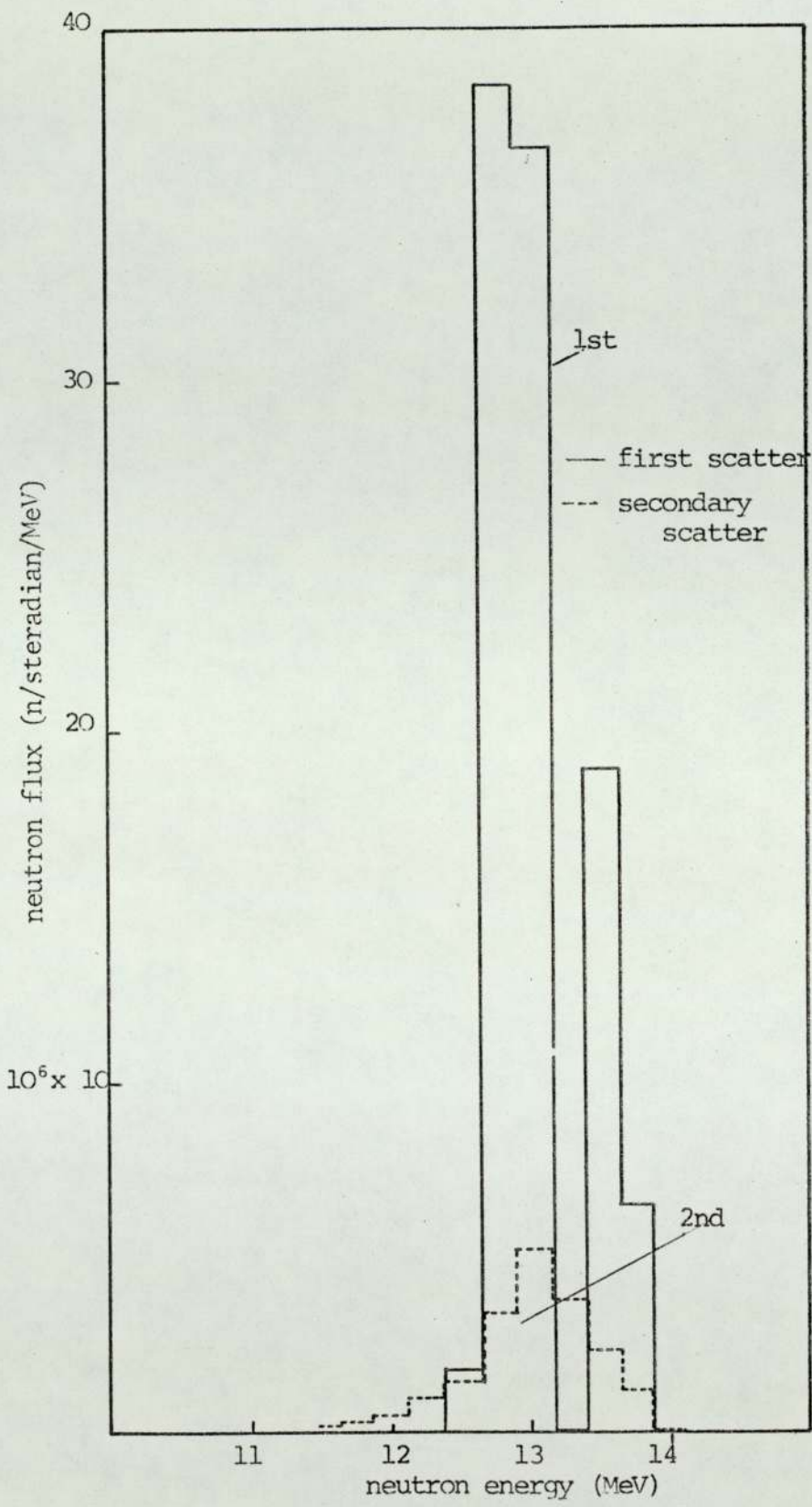


Fig. 7.49 Primary and secondary spectra from LiF (6.35cm thick) at angle $\theta=45$

FIG
7-50

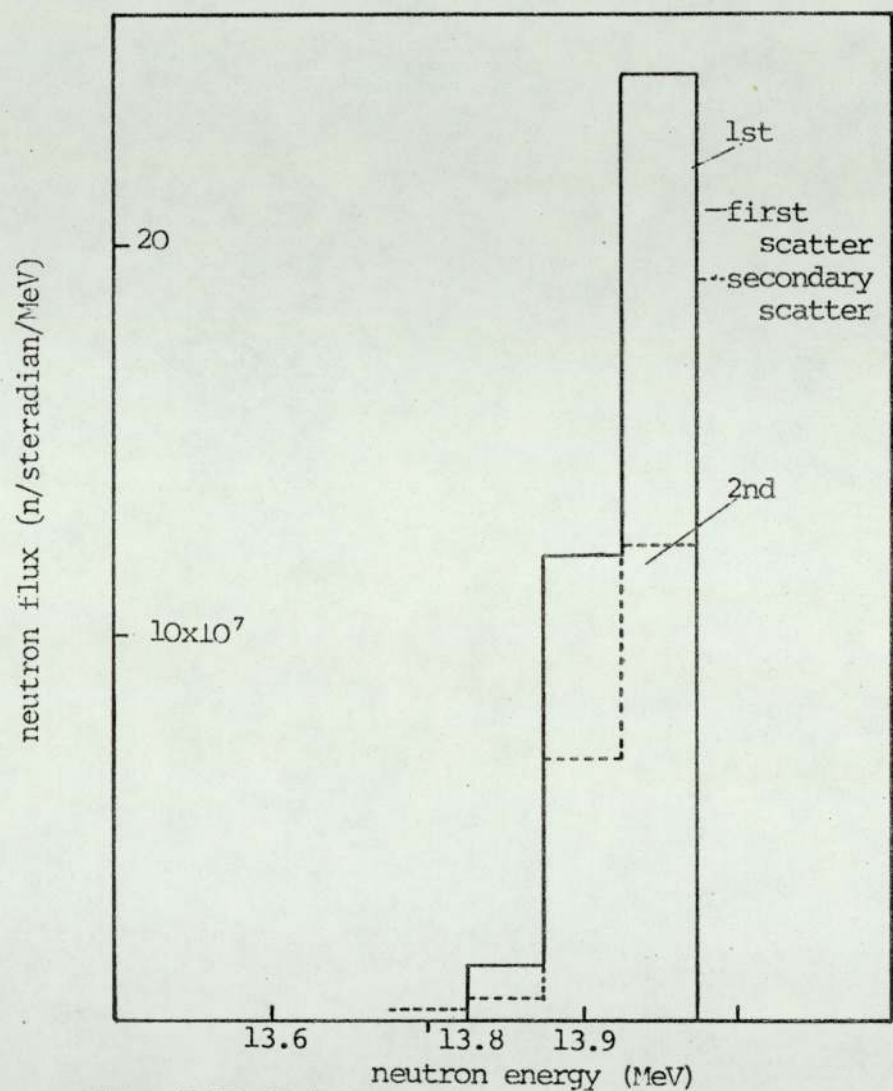


Fig. 7.50 Primary and secondary spectra from Fe (7.62cm thick) at angle $\theta=30$

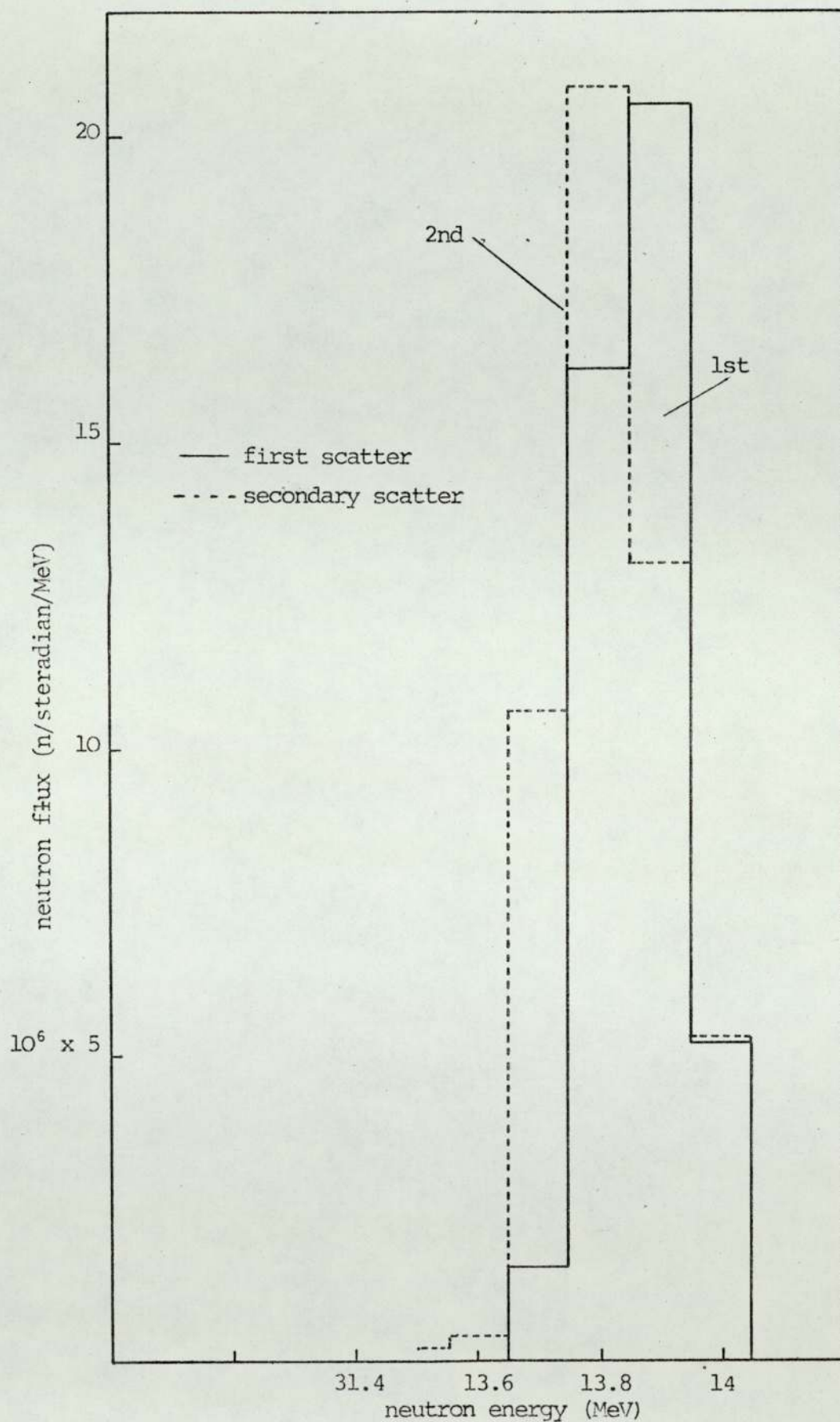
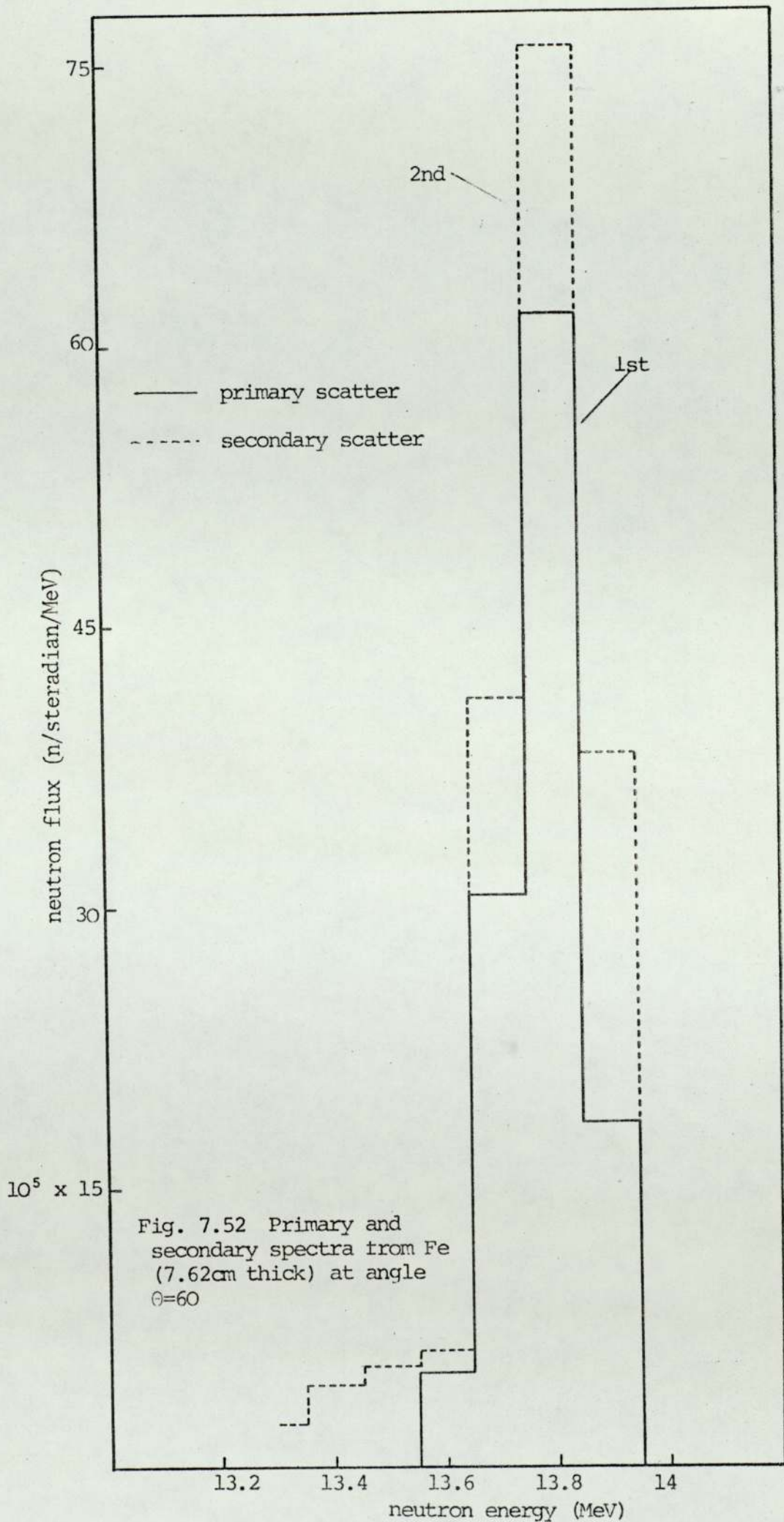


Fig. 7.51 Primary and secondary spectra from Fe (7.62cm thick) at angle $\theta=45$



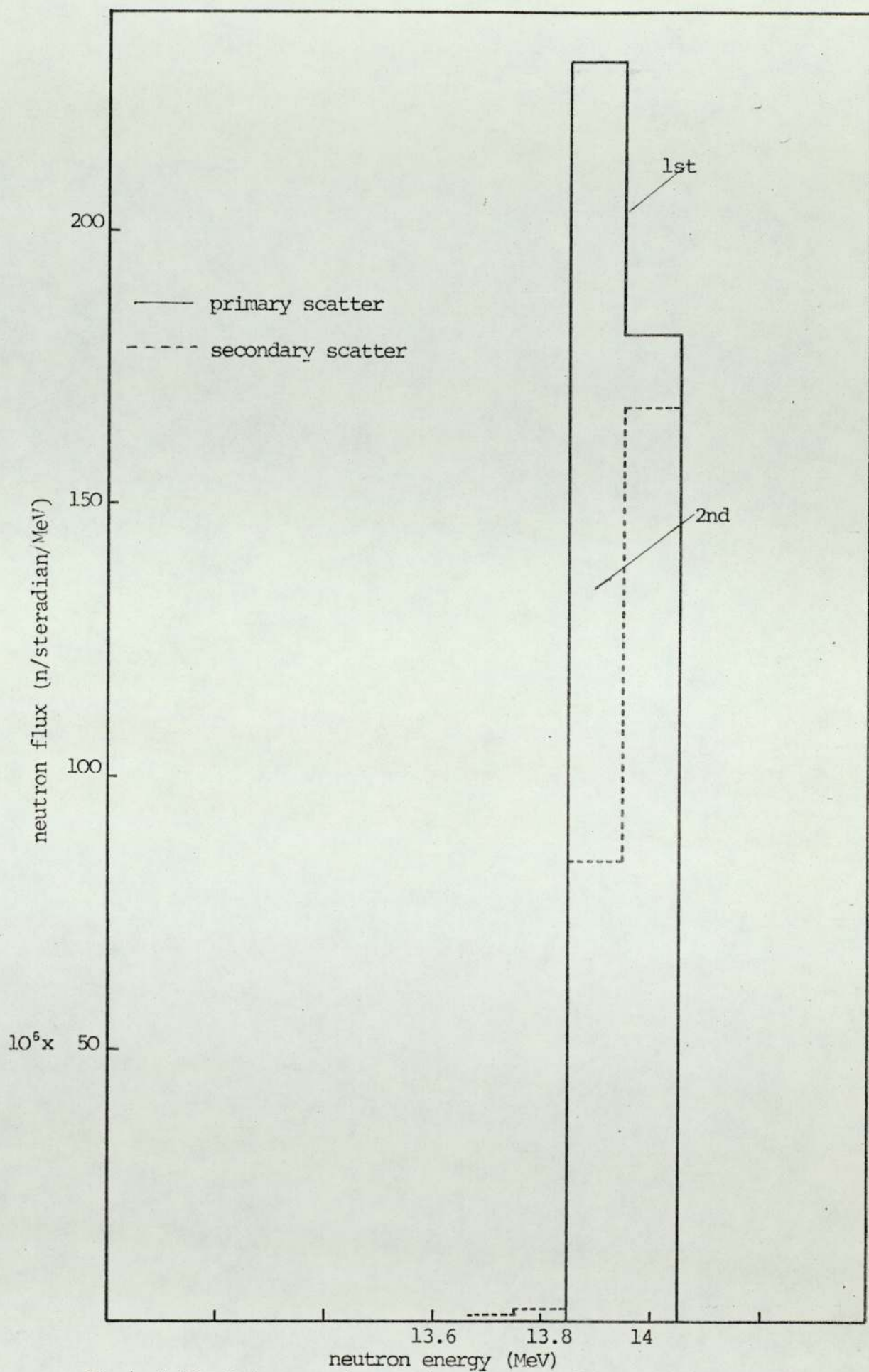


Fig. 7.53 Primary and secondary spectra from Fe (3.6cm thick) at angle $\theta=30$

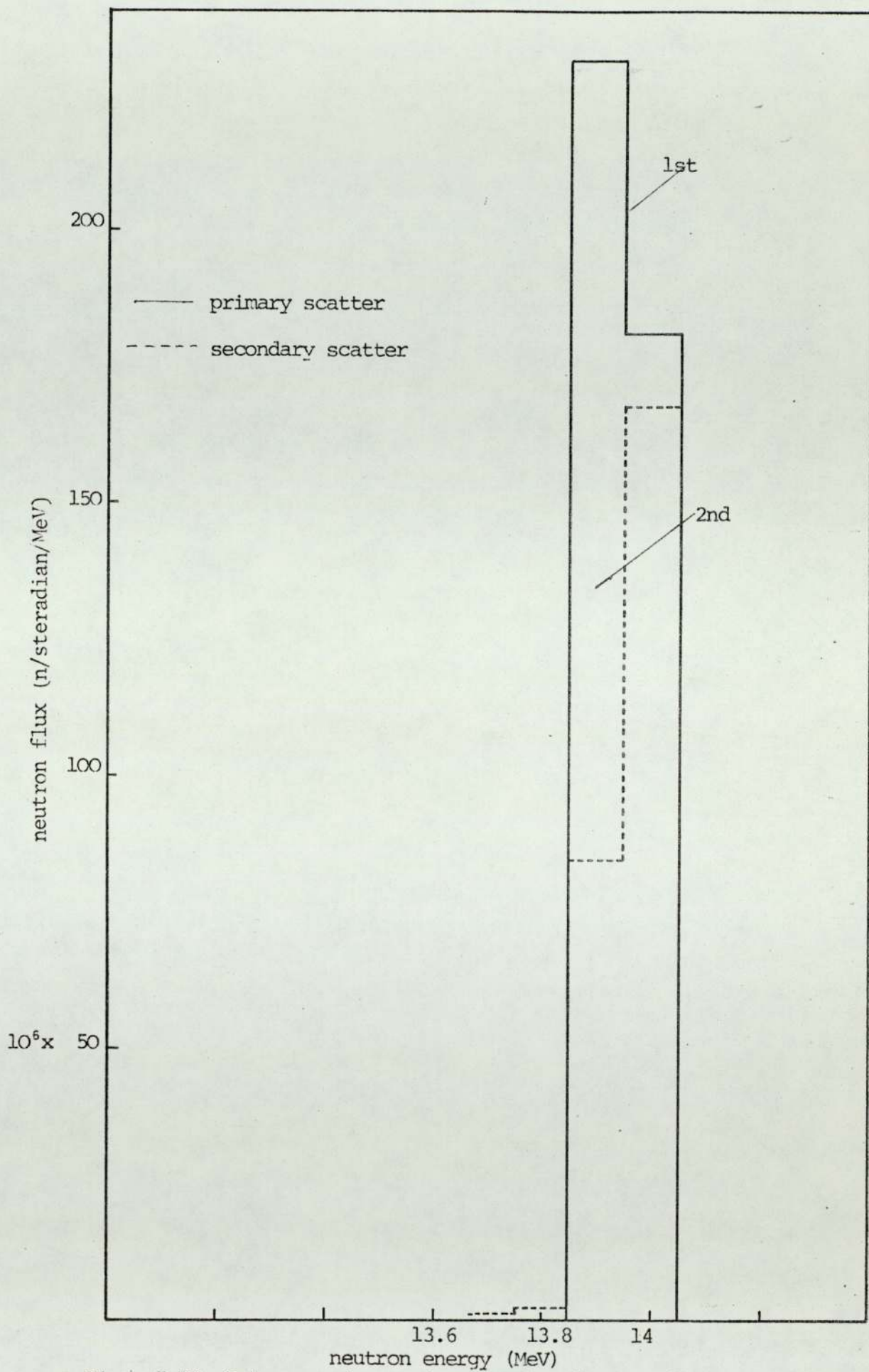


Fig. 7.53 Primary and secondary spectra from Fe (3.6cm thick) at angle $\theta=30$

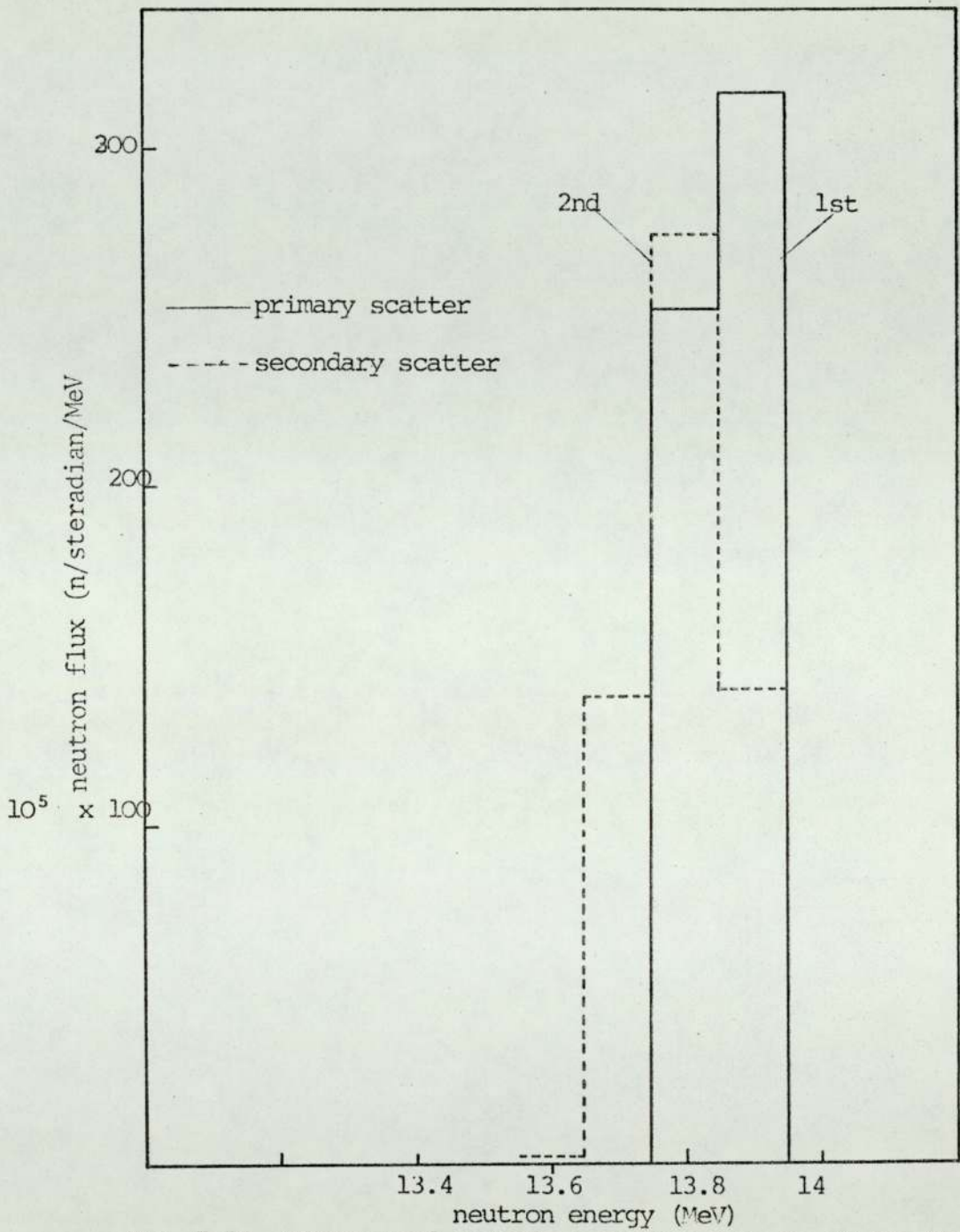


Fig. 7.54 Primary and secondary spectra from Fe (3.6cm thick) at angle $\theta=45$

CHAPTER 8

CONCLUSIONS

The results of the theoretical and experimental angular energy spectra for the scattered 14 MeV neutrons from different thicknesses of LiF and Fe samples have been discussed in Chapter 7 and the following may be concluded.

1. Validity of Cross Section

The good agreement between the theoretically calculated spectra and what has been obtained experimentally indicates the validity of the cross section data, the angular and energy distribution probability data of (U.K.N.D.L.) for ${}^6\text{Li}$, ${}^7\text{Li}$, ${}^{19}\text{F}$ and Fe used in the theoretical calculation. Both the experiment and theory show clearly that the elastic scattering gives the highest contribution to the emerging flux for both LiF and Fe samples. The other reactions do not contribute very much to the emerging flux and their contributions appear generally in the region of the spectrum below the elastic peak. Because of the cut-off energy of the neutron detector, a large proportion of the neutrons due to those reactions are not observed. Both samples show a very strong forward peak for the elastically scattered neutrons which is most pronounced for the iron.


2. Validity of the Calculation Method

The purpose of any computational model is to find out the solution to that particular problem as accurately as possible. With the primary and secondary scatter models adopted for the present work, the theoretical flux has in general been well predicted to fit that of the experimental results. The good

agreement between the theory and experiment made these mathematical models very useful ones due to the small computer time needed compared with the time needed by the other methods. The third, fourth, etc. scatter are not considered in the present work due to the large computing time involved, however the contribution to the flux from the secondary scatter is much less than that of the primary scatter except for the iron samples at large angles, and it can be deduced from the agreement in theoretical and experimental scattered intensities that the contributions from the third, fourth, etc. scatter are going to be considerably lower than the second scatter. Hence it is experimentally justified in most cases to neglect the third, fourth, etc. scatter and be satisfied with the results obtained from the primary and secondary scatter models only, especially at low angles. The iron samples are thicker than the corresponding LiF samples in terms of mean free path and have a very strongly forward peaked elastic scatter. For these samples an improved fit could be obtained by consideration of higher order scattering at higher detector angles but time and suitability of computing facilities did not allow this to be carried further in the present work. Within these limits the experiments validate the cross section data used from the (U.K.N.D.L.) file in particular elastic cross sections, total cross section and elastic angular distribution data.

3. Limitation of experiment

In the time-of-flight technique the associated particle method with the use of flat plate geometry shows its usefulness in the angular energy distribution measurements of the scattered



14MeV neutrons. However there is the time resolution limitation involved with the spectrometer such as the time uncertainty associated with the NE-102A scintillator due to its thickness and the transit time spread associated with the photomultiplier, besides the time resolution associated with the electronic circuitry. A reduction in the time uncertainty of the NE-102A scintillator could be achieved by decreasing its thickness but there is a limitation due to the decreases in the efficiency with the decrease of the scintillator thickness. The time resolution could also be improved by increasing the distance of the neutron detector as far as possible so to make the time spread in the photomultiplier tube and the associated circuitry as well as the scintillator of negligible effect on the whole flight time, but the limitation is associated with the requirement of a larger scintillator area to cover the same solid angle. Background counts will increase roughly proportional to the area of the detector i.e. with the square of the distance, and random coincidences may increase so much that the spectrum becomes meaningless for practical accumulation times.

4. Suggestions for future work

For future work the project could be improved from the experimental point of view by using a liquid scintillator such as NE-213 for neutron detection and energy measurement from the recoil proton spectrum applying the pulse shape discrimination technique to eliminate gamma radiation and using a similar detector as a monitor. The data for the angular spectra of the scattered 14 MeV neutrons could be accumulated much faster than that in the time-of-flight technique since greater neutron source strengths could be used and with improved resolution at the expense of complicated and time-consuming technique for unfolding

the spectrum from the pulse-height data. For future work it would be useful to study other materials which might be used in future fusion reactors as structure and blanket materials. Niobium, molybdenum and titanium are likely candidates for the wall materials, the material of the blanket could be pure lithium metal or a lithium compound such as LiF-BeF_2 (FLIBE) or even both in different blanket layers. Many ideas for fusion blankets exist but a choice will probably not be made until a sustained fusion reaction has been successfully demonstrated.

alan script

APPENDIX 1

MATHEMATICAL DERIVATION OF NEUTRON ENERGY

FROM THE $T(d,n)^4\text{He}$ REACTION

APPENDIX 1

Referring to figure 4.4 in the main text and to derive equation 4.1 consider the following

let the interaction be written as

$$m_1 + m_2 \rightarrow m_3 + m_4 + Q$$

$$\left. \begin{array}{l} E_1 \quad 0 \quad E_3 \quad E_4 \\ V_1 \quad 0 \quad V_3 \quad V_4 \end{array} \right\} \begin{array}{l} \text{energy and velocity} \\ \text{in Laboratory system} \end{array}$$

$$u_1 \quad u_2 \quad u_3 \quad u_4 \quad \text{velocity in C.M. system}$$

$$u_1 = V_1 - u_2$$

The conservation laws of momentum and energy in C-M system could be written as follows

Before collision

$$\text{momentum (CM)} = m_1(V_1 - u_2) = m_2 u_2$$

$$u_2 = \frac{m_1}{m_1 + m_2} V_1 = \text{velocity of CM system}$$

$$\therefore V_1 - u_2 = \frac{m_2}{m_1 + m_2} V_1$$

$$\begin{aligned} \text{K.E. (CM)} &= \frac{1}{2} m_1 u_1^2 + \frac{1}{2} m_2 u_2^2 \\ &= \frac{1}{2} m_1 \frac{m_2^2}{(m_1 + m_2)^2} V_1^2 + \frac{1}{2} m_2 \frac{m_1^2}{(m_1 + m_2)^2} V_1^2 \\ &= \frac{1}{2} m_1 V_1^2 \left[\frac{m_2^2 + m_1 m_2}{(m_1 + m_2)^2} \right] = E_1 \frac{m_2}{m_1 + m_2} = \mu E_1 \end{aligned}$$

$$\text{when } \mu = \frac{m_2}{m_1 + m_2}$$

After collision

$$\text{K.E. (CM)} = \frac{1}{2} m_3 u_3^2 + \frac{1}{2} m_4 u_4^2 = \mu E_1 + Q$$

$$\text{Momentum (CM)} \quad m_3 u_3 = m_4 u_4$$

$$u_4 = \frac{m_3}{m_4} u_3$$

$$\frac{1}{2} m_3 u_3^2 + \frac{1}{2} m_4 \frac{m_3^2}{m_4^2} u_3^2 = \mu E_1 + Q$$

$$\therefore \frac{1}{2} m_3 u_3^2 \left| 1 + \frac{m_3}{m_4} \right| = \mu E_1 + Q$$

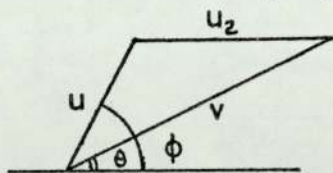
$$u_3 = \sqrt{\frac{2 (\mu E_1 + Q) m_4}{(m_3 + m_4) m_3}}$$

$$\text{also } u_3 = \frac{m_4}{m_3} u_4$$

$$\therefore \frac{1}{2} m_3 \frac{m_4^2}{m_3^2} u_4^2 + \frac{1}{2} m_4 u_4^2 = \mu E_1 + Q$$

$$u_4 = \sqrt{\frac{2 (\mu E_1 + Q) m_3}{(m_3 + m_4) m_4}} = u_3 \frac{m_3}{m_4}$$

Convert to Laboratory system:



$$u \cos \phi + u_2 = v \cos \theta$$

$$u \cos \phi = v \cos \theta - u_2$$

$$u \sin \phi = v \sin \theta$$

$$\therefore u^2 = v^2 + u_2^2 - u^2 - 2u_2 v \cos \theta$$

$$\text{or } v^2 + u_2^2 - u^2 - 2u_2 v \cos \theta = 0$$

put $V = V_3$ $u = u_3$ and multiply by $\frac{1}{2} m_3$

$$\frac{1}{2} m_3 V_3^2 + \frac{1}{2} m_3 u_3^2 - \frac{1}{2} m_3 u_3^2 - m_3 u_2 V_3 \cos \theta = 0$$

$$\text{let } V_1 = \sqrt{\frac{2E_1}{m_1}} \qquad V_3 = \sqrt{\frac{2E_3}{m_3}}$$

$$\therefore E_3 + E_1 \frac{m_1 m_3}{(m_1 + m_2)^2} - \frac{(\mu E_1 + Q) m_4}{m_3 + m_4} - \frac{2\sqrt{m_1 m_3}}{(m_1 + m_2)} E_1 E_3 \cos \theta = 0$$

$$E_3 - \sqrt{E_3} \left[\frac{2\sqrt{m_1 m_3}}{(m_1 + m_2)} \sqrt{E_1} \cos \theta \right] + \left[E_1 \frac{m_1 m_3}{(m_1 + m_2)^2} - \frac{(\mu E_1 + Q) m_4}{(m_3 + m_4)} \right] = 0$$

$$(\sqrt{E_3})^2 + b \sqrt{E_3} + c =$$

$$\sqrt{E_3} = \frac{-b \pm \sqrt{b^2 - 4c}}{2}$$

$$E_3 = (\mu E_1 + Q) \frac{m_4}{(m_3 + m_4)} + E_1 \frac{m_1 m_3}{(m_1 + m_2)^2} \cos^2 \theta$$

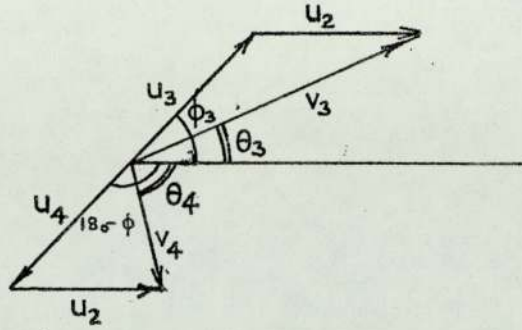
$$\pm \frac{2\sqrt{m_1 m_3}}{(m_1 + m_2)} \cos \theta \sqrt{\frac{E_1 (\mu E_1 + Q) m_4}{(m_3 + m_4)} - \frac{m_1 m_3}{(m_1 + m_2)^2} E_1^2 \sin^2 \theta} \dots \text{A.11}$$

which is the required equation. To get E_4 interchange m_3 and m_4

$$E_4 = (\mu E_1 + Q) \frac{m_3}{(m_3 + m_4)} + E_1 \frac{m_1 m_4}{(m_1 + m_2)^2} \cos^2 \theta$$

$$\pm \frac{2\sqrt{m_1 m_4}}{m_1 + m_2} \cos \theta \sqrt{E_1 \frac{(\mu E_1 + Q) m_3}{(m_3 + m_4)} - \frac{m_1 m_4}{(m_1 + m_2)^2} E_1^2 \sin^2 \theta} \dots \text{A.12}$$

Relationship between angles in CM system



$$u_3 \cos \phi + u_2 = V_3 \cos \theta_3 \quad \text{A 1.3}$$

$$u_3 \sin \phi = V_3 \sin \theta_3 \quad \text{A 1.4}$$

$$u_4 \cos (180-\phi) + u_2 = V_4 \cos \theta_4 \quad \text{A.1.5}$$

$$u_4 \sin (180-\phi) = V_4 \sin \theta_4 \quad \text{A 1.6}$$

$$-u_4 \cos \phi + u_2 = V_4 \cos \theta_4 \quad \text{A 1.7}$$

$$u_4 \sin \phi = V_4 \sin \theta_4 \quad \text{A 1.8}$$

Divide equation A 1.4 by A 1.8

$$\frac{u_3}{u_4} = \frac{V_3}{V_4} \frac{\sin \theta_3}{\sin \theta_4} = \frac{m_4}{m_3}$$

$$\therefore \sin \theta_4 = \sin \theta_3 \sqrt{\frac{m_3}{m_4}} \sqrt{\frac{E_3}{Q+E_1-E_3}}$$

From equation A 1.3 $\cos \phi = \frac{V_3}{u_3} \cos \theta_3 - \frac{u_2}{u_3}$

$$\therefore \cos \phi = \sqrt{\frac{E_3(m_3+m_4)}{(\mu E_1+Q)m_4}} \cos \theta_3 - \frac{m_1}{m_1+m_2} \sqrt{\frac{E_1(m_3+m_4)m_3}{(\mu E_1+Q)m_4 m_1}} \quad \text{A 1.9}$$

The relationship between angles in Laboratory system

From equation A 1.7

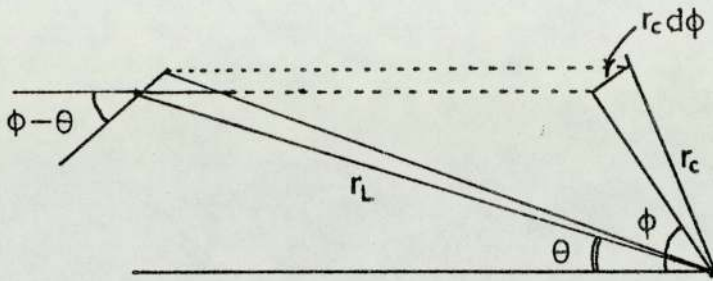
$$\cos \theta_4 = \frac{u_2}{V_4} - \frac{u_4}{V_4} \cos \phi$$

$$\cos \theta_4 = \frac{m_1}{(m_1+m_2)} \sqrt{\frac{E_1 m_4}{E_4 m_1}} - \sqrt{\frac{(\mu E_1 + Q) m_3}{E_4 (m_3+m_4)}} \cos \phi$$

$$\cos \theta_4 = \frac{m_1}{(m_1+m_2)} \sqrt{\frac{E_1 m_4}{E_4 m_1}} - \frac{E_3 m_3}{E_4 m_4} \cos \theta_3 + \frac{m_1}{(m_1+m_2)} \sqrt{\frac{E_1 m_3^2}{E_4 m_1 m_4}}$$

$$\therefore \cos \theta_4 = \sqrt{\frac{m_1}{m_4}} \sqrt{\frac{E_1}{E_4}} - \sqrt{\frac{m_3}{m_4}} \sqrt{\frac{E_3}{E_4}} \cos \theta_3 \quad \text{A 1.10}$$

The anisotropy factor



$$d\Omega_C = \frac{2\pi r_c \sin \phi r_c d\phi}{r_C^2} = 2\pi \sin \phi d\phi$$

$$d\Omega_L = \frac{2\pi r_c \sin \phi r_c d\phi \cos(\phi - \theta)}{r_L^2} = 2\pi \sin \phi d\phi \frac{r_c^2}{r_L^2} \cos(\phi - \theta)$$

if reaction is isotropic in CM system then for L-system the simple isotropic yield must be multiplied by an anisotropy factor

$$A = \frac{d\Omega_C}{d\Omega_L} = \frac{r_L^2}{r_C^2} \frac{1}{\cos(\phi - \theta)}$$

$$\frac{r_L^2}{r_C^2} = \frac{V^2}{u^2}$$

$$\frac{V_3^2}{u_3^2} = \frac{\frac{1}{2} m_3 V_3^2}{\frac{1}{2} m_3 u_3^2} = \frac{E_3}{\frac{1}{2} m_3 2 \left[\frac{u E_1 + Q}{m_3 + m_4} \right]} = \frac{E_3}{m_4 \left[\frac{u E_1 + Q}{m_3 + m_4} \right]}$$

$$\frac{V_4^2}{u^2} = \frac{\frac{1}{2} m_4 V_4^2}{\frac{1}{2} m_3 u_3^2} = \frac{E_3}{\frac{1}{2} m_3 2 \left[\frac{u E_1 + Q}{m_3 + m_4} \right]}$$

$$\cos(\phi - \theta) = \cos \theta + \sin \phi \sin \theta$$

Take equation A 1.4 and multiply both sides by $\sin \theta_3$

$$u_3 \sin \theta_3 \sin \phi = V_3 \sin^2 \theta_3$$

$$\sin \theta_3 \sin \phi = \frac{V_3}{u_3} \sin^2 \theta_3$$

Take equation A 1.3 and multiply both sides by $\cos\theta_3$

$$\cos\theta_3 \cos\phi = \frac{V_3}{u_3} \cos^2\theta_3 - \frac{u_2}{u_3} \cos\theta_3$$

$$u_2 = \frac{m_1}{m_1+m_2} V_1 = \frac{m_3}{m_1+m_2} \sqrt{\frac{2E_1}{m_1}}$$

$$\frac{u_2}{u_3} = \frac{m_1}{m_1+m_2} \sqrt{\frac{E_1}{\left[\frac{uE_1+Q}{m_3+m_4}\right] m_1 m_4}}$$

$$\frac{u_2}{u_4} = \frac{m_1}{m_1 m_2} \sqrt{\frac{E_1}{\left[\frac{uE_1+Q}{m_3+m_4}\right] m_1 m_3}}$$

$$\frac{V_3}{u_3} = \sqrt{\frac{E_3}{m_4 \left(\frac{uE_1+Q}{m_3+m_4}\right)}} \quad \frac{V_4}{u_4} = \sqrt{\frac{E_4}{m_3 \left[\frac{uE_1+Q}{m_3+m_4}\right]}}$$

$$\therefore |A_3| = \sqrt{\frac{E_3}{m_4} \left[\frac{m_3+m_4}{uE_1+Q}\right]} \bigg/ \left[1 - \frac{m_1}{m_1+m_2} \sqrt{\frac{E_1 m_3}{E_3 m_1}} \cos\theta_3 \right]$$

and the same for $|A_4|$

$$|A_4| = \sqrt{\frac{E_4}{m_3} \left[\frac{m_3+m_4}{uE_1+Q}\right]} \bigg/ \left[1 - \frac{m_1}{m_1+m_2} \sqrt{\frac{E_1 m_4}{E_4 m_1}} \cos\theta_4 \right]$$

APPENDIX 2

PROGRAMME NREACTION: COMPUTING THE NEUTRON ENERGY

AS A FUNCTION OF ANGLE FROM THE $T(d,n)^4\text{He}$ REACTION

```

'REGIM' 'COMMENT' 'SYSTEM 17, COOPER, ZNR REACTION, ENERGY, ANISOTROPY OF
NEUTRON AND ASSOCIATED PARTICLE WITH ANGLE';
'PEAL' M1, M2, M3, M4, D, R3, B4, E1, C, ANG, W, F, D3, E3, A3, E43, ANG4, D4, E4, A4, Z;
NEXT;
M1:=R*FAD;
'IF' M1<0 'THEN' 'GOTO' FINISH;
M2:=R*FAD;
M3:=R*FAD;
M4:=R*FAD;
Q:=R*FAD;
NEWLINE(3);
PRINT(M1, 2, 1); WRITETEXT('(1+1)');
PRINT(M2, 2, 1); WRITETEXT('(1=1)');
PRINT(M3, 2, 1); WRITETEXT('(1+1)');
PRINT(M4, 2, 1); WRITETEXT('(1+1)');
PRINT(Q, 2, 3); WRITETEXT('(1MEV)');
B3:=M1*M3/((M1+M2)*(M1+M2));
B4:=M1*M4/((M1+M2)*(M1+M2));
AGAIN;
E1:=R*FAD; 'IF' E1<0 'THEN' 'GOTO' NEXT;
C:=(E1*M2/(M1+M2)+Q)/(M3+M4);
NEWLINE(2);
WRITETEXT('(INCIDENT ENERGY=)');
PRINT(E1, 2, 4); WRITETEXT('(1MEV)');
NEWLINE(1);
WRITETEXT('(ANSTRPY, ENERGY, ANGLE, ENERGY, ANSTRPY,
ENERGY, ANGLE)');
'FOR' ANG:=0 'STEP' 10 'UNTIL' 181 'DO'
'REGIM'
W:=ANG/57.296;
F:=E1*SIN(W);
F:=F*F;
D3:=E1*C+M3/B3-F;
'IF' D3 'LE' 0 'THEN'
'REGIM'
F3:=0;
A3:=0;
E43:=0;
ANG4:=0;
'GOTO' PASS1;
'END';
E3:=C+M4+F1*B3+D3*W+2*B3*SQRT(D3)*COS(W);
A3:=SQRT(F3/(C*M4))/(1-M1/(M1+M2)*SQRT(E1+M3/(E3*M1))*COS(W));
E43:=D+E1-E3;
Z:=SQRT(M1*E1/(M4+E43))-SQRT(M3*E3/(M4+E43))*COS(W);
'IF' Z>0.999999 'THEN'
'REGIM' ANG4:=0; 'GOTO' PASS1; 'END';
'IF' ABS(Z)<0.001 'THEN'
'REGIM' ANG4:=90; 'GOTO' PASS1; 'END';
'IF' Z<-0.999999 'THEN'
'REGIM' ANG4:=180; 'GOTO' PASS1; 'END';
Z:=ARCTAN(SQRT(1-Z*Z)/Z);
ANG4:=90*(1-SIGN(Z))+57.296*Z;
PASS1;
D4:=E1*C+M3/B4-F;
'IF' D4 'LE' 0 'THEN'

'REGIM'
F4:=0;
A4:=0;
'GOTO' PASS2;
'END';
E4:=C+M3+E1*B4+D4*W+2*B4*SQRT(D4)*COS(W);
A4:=SQRT(E4/(C*M3))/(1-M1/(M1+M2)*SQRT(E1+M4/(E4*M1))*COS(W));
PASS2;
NEWLINE(1);
PRINT(A4, 2, 4);
PRINT(F4, 2, 4);
PRINT(ANG, 3, 3);
PRINT(F3, 2, 4);
PRINT(A3, 2, 4);
PRINT(E43, 2, 4);
PRINT(ANG4, 3, 3);
'END';
'GOTO' AGAIN;
FINISH;
'END';

```

APPENDIX 3

PROGRAMME ONESCAT: COMPUTING THE ELASTIC

ANGULAR ENERGY SPECTRUM FROM THE PRIMARY

SCATTER MODEL

```
'PROGRAM' (AXXX)
'INPUT' 0 = CR0
'INPUT' 3 = TR0
'OUTPUT' 0 = LP0
'OUTPUT' 4 = LP1
'EXTENDED DATA'

****
'TRACE' 2
'BEGIN'
'INTEGER' NY,NYMAX,NZ,NZMAX,J,K,L,LMAX,M,N,NMAT;
'REAL' X0,Y,Z,THETA,EN,E0,DENDG,R,COSN,TC,CSTHETA,PHI,THETA1,DTH,EHS,
      EMIN,DE,EMAX,DET,A,B,DY,DZ,ELD,ON,W,C,DC,S,U,V;
E0:=READ: 'COMMENT' INITIAL MEAN NEUTRON ENERGY AT 00 DEG IN MEV;
DENDG:=READ: 'COMMENT' CHANGE IN NEUTRON ENERGY PER DEGREE;
EMAX:=READ: 'COMMENT' MAXIMUM NEUTRON ENERGY IN DATA AND OUTPUT;
EMIN:=READ: 'COMMENT' MINIMUM NEUTRON ENERGY IN OUTPUT;
ELD:=READ: 'COMMENT' MINIMUM NEUTRON ENERGY IN DATA;
DE:=READ: 'COMMENT' ENERGY INTERVAL IN OUTPUT (EMAX-EMIN) MUST BE
          INTEGRAL NUMBER TIMES DE;
DET:=READ: 'COMMENT' ENERGY INTERVAL IN DATA (EMAX-ELD) MUST BE
          INTEGRAL NUMBER TIMES DE;
DC:=READ: 'COMMENT' COSINE INTERVAL IN DATA 1/DC MUST BE AN INTEGER;
NMAT:=READ: 'COMMENT' NUMBER OF MATERIALS IN SAMPLE;
LMAX:=ENTIER((EMAX-EMIN)/DE+0.1);
J:=ENTIER((EMAX-ELD)/DET+0.1);
K:=ENTIER(1/DC+0.1);
'BEGIN'
'REAL' 'ARRAY' F[0:LMAX],TC,SC[1:NMAT,0:J],P[1:NMAT,0:J,0:K],
      FF[1:NMAT,0:K],ND[1:NMAT],CT[0:J],CS[1:NMAT,0:J,0:K];
'FOR' L:=1 'STEP' 1 'UNTIL' NMAT 'DO'
'BEGIN'
'FOR' M:=0 'STEP' 1 'UNTIL' J 'DO'
'BEGIN'
TC[L,M]:=READ: 'COMMENT' TOTAL CROSS SECTION IN BARNS;
SC[L,M]:=READ: 'COMMENT' ELASTIC CROSS SECTION IN BARNS;
'FOR' N:=K 'STEP' -1 'UNTIL' 0 'DO'
P[L,M,N]:=READ: 'COMMENT' ELASTIC SCATTERING PROB BY AS FN OF COS;
```

```
'END';
'FOR' K:=K 'STEP' -1 'UNTIL' 0 'DO'
EELL,M]:=READ: 'COMMENT' FRAC ENERGY CHANGE ON SCATT AS FN OF COS:
'END';
'FOR' L:=1 'STEP' 1 'UNTIL' NMAT 'DO'
NDLL]:=READ: 'COMMENT' NUMBER DENSITY TIMES 10-24;
'FOR' M:=0 'STEP' 1 'UNTIL' J 'DO'
'BEGIN'
CT[M]:=0;
'FOR' L:=1 'STEP' 1 'UNTIL' NMAT 'DO'
'BEGIN'
CT[L]:=CT[M]+T[C[L,M]]*ND[L];
'FOR' K:=0 'STEP' 1 'UNTIL' K 'DO'
CS[L,M,N]:=SC[L,M]*ND[L]*PL[M,N];
'END';
'END';
'FOR' M:=0 'STEP' 1 'UNTIL' J 'DO'
'BEGIN'
NEWLINE(1);
PRINT((FMAX-M*DET),2,1);

PRINT(CT[M],1,6);
'END';
'FOR' L:=1 'STEP' 1 'UNTIL' NMAT 'DO'
'BEGIN'
NEWLINE(2);
PRINT(ND[L],1,6);
'FOR' M:=0 'STEP' 1 'UNTIL' J 'DO'
'BEGIN'
NEWLINE(1);
PRINT((FMAX-M*DET),2,1);
'FOR' K:=K 'STEP' -1 'UNTIL' 0 'DO'
PRINT(CS[L,M,N],1,6);
'END';
NEWLINE(1);
'FOR' M:=K 'STEP' -1 'UNTIL' 0 'DO'
PRINT(EELL,M],1,6);
'END';
QN:=READ: 'COMMENT' TOTAL NEUTRON INPUT;
Y0:=READ: 'COMMENT' SOURCE DISTANCE FROM SCATTERER INNER FACE;
TX:=READ: 'COMMENT' SCATTERER THICKNESS;
NYMAX:=READ:
DY:=READ: 'COMMENT' WIDTH OF NEUTRON BEAM=2*NYMAX*DY;
NZMAX:=READ: 'COMMENT' NZMAX MUST BE EVEN;
DZ:=READ: 'COMMENT' HEIGHT OF NEUTRON BEAM=2*NZMAX*DZ;
NEWLINE(1);
WRITETEXT('IQN=');
PRINT(QN,0,4);
NEWLINE(1);
WRITETEXT('TX=');
PRINT(TX,2,1);
NEWLINE(1);
WRITETEXT('X0=');
PRINT(X0,2,1);
NEWLINE(1);
WRITETEXT('BEAMWIDTH=');
PRINT((2*NYMAX*DY),2,1);
NEWLINE(1);
WRITETEXT('BEAMHEIGHT=');
PRINT((2*NZMAX*DZ),2,1);
AGAIN:
PHI:=READ: 'COMMENT' DETECTOR ANGLE IN DEGREES FROM NORMAL TO SCATTERER
```

```

      IN POS Y DIRECTION, DETECTOR IN X-Y PLANE;
      'IF' PHI<0 'THEN' 'GOTO' LAST;
      NEWLINE(2);
      WRITEIFXT('('PHI='));
      PRINT(PHI,3,1);
      WRITEIFXT('('DEGREES''));
      PHI:=PHI/57.296;
      'FOR' L:=0 'STEP' 1 'UNTIL' LMAX 'DO' F[L]:=0;
      'FOR' NY:=-NYMAX 'STEP' 1 'UNTIL' NYMAX 'DO'
      'FOR' NZ:=-NZMAX 'STEP' 1 'UNTIL' NZMAX 'DO'
      'BEGIN'
      Y:=NY*DY;
      Z:=NZ*DZ;
      'IF' ABS(NZ)>(NZMAX/2) 'THEN' W:=2*(1-ABS(NZ)/NZMAX) 'ELSE' W:=1;
      'COMMENT' W IS WEIGHTING FUNCTION FOR NON-UNIFORM NEUTRON BEAM;
      THETA:=ARCTAN(Y/SQRT(X0*X0+Z+Z));
      R:=SQRT(X0*X0+Y*Y+Z+Z);
      COSN:=Y/R;
      EN:=E0-THETA*57.296*DENJG;

      A:=(EMAX-EN)/DET;
      J:=ENTIFR(A);
      A:=A-J;
      U:=(CT[J]*(1-A)+CT[J+1]*A)/COSN;
      CSTHETA:=COS(PHI)*X0/R+SIN(PHI)*Y/R;
      R:=CSTHETA/DC;
      K:=ENTIFR(R);
      H:=H-K;
      'FOR' N:=1 'STEP' 1 'UNTIL' NMAX 'DO'
      'BEGIN'
      ENS:=EN*(E[N,K]*(1-B)+E[N,K+1]*B);
      'IF' ENS<EMIN 'THEN' 'GOTO' PASS1;
      C:=CS[N,J]*Y*(1-A)+(1-B)+CS[N,J,K+1]*(1-A)*B
        +(CS[N,J+1,K+1]*A*(1-B)+CS[N,J+1,K+1]*A*B);
      L:=ENTIFR((ENS-EMIN)/DE+0.5);
      V:=(EMAX-ENS)/DET;
      M:=ENTIFR(V);
      V:=V-M;
      S:=(CT[L]*(1-V)+CT[L+1]*V)/COS(PHI);
      'IF' ABS((U-S)*TX) < 0.01 'THEN'
      F[L]:=F[L]+C*EXP(-U*TX)*TX*U/COSN
      'ELSE'
      F[L]:=F[L]+C*(EXP(-S*TX)-EXP(-U*TX))*W/((U-S)*COSN);
      PASS1:
      'END';
      'END';

      NEWLINE(1);
      WRITEIFXT('('ENERGY%XXFLIX''));
      'FOR' L:=0 'STEP' 1 'UNTIL' LMAX 'DO'
      'BEGIN'
      NEWLINE(1);
      PRINT((EMIN+1*DE),2,2);
      PRINT(F[L]-UH/(3*NYMAX*NZMAX*DE),0,4);
      'END';
      'GOTO' AGAIN;
      'END';
      LAST:
      'END';

```

```

IX          LENGTH 1563
TS USED    40
#AXXX      FC

```

APPENDIX 4

PROGRAMME TWOSCAT: COMPUTING THE ELASTIC ANGULAR ENERGY

SPECTRUM FROM THE SECONDARY SCATTER MODEL

```
'PROGRAM' (AXXX)
'INPUT' 0 = CRO
'INPUT' 3 = TRO
'OUTPUT' 0 = LPO
'OUTPUT' 4 = LP1
'EXTENDED DATA'

****
'TRACE' 2
'BEGIN'
'INTEGER' NET, LMAX, NANG, I, J, K, L, M, NXMAX, NYMAX, NZMAX, NS, NX, NY, NZ,
G, H, N, NMAT:
'REAL' F0, F1, E2, DET, DE, QN, DX, DY, DZ, TX, HWY, PHI, RU, R1, R2, R3, X, Y, Z, W, C, D, H,
THETA1, THETA2, NORM, EMIN, CS1, CS0, DANG, FLD, CT1, CT2, A, B, EMAX, DC, CTO, CP, SPI
E0:=READ; 'COMMENT' INITIAL MEAN NEUTRON ENERGY AT 90 DEG IN MEV;
EMAX:=READ; 'COMMENT' MAXIMUM NEUTRON ENERGY IN DATA AND OUTPUT;
EMIN:=READ; 'COMMENT' MINIMUM NEUTRON ENERGY IN OUTPUT;
ELD:=READ; 'COMMENT' MINIMUM NEUTRON ENERGY IN DATA;
DE:=READ; 'COMMENT' ENERGY INTERVAL IN OUTPUT (EMAX-EMIN) MUST BE
INTEGRAL NUMBER TIMES DE;
DET:=READ; 'COMMENT' ENERGY INTERVAL IN DATA (EMAX-ELD) MUST BE
INTEGRAL NUMBER TIMES DET;
DC:=READ; 'COMMENT' COSINE INTERVAL IN DATA 1/DC MUST BE AN INTEGER;
NMAT:=READ; 'COMMENT' NUMBER OF MATERIALS IN SAMPLE;
LMAX:=ENTIER((EMAX-EMIN)/DE+0.1);
J:=ENTIER((EMAX-ELD)/DET+0.1);
K:=ENTIER(1/DC+0.1);
'BEGIN'
'REAL' 'ARRAY' F[0:LMAX], TC, SC[1:NMAT, 0:J], P[1:NMAT, 0:J, -K:K],
EE[1:NMAT, -K:K], ND[1:NMAT], CT[0:J], CS[1:NMAT, 0:J, -K:K];
'FOR' L:=1 'STEP' 1 'UNTIL' NMAT 'DO'
'BEGIN'
'FOR' M:=0 'STEP' 1 'UNTIL' J 'DO'
'BEGIN'
TC[L, M]:=READ; 'COMMENT' TOTAL CROSS SECTION IN BARN;
SC[L, M]:=READ; 'COMMENT' ELASTIC CROSS SECTION IN BARN;
'FOR' N:=K 'STEP' -1 'UNTIL' -K 'DO'
P[L, M, N]:=READ; 'COMMENT' ELASTIC SCATTERING PROB AS FN OF COS
```



```
'ENDI';
'FOR' K1=K 'STEP' -1 'UNTIL' -K 'DO'
EE[L,N]=READ; 'COMMENT' FRAC ENERGY CHANGE ON SCATT AS FN OF COS;
'ENDI';
'FOR' L1=1 'STEP' 1 'UNTIL' NMAX 'DO'
ND[L]=READ; 'COMMENT' NUMBER DENSITY TIMES 10=24;
'FOR' M1=0 'STEP' 1 'UNTIL' J 'DO'
'BEGIN'
CT[M]=0;
'FOR' L1=1 'STEP' 1 'UNTIL' NMAX 'DO'
'BEGIN'
CT[M]=CT[M]+TC[L,M]*ND[L];
'FOR' N1=K 'STEP' -1 'UNTIL' -K 'DO'
CSEL[M,N]=SC[L,M]*ND[L]*P[L,M,N];
'ENDI';
'ENDI';
QN:=READ; 'COMMENT' TOTAL NUMBER OF NEUTRONS INCIDENT ON SAMPLE;
DX:=READ; 'COMMENT' X-DIMENSION OF SCATTERING CELL;
NXMAX:=READ; 'COMMENT' THICKNESS=(NXMAX+1)*DX;
DY:=READ; 'COMMENT' Y-DIMENSION OF SCATTERING CELL;

NYMAX:=READ; 'COMMENT' WIDTH=(2*NYMAX+1)*DY;
DZ:=READ; 'COMMENT' Z-DIMENSION OF SCATTERING CELL;
NZMAX:=READ; 'COMMENT' HEIGHT=(2*NZMAX+1)*DZ;
TX:=(NXMAX+1)*DX; 'COMMENT' THICKNESS;
HWY:=(NYMAX+0.5)*DY; 'COMMENT' HALF WIDTH;
B:=(EMAX-EN)/DET;
J:=ENTJFR(B);
B1=B-J;
CT0:=CT[J]+(1-R)+CT[J+1]*R;
AGAIN;
PHI:=READ; 'COMMENT' ANGLE BETWEEN DETECTOR AXIS AND X-AXIS IN
DEGREES, DETECTOR IN X-Y PLANE;
'IF' PHI<0 'THEN' 'GOTO' LAST;
NEWLINE(2);
WRITETEXT(' (PHI=) ');
PRINT(PHI,3,1);
WRITETEXT(' (DEGREES) ');
PHI:=PHI/57.296;
CP:=COS(PHI);
SP:=SIN(PHI);
'FOR' L1=0 'STEP' 1 'UNTIL' LMAX 'DO' F[L]=0;
'FOR' NS1=0 'STEP' 1 'UNTIL' NXMAX 'DO'
'BEGIN'
R0:=(NS+0.5)*DX;
'FOR' NX1=0 'STEP' 1 'UNTIL' NXMAX 'DO'
'BEGIN'
X:=(NX+0.5)*DX;
W1=X-R0;
'FOR' NY1=-NYMAX 'STEP' 1 'UNTIL' NYMAX 'DO'
'BEGIN'
Y1=NY*DY;
'FOR' NZ1=-NZMAX 'STEP' 1 'UNTIL' NZMAX 'DO'
'BEGIN'
Z1=NZ*DZ;
R1=W*W+Y*Y+Z*Z;
'IF' R1<0.001 'THEN' 'GOTO' PASS2;
R1:=SQRT(R1);
'IF' PHI=0 'THEN'
'BEGIN'
R2:=(TX-X);
'GOTO' PASS1;
```

```
'END';
R2:=(TX-X)/CP;
R3:=(HWY-Y)/SP;
'IF' R3<R2 'THEN' R2:=R3;
PASS1:
A:=W/(R1*DC);
A:=0.9999*A;
I:=ENTIFR(A);
A:=A-I;
D:=(W*CP+Y*SP)/(R1*DC);
D:=0.9999*D;
G:=ENTIFR(D);
D:=D-G;
'FOR' LI=1 'STEP' 1 'UNTIL' NMAT 'DO'
'BEGIN'
E1:=E0*(EE[L,I]*(1-A)+EE[L,I+1]*A);
'IF' E1 'LE' (EMIN+0.1*DE) 'THEN' 'GOTO' PASS3;
CS0:=CS[L,J,I]*(1-B)*(1-A)+CS[L,J+1,I]*B*(1-A)
      +CS[L,J,I+1]*(1-B)*A+CS[L,J+1,I+1]*R*A;

C1:=(EMAX-E1)/DET;
N:=ENTIFR(C);
C:=C-N;
CT1:=CT[N]*(1-C)+CT[N+1]*C;
'FOR' K=1 'STEP' 1 'UNTIL' NMAT 'DO'
'BEGIN'
E2:=E1*(EE[K,G]*(1-D)+EE[K,G+1]*D);
'IF' E2 'LE' (EMIN+0.1*DE) 'THEN' 'GOTO' PASS4;
CS1:=CS[K,N,G]*(1-C)*(1-D)+CS[K,N+1,G]*C*(1-D)
      +CS[K,N,G+1]*(1-C)*D+CS[K,N+1,G+1]*C*D;
U:=(EMAX-E2)/DET;
H:=ENTIFR(U);
U:=U-H;
M:=ENTIFR((E2-EMIN)/DE+0.5);
CT2:=CT[H]*(1-U)+CT[H+1]*U;
U:=CT0*P0+CT1*R1+CT2*R2;
F[M]:=F[M]+CS0*CS1*EXP(-U)/(R1*R1);
PASS4:
'END';
PASS3:
'END';
PASS2:
'END';
'END';
'END';
'END';
NORM:=DX*DX*DY*DZ+QN/DE;
NEWLINE(1);
WRITETEXT('ENERGYXXFLUX');
'FOR' MI=0 'STEP' 1 'UNTIL' LMAX 'DO'
'BEGIN'
NEWLINE(1);
PRINT((EMIN+M*DE),2,2);
PRINT(F[M]*NORM,0,4);
'END';
'GOTO' AGAIN;
'END';
LAST;
'END';
```

```
:X          LENGTH 1437
:TS USED    36
#AXXX      EC
```

APPENDIX 5

PROGRAMME SPECTRUM: COMPUTING THE ANGULAR ENERGY

SPECTRUM FROM THE $(n, n\alpha)$, (n, n^1) , $(n, 2n)$ REACTIONS

USING THE PRIMARY SCATTER MODEL

```
!BEGIN!  
!INTEGER! J,K,L,NMAT;  
!REAL! FMAX,EMIN,DES,C,QN,TX,SC,PHI,PS,CS,A,EA;  
EMAX:=RFAD;  
EMIN:=RFAD;  
DES:=READ; !COMMENT! (FMAX-EMIN)/DES MUST BE AN INTEGER!  
J:=F+TIFR((EMAX-EMIN)/DES+0.1);  
NMAT:=READ; !COMMENT! NUMBER OF MATERIALS;  
!BEGIN!  
!REAL! ARPAY SPEC,CT,F[1,J],ND[1,NMAT];  
!FOR! L:=1 !STEP! 1 !UNTIL! J !DO! CT[L]=0;  
!FOR! K:=1 !STEP! 1 !UNTIL! NMAT !DO!  
!BEGIN!  
ND[K]:=RFAD; !COMMENT! NUMBER DENSITY TIMES 10-24;  
!FOR! L:=1 !STEP! 1 !UNTIL! J !DO!  
!BEGIN!  
C:=READ; !COMMENT! TOTAL MICROSCOPIC CROSS SECTION;  
CT[L]:=CT[L]+C*ND[K];  
!END!  
!END!  
QN:=READ; !COMMENT! NUMBER OF INCIDENT NEUTRONS;  
TX:=READ; !COMMENT! SCATTERER THICKNESS;  
NEWLINE(1);  
PRINT(TX,2,2);  
NEXT;  
K:=READ; !COMMENT! IDENTIFIES ISOTOPE INVOLVED IN REACTION;  
!IF! K<0 !THEN! !GOTO! PASS3;  
SC:=READ; !COMMENT! REACTION CROSS SECTION;  
!FOR! L:=1 !STEP! 1 !UNTIL! J !DO! SPEC[L]=READ;  
!COMMENT! EMISSION SPECTRUM OF REACTION;  
AGAIN;  
PHI:=READ; !COMMENT! DETECTOR ANGLE IN DEGREES;  
!IF! PHI<0 !THEN! !GOTO! PASS2;  
NEWLINE(2);  
PRINT(K,2,0);  
PRINT(SC,1,4);  
PRINT(PHI,2,2);  
PS:=READ; !COMMENT! DIFFERENTIAL REACTION PROB AT ANGLE PHI;  
CS:=SC*PS*ND[K];  
A:=1/COS(PHI/57.296);  
EA:=EXP(-CT[J]*TX);  
!FOR! L:=1 !STEP! 1 !UNTIL! J !DO!  
!BEGIN!  
!IF! SPEC[L]<.000001 !THEN!  
!BEGIN!  
F[L]=0;  
!GOTO! PASS1;  
!END!  
!IF! ABS(CT[J]-CT[L]*A)*TX<0.01 !THEN! F[L]=QN*CS*TX*EA*SPEC[L];  
!ELSE!  
F[L]=QN*CS*(EA-EXP(-CT[L]*A*TX))/(CT[L]*A-CT[J])*SPEC[L];  
PASS1;  
NEWLINE(1);  
PRINT((EMIN+(L-1)*DES),2,2); PRINT((FMIN+L*DES),2,2);  
PRINT(F[L],0,6);  
!END!  
!GOTO! AGAIN;  
PASS2;  
!GOTO! NEXT;  
PASS3;  
!END!  
!END!
```

```
!GOTO! AGAIN;  
PASS2;  
!GOTO! NEXT;  
PASS3;  
!END!  
!END!
```

REFERENCES

1. V.A. Dulin et al. Soviet Atomic Energy, Vol. 17,
No. 6, (1964)
2. I.V. Goryacher et al. Soviet Atomic Energy, Vol. 20,
No. 6, (1966)
3. A. Langsdorf, J.R. et al. Phy. Rev. 107 (1957) 1077
4. M.M. El-Wakil "Nuclear Energy Conversion" in text
Educational publishers 1971.
5. Glasstom and Iorberg "Controlled Thermonuclear Reactions"
D. Van Nostrand Company, Inc. 1960.
6. Artsimovich "Controlled Thermonuclear Reactions"
Trans. from Russian, Oliver & Boyd 1964.
7. S.E. Hunt "Fission fusion and the energy crisis"
Pergamon Press, New York 1974
8. "Papers presented at the Controlled Thermonuclear
Conference" United States Atomic Energy
Commission, February 3-5, 1953.
9. Reactor Handbook Vol. III, part B, Shielding (1962)
10. "Engineering Compendium on Radiation Shielding",
International Atomic Energy Agency,
Vienna Vol. 1, (1968)
11. R.P. Gardner and R.L. Ely Jr., "Radioisotope measurement
application in Engineering" Reinhold
Publishing Corporation 1967.
12. John Lamarsh "Introduction to nuclear reactor theory"
Addison-Wesley Publishing Co. Inc. 1966.
13. Glasston and Sesonski "Nuclear Reactor Engineering"
D. Van Nostrand Co. Inc. 1955.
14. H.W. Brock et al. Rev. Sci. Inst. 31 (1960) 1063
15. L.M. Brown Phy. Rev. 90 (1953) 85.
16. C.H. Johnson and C.C. Trail, Rev. Sci. Inst. 27 (1956) 468
17. R. Batchelor et al, Rev. Sci. Inst. 26 (1955) 1037.

18. J.B. Birks "The Theory and Practice of Scintillation Counting", Pergamon Press (1964)
19. W.J. Price "Nuclear Radiation Detection", McGraw-Hill Book Co. Inc. 1958
20. D.L. Smith et al. Nuclear Inst. & Meth. 64 (1968) 157-166.
21. S. Mubarakmand and M.Anwar, Nuclear Inst. & Meth. 93 (1971) 515-518
22. M. Elaim Toms, IEE Trans. Nucl. Sci. NS 17 No.3(1970) 107.
23. W.W. Lindstrom and B.D. Anderson, Nucl. Inst. & Meth 98 (1972) 413-417.
24. J.M. Paul, Nucl. Inst. & Meth. 88 (1970) 277-283.
25. J.B. Birks, proc. phys. soc. (London) 63A (1950) 1294.
26. M. Shaanan, Nucl. Inst. & Meth. 105 (1972) 69-71.
27. W.D. Allen, "Neutron Detection" Geo. Newnes Ltd., London (1960).
28. H.H. Barschall and M.H. Kanner, phy. Rev. 58 (1940) 590.
29. W.N. Hess, Rev. of Mod. Phy. 30 (1958) 368.
30. Nuclear Enterprises Ltd., Catalogue, 1970.
31. J.B. Marion and J.L. Fowler "Fast Neutron Physics, Part 1" Interscience publishers Inc. (1966)
32. M.W. McNaughton et al. Nucl. Inst. & Meth. 116 (1974) 25-28.
33. J.B. Hunt, Nucl. Inst. & Meth. 85 (1970) 269-276.
34. J.B. Birks, proc. phys. soc., (London) 63A (1950) 1294.
35. J.M. Fowler and C.E. Roos, phy. Rev. 93 (1955) 996.
36. W. Franzen et al. phy. Rev. 79 (1950) 742.
37. H.C. Evans and E.H. Bellamy. proc. phys. soc.(London) 74 (1959) 483.

38. M. Rich and R. Madey, Range Energy Tables, UCRL 2301 (1954)
39. P. Leleux et al. Nucl. Inst. & Meth. 116 (1974) 41-43.
40. L.P. Wishart et al. Nucl. Inst. & Meth. 57 (1967) 237-244).
41. F. de la Bayre, Nucl. Inst. & Meth. 102 (1972) 77-86.
42. R.D. Connor and M.K. Husain Nucl. Inst. & Meth. 6 (1960) 337-342.
43. A.K. Enrstrom et al. Necleonics 10 (1952) 58.
45. J.C. Hopkins et al. Nucl. Inst. & Meta. 56 (1967) 175-176.
46. Technical Bulletin Societe Anonym de Machines Electrostatiques, Grenoble, France, June (1961)
47. D.E. Baynham, Ph.D. Thesis, University of Aston in Birmingham (1971).
48. D.J. Hughes "pile neutron research", Addison-Wesley Publishing Co. Inc. (1953)
49. T.W. Bonner et al. Phy. Rev. 88 (1952) 473.
50. A.O. Hanson, Rev. of Mod. Phy. 21 (1949) 635.
51. J. Benvensite and J. Zenger, UCRL, 4266 (1954).
52. J.L. Fowler and J.E. Brolley jr. Rev. Mod. Phy. 28 (1956) 103.
53. D.L. Allen and M.J. Poole, proc. phys.soc. (London) A204 (1951) 500.
54. S.M. Kabin, Nucl. Inst. & Meth. 109 (1973) 533.
55. H.V. Argo et al, phy. Rev. 87 (1952) 612.
56. J.P. Connor et al. phy. Rev. 88 (1952) 468.
57. W.R. Arnold et al. phy. Rev. 93 (1954) 483.
58. S.D. Warshaw, phy. Rev. 76 (1949) 1759.

59. S.E.R.L. Technical Report No. N.61. E.W. Saker and L.H. Wood.
60. H.K. Reynolds et al. *Phy. Rev.* 92 (1953) 742.
61. H.M. Mann and J.L. Yutema *I.E.E.E. trans. Nucl.Sci.* NS 11 No.3 (1964) 201.
62. J.B. Marion and F.C. Young "Nuclear Reaction Analysis" graphs and tables, North-Holland publishing Co., Amsterdam 1968.
63. H. Van Halem et al. *Nucl. Inst. & Meth.* 98 (1972) 175.
64. G.K. O'Neill *phy. Rev.* 95 (1954) 1235.
65. P.M. Endt and P.B. Smith 'Nuclear reactions' Vol. 11, North-Holland publishing Co. Amsterdam 1962.
66. J.B. Garg *Nucl. Inst. & Meth.* 6 (1960) 72.
67. C.F. Cook, *Nucl. Inst. & Meth.* 15 (1962) 137.
68. E.W. Bennett et al. *Rev. Sci. Inst.* 29 (1958) 982.
69. J. Rethmeier, *Nucl. Inst. & Meth.* 17 (1962) 273.
70. G.C. Nelson et al. *Rev. Sci. Inst.* 30 (1959) 963.
71. T.A. Love et al. *Rev. Sci. Inst.* 39 (1968) 541.
72. W.J. McDonald and J.M. Robson, *Nucl. Phy.* 59 (1964) 321.
73. P.B. Johnson et al. *Nucl. Inst. & Meth.* 100 (1972) 141.
74. P.H. Stelson et al. *Nucl. Phy.* 68 (1965) 97.
75. J.C. Alder and B. Voucher, *Nucl. Phy.* A147 (1970) 657.
76. M. Matoba et al. *Nucl. Inst. & Meth.* 116 (1974) 405.
77. ORTEC catalogue 1971 100 MHZ Discriminator.
78. Ortec Catalogue 1971 Timer
79. Glasston and Edlund "The elements of Nuclear Reactor Theory" D. Van Nostrand Co. Inc. 1952.
80. ISBIN "Introductory Nuclear Reactor Theory" Reinhold Publishing Corpn. 1963.
81. Harold Etherington, Ed. "Nuclear Engineering Handbook" McGraw-Hill, 1958.

82. Weinberg & Wigner "The Physical Theory of Neutron Chain Reaction" University of Chicago Press, Chicago 1958.
83. Robert V. Meghreblian and D.K. Holmes "Reactor Analysis" McGraw-Hill, 1960.
84. Joseph J. McInerney, Nucl. Sci. & Eng. 22 (1965) 215.
85. Nikolai Papmchl, Nucl. Sci. & Eng. 22 (1965) 451.
86. B. Davison "Neutron transport Theory", Oxford at the Clarendon Press 1957.
87. Ornstein and Uhlenbeck, Physica 4 (1937) 478.
88. P.F. Zweifel "Reactor Physics", McGraw-Hill, 1973.
89. R.E. Marshak, Rev. Mod. Phy. 19 (1947) 185.
90. M.H. Kalos et al. Nucleonics 15 (1957) 64.
91. J. Black and C.C. Janker, Physica 18 (1952) 809.
92. R.O. Lane and W.F. Miller, Nucl. Inst. & Meth. 16 (1962) 1.
93. B. Minetti and A. Pasquarell, Nucl. Inst. & Meth. 120 (1974) 509.
94. E.L. Slaggie, Nucl. Sci. & Eng. 30 (1967) 199.
95. S.A. Cox, Nucl. Inst. & Meth. 56 (1967) 245.
96. G. Placjek, Phy. Rev. 12 (1947) 556.
97. I.A. Blech and B.L. Averbach, Phy. Rev. A137 (1965) A1113.
98. G.H. Vineyard, Phy. Rev. 96 (1954) 93.